Multifluid Kelvin-Helmholtz Instability in Weakly Ionised Astrophysical Plasmas

Aoife Clare Jones
B.A.mod.

A Dissertation Submitted for the Degree of Doctor of Philosophy
Dublin City University

Supervisor:
Dr. Turlough Downes
School of Mathematical Sciences
Dublin City University

January 2011

Declaration

I hereby certify that this material, which I now submit for assessment on the programme of study leading to the award of Doctor of Philosophy in Mathematics is entirely my own work, that I have exercised reasonable care to ensure that the work is original, and does not to the best of my knowledge breach any law of copyright, and has not been taken from the work of others save and to the extent that such work has been cited and acknowledged within the text of my work.

Signed: ________________________________

ID Number: 55144462

Date: 18 January 2011

Acknowledgements

I would like to thank my supervisor, Turlough Downes, for all of his support through the years.

I would also like to thank the other members of our astrophysics group, Seán, Steve, Sarah, Mohsen and Wayne for giving me their help along the way. And thanks to Gareth and everyone else I've met in DIAS and through the JETSET conferences. I would also like to thank the other postgrads (past and present), Karen and the staff in DCU for their help and support, and thanks to the School of Mathematics for the financial support during my fourth year.

I wish to acknowledge the SFI/HEA Irish Centre for High-End Computing (ICHEC) and SCI-SYM for the provision of computational facilities and support.

I would like to say thanks to my family, as well as my friends who will be expecting a well-deserved thank you for putting up with me over the years: Danni, Ingrid, Moss, Sally, Vanessa, Paul, Fiona, John, Jim, Ben, Louise, Laura, Mic and Kieran, and anyone else that I've forgotten.

But mostly I need to thank my parents, who have been there for me every step of the way.

This work was partly funded by the CosmoGrid project, funded under the Programme for Research in Third Level Institutions (PRTLI) administered by the Irish Higher Education Authority under the National Development Plan and with partial support from the European Regional Development Fund.

Contents

Abstract

By expanding on the principles of ideal magnetohydrodynamics (MHD), we examine the dynamics of weakly ionised astrophysical plasma flows in a multifluid regime. This numerical study is carried out using the multifluid MHD code HYDRA. An outline of the structure of this code is given in chapter 2 and the schemes which are implemented integrates the MHD equations.

We are interested in multifluid effects on fluid instabilities, in particular the Kelvin-Helmholtz (KH) instability. The KH instability could, for example, play a role in the momentum transfer between the bowshock of a protostellar jet and its surrounding molecular cloud. In particular, changes to the development of the KH instability as a result of including the multlifluid effects of ambipolar diffusion and the Hall effect are isolated and individually studied in chapters 4 and 5 respectively. Finally, chapter 6 provides an in-depth examination of the respective roles these nonideal effects have in a multifluid astrophysical system in which both are expected to occur, such as a molecular cloud.

Multifluid effects on protostellar jets are then examined in a broader context in chapter 7. As a jet propagates into a molecular cloud, it forms a bowshock of swept-up ambient material. As the molecular cloud material is weakly ionised, the bowshock is strongly susceptible to nonideal MHD effects below some characteristic length scale. Large-scale 3D simulations allow us to begin to understand the resulting dynamical differences in both the jet propagation and the structural evolution of the magnetic fields.

Chapter 1

Introduction

This thesis is a study of multifluid magnetohydrodynamic (MHD) effects on the development of the Kelvin-Helmholtz (KH) instability in weakly ionised plasmas. One such weakly ionised plasma is the material found in molecular clouds. Due to the low fraction of ionisation in this plasma, the fluid cannot be described using ideal MHD and multifluid MHD effects must be taken into account. This Introduction provides the background knowledge needed for this study. This includes a knowledge of the structure of molecular clouds, the theory and equations that govern ideal and nonideal MHD, and the applicability of the Kelvin-Helmholtz instability to protostellar jets as well as a review of previous work carried out in this area.

1.1 Molecular Clouds

1.1.1 The Structure of Molecular Clouds

The first theories on the process of star formation were developed by Immanuel Kant and Pierre Simon de Laplace during the 18th century (Kant, 1755; LaPlace, 1796). They postulated that both stars and planets form within rotating, contracting clouds of interstellar gas.

This theory remains the basis for the modern theory of star formation. It is now known that stars form inside relatively dense concentrations of interstellar gas and dust known as molecular clouds (Shu et al., 1987).

Giant Molecular Clouds Molecular clouds vary widely in terms of size and mass. The star formation process occurs in the *giant molecular clouds*, which are typically between tens and hundreds of parsecs (pc) across and contain up to 10^6 solar masses ($M_\odot$) of gas and dust. Our galaxy contains thousands of giant molecular clouds, the nearest of which is the Orion Molecular Cloud, about 450 pc away.

A giant molecular cloud consists of smaller, dense clumps of interstellar material. Each of these clumps are a few parsecs across, contain between 10^3 and 10^4 $M_\odot$ of gas and dust, and are very cold, with temperatures of only about 10 K. The star formation itself takes place in the cloud cores situated at the centres of many of these clumps.

Cloud Cores There is much evidence to support the theory that the process of star formation takes place in the cores of giant molecular clouds (Fix, 1995). Young stars have frequently been found in the vicinity of these cores, and the cloud cores have also been found to be a strong source of intense radiation, the cause of which has been identified as protostars - stars still in their early stage of formation. The cloud core can be either cold or warm. Cold cores, which have temperatures of about 10 K, are about 0.1 pc across and contain between a few tenths and 10 $M_\odot$. Warm cores have temperatures of 30 to 100 K, are between a few tenths and 3 pc across, and contain between 10 and 1000 $M_\odot$ of material. The young stars found to be formed in a cold cloud core generally have masses of 1 $M_\odot$ or smaller. In the case of warm cores, the young stars are usually more massive. Warm cores are so massive that they seem to be capable of forming many young stars rather than just a single one.

Collapse of Cloud Cores Although the process of the formation of cloud cores is still not well understood, it is known that these cores, and the clumps of gas that surround them, are susceptible to gravitational collapse. That is, the core exerts a strong enough gravitational force on itself to overwhelm the internal gas pressure of the core. The critical mass and density above which the magnitude of the gravitational potential energy is larger than the internal kinetic energy, thus causing the collapse, are called the *Jeans* mass and density, and can be approximated as below (Phillips, 1994).

The gravitational potential energy and the thermal kinetic energy for a cloud of mass M and radius R, containing N particles of average mass $\overline{m}$ at a uniform temperature T, can be written as:

$$E_{\mathrm{GR}} = -f\frac{GM^2}{R}\,, \qquad \text{and} \qquad E_{\mathrm{KE}} = \frac{3}{2}NkT\,, \tag{1.1}$$

where a numerical factor of $f = \frac{3}{5}$ describes a spherical cloud of uniform density distribution, but is taken here as unity to describe the density distribution of a cloud that is more dense at the centre.

The cloud will then undergo collapse only if the gravitational force is sufficiently large, that is, if its mass, or equivalently its density, exceed the critical Jeans values:

$$M_{\mathrm{J}} = \frac{3kT}{2G\overline{m}}R\,, \qquad \text{and} \qquad \rho_{\mathrm{J}} = \frac{3}{4\pi M^2}\left[\frac{3kT}{2G\overline{m}}\right]^3\,. \tag{1.2}$$

The conditions as above for gravitational collapse are well understood. What is not as well understood is why the collapse happens so slowly. It would be expected that the galaxy would produce far more new stars each year than it actually does, if it wasn't for a force retarding the collapse of the cloud cores. It is generally believed that magnetic fields are responsible for this. The magnetic field influences the motions of both the charged and uncharged particles in the cloud. The charged particles, such as protons and electrons, are tied to the interstellar magnetic field, and are thus free to move along the field lines but not to cross them. On the other hand, the uncharged particles, such as atoms and molecules, can flow across field lines with no difficulty. However, when these neutral particles cross the field lines, they collide with charged particles that are following the magnetic field. As a result, the motion of the uncharged particles toward the centre of the cloud core is impeded and the collapse of the core is slowed down. This interaction is also the cause of ambipolar diffusion, which will be discussed later in section 1.3.1.

However, as the uncharged atoms and molecules gradually slip across the magnetic field lines, the density of the core increases, and eventually the gravitational pull of the core increases until it overwhelms the support provided by the magnetic field. To reach this point can take anywhere from 1 million to 10 million years, but after this the rest of core collapse can occur much more rapidly, in as little as 100,000 years. After this core collapse, what remains is a newly formed individual star, a protostar, or a multiple star system.

Rotation and Disks The rotation of the interstellar cloud is very important in the development of the protostar system. While the cloud core is very large, the rotation may be very slow, perhaps once every few million years. However, as the cloud undergoes rapid collapse, this rotation increases proportionally, in order to conserve angular momentum. In the equatorial plane of the core and protostar, the cloud matter experiences a centrifugal acceleration due to the rotation that partially counteracts the gravitational pull of the core centre. This slows the material's inward motion and that of the collapsing cloud. As the cloud core contracts even more, the rotation increases to a stage where the infalling gas and dust is no longer accreted onto the star, but accumulates in a rotating nebular disk in the core's equatorial plane. Away from the equatorial plane however, at the rotational poles of the cloud core, the infalling material is unaffected by this rotation, and falls directly onto the protostar. The collapsing cloud has now given form to a central protostar, with a revolving nebular disk, surrounded by a region of gas and dust still being drawn toward the core.

1.1.2 Observable Properties of Molecular Clouds

The modern theories on star formation were inspired by astronomical observations of stars and star forming regions. As these observations have increased in number and improved in accuracy, the evidence has grown to support the current model.

General Properties of the Molecular Cloud The molecular clouds themselves tend to be formed in the high density regions of the spiral arms, in both our Milky Way and in other spiral galaxies. This is backed up by observations of these other galaxies that show most of their molecular gas being concentrated in these spiral arms (e.g. Helfer et al., 2003; Engargiola et al., 2003). In the Milky Way, it is observed that the most massive clouds that contain the most mass and star forming regions are also found preferentially in the galaxy's spiral arms (Solomon et al., 1985).

The mean density of a molecular cloud can be difficult to determine. While the typical density of molecular gas in the Galactic plane has been found to be $n_{\mathrm{H}} \approx 3 \times 10^3\,\mathrm{cm}^{-3}$ (Liszt, 1993), this represents more accurately a dense clump within the molecular cloud where a typical molecule would most likely be found, rather than the cloud itself. By normalising the column density to the typical value found in the Solomon et al. (1987) sample, the mean density in a molecular cloud is found to be much lower, approximately $\overline{n}_{\mathrm{H}} = 84\,\mathrm{cm}^{-3}$.

The lifetime of a molecular cloud is also difficult to determine from observations. Blitz et al. (2007) studied molecular clouds in the Large Magellanic Cloud (LMC) and M33 in order to determine a statistical estimated lifetime. It was found that 25% of clouds had not yet any sign of high-mass star formation. This initial starless stage was estimated to last approximately 7 Myr. As they observed slightly more than twice as many clouds with small HII regions than those with large HII regions, Blitz et al. (2007) estimated a lifetime of 14 Myr for this stage. Finally, it was found that, while older star clusters showed no siginificant spatial correlation with molecular clouds, about 60% of star clusters with ages less than 10 Myr are within 40 pc of a molecular cloud. The conclusion was that molecular clouds are destroyed within about 6 Myr of cluster formation. This gave them a final total approximate lifetime of 27 Myr for a molecular cloud.

The Magnetic Field From the strongly magnetised interstellar medium (ISM) to the weakly magnetised stars, magnetic fields play a vital role in all stages of the star formation process. The strength of the magnetic field of an object can be calculated by observers using either the Zeeman effect or the Chandrasekhar-Fermi method. However, the calculation can depend on the morphology of the field, and results can therefore vary. In the ISM, the median magnetic field has been be measured observationally as $6.0 \pm 1.8\,\mu$G (Heiles & Troland, 2005). The importance of the magnetic field to the structure of a cloud can be determined by the ratio of its mass to the magnetic critical mass, $\mu_\Phi \equiv M/M_\Phi$. The magnetic critical mass is the mass below which a cloud is supported against gravitational collapse by the magnetic flux, Φ, threading the cloud. For the ISM, it is found that $\mu_\Phi < 0.16$, which is highly subcritical, and thus it is prevented from collapsing under gravity. In the molecular clouds however, this ratio is to increase to $\mu_\Phi \geq 2$ so that stars can be formed.

Crutcher (1999) has the largest compilation of magnetic field strengths in molecular clouds. He found that the cores and clumps within his sample are in approximate virial equilibrium, that is, the kinetic and magnetic energies are roughly equal to one another. This had also been predicted theoretically by Zweibel & McKee (1995). Correspondingly, he also found the Alfvén Mach number to be $M_A \approx 1$. Adopting this value, a median magnetic field strength is deduced to be $\overline{B}_{\rm med} = 30\,\mu$G, or an average value of $\overline{B} = 7.60\,\mu$G. However, for the observed parameters, typical molecular clouds would have a critical magnetic field strength of $B_{cr} = 57\,\mu$G. Although the sample by Crutcher (1999) favours warmer, denser cores (median temperatures recorded of 40 K are significantly greater than average), even for the highest line-of-sight magnetic field strengths observed, it can be concluded that molecular clouds are supercritical. These clouds therefore, in the absence of other forces such as thermal pressure and rotation, will be subject to gravitational collapse.

Ionisation of a Molecular Cloud The effect the magnetic field has on the dynamics of a cloud is related directly to the abundance of charged particles in that cloud. This is called the fractional ionisation, $\chi \equiv \frac{n_{\rm e}}{n_{\rm H}}$. The number density of hydrogen atoms is defined here by $n_{\rm H} \equiv n({\rm H}) + 2n({\rm H_2})$. Within star-forming regions, the fractional ionisation can vary greatly, and is dependent on the density of the cloud, which can vary considerably and can be difficult to observe accurately.

In diffuse molecular clouds with densities of $n_{\rm H} \approx 10^2\,{\rm cm}^{-3}$, the primary source of ionisation is from ambient ultraviolet radiation from the interstellar radiation field. The ionisation fraction in these cases are around 10^{-4} (Draine et al., 1983). For dark clouds and dense cores with densities of $n_{\rm H} \approx 10^4\,{\rm cm}^{-3}$ and $n_{\rm H} \approx 10^6\,{\rm cm}^{-3}$ respectively, the UV radiation does not penetrate the cloud as well, and so cannot ionise as much of the contained mass. Instead, cosmic rays tend to be the primary source of ionisation, and the ionisation fractions are considerably lower, approximately $\chi = 10^{-7}$ and $\chi = 10^{-8}$ respectively. (Guelin et al., 1977; Elmegreen, 1979).

Structure and Evolution of a Cloud Core The dense clumps and cores within molecular clouds contain the majority of the mass of the cloud, and appear to be gravitationally bound (Bertoldi & McKee, 1992). As mentioned above, the density of a hydrogen molecule in a cloud clump is $n_{\mathrm{H}} \approx 3 \times 10^3\,\mathrm{cm}^{-3}$. These cores and clumps also have a variety of shapes and sizes, which relate to the set-up of their embedded magnetic fields. In the absence of a magnetic field, for example, a bound cloud is approximately spherical. If the magnetic field in a cloud is such that it tends to compress the cloud, it will be prolate (Fiege & Pudritz, 2000). However, if the field acts in such a way that is supports the cloud against compression by gravity, its shape will be oblate. When the turbulence and support from the magnetic field in a core have reached a low enough level, the core undergoes gravitational collapse. The lifetime of these cores can be approximated using chemical analysis of the more complex molecules, or by statistical analysis. A study by Goldsmith & Li (2005) found lifetimes for cold dark cloud cores to be $10^{6.5-7}$ years, using observed values of the H^0/H_2 ratio. A statistical study of T Tauri stars by Ward-Thompson et al. (2007) found lifetimes of 3 to 5 free-fall times for the observed cores. However, the observational statistics were subject to the approximation that most of the starless cores would eventually become stars and selection effects meant that cores that quickly became supercritical and collapsed were not counted among the starless population.

Formation Processes and Turbulence in a Molecular Cloud Since the 1980s, studies of molecular clouds have focused on large-scale instabilities in the ISM as the trigger for their formation, (e.g. Elmegreen, 1979). The Parker instability (Parker, 1966) and Jeans instability have been found to be the most likely causes. While these large-scale self-gravitating instabilities explain why the molecular clouds are initially turbulent, they are not capable of forming large scale molecular clouds without having unrealistically high star-formation rates (Zuckerman & Palmer, 1974; Vázquez-Semadeni et al., 2007). Mestel & Spitzer (1956) also concluded that this turbulence would decay too soon, and thus rejected it as a mechanism to support the cloud against collapse. The more likely scenario is that while these large-scale instabilities provide the initial turbulence in a cloud, there is a significant contribution made at later stages by the conversion of gravitational energy to turbulent energy during contraction, and from the energy injected back into the cloud from newly formed stars. While new energy injection into the cloud would help to explain the fact that turbulence in molecular clouds is observed to be ubiquitous, if this energy came solely from feedback from young stars, it would be expected that the new turbulence would be more intermittent in both space and time.

Before observations of outflows from protostars were available, Norman & Silk (1980) studied winds from T Tauri stars as a possible source of the injected energy. By measuring the mass, velocity and momentum of the outflows, they calculated the amount of energy that was available to drive the turbulence in a cloud. It was estimated by them, and by Franco (1983) who included winds from protostars in his study, that the energy injection rate was sufficient to support the clouds against collapse. However, more recent observations by Bontemps et al. (1996) have shown that the average outflow momentum may be considerably smaller than was previously assumed (Walawender et al., 2005). Current estimates are that protostellar outflows provide enough momentum to support clouds only with masses less than or equal to $4 \times 10^4 M_\odot$ (Matzner, 2002).

1.2 Magnetohydrodynamics (MHD)

In the plasma physics description of a fluid, the fluid can be treated as consisting of separate ion and electron components, with separate distribution functions corresponding to each. This then leads to a description involving two different fluid velocities for the two components. However, there exist several astrophysical situations in which the electrostatic forces acting on the plasma are such that the electrons and ions move together, allowing the fluid to be described by a single velocity. The analysis then becomes considerably less complicated as the plasma can be treated as a single fluid. This approximation leads to a description of the dynamics of such a plasma known as magnetohydrodynamics (MHD).

1.2.1 The Assumptions behind MHD

MHD is realised only under certain conditions. These require that the electrostatic forces are such that the Lorentz force is significant, that the plasma is locally electrically neutral, that the dynamics of a single fluid can be applied, and that Ohm's Law can be used (Pelletier, 2007). While these conditions will never fully hold true, they are a good approximation for cold, collisional plasmas at lengthscales much greater than that of the mean free path of the particle. Also, although the fluid is being treated using the single fluid approximation, it is important to include the tiny velocity difference between the ion and electron velocities in order to not neglect the electric current that will thus be produced, as well as the resulting generated magnetic field. So while this velocity difference is very small and can be neglected in discussing the macroscopic flow, it must be retained while calculating the electromagnetic field. Similarly, it is required that the current can be described by Ohm's Law in the rest frame of the plasma, $\mathbf{J}' = \sigma \mathbf{E}'$, where the conductivity σ is assumed to be so large that even a very weak electric field can cause significant currents.

Non-relativistic MHD also relies on the magnetostatic approximation, that is, that the magnitude of the Alfvén velocity is much smaller than the speed of light. This allows for the displacement current to be neglected in the Ampère-Maxwell equation.

1.2.2 The Equations of MHD

Maxwell's Equations The MHD equations determine the interaction of magnetised plasmas, and are largely derived from Maxwell's equations:

$$\nabla \cdot \mathbf{E} = 4\rho_{\mathrm{c}} \,, \qquad \nabla \cdot \mathbf{B} = 0 \,,$$

$$\nabla \times \mathbf{E} = -\frac{\partial \mathbf{B}}{\partial t} \,, \quad \nabla \times \mathbf{B} = \mathbf{J} + \frac{\partial \mathbf{E}}{\partial t} \,. \tag{1.3}$$

Here the magnetic field, electric field and current density are represented by $\mathbf{B}$, $\mathbf{E}$, and $\mathbf{J}$ respectively, while ρ_{c} symbolises the charge density. Also, factors of 4π and the speed of light c have been incorporated into the terms for the electric and magnetic fields. The approximations behind MHD then help to obtain the MHD equations as needed.

The magnetostatic approximation, for a non-relativistic fluid, allows for the displacement current term to be neglected in the relevant Maxwell's equation, resulting in:

$$\nabla \times \mathbf{B} \cong \mathbf{J} \,. \tag{1.4}$$

The single fluid approximation requires that the electron and ion fluid are locked together. The result of this is that in the rest frame of the fluid, the plasma is approximately electrically neutral and the charge density is far less than the current density, $\rho_{\mathrm{c}}' \ll |\mathbf{J}'|$. This also implies that $\rho_{\mathrm{c}} \ll |\mathbf{J}|$. Comparing the equation $\nabla \cdot \mathbf{E} = \rho$ with $\nabla \times \mathbf{B} = \mathbf{J}$, it is found that $|\mathbf{E}| \ll |\mathbf{B}|$.

The MHD approximation thus consists of the following conditions (Padmanabhan, 2002):

$$\left|\frac{\mathbf{v}}{c}\right| \ll 1 \,, \quad |\mathbf{E}| \ll |\mathbf{B}| \;, \quad \rho_{\mathrm{c}} \ll |\mathbf{J}| \;, \quad \left|\frac{\partial \mathbf{E}}{\partial t}\right| \ll |\mathbf{J}| \;. \tag{1.5}$$

Differential Equations The differential equations governing MHD can now be derived under the above approximations. The equation to determine the evolution of the magnetic field is found by starting with Maxwell's equation $\frac{\partial \mathbf{B}}{\partial t} = -(\nabla \times \mathbf{E})$ and substituting $\mathbf{J}$ for $\mathbf{E}$ using Ohm's Law in the rest frame of the fluid:

$$\mathbf{J} \simeq \mathbf{J}' \simeq \sigma \mathbf{E}' \cong \sigma \left[\mathbf{E} + (\mathbf{v} \times \mathbf{B}) \right] \ . \tag{1.6}$$

This gives us:

$$\frac{\partial \mathbf{B}}{\partial t} = -\nabla \times \left[\frac{\mathbf{J}}{\sigma} - (\mathbf{v} \times \mathbf{B}) \right] \ . \tag{1.7}$$

Then, substituting for the current density using $\mathbf{J} = \nabla \times \mathbf{B}$, this leads to:

$$\frac{\partial \mathbf{B}}{\partial t} = \nabla \times (\mathbf{v} \times \mathbf{B}) - \nabla \times \left(\frac{1}{\sigma} \nabla \times \mathbf{B} \right) = \nabla \times (\mathbf{v} \times \mathbf{B}) + \frac{1}{\sigma} \nabla^2 \mathbf{B} \ . \tag{1.8}$$

In order to obtain the last equation, the identity $\nabla \times (\nabla \times \mathbf{F}) = \nabla(\nabla \cdot \mathbf{F}) - \nabla^2 \mathbf{F}$ was used, along with the fact that $\nabla \cdot \mathbf{B} = 0$. Note that if $\nabla \cdot \mathbf{B} = 0$ initially, this equation will preserve that condition. This is necessary for consistency. This equation thus determines the evolution of the magnetic field.

Conservation Equations The equations obtained above must be supplemented by the fluid equations for a plasma in order to determine the evolution of the system completely. The first such equation is the equation of continuity, representing the conservation of mass:

$$\frac{\partial \rho}{\partial t} + \nabla \cdot (\rho \mathbf{v}) = 0 \ . \tag{1.9}$$

The Euler equation for conservation of momentum, $\left(\rho \frac{d\mathbf{v}}{dt} + \nabla p = 0 \right)$, must be modified because of the presence of the magnetic field. The force on a particle of charge q is given by $q(\mathbf{v} \times \mathbf{B})$. Hence the force per unit volume on the fluid can be written as $\mathbf{J} \times \mathbf{B}$. Substituting for the current density using $\mathbf{J} = \nabla \times \mathbf{B}$, this additional magnetic force is determined to be $(\nabla \times \mathbf{B}) \times \mathbf{B}$. Thus the Euler equation becomes:

$$\rho \frac{d\mathbf{v}}{dt} = -\nabla p + (\nabla \times \mathbf{B}) \times \mathbf{B} \ . \tag{1.10}$$

.

These three equations ((1.8), (1.9) and (1.10)), together with the isothermal equation of state $p = p(\rho)$, constitute a set of four equations for the four unknowns (ρ, p, $\mathbf{v}$, and $\mathbf{B}$) without the need to solve the energy equation. Once $\mathbf{B}$ has been determined, the current density and the electric field can be calculated from the relations $\mathbf{J} = \nabla \times \mathbf{B}$ and $\mathbf{E} = \left[\frac{\mathbf{J}}{\rho} - (\mathbf{v} \times \mathbf{B})\right]$, thus completely solving the problem.

Significance of the magnetic field There is a noteworthy peculiarity in the study of MHD. In conventional electrodynamics, the charge and current densities are specified and the electric and magnetic fields are then subsequently calculated. In MHD on the other hand, ρ, $\mathbf{v}$, and $\mathbf{B}$ are solved for using the evolution equations, and once the magnetic field is known, $\mathbf{J}$ and $\mathbf{E}$ are calculated as secondary quantities. Thus the magnetic field is clearly of primary importance when plasma is treated in the MHD approximation.

Examining again the equation for the evolution of the magnetic field (1.8):

$$\frac{\partial \mathbf{B}}{\partial t} = \nabla \times (\mathbf{v} \times \mathbf{B}) - \nabla \times \left(\frac{1}{\sigma}\nabla \times \mathbf{B}\right) = \nabla \times (\mathbf{v} \times \mathbf{B}) + \frac{1}{\sigma}\nabla^2 \mathbf{B} \, ,$$

it is seen that the field $\mathbf{B}$ is determined by two different processes. The first term, $\nabla \times (\mathbf{v} \times \mathbf{B})$, has magnitude of order $\left(\frac{vB}{L}\right)$, where L is the scale over which the magnetic field changes. This term causes the magnetic field to flow along with the fluid, by a process called advection. The second term, $\frac{1}{\sigma}\nabla^2 B$, is of the order $\frac{1}{\sigma}\frac{B}{L^2}$. It causes the magnetic field to diffuse through the fluid. The magnetic Reynold's number is defined by the ratio of the magnitudes of the advection term to the diffusion term:

$$R_M = \sigma v L \, . \tag{1.11}$$

This means that when $R_M \gg 1$, the advection term dominates the system, and when $R_M \ll 1$, the diffusion term dominates. In the first case the diffusion term can be ignored, giving

$$\frac{\partial \mathbf{B}}{\partial t} - \nabla \times (\mathbf{v} \times \mathbf{B}) = 0 \, . \tag{1.12}$$

This situation can be interpreted as the magnetic field being frozen into the fluid and carried with it. On the other hand, when $R_M \ll 1$, the advection term is neglected, and the following diffusion equation is obtained:

$$\frac{\partial \mathbf{B}}{\partial t} = \frac{1}{\sigma}\nabla^2\mathbf{B} \simeq \frac{1}{\sigma L^2}\mathbf{B}\,. \tag{1.13}$$

This shows that the diffusion time scale is $t \simeq \sigma L^2$.

In many astrophysical contexts, the magnetic diffusion can be taken as negligible due to the long lengthscales normally involved, and thus the extremely large resulting diffusion timescale. The magnetic field can then be treated as frozen into the fluid and thus described by the first of the two above equations. However, in the case of laboratory plasmas, diffusion can become very important, because of the very different length scales involved.

1.3 The Generalised Ohm's Law

1.3.1 Introduction to Multifluid effects

The Generalised Ohm's Law (Spitzer, 1956) is an expression relating the current density $\mathbf{J}$ in a plasma to the electric field $\mathbf{E}$ acting on it. For an ideal fluid, Ohm's Law is very familiar and is given by:

$$\mathbf{J} = \sigma \mathbf{E} \,, \tag{1.14}$$

where σ is the conductivity of the fluid. Various other terms must be included in this equation for a non-ideal fluid, in order to take into account further forces acting on the plasma. As the expression becomes more complicated, the Generalised Ohm's Law allows for the calculation of the electric field without the need to solve the Poisson equation. There are several resistivity terms that must be included in the non-ideal case, as they cause the dissipation of the electric field (Goldreich & Reisenegger, 1992). They are described qualitatively here, but their actual forms will be derived over the next sections.

Ohmic resistivity is an effect caused by charged particles undergoing collisions with other charged or uncharged particles. This results in an opposition to the flow of current. This resistivity occurs independently of the magnetic field $\mathbf{B}$ and is that which is observed in the Ohm's Law for an ideal fluid. This resistivity occurs in the direction of current. In the presence of a magnetic field, the current can be decomposed into two components, a component parallel to the magnetic field and a component perpendicular to the magnetic field. For the purpose of the following calculations, only the resistivity that acts on the current parallel to the magnetic field is referred to as ohmic resistivity, r_0, from this point onwards. The remaining resistivity, that acting on the component of the current perpendicular to the magnetic field, is dealt with together with the ambipolar resistivity, described in the next paragraph. The magnitude of the ohmic resistivity depends on how easily the charged particles can be impeded from flowing with the field lines. This depends on the Hall parameter of the particle (see section 1.3.2), which is a measure of how well tied to the field line a particular particle is. As all cases examined in this study include at least one particle species with a high Hall parameter, the effect of this particular resistivity is found to be very small, and thus neglected.

Ambipolar resistivity, as mentioned earlier (section 1.1.1), is again a result of collisions between the charged and uncharged particles. As the charged particles experience a Lorentz force from the magnetic field and the neutrals do not, there will exist a velocity difference between them, in a direction perpendicular to the magnetic field. However, as the ions and neutrals are coupled together by normal molecular collisions, a frictional drag force arises between them that causes a diffusion of the magnetic field through the neutral fluid in this direction. Also acting in this direction is the remaining component of the ohmic resistivity. From this point onwards, the resistivity term r_2 incorporates both of these phenomena.

Finally, Hall resistivity r_1 is due to the dispersion of energy as a result of the Hall effect. In the presence of a magnetic field, the moving charged particles experience a Lorentz force, causing a change in their paths. Due to their opposite charges, the force experienced by the electrons and ions acts in opposite directions. This causes a separation of the charged velocities that results in the generation of an electric field. This is known as the Hall effect (Wardle, 2004a), and in this case, leads to a re-orientation of the magnetic field.

The relative importance of these terms depends on the structure of the plasma in question and its ionisation fraction. Astrophysical plasmas can have a wide variety of degrees of ionisation. It is also possible for the same astrophysical object to have both high and low ionisation fractions (Song et al., 2001). For example, an accretion disk around a young star is often approximated to be cold and weakly ionised (Wardle, 2004b). However, at the centre of the disk, closest to the central star, it can have both high temperatures and high fractions of ionisation, due to radiation from the central object.

The approximations that can be made are thus dependent on the astrophysical process in question. Making certain assumptions however does greatly simplify the derivation of the Generalised Ohm's Law. This expression is derived from the momentum equations of the constituent particle fluids in the plasma. The equation takes into account all forces acting on the plasma particles (Krall & Trivelpiece, 1973), including the electric field and Lorentz force, the pressure gradient, the drag force due to collisions with other particles, and the inertia and resultant acceleration. It is written in the form:

$$\alpha_i \rho_i \left(\mathbf{E} + \mathbf{v}_i \times \mathbf{B}\right) = \nabla p_i + \rho_i \frac{D_i \mathbf{v}_i}{Dt} - \sum_{j \neq i}^{N} \mathbf{f}_{ij} \ , \tag{1.15}$$

where α_i is the charge to mass ratio of the particle fluid i, ρ_i the mass density, $\mathbf{v}_i$ the velocity, p_i the partial pressure, $\mathbf{f}_{ij}$ the collisional term between particle fluids i and j, and the Lagrangian derivative is defined as

$$\frac{D_i}{Dt} \equiv \frac{\partial}{\partial t} + \left(\mathbf{v}_i \cdot \nabla\right) . \tag{1.16}$$

The relative importance of each of the terms in (1.15) depends, however, on the physical assumptions being made.

1.3.2 Generalised Ohm's Law for a weakly ionised plasma

In the case of assuming a weakly ionised plasma, the derivation begins with the momentum equation (1.15) and by making certain approximations.

Firstly, it is assumed that a fluid of neutral particles makes up the majority of the plasma. Therefore the velocity of the fluid as a whole, $\mathbf{v}$, can be approximated to be roughly equal to that of the neutral fluid, $\mathbf{v}_1$ (where the subscript 1 is used to denote the neutral species). Also, it can be assumed that the majority of collisions experienced by each charged particle will be with the neutral fluid, and so all other collisions can be neglected. Finally it is assumed that the inertia, the pressure gradients, and the resultant accelerating force of the charged particle fluids have negligible effects. This is a valid approximation as the mean free path of the neutral species fluid is generally much longer than that of either the mean free path or the Larmor radius of the charged fluids i.

The N-fluid momentum equation for each charged particle fluid then reduces to:

$$\alpha_i \rho_i \left(\mathbf{E} + \mathbf{v}_i \times \mathbf{B} \right) + \mathbf{f}_{i1} = 0 \,. \tag{1.17}$$

for each charged fluid $i = 2, \ldots, N$.

The collision term is then written as an expression for the momentum transfer between the two fluids as $\mathbf{f}_{ij} \equiv \mathbf{C}_{ij} + s_{ij}\mathbf{v}_j - s_{ji}\mathbf{v}_i$ (Falle, 2003), where $\mathbf{C}_{ij} = \rho_i \rho_j K_{ij}(\mathbf{v}_j - \mathbf{v}_i)$, K_{ij} relates to the collisional frequency between fluids i and j, and the source terms s_{ij} can be neglected under the assumption of no mass transfer between species. This assumption results in neglecting charge exchange processes, which is taken to be acceptable in the case of weakly ionised plasmas such as the molecular clouds examined in the following studies.

The current density $\mathbf{J}$ is defined as:

$$\mathbf{J} \equiv \sum_{i=1}^{N} \alpha_i \rho_i \mathbf{v}_i \,, \tag{1.18}$$

and the Hall parameter, β_i, is introduced, as a measure of how closely tied to the field line a charged particle of characteristic velocity v_c is. It is defined as the ratio of the collisional length scale $\left(l_{\mathrm{c}i} \equiv \frac{v_\mathrm{c}}{K_{1i}\rho_1} \right)$ of the particle with its Larmor radius,

$\left(l_{\mathrm{e}i} \equiv \frac{v_{\mathrm{c}}}{\alpha_i B}\right)$:

$$\beta_i \equiv \frac{l_{\mathrm{c}i}}{l_{\mathrm{e}i}} = \frac{\alpha_i B}{K_{1i}\rho_1} \,. \tag{1.19}$$

The requirement for charge neutrality is stated as:

$$\sum_{i=1}^{N} \alpha_i \rho_i = 0 \,. \tag{1.20}$$

The momentum equation is then re-written in terms of velocities relative to that of the bulk fluid velocity, $\mathbf{v}_i' \equiv \mathbf{v}_i - \mathbf{v}$, where $\mathbf{v} = \mathbf{v}_1$ as previously assumed. Having thus moved into the reference frame of the bulk mass, the electric field is also re-written as the equivalent electric field, $\mathbf{E}' \equiv \mathbf{E} + \mathbf{v} \times \mathbf{B}$,

This thus gives:

$$\begin{aligned} 0 &= \alpha_i \rho_i \left(\mathbf{E}' + \mathbf{v}_i' \times \mathbf{B}\right) + \rho_i \rho_1 K_{i1}(-\mathbf{v}_i') \\ &= \alpha_i \rho_i \left(\mathbf{E}' + \mathbf{v}_i' \times \mathbf{B}\right) - \frac{B}{\beta_i}(\alpha_i \rho_i \mathbf{v}_i') \,. \end{aligned} \tag{1.21}$$

This can then be examined in each of the three dimensions. The magnetic field is set parallel to the z-direction, and thus the component of the equivalent electric field parallel to this magnetic field can be written as $\mathbf{E}_{\parallel}'$. This gives a unit vector in the z-direction $\frac{1}{E_{\parallel}'}\mathbf{E}_{\parallel}'$. Similarly the y-direction is set so that the electric field lies entirely in the yz-plane. Thus the component of the electric field perpendicular to the magnetic field, $\mathbf{E}_{\perp}'$, lies in the y-direction, giving a unit vector $\frac{1}{E_{\perp}'}\mathbf{E}_{\perp}'$ in the y-direction. And finally the x-direction is represented by the cross-product $\mathbf{E}' \times \mathbf{B}$, with unit vector $\frac{1}{E_{\perp}'}(\mathbf{E}' \times \mathbf{b})$ in this direction, where $\mathbf{b} \equiv \frac{1}{B}\mathbf{B}$.

Examining equation (1.21) this gives:

$$\text{in the } x\text{-direction:} \quad 0 = \quad \alpha_i \rho_i \left((v_i')_y B \right) - \frac{B}{\beta_i} \alpha_i \rho_i (v_i')_x \, , \tag{1.22}$$

$$\text{in the } y\text{-direction:} \quad 0 = \quad \alpha_i \rho_i \left(E_\perp' - (v_i')_x B \right) - \frac{B}{\beta_i} \alpha_i \rho_i (v_i')_y \, , \tag{1.23}$$

$$\text{in the } z\text{-direction:} \quad 0 = \quad \alpha_i \rho_i \left(E_\parallel' \right) - \frac{B}{\beta_i} \alpha_i \rho_i (v_i')_z \, . \tag{1.24}$$

Manipulating the expressions for the x- and y- directions gives:

$$\alpha_i \rho_i (v_i')_x \;=\; \frac{1}{B} \frac{\alpha_i \rho_i \beta_i^2}{(1+\beta_i^2)} E_\perp' \, , \tag{1.25}$$

$$\alpha_i \rho_i (v_i')_y \;=\; \frac{1}{B} \frac{\alpha_i \rho_i \beta_i}{(1+\beta_i^2)} E_\perp' \, , \tag{1.26}$$

while that for the z-direction gives us:

$$\alpha_i \rho_i (v_i')_z = \frac{1}{B} \alpha_i \rho_i \beta_i E_\parallel' \, . \tag{1.27}$$

These are then summed over the charged particles i to get:

$$(J)_x \;= \textstyle\sum_{i=1}^N \alpha_i \rho_i (v_i')_x \;= \displaystyle\frac{1}{B} \sum_{i=1}^N \frac{\alpha_i \rho_i \beta_i^2}{(1+\beta_i^2)} E_\perp' = \sigma_{\mathrm{H}} E_\perp' \, , \tag{1.28}$$

$$(J)_y \;= \textstyle\sum_{i=1}^N \alpha_i \rho_i (v_i')_y \;= \displaystyle\frac{1}{B} \sum_{i=1}^N \frac{\alpha_i \rho_i \beta_i}{(1+\beta_i^2)} E_\perp' = \sigma_\perp E_\perp' \, , \tag{1.29}$$

$$(J)_z \;= \textstyle\sum_{i=1}^N \alpha_i \rho_i (v_i')_z \;= \displaystyle\frac{1}{B} \sum_{i=1}^N \alpha_i \rho_i \beta_i E_\parallel' = \sigma_\parallel E_\parallel' \, , \tag{1.30}$$

where the conductivities are defined as:

$$\begin{aligned}
\sigma_{\mathrm{H}} &\equiv \frac{1}{B}\sum_{i=1}^{N}\frac{\alpha_i\rho_i\beta_i^2}{(1+\beta_i^2)} = -\frac{1}{B}\sum_{i=1}^{N}\frac{\alpha_i\rho_i}{(1+\beta_i^2)}\ , && (1.31)\\
\sigma_{\perp} &\equiv \frac{1}{B}\sum_{i=1}^{N}\frac{\alpha_i\rho_i\beta_i}{(1+\beta_i^2)}\ , && (1.32)\\
\sigma_{\|} &\equiv \frac{1}{B}\sum_{i=1}^{N}\alpha_i\rho_i\beta_i\ . && (1.33)
\end{aligned}$$

Note that (1.31) can be easily verified by bringing both terms to one side and adding, and recalling the condition of charge neutrality.

So, bringing all three terms together, the current density $\mathbf{J}$ is found to be (Mitchner & Kruger, 1973; Piddington, 1954):

$$\mathbf{J} = \sigma_{\|}\mathbf{E}'_{\|} + \sigma_{\perp}\mathbf{E}'_{\perp} + \sigma_H(\mathbf{E}' \times \mathbf{b})\ . \tag{1.34}$$

At this stage it is interesting to review the various conductivities at work here, and their relation to the resistive processes discussed in section 1.3.1. There is an Ohmic conductivity term, $\sigma_{\|}$, as would be expected for an ideal fluid. This term affects the direction parallel to the magnetic field. There is also a Pedersen (ambipolar) conductivity term, $\sigma_{\perp}$, acting in the direction perpendicular to the magnetic field. And finally there is a Hall conductivity term, σ_{H}, operating perpendicular to both the electric and magnetic fields (Pandey & Wardle, 2006).

The next step in the derivation is to write the expression for the current density in Cartesian tensor form and to examine it using matrices:

$$J_\alpha = \sigma_{\alpha\beta}E'_\beta\ . \tag{1.35}$$

In this case, the matrix $\sigma_{\alpha\beta}$ is defined as:

$$\sigma_{\alpha\beta} \equiv \begin{pmatrix} \sigma_{\perp} & \sigma_{\mathrm{H}} & 0 \\ -\sigma_{\mathrm{H}} & \sigma_{\perp} & 0 \\ 0 & 0 & \sigma_{\|} \end{pmatrix}\ . \tag{1.36}$$

This can be confirmed by multiplication:

$$\begin{aligned}\mathbf{J} &= (\sigma_\perp E'_x + \sigma_\mathrm{H} E'_y)\hat{\imath} + (-\sigma_\mathrm{H} E'_x + \sigma_\perp E'_y)\hat{\jmath} + (\sigma_\parallel E'_z)\hat{k} \\ &= \sigma_\parallel \mathbf{E}'_z + \sigma_\perp(\mathbf{E}'_x + \mathbf{E}'_y) + \sigma_\mathrm{H}(E'_y\hat{\imath} - E'_x\hat{\jmath}) \\ &= \sigma_\parallel \mathbf{E}'_\parallel + \sigma_\perp \mathbf{E}'_\perp + \sigma_\mathrm{H}(\mathbf{E}' \times \mathbf{b})\,. \qquad (1.37)\end{aligned}$$

The next step is to manipulate this expression for the current density in terms of the electric field, in order to obtain an expression for the electric field in terms of the current density. The form $E'_\alpha = (\sigma_{\alpha\beta})^{-1} J_\beta$ is used, where the inverted matrix can be calculated as:

$$\sigma^{-1}_{\alpha\beta} = \begin{pmatrix} \frac{\sigma_\perp}{\sigma_\perp^2+\sigma_\mathrm{H}^2} & -\frac{\sigma_\mathrm{H}}{\sigma_\perp^2+\sigma_\mathrm{H}^2} & 0 \\ \frac{\sigma_\mathrm{H}}{\sigma_\perp^2+\sigma_\mathrm{H}^2} & \frac{\sigma_\perp}{\sigma_\perp^2+\sigma_\mathrm{H}^2} & 0 \\ 0 & 0 & \frac{1}{\sigma_\parallel} \end{pmatrix} = \begin{pmatrix} r_2 & -r_1 & 0 \\ r_1 & r_2 & 0 \\ 0 & 0 & r_0 \end{pmatrix}\,, \qquad (1.38)$$

where the resistivities are defined as:

$$r_0 \equiv \frac{1}{\sigma_\parallel}\,,\, r_1 \equiv \frac{\sigma_\mathrm{H}}{\sigma_\perp^2 + \sigma_\mathrm{H}^2}\,,\, r_2 \equiv \frac{\sigma_\perp}{\sigma_\perp^2 + \sigma_\mathrm{H}^2}\,. \qquad (1.39)$$

By multiplying out $E'_\alpha = (\sigma_{\alpha\beta})^{-1} J_\beta$ and using the fact that

$$\mathbf{J} \times \mathbf{b} = \begin{vmatrix} \hat{\imath} & \hat{\jmath} & \hat{k} \\ J_x & J_y & J_z \\ 0 & 0 & 1 \end{vmatrix} = J_y\hat{\imath} - J_x\hat{\jmath}\,, \qquad (1.40)$$

and thus that

$$\mathbf{b} \times (\mathbf{J} \times \mathbf{b}) = \begin{vmatrix} \hat{\imath} & \hat{\jmath} & \hat{k} \\ 0 & 0 & 1 \\ J_y & -J_x & 0 \end{vmatrix} = J_x\hat{\imath} + J_y\hat{\jmath}\,, \qquad (1.41)$$

the following is found:

$$\begin{aligned}\mathbf{E}' &= (r_2 J_x - r_1 J_y)\hat{\imath} + (r_1 J_x + r_2 J_y)\hat{\jmath} + (r_0 J_z)\hat{k} \\ &= r_0 \mathbf{J}_z + r_1(-J_y\hat{\imath} + J_x\hat{\jmath}) + r_2(J_x\hat{\imath} + J_y\hat{\jmath}) \\ &= r_0(\mathbf{J}\cdot\mathbf{b})\mathbf{b} + r_1\mathbf{b}\times\mathbf{J} + r_2\mathbf{b}\times(\mathbf{J}\times\mathbf{b}) \\ &= r_0\frac{(\mathbf{J}\cdot\mathbf{B})\mathbf{B}}{B^2} + r_1\frac{\mathbf{B}\times\mathbf{J}}{B} + r_2\frac{\mathbf{B}\times(\mathbf{J}\times\mathbf{B})}{B^2}\,. \qquad (1.42)\end{aligned}$$

And so, finally, the Generalised Ohm's Law for a weakly ionised plasma is obtained, (Falle, 2003; Ciolek & Roberge, 2002),

$$\mathbf{E} = -\mathbf{v}\times\mathbf{B} + r_0\frac{(\mathbf{J}\cdot\mathbf{B})\mathbf{B}}{B^2} + r_1\frac{\mathbf{B}\times\mathbf{J}}{B} + r_2\frac{\mathbf{B}\times(\mathbf{J}\times\mathbf{B})}{B^2}\,. \qquad (1.43)$$

This concludes the derivation of the Generalised Ohm's Law for a weakly ionised plasma. It will be shown in section 2.4.1 that the same derivation method can be used for the case of a fully ionised plasma. This leads to a derivation of the Generalised Ohm's Law for a fully ionised plasma in the same format as that for the weakly ionised plasma.

1.4 The Kelvin-Helmholtz Instability

A system can be defined as stable or unstable, depending on the result of imposing a small external perturbation on it. If the system recovers and returns to its original state, it is said to be *stable*. If the perturbation grows with time (often exponentially), the system is then said to be *unstable*. The Kelvin-Helmholtz (KH) instability is one of the simplest forms of fluid instabilities. It occurs at the interface between two fluids that have a velocity relative to each other. As such, it is a very common and very important fluid instability.

Due to its broad range of terrestrial and astrophysical applications, the KH instability has been studied extensively. One of the first such studies was done by Chandrasekhar (1961). He studied this effect analytically, in both incompressible hydrodynamical and MHD systems. Using perturbation analysis, Chandrasekhar derived initial conditions for such an instability to arise, as well as solving the dispersion relation for a number of systems and finding the resulting growth rates. This study was extended by Blumen (1970) to the compressible case. In the context of astrophysical jets and outflows, the KH instability was studied again using linear analysis by Massaglia et al. (1992) and Hardee & Stone (1997). However, the Kelvin-Helmholtz instability develops in a way that can be described using a linear regime only up to a certain point. After this, analytical approximations are no longer valid. The KH instability is a fluid dynamical phenomenon, requiring that it be treated only using nonlinear methods.

1.4.1 Growth rates of the KH Instability

Linear analysis of the Kelvin-Helmholtz instability involves starting with the MHD equations for a fluid, and subjecting them to a small perturbation. This is performed by expanding each physical variable Q_i as:

$$Q_i \equiv Q_{0,i} + q_i \tag{1.44}$$

where $q_i \ll Q_{0,i}$ and all terms of order $(q_i)^2$ can be neglected. These are then substituted back into the MHD equations, which, by neglecting small terms and using $\nabla \cdot \mathbf{v} = 0$ and $\nabla \cdot \mathbf{B} = 0$ for an incompressible, divergence-free plasma, reduce to a set of simplified linear equations. The perturbation components are then written as exponential functions

$$q_i \propto \exp[i(\mathbf{k} \cdot \mathbf{r} - \omega_{\mathbf{k}} t)] \tag{1.45}$$

such that its derivatives can be written as $\frac{\partial}{\partial t} = -i\omega$ and $\frac{\partial}{\partial x_{1,2,3}} = ik_{x_{1,2,3}}$. This leads to a dispersion relation:

$$\mathcal{D}(\mathbf{k}, \omega_{\mathbf{k}}; Q_{0,i}) = 0 \; . \tag{1.46}$$

This dispersion relation provides $\omega(\mathbf{k})$ for a fixed $\mathbf{k}$. Writing $\omega = \mathrm{Re}(\omega) + i\mathrm{Im}(\omega)$, the system is said to be unstable if $\mathrm{Im}(\omega) > 0$, and the instability can be seen to have growth rate $\mathrm{Im}(\omega)$.

1.4.2 KH Instability in Stellar Jets

The Kelvin-Helmholtz instability is of great interest in the study of protostellar jets, as well as various other astrophysical outflows. Protostellar jets have been observed in great detail using high resolution observations, and their structure implies evolution processes that are not yet well understood. Processes such as variability at the source of the jet and the Rayleigh-Taylor instability at the head of the jet have been studied as possible candidates to explain some of the observed phenomena. Other examples such as the possibility of the Kelvin-Helmholtz instability occurring between the jet-driven molecular outflow and the ambient medium have yet to be examined.

Formation of structure within the jet It was proposed by Rees (1971) that extended radio lobes in extragalactic sources could receive energy from the central source via collimated outflows and the KH instability. When collimated outflows with similar structure were then observed from young stars (Mundt & Fried, 1983; Bührke et al., 1988) and at much higher resolution, a further investigation of this process was possible (Muxlow & Garrington, 1991; Padman et al., 1991). It was recognised that even a steady isolated jet could form structure through the growth of KH modes. This includes the “wiggling” motion seen in a number of protostellar jets (Lopéz at al., 1995), or even strong shocks along the jet beam (Stone et al., 1997). Bührke et al. (1988) were amongst the first to propose that the emission knots observed in some protostellar jets could be produced by the growth of the KH pinch modes. While it has since been shown that stars with variable accretion rates could cause the variability in an outflow required to form these knots (Reipurth, 1989; Stone & Norman, 1993; Raga & Cabrit, 1993) it is still possible that the KH instability has a role to play in the finer level of their structure (Hardee & Stone, 1997). However, considering the large density differences between the stellar jet and ambient medium, as well as the high Mach numbers involved, the KH instability is quickly becoming a less likely candidate for causing such structure in the jet itself.

Further disruption to the jet The Kelvin-Helmholtz instability was also considered as possibly leading to the destruction of a protostellar jet. Bodo et al. (1994) found that the amount of energy emitted, under the conditions in which the KH instability occurs, may only be a small fraction of the total energy of the jet, and thus did not necessarily lead to disruption of the bulk motion of the jet. Stone et al. (1997) showed through simulations that, if the growth rate of a surface wave reached a particular resonant frequency, large amplitude oscillations could theoretically disrupt and possibly destroy the jet. This agreed with previous simulations by Hardee & Norman (1988) and Hardee & Norman (1989) who found that using particular parameters, a 2D slab jet could be destroyed on a timescale similar to the growth timescale of unstable KH surface perturbations.

Entrainment and momentum exchange Another important process present in jets is interaction between the internal and external medium. Observations showing varying degrees of ionisation within stellar jets (Padman et al., 1991; Bacciotti et al., 2003) suggest that mixing at the bowshock is quite likely. This mixing process can be as a result of the KH instability. Bodo et al. (1994) find that as the bowshock of the jet accelerates material from the ambient medium, momentum and energy are effectively transferred into the surrounding region. This becomes an injection of momentum from the jet into the parent molecular cloud through the resulting bowshock as discussed in section 1.1.2. Time-dependent simulations by Stone et al. (1997) show that shocks generated by surface waves are capable of driving molecular outflows, by accelerating the ambient gas at large distances from the jet. They conclude that disruptions to the jet by the KH instability result in entrainment of the ambient gas. This is in addition to the acceleration provided by “prompt” entrainment of ambient material near the head of the jet (Padman et al., 1997). However, more recent studies indicate that jet-driven bowshocks are in fact very inefficient at accelerating ambient gas in these manners (Downes & Ray, 1999).

Linear and numerical studies Studies of the Kelvin-Helmholtz instability in protostellar jets have been carried out using perturbative linear analysis, as described in Section 1.4.1. These initial studies (as reviewed by Birkinshaw, 1991) examine the fluid equations under set-ups of various combinations of magnetic field and shear layers, etc. By approaching the problem using a simple mathematical treatment, the effect of each physical parameter can be followed closely. Hardee et al. (1997), for example, investigate the KH instability in jets by solving the dispersion relations for KH modes over a wide range of perturbation frequencies. However, these studies are limited to the linear regime of the instability, and the evolution of stellar jets, under the KH instability, is very much governed by nonlinear phenomena (Bodo et al., 1994). Subsequent studies have followed the growth of the KH instability in jets using time-dependent numerical simulations. Stone et al. (1997) and Downes & Ray (1998), to name just a few, impose linear perturbations onto an initially stable set-up to observe the behaviour of the instability into the non-linear regime and the effect it can have in stellar jets.

This concludes our review of the KH instability in protostellar jets. There are studies of the instability however in a broader context that have been carried out in greater detail and are equally relevant to our work. These are reviewed in the following section.

1.5 Review of Kelvin-Helmholtz instability studies

Since the first in-depth study of the Kelvin-Helmholtz instability by Chandrasekhar (1961), numerous applications of the instability have been found, and many studies have been carried out. Early studies of the instability in MHD systems used linear analysis, but this is limited to the initial linear regime of the instability, and cannot predict the subsequent nonlinear behaviour. For this reason, emphasis has since turned to numerical studies. Focus originally lay on ideal MHD systems, but in recent years, the need for including nonideal effects has been recognised.

1.5.1 Numerical ideal MHD studies of KH instability

As well as the studies on the Kelvin-Helmholtz instability in protostellar jets mentioned in section 1.4.2, a number of more general numerical studies have been carried out. Using numerical simulations, the nonlinear behaviour of the instability is studied by examining how the flow relaxes after saturation. Frank et al. (1996) studied this nonlinear evolution for the case of a strong and weak magnetic field in two dimensions. They find that while the strong magnetic field quickly returned the plasma to laminar flow after the instability, the weak field case involved many more dynamically interesting phenomena, including reconnection and intermittent vortices. That same year Malagoli et al. (1996) also carried out a study of the nonlinear regime of Kelvin-Helmholtz instabilities in 2D in the presence of a magnetic field. They found that even if a magnetic field was not strong enough to prevent the KH instability, it was still possible for it to contribute to its subsequent decay. The following year, Jones et al. (1997) examined the effect of the orientation of the field on the nonlinear evolution of the KH instability by expanding their study into 2.5 dimensions. The conclusion of this study was there was very little difference between a very weak field parallel to the flow and a strong field at an angle such that its projection onto the plane of flow was very weak. For very weak fields, the extra degrees of freedom allowed in 2.5 dimensions were found to have no significant effect on the KH instability. Also that year, Hardee et al. (1997) carried out a full 3D numerical analysis of radiatively cooled jets. This paper concluded that adiabatic jets could be used to model cooled jets, in the case of a sufficiently strong magnetic field.

A couple of years later, Keppens et al. (1999) studied both the linear growth and subsequent nonlinear saturation of the KH instability using resistive MHD numerical simulations. The inclusion of diffusion allowed for magnetic reconnection, and these nonideal effects were observed through tearing instabilities and the formation of magnetic islands. The case in support of using numerical diffusion in order to simulate nonideal MHD effects was argued the following year by Jeong et al. (2000), as analogous to the similar practice used to simulate nonideal HD flows of high Reynolds number.

Palotti et al. (2008) also carried out a series of simulations using resistive MHD. They found that, following its initial growth, the KH instability decays at a rate that decreases with decreasing plasma resistivity, at least within the range of of resistivities accessible to their simulations. They also found that magnetisation increased the efficiency of momentum transport, and that the transport increased with decreasing resistivity.

However, in order to study the Kelvin-Helmholtz instability in the context of molecular clouds or a similarly weakly ionised system, models can be improved with the inclusion of the nonideal effects that are likely occur.

1.5.2 Numerical multifluid MHD studies of the KH instability

In recent years, the emphasis of KH studies has been on including nonideal effects. Birk & Wiechen (2002) examined the case of a partially ionised dusty plasma, using a multifluid approach in which collisions could be included or ignored. It is the first study in which unstable shear flows in partially ionized dusty plasmas were studied analytically and numerically. They found that collisions between the neutral fluid and dust particles could lead to the stabilisation of KH modes of particular wavelengths. The unstable modes led to a significant local amplification of the magnetic field strength through the formation of vortices and current sheets. In the nonlinear regime, they observed the magnetic flux being redistributed by magnetic reconnection. It was suggested that this could be applicable to dense molecular clouds and have important implication for the magnetic flux loss problem (Umebayashi & Nakano, 1990).

A comprehensive study was carried out by Wiechen (2006) in which he demonstrated visually the effect of dealing with the plasma using a multifluid scheme. These simulations were the first systematic numerical parameter studies of Kelvin-Helmholtz modes in partially ionized dusty plasmas. Unlike simulations in previous studies in which the magnetic field and plasma were modeled as frozen together and with their dynamics mirroring each other, this paper shows a clear difference between the behaviour of the two, due to the decoupling of the plasma from the field. The focus of this study is on the effect of varying the properties of the dust grains. The results of the simulations lead to the conclusions that more massive dust grains have a stabilising effect on the system, while higher charged numbers have a destabilizing effect. It is found that there is no significant dependence on the charge polarity of the dust.

1.5.3 Linear multifluid MHD studies of the KH instability

As well multifluid numerical studies, there have been a few examples of linear analyses of the KH instability in the multifluid case. Two of the most relevant papers are focused on below. In their study of stellar outflows, Watson et al. (2004) described how the charged and neutral fluids are affected differently by the presence of a magnetic field. This study is carried out using parameters chosen to reflect those of molecular clouds, and so is particularly relevant to our own study. The principal result of this paper is that for much of the relevant parameter space, neutrals and ions are sufficiently decoupled that the neutrals are unstable while the ions are held in place by the magnetic field. The study finds that, since the magnetic field is frozen to the ionised plasma, it is not tangled by the turbulence in the boundary layer. They predict that with well-resolved observations, there should be a detectably narrower line profile in ionised species tracing the stellar outflow compared with neutral species, since ionised species are not participating in the turbulent interface with the ambient interstellar medium. The paper also includes a study of the growth rate of the instability. It is found that at short lengthscales, the growth rate is well approximated by the growth rate of the hydrodynamic system. At longer lengthscales and for super-Alfvénic flows, the fastest growing mode is equal to that of the ideal MHD case.

Shadmehri & Downes (2008) carried out an analytical study of the Kelvin-Helmholtz instability in dusty and partially ionised outflows. They investigated primarily the effect of the presence of dust particles by varying their mass, charge and charge polarity. It was found that as the charge of the grain increased, the growth timescales also increased, implying a stabilising effect on the system. The stability of the system was also examined for dependence on the mass of the dust particles. It was found that for stronger magnetic fields, this did not affect the stability of the system. However, for weaker magnetic fields, the larger dust particles had a stabilising effect on the growing modes. This was in agreement with previous laboratory experiments (Luo et al., 2001) and numerical simulations (Wiechen, 2006). Finally, as the magnetic field strength increased, the growth timescale of the unstable modes at a particular perturbation wavelength decreased. It was thus concluded that the magnetic field was effectively destabilising the system. This is in contradiction to the expected results, as the magnetic field generally tends to stabilise a system against the growth of the Kelvin-Helmholtz instability. By examining the combinations of the wavelength of the perturbation used, and the resultant growth timescales of the instability, Shadmehri & Downes (2008) concluded that the Kelvin-Helmholtz instability is a possible candidate for causing the formation of some of the physical structures observed in molecular outflows from young stars (as mentioned in section 1.4.2).

It has thus been seen that multifluid effects can influence the development of the Kelvin-Helmholtz instability. This drives the motivation for this thesis, as a study of the effects of multifluid MHD on the KH instability in a weakly ionised plasma. The structure of the remainder of the thesis is thus as follows: In chapter 2 we outline the methods of solving the multifluid MHD equations implemented by the numerical code used to carry out the simulations in our study. The code is then tested for simulating the KH instability against previous linear and numerical results in chapter 3. Chapters 4 and 5 outline the changes to the development of the KH instability caused by including either ambipolar diffusion or the Hall effect in the system, respectively. Chapter 6 provides an in-depth examination of the respective roles played by these nonideal effects when they occur together in a study simulating a molecular cloud. Finally, the effects on the jet-driven bowshock are then studied under multifluid MHD conditions, and the changes to the general properties of the system are examined. The results are then summarised and conclusions given in chapter 8.

Chapter 2

Numerical Code for Multifluid MHD

In order to observe the dynamics of astrophysical plasmas, we carry out computational simulations using the numerical code HYDRA (O'Sullivan & Downes, 2007, 2006). This code uses an explicit scheme to integrate the equations of non-ideal MHD for a weakly ionised plasma in an isothermal system. The advantage of using an explicit scheme is that the code can then be implemented using parallel computing, which is crucial for carrying out multifluid MHD simulations of large-scale astrophysical systems.

2.1 Solving the multifluid gas equations

Assuming a piecewise constant solution at time t^n on a uniform mesh of spacing h in each of the x, y and z directions, the solution at a later time $t^{n+1} = t^n + \tau$ is sought. The state in cell (i, j, k) represents the average over the volume V defined by $(x, y, z)\ :\ \left(i - \frac{1}{2}\right) h \le x \le \left(i + \frac{1}{2}\right) h, \left(j - \frac{1}{2}\right) h \le y \le \left(j + \frac{1}{2}\right) h, \left(k - \frac{1}{2}\right) h \le z \le \left(k + \frac{1}{2}\right) h$.

2.1.1 The multifluid MHD equations

The equations that govern the evolution of a weakly ionised plasma and that are solved by this code are as follows:

$$\frac{\partial \rho_i}{\partial t} + \nabla \cdot (\rho_i \mathbf{v}_i) = 0 \tag{2.1}$$

$$\frac{\partial \rho_1 \mathbf{v}_1}{\partial t} + \nabla \cdot (\rho_1 \mathbf{v}_1 \mathbf{v}_1 + p_1 \mathbf{I}) = \mathbf{J} \times \mathbf{B} \tag{2.2}$$

$$\frac{\partial \mathbf{B}}{\partial t} + \nabla \cdot (\mathbf{v}_1 \mathbf{B} - \mathbf{B} \mathbf{v}_1) = -\nabla \times \mathbf{E}' \tag{2.3}$$

$$\alpha_i \rho_i (\mathbf{E} + \mathbf{v} \times \mathbf{B}) + \rho_i \rho_1 K_{i1} (\mathbf{v}_1 - \mathbf{v}_i) = 0 \tag{2.4}$$

$$\nabla \cdot \mathbf{B} = 0 \tag{2.5}$$

$$\mathbf{J} = \nabla \times \mathbf{B} \tag{2.6}$$

$$\sum_{i=2}^{N} \alpha_i \rho_i = 0 \tag{2.7}$$

$$\sum_{i=2}^{N} \alpha_i \rho_i \mathbf{v}_i = \mathbf{J} \tag{2.8}$$

In these equations the subscripts denote the species, with a subscript of 1 indicating the neutral fluid. The variables ρ_i, $\mathbf{v}_i$ and p_i are the mas density, velocity and pressure, respectively, of species i. The charge-to-mass ratio of species i is denoted by α_i and K_{i1} describes the collisional interaction with the neutral fluid. The identity matrix, current density and magnetic flux density are represented by $\mathbf{I}$, $\mathbf{J}$ and $\mathbf{B}$ respectively. The matrix $\mathbf{v}_1\mathbf{B}$ is the dyadic formed from the neutral velocity and the magnetic field. Finally, the equivalent electric field $\mathbf{E}'$ is related to the full electric field $\mathbf{E}$ by $\mathbf{E}' = \mathbf{E} + \mathbf{v}_1 \times \mathbf{B}$. These above equations are closed under the isothermal approximation used in this study by the equation of state

$$c_s^2 = \frac{p_1}{\rho_1} \tag{2.9}$$

where c_s is the (constant) isothermal soundspeed.

2.1.2 Strang operator splitting

To obtain the full solution at time $t^n + \tau$, standard finite volume integration methods are applied to all terms in the above partial differential equations of the form $\frac{\partial \mathbf{u}}{\partial t} + \nabla \cdot \mathbf{f}(\mathbf{u}) = 0$. The time integration is split into several operations, each of which is carried out to second order spatial and temporal accuracy. By permuting the order of the operations, overall second order accuracy in time is maintained (Strang, 1968).

In the first operation, the neutral fluid component of the plasma is advanced. The mass density of the neutral fluid is evolved using the continuity equation (2.1. The corresponding momentum can be advanced using equation (2.2). Finally, the advective part of the induction equation (equation 2.3) is also implemented.

The second operation advances the velocities and the densities of the charged particle fluids. The densities of the charged fluids i are advanced using the continuity equation (2.1). The charged species velocities are then found analytically. The magnetic field is first used to calculate the current density, $\mathbf{J} = \vec{\nabla} \times \mathbf{B}$, which in turn determines the electric field by the Generalised Ohm's law, $\mathbf{E}' = r_0 \mathbf{J}_{\|} + r_1 \mathbf{J}_{\wedge} + r_2 \mathbf{J}_{\perp}$. The momentum equation for the charged fluid (equation 2.4) is then re-written in terms of the charged velocity relative to the neutral fluid, $\mathbf{v}'_i = \mathbf{v}_i - \mathbf{v}$. Using the calculated value of the equivalent electric field $\mathbf{E}'$, this gives $\alpha_i \rho_i \left(\mathbf{E}' + \mathbf{v}'_i \times \mathbf{B}\right) - \rho_i \rho_1 K_i(\mathbf{v}'_i) = 0$. This is then solved for the relative velocity by re-writing the equations using matrices:

$$\mathbf{v}'_i = (\mathbf{A})^{-1} \mathbf{E}' \,. \tag{2.10}$$

for a certain matrix $\mathbf{A}$. The actual velocity of the charged fluid is then calculated as $\mathbf{v}_i = \mathbf{v}'_i + \mathbf{v}$.

The third and final operation advances the magnetic field. The evolution of the magnetic field is described by the induction equation (2.3). This is derived directly from Faraday's Law

$$\vec{\nabla} \times \mathbf{E} = -\frac{\partial \mathbf{B}}{\partial t} \,, \tag{2.11}$$

by substituting in the expression for the equivalent electric field.

In order to integrate the induction equation, the electric field is written as a function of the magnetic field. We start with the Generalised Ohm's Law, (equation 1.43):

$$\mathbf{E}' = \mathbf{E} + \mathbf{v} \times \mathbf{B} = r_0 \frac{(\mathbf{J} \cdot \mathbf{B})\mathbf{B}}{B^2} + r_1 \frac{\mathbf{B} \times \mathbf{J}}{B} + r_2 \frac{\mathbf{B} \times (\mathbf{J} \times \mathbf{B})}{B^2} . \qquad (2.12)$$

The terms on the right hand side of this expression can be re-written as the product of a matrix and the current density vector, to get

$$\mathbf{E}' = -r_0 \mathbf{R}_0 \mathbf{J} - r_1 \mathbf{R}_1 \mathbf{J} - r_2 \mathbf{R}_2 \mathbf{J} \ , \qquad (2.13)$$

where the matrices $\mathbf{R}_0$, $\mathbf{R}_1$, and $\mathbf{R}_2$ are defined as:

$$\mathbf{R}_0 \equiv -\frac{1}{B^2} \begin{pmatrix} B_x^2 & B_x B_y & B_x B_z \\ B_x B_y & B_y^2 & B_y B_z \\ B_x B_z & B_y B_z & B_z^2 \end{pmatrix} , \qquad (2.14)$$

$$\mathbf{R}_1 \equiv -\frac{1}{B} \begin{pmatrix} 0 & -B_z & B_y \\ B_z & 0 & -B_x \\ -B_y & B_x & 0 \end{pmatrix} , \qquad (2.15)$$

$$\mathbf{R}_2 \equiv -\frac{1}{B^2} \begin{pmatrix} B_y^2 + B_z^2 & -B_x B_y & -B_x B_z \\ -B_x B_y & B_x^2 + B_z^2 & -B_y B_z \\ -B - x B_z & -B_y B_z & B_x^2 + B_y^2 \end{pmatrix} . \qquad (2.16)$$

Using Ampère's Law for a non-relativistic flow (where factors of 4π and the speed of light c have been incorporated into the magnetic field term):

$$\vec{\nabla} \times \mathbf{B} = \mathbf{J} + \frac{\partial \mathbf{E}}{\partial t} \approx \mathbf{J} \ , \qquad (2.17)$$

the induction equation becomes

$$\frac{\partial \mathbf{B}}{\partial t} + \vec{\nabla} \cdot (\mathbf{v}_1 \mathbf{B} - \mathbf{B} \mathbf{v}_1) = \vec{\nabla} \times \Big(\mathbf{R}(\vec{\nabla} \times \mathbf{B}) \Big) \ . \qquad (2.18)$$

where

$$\mathbf{R} \equiv r_0\mathbf{R}_0 + r_1\mathbf{R}_1 + r_2\mathbf{R}_2.$$

However, as will be seen in the next section, we must be careful when integrating this equation to solve for $\mathbf{B}$, as the stable time step is prone to vanishing towards zero in the limit of high Hall resistivity.

2.2 Stability and timestep analysis

A stability analysis is performed in order to examine the timestep restrictions of the code when solving the induction equation (equation 2.18). The hyperbolic flux term, $\vec{\nabla} \cdot (\mathbf{v}_1\mathbf{B} - \mathbf{B}\mathbf{v}_1)$, is first split from the equation and dealt with separately. The assumption is then made that the Ohmic resistivity r_0 is negligibly small, on the basis that the collisional drag on the charged fluids is dominated by magnetic forces. Finally, under the assumption of small perturbations in $\mathbf{B}$ about a mean field, we neglect the second-order terms on the right-hand side of the induction equation for the purpose of this analysis. These simplifications leave only the linear ambipolar and Hall terms remaining for our analysis of the stability of the integration scheme. This reduced induction equation is of the form

$$\frac{\partial \mathbf{B}}{\partial t} = -\mathbf{G}\mathbf{B}\,, \tag{2.19}$$

where the matrix operator $\mathbf{G}$ comprises of Hall and ambipolar parts, $\mathbf{G} = \mathbf{G}_{\mathrm{H}} + \mathbf{G}_{\mathrm{A}}$. Using a unit vector in the direction of the magnetic field, $\mathbf{b} \equiv \mathbf{B}/B$, it is possible to write:

$$\mathbf{G}_{\mathrm{H}} = -r_1(\mathbf{b}\cdot\nabla)(\nabla\times\cdot) \tag{2.20}$$

$$\mathbf{G}_{\mathrm{A}} = r_2[\mathbf{b}\cdot(\nabla\times(\nabla\times\cdot))]\mathbf{b} - r_2[(\mathbf{b}\cdot\nabla)(\nabla\times\cdot)]\times\mathbf{b} \tag{2.21}$$

2.2.1 Standard discretisation

Second-order derivative discretisations of $\mathbf{B}$ are written in the form

$$\left(\frac{\partial^2 \mathbf{B}}{\partial x^2}\right)_i = \frac{B_{i+1} - 2B_i + B_{i-1}}{h^2}\,, \tag{2.22}$$

$$\left(\frac{\partial^2 \mathbf{B}}{\partial x \partial y}\right)_{ij} = \frac{B_{i+1j+1} - B_{i+1j-1} - B_{i-1j+1} + B_{i-1j-1}}{4h^2}\,, \tag{2.23}$$

and so on for the remaining discretisations. The second-order derivative operators of $\mathbf{B}$ are then found by writing the magnetic field as a numerical wave in the form $\mathbf{B}^n_j = \mathbf{B}^n e^{\mathrm{i}\omega\cdot\mathbf{i}}$ where $\mathrm{i} = \sqrt{-1}$, $\mathbf{i} = (i, j, k)$ and $\omega = (\omega_x, \omega_y, \omega_z)$. The derivatives can then be calculated and defined by:

$$\left(\frac{\partial^2}{\partial x^2}\right)_i \quad \rightarrow \quad \lambda_{xx} \equiv -2(1-\cos\omega_x)\ , \tag{2.24}$$

$$\left(\frac{\partial^2}{\partial x \partial y}\right)_{ij} \quad \rightarrow \quad \lambda_{xy} \equiv -\sin\omega_x \sin\omega_y\ , \tag{2.25}$$

and so on for the remaining derivatives. A matrix Λ can then be defined whose (x, y) elements are given by λ_{xy}.

By examining the discretised operators $\mathbf{G}^n_{\mathrm{H}}$ and $\mathbf{G}^n_{\mathrm{A}}$ in equations (2.20) and (2.21), we find matrices $\mathbf{A}_H \equiv \frac{h^2}{r_1}\mathbf{G}_H$ and $\mathbf{A}_A \equiv \frac{h^2}{r_2}\mathbf{G}_A$ to be

$$\mathbf{A}_{\mathrm{H}} = \begin{pmatrix} 0 & \zeta_z & -\zeta_y \\ -\zeta_z & 0 & \zeta_x \\ \zeta_y & -\zeta_x & 0 \end{pmatrix} \tag{2.26}$$

and

$$\mathbf{A}_{\mathrm{A}} = \mathbf{b}\zeta + \zeta\mathbf{b} - \mathrm{tr}(\Lambda)\mathbf{b}\mathbf{b} - \mathbf{b}^T\zeta\mathbf{I} \tag{2.27}$$

where $\zeta \equiv \Lambda\mathbf{b}$ and $\mathbf{b}\zeta$ is the dyadic formed from $\mathbf{b}$ and ζ. It is worth noting about these two matrices that $\mathbf{A}_{\mathrm{H}}$ is skew-symmetric, while $\mathbf{A}_{\mathrm{A}}$ is symmetric.

The standard discretisation scheme can then be written as

$$\mathbf{B}^{n+1} = (\mathbf{I} - \tau\mathbf{G}^n_{\mathrm{H}} - \tau\mathbf{G}^n_{\mathrm{A}})\mathbf{B}^n \tag{2.28}$$

or as

$$\mathbf{B}^{n+1} = (\mathbf{I} - \alpha r_1\mathbf{A}_{\mathrm{H}} - \alpha r_2\mathbf{A}_{\mathrm{A}})\mathbf{B}^n \tag{2.29}$$

where $\alpha \equiv \tau/h^2$.

2.2.2 Von Neumann Stability Analysis

The relative importance of the ambipolar and Hall resistivities may be parameterised by a factor $\eta \equiv r_2/|r_1|$. The characteristic cell crossing time $\tau^\perp$ for diffusion perpendicular to the magnetic field is given by

$$\tau^{\perp} = \frac{h^2}{2\sqrt{r_1^2 + r_2^2}} \tag{2.30}$$

and for the following analysis, time intervals are normalised by this term such that $\overline{\tau} \equiv \tau/\tau^{\perp}$.

Ambipolar diffusion In the case of ambipolar diffusion only, the amplification matrix for the evolution of the magnetic field reduces to $(\mathbf{I} - \alpha r_2 \mathbf{A}_\mathrm{A})$. The eigenvalues of this matrix can be found to be

$$\begin{aligned} \mu_1 &= 1 + \alpha r_\mathrm{A} \mathbf{b}^T \zeta && (2.31) \\ \mu_{2,3} &= 1 + \frac{1}{2}\alpha r_2 [\mathrm{tr}(\Lambda) \pm |\mathrm{tr}(\Lambda)\mathbf{b} - 2\zeta|] && (2.32) \end{aligned}$$

The spectral radius of the matrix is thus found at $\omega = \pi(1,1,1)$ for an arbitrary orientation of $\mathbf{B}$. The normalised stability limit for the ambipolar case is then given by

$$\overline{\tau}_\mathrm{A}^\mathrm{STD} \leq \frac{1}{2}\frac{\sqrt{1+\eta^2}}{\eta}. \tag{2.33}$$

.

Hall diffusion In the case of Hall diffusion only, the amplification matrix for the evolution of the magnetic field reduces to $(\mathbf{I} - \alpha r_1 \mathbf{A}_\mathrm{H})$, with eigenvalues

$$\begin{aligned} \mu_1 &= 1 && (2.34) \\ \mu_{2,3} &= 1 \pm \mathrm{i}\alpha \mathrm{r}_1 \zeta && (2.35) \end{aligned}$$

The spectral radius of this matrix is clearly greater than unity for all $\tau > 0$. Furthermore,

$$\overline{\tau}_\mathrm{H}^\mathrm{STD} \to 0 \text{ as } \eta \to 0. \tag{2.36}$$

This vanishing timestep for the case of significant Hall resistivity results in the standard discretisation being impractical to use in Hall-dominant systems. A new method is used instead, known as the Hall Diffusion Scheme (O'Sullivan

& Downes, 2006), which will be explained in further detail in section 2.2.4.

2.2.3 Super Time-Stepping

As HYDRA uses an explicit scheme to integrate the MHD equations, it can take advantage of a technique used to accelerate parabolic problems. The "super time-stepping" method involves carefully choosing a substep $d\tau_j$, over which the normal stability restrictions can be relaxed when performing the integrations. A composite timestep is then built up from a series of N_{STS} substeps. This is known as the "superstep", and first order accuracy in time is maintained over each such superstep (Alexiades et al., 1996):

$$\tau^{\mathrm{STS}} = \sum_{j=1}^{\mathrm{N_{STS}}} d\tau_j$$

This process can be implemented when integrating the ambipolar diffusion term. For a timestep limit $\overline{\tau}_{\mathrm{A}}^{\mathrm{STD}}$ in the standard discretisation case, super timestepping results in a stability limit:

$$\lim_{\nu \to 0} \overline{\tau}_{\mathrm{A}}^{\mathrm{STS}} \to N_{\mathrm{STS}}^2 \overline{\tau}_{\mathrm{A}}^{\mathrm{STD}}$$

where ν is a damping factor.

The method of super time-stepping is then extended to second order in time using Richardson extrapolation (Richardson, 1911).

2.2.4 Hall Diffusion Scheme

The basis of the Hall Diffusion Scheme (HDS) (O'Sullivan & Downes, 2006) is the matrix format of the discretised operator, $\mathbf{G}_{\mathrm{H}}$, for the Hall diffusion term. It has been seen that this matrix is skew-symmetric. As a result, the reduced induction equation in a Hall-only system, $\frac{\partial \mathbf{B}}{\partial t} = -\mathbf{G}_{\mathrm{H}}\mathbf{B}$, can be written to describe the evolution of the magnetic field through the following strictly explicit equations:

$$
\begin{aligned}
B_x^{n+1} &= B_x^n - \tau\left(G_{xy}^n B_y^n + G_{xz}^n B_z^n\right) && (2.37)\\
B_y^{n+1} &= B_y^n - \tau\left(G_{yz}^n B_z^n + G_{yx}^n B_x^{n+1}\right) && (2.38)\\
B_z^{n+1} &= B_z^n - \tau\left(G_{zx}^n B_x^{n+1} + G_{zy}^n B_y^{n+1}\right) && (2.39)
\end{aligned}
$$

In matrix form, this HDS is written as

$$
\mathbf{B}^{n+1} = \left(\mathbf{I} - \alpha r_{\mathrm{H}} \hat{\mathbf{k}}\hat{\mathbf{k}} \mathbf{A}_{\mathrm{H}}\right)\left(\mathbf{I} - \alpha r_{\mathrm{H}} \hat{\boldsymbol{\jmath}}\hat{\boldsymbol{\jmath}} \mathbf{A}_{\mathrm{H}}\right)\left(\mathbf{I} - \alpha r_{\mathrm{H}} \hat{\boldsymbol{\imath}}\hat{\boldsymbol{\imath}} \mathbf{A}_{\mathrm{H}}\right)\mathbf{B}^n \qquad (2.40)
$$

where $\hat{\boldsymbol{\imath}}\hat{\boldsymbol{\imath}}$, $\hat{\boldsymbol{\jmath}}\hat{\boldsymbol{\jmath}}$ and $\hat{\mathbf{k}}\hat{\mathbf{k}}$ are dyadics formed from the unit vectors $\hat{\imath}$, $\hat{\jmath}$ and $\hat{k}$.

Examining the eigenvalues of this evolution operator, we find:

$$
\begin{aligned}
\mu_1 &= 1 && (2.41)\\
\mu_{2,3} &= 1 - \frac{1}{2}g \pm \frac{1}{2}\sqrt{g(g-4)} && (2.42)
\end{aligned}
$$

where

$$
0 \leq g \leq 4. \qquad (2.43)
$$

For the most stringent restrictions and N_{HDS} substeps per full time-step, we find

$$
\overline{\tau}_{\mathrm{H}}^{\mathrm{HDS}} \leq N_{\mathrm{HDS}} \frac{4}{\sqrt{27}} \sqrt{1+\eta^2} \qquad (2.44)
$$

As in the super-timestepping scheme, Richardson extrapolation is used here to bring HDS to second-order temporal accuracy.

For the integration of both ambipolar and Hall diffusion terms, a combined STS/HDS scheme is used. The effective stable time-step limit for this may be estimated as the minimum of $\overline{\tau}_{\mathrm{A}}^{\mathrm{STS}}$ and $\overline{\tau}_{\mathrm{H}}^{\mathrm{HDS}}$ (O'Sullivan & Downes, 2007).

2.3 Divergence of the magnetic field

As with any MHD code, care must be taken to maintain a divergence-free magnetic field within the system, that is,

$$\nabla \cdot \mathbf{B} = 0 \, ,$$

in order to avoid divergence errors from accumulating and leading to an incorrect solution.

In this numerical code, the Dedner method (Dedner et al., 2002) is used to minimise the divergence error. This method does not use the introduction of divergence source terms to eliminate the error. Instead, the divergence errors are dealt with by both damping them and advecting them toward the domain boundaries. A parabolic correction term within the scheme leads to the dissipation and smoothing out of the error, while a hyperbolic correction term propagates the error towards the boundary with the maximal admissible speed. This scheme is controlled within the code by setting a constant factor which determines the ratio in which the two correction terms are applied. Dedner et al. (2002) include a test problem on the KH instability, in which the success of the scheme is clearly observed. Incorporating this divergence cleaning method into HYDRA has yielded a stable scheme with suitably low divergence errors.

2.4 The MHD Equations for a Fully Ionised Plasma

The numerical code HYDRA is designed to simulate a weakly ionised plasma. However it is straightforward to adapt the code for a fully ionised plasma by deriving the MHD equations so that they are of the same form as the weakly ionised MHD equations. The following derivation is an original derivation we have carried out in order to obtain the Generalised Ohm's Law for a fully ionised plasma in the same format as is used in HYDRA for a weakly ionised plasma. Certain approximations made previously however must be re-examined. The plasma is now considered as being composed of a fluid of electrons of charge $-e$, and a fluid of positive ions of charge Ze. With no fluid of neutrals, the bulk mass velocity must be re-defined and is given by $\mathbf{v} = \frac{1}{\rho}(\rho_{\text{ion}}\mathbf{v}_{\text{ion}} + \rho_{\text{e}}\mathbf{v}_{\text{e}})$, where the parameters with no subscripts continue to represent the fluid as a whole. Also, charge neutrality in the fully ionised case now requires that $Zn_{\text{ion}} = n_{\text{e}}$.

In this case the inertia and partial pressures of the charged particles are no longer considered to be negligible. The partial pressure of each charged particle fluid is defined as $p_i \equiv \frac{n_i}{N}p$, where n_i is the number density of particles of fluid i, and $N = n_{\text{e}} + n_{\text{ion}}$ is the total number density of particles. This gives the partial pressures of each of the two fluids as $p_{\text{ion}} = \frac{1}{Z+1}p$ and $p_{\text{e}} = \frac{Z}{Z+1}p$. The particle's acceleration and inertia is then included in the Lagrangian derivative, defined as:

$$\frac{D_i}{Dt} \equiv \frac{\partial}{\partial t} + (\mathbf{v}_i \cdot \vec{\nabla})\,. \tag{2.45}$$

The following sections contain an original derivation of the fully ionised Generalised Ohm's Law under these conditions, as well as an investigation of this equation in order to compare it with those derived in previous literature.

2.4.1 The Generalised Ohm's Law for a Fully Ionised Plasma

Working under the conditions outlined above, the starting point for this derivation, as in the case of the weakly ionised Generalised Ohm's Law, is the momentum equation:

$$\alpha_i \rho_i \left(\mathbf{E} + \mathbf{v}_i \times \mathbf{B}\right) + \sum_{j \neq i}^{N=2} \mathbf{f}_{ij} = \vec{\nabla} p_i + \rho_i \frac{D_i \mathbf{v}_i}{Dt} \,. \tag{2.46}$$

Defining the collision term $\mathbf{f}_{ij}$ as before, we now examine it under the two-fluid approximation. This gives us:

$$\begin{aligned}
\mathbf{f}_{ij} &= \rho_i \rho_j K_{ij} (\mathbf{v}_j - \mathbf{v}_i) \\
&= \rho_i \rho_j K_{ij} (\mathbf{v}'_j - \mathbf{v}'_i) \\
&\quad \text{(where the relative velocity is defined as before, } \mathbf{v}'_i \equiv \mathbf{v}_i - \mathbf{v}\text{)} \\
&= \rho_i \rho_j K_{ij} \left(\frac{-\rho_i}{\rho_j} \mathbf{v}'_i - \mathbf{v}'_i \right) \\
&\quad \text{(as } \rho_i \mathbf{v}'_i + \rho_j \mathbf{v}'_j = 0 \text{ from the definition of the bulk mass velocity)} \\
&= -\rho_i \rho_j K_{ij} \left(\frac{\rho}{\rho_j} \right) \mathbf{v}'_i \\
&= -\alpha_i \rho_i B \left(\frac{K_{ij} \rho}{\alpha_i B} \right) \mathbf{v}'_i \\
&= -\alpha_i \rho_i \frac{B}{\beta'_i} \mathbf{v}'_i \,.
\end{aligned} \tag{2.47}$$

Here the Hall parameter β_i is still defined as the ratio of the collisional length scale $\left(l_{ci} \equiv \frac{v_c}{\sum_j K_{ij} \rho_j} \right)$ of the particle with its Larmor radius, $\left(l_{ei} \equiv \frac{v_c}{\alpha_i B} \right)$, to get, in this case:

$$\beta_i = \sum_{j \neq i}^{N=2} \beta_{ij} = \beta_{ij} \equiv \frac{\alpha_i B}{K_{ij} \rho_j} \,, \tag{2.48}$$

but we use here in our solution a new parameter:

$$\beta'_i \equiv \frac{\rho_j}{\rho} \cdot \beta_i = \frac{\alpha_i B}{K_{ij} \rho} \,. \tag{2.49}$$

We again write the velocities relative to that of the bulk mass velocity, $\mathbf{v}'_i \equiv \mathbf{v}_i - \mathbf{v}$, and the equivalent electric field, $\mathbf{E}' \equiv \mathbf{E} + \mathbf{v} \times \mathbf{B}$.

Using these, the momentum equation (2.46) is re-written as:

$$\vec{\nabla} p_i + \rho_i \frac{D_i \mathbf{v}_i}{Dt} = \alpha_i \rho_i \left(\mathbf{E}' + \mathbf{v}'_i \times \mathbf{B}\right) - \frac{B}{\beta'_i} (\alpha_i \rho_i \mathbf{v}'_i) \,. \tag{2.50}$$

Using the same directional analysis as before, with the unit vectors $\frac{1}{E'_{\|}}\mathbf{E}'_{\|}$, $\frac{1}{E'_{\perp}}\mathbf{E}'_{\perp}$ and $\frac{1}{E'_{\perp}}(\mathbf{E}' \times \mathbf{b})$ representing the z-, y- and x- directions respectively, we get:

in the x-direction:

$$(\vec{\nabla} p_i)_x + \rho_i \frac{D_i}{Dt}(v_i)_x = \alpha_i \rho_i \left((v'_i)_y B\right) - \frac{B}{\beta'_i} \alpha_i \rho_i (v'_i)_x \, , \tag{2.51}$$

in the y-direction:

$$(\vec{\nabla} p_i)_y + \rho_i \frac{D_i}{Dt}(v_i)_y = \alpha_i \rho_i \left(E'_{\perp} - (v'_i)_x B\right) - \frac{B}{\beta'_i} \alpha_i \rho_i (v'_i)_y \, , \tag{2.52}$$

in the z-direction:

$$(\vec{\nabla} p_i)_z + \rho_i \frac{D_i}{Dt}(v_i)_z = \alpha_i \rho_i (E'_{\|}) - \frac{B}{\beta'_i} \alpha_i \rho_i (v'_i)_z \, . \tag{2.53}$$

Following the same manipulation as before, we get:

$$\begin{aligned}
\alpha_i \rho_i (v'_i)_x &= \frac{1}{B} \frac{\alpha_i \rho_i \beta'^2_i}{(1+\beta'^2_i)} E'_{\perp} - \frac{1}{B} \frac{\beta'_i}{1+\beta'^2_i} (\vec{\nabla} p_i)_x - \frac{1}{B} \frac{\beta'^2_i}{1+\beta'^2_i} (\vec{\nabla} p_i)_y \\
&\quad - \frac{1}{B} \frac{\beta'_i \rho_i}{1+\beta'^2_i} \frac{D_i}{Dt}(v_i)_x - \frac{1}{B} \frac{\beta'^2_i \rho_i}{1+\beta'^2_i} \frac{D_i}{Dt}(v_i)_y \, , && (2.54) \\
\alpha_i \rho_i (v'_i)_y &= \frac{1}{B} \frac{\alpha_i \rho_i \beta'_i}{(1+\beta'^2_i)} E'_{\perp} + \frac{1}{B} \frac{\beta'^2_i}{1+\beta'^2_i} (\vec{\nabla} p_i)_x - \frac{1}{B} \frac{\beta'_i}{1+\beta'^2_i} (\vec{\nabla} p_i)_y \\
&\quad + \frac{1}{B} \frac{\beta'^2_i \rho_i}{1+\beta'^2_i} \frac{D_i}{Dt}(v_i)_x - \frac{1}{B} \frac{\beta'_i \rho_i}{1+\beta'^2_i} \frac{D_i}{Dt}(v_i)_y \, , && (2.55) \\
\alpha_i \rho_i (v'_i)_z &= \frac{1}{B} \alpha_i \rho_i \beta'_i E'_{\|} - \frac{1}{B} \beta'_i (\vec{\nabla} p_i)_z - \frac{1}{B} \beta'_i \rho_i \frac{D_i}{Dt}(v_i)_z \, , && (2.56)
\end{aligned}$$

which can then be written as:

$$\begin{aligned}(J)_x &= \sum_{i=1}^{N} \alpha_i \rho_i (v'_i)_x \\ &= \sigma_H E'_\perp - a_\perp(\vec{\nabla} p)_x - a_H(\vec{\nabla} p)_y - (b_\perp)_x - (b_H)_y \,, \qquad (2.57)\\ (J)_y &= \sum_{i=1}^{N} \alpha_i \rho_i (v'_i)_y \\ &= \sigma_\perp E'_\perp + a_H(\vec{\nabla} p)_x - a_\perp(\vec{\nabla} p)_y + (b_H)_x - (b_\perp)_y \,, \qquad (2.58)\\ (J)_z &= \sum_{i=1}^{N} \alpha_i \rho_i (v'_i)_z \\ &= \sigma_\parallel E'_\parallel - a_\parallel(\vec{\nabla} p)_z - (b_\parallel)_z \,, \qquad (2.59)\end{aligned}$$

where the conductivities are defined as:

$$\sigma_H \equiv \frac{1}{B}\sum_{i=1}^{N} \frac{\alpha_i \rho_i \beta_i'^2}{(1+\beta_i'^2)} = -\frac{1}{B}\sum_{i=1}^{N} \frac{\alpha_i \rho_i}{(1+\beta_i'^2)} \,, \qquad (2.60a)$$

$$\sigma_\perp \equiv \frac{1}{B}\sum_{i=1}^{N} \frac{\alpha_i \rho_i \beta'_i}{(1+\beta_i'^2)} \,, \qquad (2.60b)$$

$$\sigma_\parallel \equiv \frac{1}{B}\sum_{i=1}^{N} \alpha_i \rho_i \beta'_i \,, \qquad (2.60c)$$

and, by writing $\vec{\nabla} p_i = \vec{\nabla}(\frac{n_i}{N} p) = \frac{n_i}{N} \vec{\nabla} p$ (as the ratios $\frac{n_\mathrm{e}}{N} = \frac{Z}{Z+1}$ and $\frac{n_\mathrm{ion}}{N} = \frac{1}{Z+1}$ do not vary through the plasma), the coefficients are defined as:

$$a_H \equiv \frac{1}{NB}\sum_{i=1}^{N} \frac{n_i \beta_i'^2}{(1+\beta_i'^2)} \,, \qquad (2.61a)$$

$$a_\perp \equiv \frac{1}{NB}\sum_{i=1}^{N} \frac{n_i \beta'_i}{(1+\beta_i'^2)} \,, \qquad (2.61b)$$

$$a_\parallel \equiv \frac{1}{NB}\sum_{i=1}^{N} n_i \beta'_i \,, \qquad (2.61c)$$

and the vector components are written as:

$$
\begin{aligned}
(b_H)_{x,y} &\equiv \frac{1}{B}\sum_{i=1}^{N}\frac{\beta_i'^2\rho_i}{(1+\beta_i'^2)}\frac{D_i}{Dt}(v_i)_{x,y}\ , && \text{(2.62a)}\\
(b_\perp)_{x,y} &\equiv \frac{1}{B}\sum_{i=1}^{N}\frac{\beta_i'\rho_i}{(1+\beta_i'^2)}\frac{D_i}{Dt}(v_i)_{x,y}\ , && \text{(2.62b)}\\
(b_\parallel)_z &\equiv \frac{1}{B}\sum_{i=1}^{N}\beta_i'\rho_i\frac{D_i}{Dt}(v_i)_z\ . && \text{(2.62c)}
\end{aligned}
$$

And so, adding these three components of the current density $\mathbf{J}$, we get:

$$
\begin{aligned}
\mathbf{J} \;=\;& \sigma_\parallel\mathbf{E}'_\parallel + \sigma_\perp\mathbf{E}'_\perp + \sigma_H(\mathbf{E}'\times\mathbf{b})\\
& -a_\parallel(\vec{\nabla}p)_\parallel - a_\perp(\vec{\nabla}p)_\perp - a_H(\vec{\nabla}p\times\mathbf{b})\\
& -(\vec{b_\parallel})_\parallel - (\vec{b_\perp})_\perp - ((\vec{b_H})\times\mathbf{b})\ , \qquad \text{(2.63)}
\end{aligned}
$$

where for any vector $\mathbf{u}\equiv u_x\hat{\imath}+u_y\hat{\jmath}+u_z\hat{k}$,

$$
\begin{aligned}
\mathbf{u}_\parallel &\equiv u_z\hat{k}\ , && \text{(2.64)}\\
\mathbf{u}_\perp &\equiv u_x\hat{\imath}+u_y\hat{\jmath}\ , && \text{(2.65)}\\
\mathbf{u}\times\mathbf{b} &\equiv u_y\hat{\imath}-u_x\hat{\jmath}\ . && \text{(2.66)}
\end{aligned}
$$

Having obtained an expression for the current density $\mathbf{J}$ in terms of the electric field $\mathbf{E}'$, we invert this expression in order to find an expression for $\mathbf{E}'$ in terms of $\mathbf{J}$. This first step in this process is to write this equation in Cartesian tensor form:

$$
J_\alpha = \sigma_{\alpha\beta}E'_\beta - a_{\alpha\beta}(\vec{\nabla}p)_\beta - b_{\alpha\beta}n_\beta\ , \qquad \text{(2.67)}
$$

where $\vec{n}\equiv\hat{\imath}+\hat{\jmath}+\hat{k}$ and the matrices are defined as:

$$\sigma \equiv \begin{pmatrix} \sigma_\perp & \sigma_H & 0 \\ -\sigma_H & \sigma_\perp & 0 \\ 0 & 0 & \sigma_\parallel \end{pmatrix} , \tag{2.68}$$

and

$$a \equiv \begin{pmatrix} a_\perp & a_H & 0 \\ -a_H & a_\perp & 0 \\ 0 & 0 & a_\parallel \end{pmatrix} \text{, and } b \equiv \begin{pmatrix} (b_\perp)_x & (b_H)_y & 0 \\ -(b_H)_x & (b_\perp)_y & 0 \\ 0 & 0 & (b_\parallel)_z \end{pmatrix} . \tag{2.69}$$

As before, this can be confirmed by multiplication. We once again orient our vector space so that the z-direction is aligned with the magnetic field $\mathbf{B}$. This gives us:

$$\begin{aligned} \mathbf{J} &= (\sigma_\perp E'_x + \sigma_H E'_y)\hat{\imath} + (-\sigma_H E'_x + \sigma_\perp E'_y)\hat{\jmath} + (\sigma_\parallel E'_z)\hat{k} \\ &\quad -(a_\perp \vec{\nabla} p_x + a_H \vec{\nabla} p_y)\hat{\imath} - (-a_H \vec{\nabla} p_x + a_\perp \vec{\nabla} p_y)\hat{\jmath} - (a_\parallel \vec{\nabla} p_z)\hat{k} \\ &\quad -((b_\perp)_x + (b_H)_y)\hat{\imath} - (-(b_H)_x + (b_\perp)_y)\hat{\jmath} - (b_\parallel)_z \hat{k} \\ &= \sigma_\parallel \mathbf{E}'_z + \sigma_\perp(\mathbf{E}'_x + \mathbf{E}'_y) + \sigma_H(E'_y \hat{\imath} - E'_x \hat{\jmath}) \\ &\quad -a_\parallel(\vec{\nabla} p_z \hat{k}) - a_\perp(\vec{\nabla} p_x \hat{\imath} + \vec{\nabla} p_y \hat{\jmath}) - a_H(\vec{\nabla} p_y \hat{\imath} - \vec{\nabla} p_x \hat{\jmath}) \\ &\quad -b_\parallel \hat{k} - ((b_\perp)_x \hat{\imath} + (b_\perp)_y \hat{\jmath}) - ((b_H)_y \hat{\imath} - (b_H)_x \hat{\jmath}) \\ &= \sigma_\parallel \mathbf{E}'_\parallel + \sigma_\perp \mathbf{E}'_\perp + \sigma_H(\mathbf{E}' \times \mathbf{b}) \\ &\quad -a_\parallel \vec{\nabla} p_\parallel - a_\perp \vec{\nabla} p_\perp - a_H(\vec{\nabla} p \times \mathbf{b}) \\ &\quad -\vec{b_\parallel} - \vec{b_\perp} - \vec{b_H} \times \mathbf{b} \, . \end{aligned} \tag{2.70}$$

Thus it is possible to write the electric field as an expression of the current, using $E'_\alpha = (\sigma_{\alpha\beta})^{-1} J_\beta + (\sigma_{\alpha\beta})^{-1}(a_{\alpha\beta})(\vec{\nabla} p)_\beta + (\sigma_{\alpha\beta})^{-1}(b_{\alpha\beta})_\beta$, where the inverted matrix can be calculated as:

$$\sigma_{\alpha\beta}^{-1} = \begin{pmatrix} \frac{\sigma_\perp}{\sigma_\perp^2+\sigma_H^2} & -\frac{\sigma_H}{\sigma_\perp^2+\sigma_H^2} & 0 \\ \frac{\sigma_H}{\sigma_\perp^2+\sigma_H^2} & \frac{\sigma_\perp}{\sigma_\perp^2+\sigma_H^2} & 0 \\ 0 & 0 & \frac{1}{\sigma_\parallel} \end{pmatrix} = \begin{pmatrix} r_2 & -r_1 & 0 \\ r_1 & r_2 & 0 \\ 0 & 0 & r_0 \end{pmatrix} , \tag{2.71}$$

and

$$(\sigma_{\alpha\beta}^{-1})(a_{\alpha\beta}) = \begin{pmatrix} r_2 & -r_1 & 0 \\ r_1 & r_2 & 0 \\ 0 & 0 & r_0 \end{pmatrix} \begin{pmatrix} a_\perp & a_H & 0 \\ -a_H & a_\perp & 0 \\ 0 & 0 & a_\parallel \end{pmatrix} = \begin{pmatrix} s_2 & -s_1 & 0 \\ s_1 & s_2 & 0 \\ 0 & 0 & s_0 \end{pmatrix} , \tag{2.72}$$

and

$$(\sigma_{\alpha\beta}^{-1})(b_{\alpha\beta}) = \begin{pmatrix} r_2 & -r_1 & 0 \\ r_1 & r_2 & 0 \\ 0 & 0 & r_0 \end{pmatrix} \begin{pmatrix} (b_\perp)_x & (b_H)_y & 0 \\ -(b_H)_x & (b_\perp)_y & 0 \\ 0 & 0 & (b_\parallel)_z \end{pmatrix} = \begin{pmatrix} (t_2)_x & -(t_1)_y & 0 \\ (t_1)_x & (t_2)_y & 0 \\ 0 & 0 & (t_0)_z \end{pmatrix} , \tag{2.73}$$

where

$$r_0 = \frac{1}{\sigma_\parallel} \text{ , } r_1 = \frac{\sigma_H}{\sigma_\perp^2 + \sigma_H^2} \text{ , and } r_2 = \frac{\sigma_\perp}{\sigma_\perp^2 + \sigma_H^2} , \tag{2.74}$$

and

$$s_0 = r_0 a_\parallel \text{ , } s_1 = r_1 a_\perp - r_2 a_H \text{ , and } s_2 = r_1 a_H + r_2 a_\perp , \tag{2.75}$$

and

$$t_0 = r_0 (b_\parallel)_z \text{ , } (t_1)_x = r_1 (b_\perp)_x - r_2 (b_H)_x \text{ , } (t_1)_y = r_1 (b_\perp)_y - r_2 (b_H)_y ,$$

$$(t_2)_x = r_1 (b_H)_x + r_2 (b_\perp)_x \text{ , } (t_2)_y = r_1 (b_H)_y + r_2 (b_\perp)_y . \tag{2.76}$$

By multiplying out $E'_\alpha = (\sigma_{\alpha\beta})^{-1} J_\beta + (\sigma_{\alpha\beta})^{-1} (a_{\alpha\beta}) (\vec{\nabla} p)_\beta + (\sigma_{\alpha\beta})^{-1} (b_{\alpha\beta}) n_\beta$

and using the fact that:

$$\mathbf{J}\times\mathbf{b} = \begin{vmatrix} \hat{\imath} & \hat{\jmath} & \hat{k} \\ J_x & J_y & J_z \\ 0 & 0 & 1 \end{vmatrix} = J_y\hat{\imath} - J_x\hat{\jmath}\,, \tag{2.77}$$

and thus that:

$$\mathbf{b}\times(\mathbf{J}\times\mathbf{b}) = \begin{vmatrix} \hat{\imath} & \hat{\jmath} & \hat{k} \\ 0 & 0 & 1 \\ J_y & -J_x & 0 \end{vmatrix} = J_x\hat{\imath} + J_y\hat{\jmath}\,, \tag{2.78}$$

we get:

$$\begin{aligned}
\mathbf{E}' &= (r_2J_x - r_1J_y)\hat{\imath} + (r_1J_x + r_2J_y)\hat{\jmath} + (r_0J_z)\hat{k} \\
&\quad +(s_2\vec{\nabla}p_x - s_1\vec{\nabla}p_y)\hat{\imath} + (s_1\vec{\nabla}p_x + s_2\vec{\nabla}p_y)\hat{\jmath} + (s_0\vec{\nabla}p_z)\hat{k} \\
&\quad +((t_2)_x - (t_1)_y)\hat{\imath} + ((t_1)_x + (t_2)_y)\hat{\jmath} + ((s_0)_z)\hat{k} \\
&= r_0J_z + r_1(-J_y\hat{\imath} + J_x\hat{\jmath}) + r_2(J_x\hat{\imath} + J_y\hat{\jmath}) \\
&\quad +s_0\vec{\nabla}p_z\hat{k} + s_1(-\vec{\nabla}p_y\hat{\imath} + \vec{\nabla}p_x\hat{\jmath}) + s_2(\vec{\nabla}p_x\hat{\imath} + \vec{\nabla}p_y\hat{\jmath}) \\
&\quad +(t_0)_z\hat{k} + (-(t_1)_y\hat{\imath} + (t_1)_x\hat{\jmath}) + ((t_2)_x\hat{\imath} + (t_2)_y\hat{\jmath}) \\
&= r_0(\mathbf{J}\cdot\mathbf{b})\mathbf{b} + r_1\mathbf{b}\times\mathbf{J} + r_2\mathbf{b}\times(\mathbf{J}\times\mathbf{b}) \\
&\quad +s_0(\vec{\nabla}p\cdot\mathbf{b})\mathbf{b} + s_1\mathbf{b}\times\vec{\nabla}p + s_2\mathbf{b}\times(\vec{\nabla}p\times\mathbf{b}) \\
&\quad +(\vec{t_0}\cdot\mathbf{b})\mathbf{b} + \mathbf{b}\times\vec{t_1} + \mathbf{b}\times(\vec{t_2}\times\mathbf{b}) \\
&= r_0\frac{(\mathbf{J}\cdot\mathbf{B})\mathbf{B}}{B^2} + r_1\frac{\mathbf{B}\times\mathbf{J}}{B} + r_2\frac{\mathbf{B}\times(\mathbf{J}\times\mathbf{B})}{B^2} \\
&\quad +s_0\frac{(\vec{\nabla}p\cdot\mathbf{B})\mathbf{B}}{B^2} + s_1\frac{\mathbf{B}\times\vec{\nabla}p}{B} + s_2\frac{\mathbf{B}\times(\vec{\nabla}p\times\mathbf{B})}{B^2} \\
&\quad +\frac{(\vec{t_0}\cdot\mathbf{B})\mathbf{B}}{B^2} + \frac{\mathbf{B}\times\vec{t_1}}{B} + \frac{\mathbf{B}\times(\vec{t_2}\times\mathbf{B})}{B^2}\,,
\end{aligned} \tag{2.79}$$

where

$$\vec{t_0} \equiv (t_0)_x\hat{\imath} + (t_0)_y\hat{\jmath} + (t_0)_z\hat{k}\,, \tag{2.80}$$

and similarly for $\vec{t_1}$ and $\vec{t_2}$.

This finally gives us

$$\begin{aligned} \mathbf{E} \;=\; & -\mathbf{v}\times\mathbf{B} + r_0\frac{(\mathbf{J}\cdot\mathbf{B})\mathbf{B}}{B^2} + r_1\frac{\mathbf{B}\times\mathbf{J}}{B} + r_2\frac{\mathbf{B}\times(\mathbf{J}\times\mathbf{B})}{B^2} \\ & + s_0\frac{(\vec{\nabla}p\cdot\mathbf{B})\mathbf{B}}{B^2} + s_1\frac{\mathbf{B}\times\vec{\nabla}p}{B} + s_2\frac{\mathbf{B}\times(\vec{\nabla}p\times\mathbf{B})}{B^2} \\ & + \frac{(\vec{t_0}\cdot\mathbf{B})\mathbf{B}}{B^2} + \frac{\mathbf{B}\times\vec{t_1}}{B} + \frac{\mathbf{B}\times(\vec{t_2}\times\mathbf{B})}{B^2}\;. \end{aligned} \tag{2.81}$$

However, this expression can be simplified by examining the various coefficient terms. The only assumption made here is that the mass of the electron is much smaller than that of the ion, $m_{\mathrm{e}} \ll m_{\mathrm{ion}}$. By making this approximation, we can see that our Generalised Ohm's Law can be greatly simplified.

We start by examining the Hall parameter β_i and the new parameter $\beta_i' \equiv \frac{\rho_j}{\rho}\beta_i$ introduced in equation (2.49).

From the definitions $\beta_{\mathrm{e}} = \frac{\alpha_{\mathrm{e}}B}{K_{\mathrm{e,ion}}\rho_{\mathrm{ion}}}$ and $\beta_{\mathrm{ion}} = \frac{\alpha_{\mathrm{ion}}B}{K_{\mathrm{ion,e}}\rho_{\mathrm{e}}}$ and the requirement of charge neutrality, we can see that

$$\left|\frac{\beta_{\mathrm{e}}}{\beta_{\mathrm{ion}}}\right| = 1\;. \tag{2.82}$$

For the case of a two-fluid of electrons and ions, we now make the approximation that $m_{\mathrm{e}} \ll m_{\mathrm{ion}}$, so that:

$$\frac{\rho_{\mathrm{e}}}{\rho} \ll 1\;,\ \text{and}\ \frac{\rho_{\mathrm{ion}}}{\rho} \approx 1\;, \tag{2.83}$$

and so

$$\beta_{\mathrm{e}}' = \tfrac{\rho_{\mathrm{ion}}}{\rho}\beta_{\mathrm{e}} \approx \beta_{\mathrm{e}}\;, \tag{2.84}$$

and

$$\beta_{\mathrm{ion}}' = \tfrac{\rho_{\mathrm{e}}}{\rho}\beta_{\mathrm{ion}} \ll \beta_{\mathrm{ion}}\;, \tag{2.85}$$

which tells us that, using equation (2.82):

$$|\beta'_{\text{ion}}| \ll |\beta'_{\text{e}}| \,. \tag{2.86}$$

As the resistivities r are calculated in the code, they do not need to be simplified at this stage. Instead we concentrate on s and t, defined in equations (2.75) and (2.76), where the resistivities and conductivities are defined in equations (2.74) and (2.60) and the remaining necessary terms are defined in equations (2.61) and (2.62).

We start with s_0:

$$\begin{aligned}
s_0 \;&\equiv\; r_0 a_0 = \frac{a_0}{\sigma_{\|}} \\
&= \frac{\frac{1}{NB}\left(n_{\text{e}}\beta'_{\text{e}} + n_{\text{ion}}\beta'_{\text{ion}}\right)}{\frac{1}{B}\left(\alpha_{\text{e}}\rho_{\text{e}}\beta'_{\text{e}} + \alpha_{\text{ion}}\rho_{\text{ion}}\beta'_{\text{ion}}\right)} \\
&\frac{1}{N}\frac{n_{\text{e}}\left(\beta'_{\text{e}} + \frac{n_{\text{ion}}}{n_{\text{e}}}\beta'_{\text{ion}}\right)}{\alpha_{\text{e}}\rho_{\text{e}}\left(\beta'_{\text{e}} - \beta'_{\text{ion}}\right)} \\
&\approx \frac{1}{N}\frac{n_{\text{e}}}{\alpha_{\text{e}}\rho_{\text{e}}} = -\frac{1}{eN}
\end{aligned} \tag{2.87}$$

We next examine $s_1 = r_1 a_\perp - r_2 a_H = \frac{\sigma_H a_\perp}{\sigma_H^2 + \sigma_\perp^2} - \frac{\sigma_\perp a_H}{\sigma_H^2 + \sigma_\perp^2}$. First we look at the bottom of this fraction.

$$\begin{aligned}
\sigma_H^2 + \sigma_\perp^2 \;&=\; \left(\frac{1}{B}\sum \frac{\alpha_i\rho_i\beta_i'^2}{1+\beta_i'^2}\right)^2 + \left(\frac{1}{B}\sum \frac{\alpha_i\rho_i\beta'_i}{1+\beta_i'^2}\right)^2 \\
&=\; \frac{1}{B^2}\Bigg(\left(\frac{\alpha_{\text{e}}\rho_{\text{e}}\beta_{\text{e}}'^2}{1+\beta_{\text{e}}'^2}\right)^2 + \left(\frac{\alpha_{\text{ion}}\rho_{\text{ion}}\beta_{\text{ion}}'^2}{1+\beta_{\text{ion}}'^2}\right)^2 + 2\left(\frac{\alpha_{\text{e}}\rho_{\text{e}}\beta_{\text{e}}'^2}{1+\beta_{\text{e}}'^2}\right)\left(\frac{\alpha_{\text{ion}}\rho_{\text{ion}}\beta_{\text{ion}}'^2}{1+\beta_{\text{ion}}'^2}\right) \\
&\quad + \left(\frac{\alpha_{\text{e}}\rho_{\text{e}}\beta'_{\text{e}}}{1+\beta_{\text{e}}'^2}\right)^2 + \left(\frac{\alpha_{\text{ion}}\rho_{\text{ion}}\beta'_{\text{ion}}}{1+\beta_{\text{ion}}'^2}\right)^2 + 2\left(\frac{\alpha_{\text{e}}\rho_{\text{e}}\beta'_{\text{e}}}{1+\beta_{\text{e}}'^2}\right)\left(\frac{\alpha_{\text{ion}}\rho_{\text{ion}}\beta'_{\text{ion}}}{1+\beta_{\text{ion}}'^2}\right)\Bigg) \\
&\quad \text{which, using the condition of charge neutrality, simplifies to} \\
&=\; \frac{1}{B^2}\left(\frac{\left(\alpha_{\text{e}}\rho_{\text{e}}\beta'_{\text{e}} + \alpha_{\text{ion}}\rho_{\text{ion}}\beta'_{\text{ion}}\right)^2}{(1+\beta_{\text{e}}'^2)(1+\beta_{\text{ion}}'^2)}\right)
\end{aligned} \tag{2.88}$$

We are now able to examine the top of the fraction of s_1:

$$\begin{aligned}
& \sigma_H a_\perp - \sigma_\perp a_H \\
= \; & \left(\frac{1}{B}\sum \frac{\alpha_i\rho_i\beta_i'^2}{1+\beta_i'^2}\right)\left(\frac{1}{NB}\sum \frac{n_i\beta_i'}{1+\beta_i'^2}\right) - \left(\frac{1}{B}\sum \frac{\alpha_i\rho_i\beta_i'}{1+\beta_i'^2}\right)\left(\frac{1}{NB}\sum \frac{n_i\beta_i'^2}{1+\beta_i'^2}\right)
\end{aligned}$$

which, using the condition of charge neutrality, simplifies to

$$= \frac{1}{B^2}\frac{\alpha_{\mathrm{e}}\rho_{\mathrm{e}}\beta_{\mathrm{e}}'\beta_{\mathrm{ion}}'(\beta_{\mathrm{e}}'-\beta_{\mathrm{ion}}')}{(1+\beta_{\mathrm{e}}'^2)(1+\beta_{\mathrm{ion}}'^2)} \tag{2.89}$$

We can now calculate s_1:

$$\begin{aligned}
s_1 &= \frac{\alpha_{\mathrm{e}}\rho_{\mathrm{e}}\beta_{\mathrm{e}}'\beta_{\mathrm{ion}}'(\beta_{\mathrm{e}}'-\beta_{\mathrm{ion}}')}{(\alpha_{\mathrm{e}}\rho_{\mathrm{e}}\beta_{\mathrm{e}}'+\alpha_{\mathrm{ion}}\rho_{\mathrm{ion}}\beta_{\mathrm{ion}}')^2} \\
&= \frac{\beta_{\mathrm{e}}'\beta_{\mathrm{ion}}'}{\beta_{\mathrm{e}}'-\beta_{\mathrm{ion}}'}\frac{1}{\alpha_{\mathrm{e}}\rho_{\mathrm{e}}} \text{ ... by charge neutrality} \\
&\approx \beta_{\mathrm{ion}}'\frac{1}{\alpha_{\mathrm{e}}\rho_{\mathrm{e}}} \qquad (2.90)
\end{aligned}$$

To calculate $s_2 = r_1 a_H + r_2 a_\perp = \frac{\sigma_H a_H}{\sigma_H^2+\sigma_\perp^2} + \frac{\sigma_\perp a_\perp}{\sigma_H^2+\sigma_\perp^2}$, we start with the top of the fraction.

$$\begin{aligned}
& \sigma_H a_H + \sigma_\perp a_\perp \\
= \; & \left(-\frac{1}{B}\sum \frac{\alpha_i\rho_i}{1+\beta_i'^2}\right)\left(\frac{1}{NB}\sum \frac{n_i\beta_i'^2}{1+\beta_i'^2}\right) + \left(\frac{1}{B}\sum \frac{\alpha_i\rho_i\beta_i'}{1+\beta_i'^2}\right)\left(\frac{1}{NB}\sum \frac{n_i\beta_i'}{1+\beta_i'^2}\right)
\end{aligned}$$

which can be simplified to

$$= \frac{1}{NB^2}\left(\frac{\alpha_{\mathrm{e}}\rho_{\mathrm{e}}n_{\mathrm{ion}}\beta_{\mathrm{e}}'\beta_{\mathrm{ion}}' + \alpha_{\mathrm{ion}}\rho_{\mathrm{ion}}n_{\mathrm{e}}\beta_{\mathrm{e}}'\beta_{\mathrm{ion}}' - \alpha_{\mathrm{e}}\rho_{\mathrm{e}}n_{\mathrm{ion}}\beta_{\mathrm{ion}}'^2 - \alpha_{\mathrm{ion}}\rho_{\mathrm{ion}}n_{\mathrm{e}}\beta_{\mathrm{e}}'^2}{(1+\beta_{\mathrm{e}}'^2)(1+\beta_{\mathrm{ion}}'^2)}\right) \tag{2.91}$$

So then s_2 can be calculated as:

$$\begin{aligned}
s_2 &= \frac{1}{N}\frac{\alpha_{\text{e}}\rho_{\text{e}}n_{\text{ion}}\beta'_{\text{e}}\beta'_{\text{ion}} + \alpha_{\text{ion}}\rho_{\text{ion}}n_{\text{e}}\beta'_{\text{e}}\beta'_{\text{ion}} - \alpha_{\text{e}}\rho_{\text{e}}n_{\text{ion}}\beta'^2_{\text{ion}} - \alpha_{\text{ion}}\rho_{\text{ion}}n_{\text{e}}\beta'^2_{\text{e}}}{(\alpha_{\text{e}}\rho_{\text{e}}\beta'_{\text{e}} + \alpha_{\text{ion}}\rho_{\text{ion}}\beta_{\text{ion}})^2} \\
&= \frac{1}{N}\frac{1}{\alpha_{\text{e}}\rho_{\text{e}}}\frac{n_{\text{e}}\beta'_{\text{e}} + n_{\text{ion}}\beta'_{\text{ion}}}{\beta'_{\text{e}} - \beta_{\text{ion}}} \text{ .. after some algebra} \\
&\approx \frac{1}{N}\frac{1}{\alpha_{\text{e}}\rho_{\text{e}}}n_{\text{e}} = -\frac{1}{eN} \qquad (2.92)
\end{aligned}$$

This can now be repeated for t_0, t_1 and t_2.

We start with t_0:

$$\begin{aligned}
t_0 &\equiv r_0 b_0 = \frac{b_0}{\sigma_\|} \\
&= \frac{\frac{1}{B}\left(\rho_{\text{e}}\beta'_{\text{e}}\frac{D_{\text{e}}}{Dt}v_{\text{e}} + \rho_{\text{ion}}\beta'_{\text{ion}}\frac{D_{\text{ion}}}{Dt}v_{\text{ion}}\right)}{\frac{1}{B}\left(\alpha_{\text{e}}\rho_{\text{e}}\beta'_{\text{e}} + \alpha_{\text{ion}}\rho_{\text{ion}}\beta'_{\text{ion}}\right)} \\
&\ \frac{\rho_{\text{e}}\beta'_{\text{e}}\left(\frac{D_{\text{e}}}{Dt}v_{\text{e}} - \frac{D_{\text{ion}}}{Dt}v_{\text{ion}}\right)}{\rho_{\text{e}}\beta'_{\text{e}}\left(\alpha_{\text{e}} - \alpha_{\text{ion}}\right)} \\
&= \frac{1}{\alpha_{\text{e}} - \alpha_{\text{ion}}}\left(\frac{D_{\text{e}}}{Dt}v_{\text{e}} - \frac{D_{\text{ion}}}{Dt}v_{\text{ion}}\right) \qquad (2.93)
\end{aligned}$$

We next examine $t_1 = r_1 b_\perp - r_2 b_H = \frac{\sigma_H b_\perp}{\sigma_H^2 + \sigma_\perp^2} - \frac{\sigma_\perp b_H}{\sigma_H^2 + \sigma_\perp^2}$. We examine the top of this fraction of t_1:

$$\begin{aligned}
&\sigma_H b_\perp - \sigma_\perp b_H \\
= &\left(\frac{1}{B}\sum\frac{\alpha_i\rho_i\beta'^2_i}{1+\beta'^2_i}\right)\left(\frac{1}{B}\sum\frac{\rho_i\beta'_i}{1+\beta'^2_i}\frac{D_i}{Dt}v_i\right) - \left(\frac{1}{B}\sum\frac{\alpha_i\rho_i\beta'_i}{1+\beta'^2_i}\right)\left(\frac{1}{B}\sum\frac{\rho_i\beta'^2_i}{1+\beta'^2_i}\frac{D_i}{Dt}v_i\right) \\
&\text{which can be simplified to} \\
= &\frac{1}{B^2}\frac{\rho_{\text{e}}\rho_{\text{ion}}\beta'_{\text{e}}\beta'_{\text{ion}}(\beta'_{\text{e}} - \beta'_{\text{ion}})(\alpha_{\text{e}}\frac{D_{\text{ion}}}{Dt}v_{\text{ion}} + \alpha_{\text{ion}}\frac{D_{\text{e}}}{Dt}v_{\text{e}})}{(1+\beta'^2_{\text{e}})(1+\beta'^2_{\text{ion}})} \qquad (2.94)
\end{aligned}$$

We can now calculate t_1:

$$\begin{aligned} t_1 &= \frac{\rho_{\text{e}}\rho_{\text{ion}}\beta'_{\text{e}}\beta'_{\text{ion}}(\beta'_{\text{e}}-\beta'_{\text{ion}})}{(\alpha_{\text{e}}\rho_{\text{e}}\beta'_{\text{e}}+\alpha_{\text{ion}}\rho_{\text{ion}}\beta'_{\text{ion}})^2}\left(\alpha_{\text{e}}\frac{D_{\text{ion}}}{Dt}v_{\text{ion}}+\alpha_{\text{ion}}\frac{D_{\text{e}}}{Dt}v_{\text{e}}\right) \\ & \quad \text{which can be simplified to} \\ &= \frac{\beta'_{\text{e}}\beta'_{\text{ion}}}{\beta'_{\text{e}}-\beta'_{\text{ion}}}\left(\frac{1}{\alpha_{\text{e}}}\frac{D_{\text{e}}}{Dt}v_{\text{e}}-\frac{1}{\alpha_{\text{ion}}}\frac{D_{\text{ion}}}{Dt}v_{\text{ion}}\right) \\ &\approx \beta'_{\text{ion}}\left(\frac{1}{\alpha_{\text{e}}}\frac{D_{\text{e}}}{Dt}v_{\text{e}}-\frac{1}{\alpha_{\text{ion}}}\frac{D_{\text{ion}}}{Dt}v_{\text{ion}}\right) \end{aligned} \tag{2.95}$$

To calculate $t_2 = r_1 b_H + r_2 b_\perp = \frac{\sigma_H b_H}{\sigma_H^2+\sigma_\perp^2} + \frac{\sigma_\perp b_\perp}{\sigma_H^2+\sigma_\perp^2}$, we start with the top of the fraction.

$$\begin{aligned} & \sigma_H b_H + \sigma_\perp b_\perp \\ =\ & \left(-\frac{1}{B}\sum\frac{\alpha_i\rho_i}{1+\beta'^2_i}\right)\left(\frac{1}{N}\sum\frac{\rho_i\beta'^2_i}{1+\beta'^2_i}\frac{D_i}{Dt}v_i\right)+\left(\frac{1}{B}\sum\frac{\alpha_i\rho_i\beta'_i}{1+\beta'^2_i}\right)\left(\frac{1}{B}\sum\frac{\rho_i\beta'_i}{1+\beta'^2_i}\frac{D_i}{Dt}v_i\right) \\ & \text{which can be simplified to} \\ =\ & \frac{1}{B^2}\left(\frac{(\alpha_{\text{e}}\rho_{\text{e}})(\rho_{\text{e}}\beta'_{\text{e}})(\beta'_{\text{e}}-\beta'_{\text{ion}})(\frac{D_{\text{e}}}{Dt}v_{\text{e}}-\frac{D_{\text{ion}}}{Dt}v_{\text{ion}})}{(1+\beta'^2_{\text{e}})(1+\beta'^2_{\text{ion}})}\right) \end{aligned} \tag{2.96}$$

So then t_2 can be calculated as:

$$\begin{aligned} t_2 &= \frac{(\alpha_{\text{e}}\rho_{\text{e}})(\rho_{\text{e}}\beta'_{\text{e}})(\beta'_{\text{e}}-\beta'_{\text{ion}})\left(\frac{D_{\text{e}}}{Dt}v_{\text{e}}-\frac{D_{\text{ion}}}{Dt}v_{\text{ion}}\right)}{(\alpha_{\text{e}}\rho_{\text{e}}\beta'_{\text{e}}+\alpha_{\text{ion}}\rho_{\text{ion}}\beta_{\text{ion}})^2} \\ & \quad \text{which can be simplified to} \\ &= \frac{1}{\alpha_{\text{e}}-\alpha_{\text{ion}}}\left(\frac{D_{\text{e}}}{Dt}v_{\text{e}}-\frac{D_{\text{ion}}}{Dt}v_{\text{ion}}\right) \end{aligned} \tag{2.97}$$

So then the Generalised Ohm’s Law can be written from equation (2.81) as:

$$\begin{aligned}\mathbf{E} &= -\mathbf{v}\times\mathbf{B} + r_0\frac{(\mathbf{J}\cdot\mathbf{B})\mathbf{B}}{B^2} + r_1\frac{\mathbf{B}\times\mathbf{J}}{B} + r_2\frac{\mathbf{B}\times(\mathbf{J}\times\mathbf{B})}{B^2} \\ &\quad -\frac{1}{eN}\vec{\nabla}p + \frac{\beta'_{\mathrm{ion}}}{\alpha_{\mathrm{e}}\rho_{\mathrm{e}}}\frac{\mathbf{B}\times\vec{\nabla}p}{B} \\ &\quad +\frac{1}{\alpha_{\mathrm{e}}-\alpha_{\mathrm{ion}}}\left(\frac{D_{\mathrm{e}}}{Dt}\mathbf{v}_{\mathrm{e}} - \frac{D_{\mathrm{ion}}}{Dt}\mathbf{v}_{\mathrm{ion}}\right) + \frac{\mathbf{B}\times\beta'_{\mathrm{ion}}\left(\frac{1}{\alpha_{\mathrm{e}}}\frac{D_{\mathrm{e}}}{Dt}\mathbf{v}_{\mathrm{e}} - \frac{1}{\alpha_{\mathrm{ion}}}\frac{D_{\mathrm{ion}}}{Dt}\mathbf{v}_{\mathrm{ion}}\right)}{B}\,.\end{aligned}$$

It can be seen clearly that the terms in the last line of this expression are negligible in comparison to the rest, as the charge-to-mass ratios α_i are so large and as α_{e} has an opposite sign to α_{ion}. Therefore the Generalised Ohm's Law can be written in its final form as

$$\begin{aligned}\mathbf{E} &= -\mathbf{v}\times\mathbf{B} + r_0\frac{(\mathbf{J}\cdot\mathbf{B})\mathbf{B}}{B^2} + r_1\frac{\mathbf{B}\times\mathbf{J}}{B} + r_2\frac{\mathbf{B}\times(\mathbf{J}\times\mathbf{B})}{B^2} \\ &\quad -\frac{1}{eN}\vec{\nabla}p + \frac{\beta'_{\mathrm{ion}}}{\alpha_{\mathrm{e}}\rho_{\mathrm{e}}}\frac{\mathbf{B}\times\vec{\nabla}p}{B}\,. \qquad (2.98)\end{aligned}$$

By being written in this format, only minimal changes to the numerical code must be made in order to adapt HYDRA for use with a fully ionised plasma.

2.4.2 Investigation of the Generalised Ohm's Law for a Fully Ionised Plasma

The first thing that can be observed about this Generalised Ohm's Law for a fully ionised plasma, equation (2.98), is that it is more complicated than would be expected. The difference between the derivation above and that done by Cowling (1957), Mitchner & Kruger (1973), and Spitzer (1956), is that they have used further approximations in order to simplify the equation further. However, it can be seen that their version can be recovered from ours using the same approximations. In each of the above cases, the equations used represent the 2-fluid Hall MHD equations. Hall MHD requires one fluid, in this case the electron fluid, to be well-tied to the magnetic field, and for the other fluid, in this case the ion fluid, to be strongly decoupled from the magnetic field. This can be represented using the effective Hall parameters, β'_i, for the two fluids, such that:

$$|\beta'_{\mathrm{ion}}| \ll 1\,,\, |\beta'_{\mathrm{e}}| > 1 \tag{2.99}$$

In fact, the restrictions on the Hall parameters for Hall MHD are stricter than this, requiring:

$$|\beta'_{\mathrm{ion}}| \ll \frac{1}{|\beta'_{\mathrm{e}}|} < 1 \tag{2.100}$$

Using this, we re-examine equation (2.98):

$$\begin{aligned}\mathbf{E} \;=\; & -\mathbf{v}\times\mathbf{B} + r_0\frac{(\mathbf{J}\cdot\mathbf{B})\mathbf{B}}{B^2} + r_1\frac{\mathbf{B}\times\mathbf{J}}{B} + r_2\frac{\mathbf{B}\times(\mathbf{J}\times\mathbf{B})}{B^2} \\ & -\frac{1}{eN}\vec{\nabla}p + \frac{\beta'_{\mathrm{ion}}}{\alpha_{\mathrm{e}}\rho_{\mathrm{e}}}\frac{\mathbf{B}\times\vec{\nabla}p}{B}\,.\end{aligned}$$

We first note that now $\beta'_{\mathrm{ion}} \ll 1$. In this case, the last term of the above equation is clearly negligible in comparison to the previous term, and so it can be ignored. This results in:

$$\mathbf{E} = -\mathbf{v}\times\mathbf{B} + r_0\frac{(\mathbf{J}\cdot\mathbf{B})\mathbf{B}}{B^2} + r_1\frac{\mathbf{B}\times\mathbf{J}}{B} + r_2\frac{\mathbf{B}\times(\mathbf{J}\times\mathbf{B})}{B^2} - \frac{1}{eN}\vec{\nabla}p\,. \tag{2.101}$$

We then examine the conductivities derived earlier, σ_H, $\sigma_\perp$ and $\sigma_\parallel$, under the above approximations. We find:

$$
\begin{aligned}
\sigma_\parallel &\equiv \frac{1}{B}\sum_{i=1}^{N}\alpha_i\rho_i\beta'_i = \frac{1}{B}\left(\alpha_{\rm e}\rho_{\rm e}\beta'_{\rm e} + \alpha_{\rm ion}\rho_{\rm ion}\beta'_{\rm ion}\right) \\
&= \frac{1}{B}\alpha_{\rm e}\rho_{\rm e}(\beta'_{\rm e} - \beta'_{\rm ion}) \approx \frac{1}{B}\alpha_{\rm e}\rho_{\rm e}\beta'_{\rm e} \qquad (2.102) \\
\sigma_H &\equiv \frac{1}{B}\sum_{i=1}^{N}\frac{\alpha_i\rho_i\beta'^2_i}{(1+\beta'^2_i)} = -\frac{1}{B}\sum_{i=1}^{N}\frac{\alpha_i\rho_i}{(1+\beta'^2_i)} \\
&\ \text{(this can be confirmed by bringing the two terms together and adding to get zero)} \\
&= -\frac{1}{B}\left(\frac{\alpha_{\rm e}\rho_{\rm e}}{1+\beta'^2_{\rm e}} + \frac{\alpha_{\rm ion}\rho_{\rm ion}}{1+\beta'^2_{\rm ion}}\right) = -\frac{\alpha_{\rm e}\rho_{\rm e}}{B}\left(\frac{1}{1+\beta'^2_{\rm e}} - \frac{1}{1+\beta'^2_{\rm ion}}\right) \\
&\approx \frac{\alpha_{\rm e}\rho_{\rm e}}{B} \qquad (2.103) \\
\sigma_\perp &\equiv \frac{1}{B}\sum_{i=1}^{N}\frac{\alpha_i\rho_i\beta'_i}{(1+\beta'^2_i)} = \frac{1}{B}\left(\frac{\alpha_{\rm e}\rho_{\rm e}\beta'_{\rm e}}{1+\beta'^2_{\rm e}} + \frac{\alpha_{\rm ion}\rho_{\rm ion}\beta'_{\rm ion}}{1+\beta'^2_{\rm ion}}\right) \\
&= \frac{\alpha_{\rm e}\rho_{\rm e}}{B}\left(\frac{\beta'_{\rm e}}{1+\beta'^2_{\rm e}} - \frac{\beta'_{\rm ion}}{1+\beta^2_{\rm ion}}\right) \approx \frac{\alpha_{\rm e}\rho_{\rm e}}{B}\left(\frac{1}{\beta'_{\rm e}} - \beta'_{\rm ion}\right) \\
&\approx \frac{\alpha_{\rm e}\rho_{\rm e}}{B}\frac{1}{\beta'_{\rm e}}\,. \qquad (2.104)
\end{aligned}
$$

Recalculating our resistive terms, r_0, r_1 and r_2, using these above values, we get:

$$
\begin{aligned}
r_0 &\equiv \tfrac{1}{\sigma_\parallel} &&\approx \frac{B}{\alpha_{\rm e}\rho_{\rm e}}\frac{1}{\beta'_{\rm e}}\,, && (2.105) \\
r_1 &\equiv \tfrac{\sigma_H}{\sigma_\parallel^2+\sigma_H^2} &&\approx \frac{\frac{\alpha_{\rm e}\rho_{\rm e}}{B}}{\left(\frac{\alpha_{\rm e}\rho_{\rm e}}{B}\right)^2\left(1+\frac{1}{\beta'^2_{\rm e}}\right)} \approx \frac{B}{\alpha_{\rm e}\rho}\,, && (2.106) \\
r_2 &\equiv \tfrac{\sigma_\perp}{\sigma_\perp^2+\sigma_H^2} &&\approx \frac{\frac{\alpha_{\rm e}\rho_{\rm e}}{B\beta'_{\rm e}}}{\left(\frac{\alpha_{\rm e}\rho_{\rm e}}{B}\right)^2\left(1+\frac{1}{\beta'^2_{\rm e}}\right)} \approx \frac{B}{\alpha_{\rm e}\rho_{\rm e}}\frac{1}{\beta'_{\rm e}}\,. && (2.107)
\end{aligned}
$$

We note that $r_0 = r_2$. This means that in Hall MHD there is no resistivity in the direction $\mathbf{J}_\perp$ other than the ohmic resistivity, $r_0(\mathbf{J}_\parallel + \mathbf{J}_\perp)$. The extra diffusion in this direction had been caused by ambipolar diffusion. However, in Hall MHD, this process is ignored.

This finally reduces our Generalised Ohm's Law from (2.101) to:

$$\mathbf{E} = -\mathbf{v} \times \mathbf{B} + \frac{B}{\alpha_\mathrm{e}\rho_\mathrm{e}\beta'_\mathrm{e}}\mathbf{J} + \frac{1}{\alpha_\mathrm{e}\rho_\mathrm{e}}(\mathbf{B} \times \mathbf{J}) - \frac{1}{eN}\vec{\nabla}p\,. \tag{2.108}$$

We can compare this expression to that by Cowling (1957) for a fully ionised plasma:

$$\mathbf{E} + \mu\mathbf{v} \times \mathbf{B} + \frac{1}{n_\mathrm{e}e}\vec{\nabla}p_\mathrm{e} = \frac{1}{\sigma}\mathbf{J} + \frac{1}{\sigma}\frac{\mu e\tau}{m_\mathrm{e}}\mathbf{J} \times \mathbf{B}\,, \tag{2.109}$$

where

$$\sigma \equiv \frac{n_\mathrm{e}e^2\tau}{m_\mathrm{e}}\,, \text{ and } \mu = \frac{1}{c}\,, \tag{2.110}$$

and comparison of the form of the collision terms tells us that:

$$\tau = \frac{1}{\rho_\mathrm{ion}K_\mathrm{e,ion}} = \frac{\beta_\mathrm{e}}{\alpha_\mathrm{e}B} \approx \frac{\beta'_\mathrm{e}}{\alpha_\mathrm{e}B}\,. \tag{2.111}$$

If we also recall that $\vec{\nabla}p_\mathrm{e} = \frac{n_\mathrm{e}}{N}\vec{\nabla}p$, then using these relations, equation (2.109) becomes:

$$\mathbf{E} = -\mathbf{v} \times \mathbf{B} + \frac{B}{(-en_\mathrm{e})\beta'_\mathrm{e}}\mathbf{J} + \frac{1}{en_\mathrm{e}}\mathbf{J} \times \mathbf{B} - \frac{1}{eN}\vec{\nabla}p\,, \tag{2.112}$$

which we can see is clearly equivalent to our own, where we have incorporated factors of the speed of light c into the equations for the magnetic field $\mathbf{B}$.

Chapter 3

Numerical ideal MHD study of the KH instability

Our study of the Kelvin-Helmholtz instability in a weakly ionised molecular cloud is carried out using the numerical code HYDRA, as described in Chapter 2. However, before carrying out the simulations of the KH instability for a nonideal MHD system, a number of comparative tests were performed in order to prove the code's ability to reproduce previous work on the instability in the ideal MHD case. These included comparisons with previous linear analyses as well as numerical studies.

3.1 Comparisons with linear analysis

Linear analysis of the KH instability is based on solving the dispersion relation and calculating the growth rate of the instability. For this reason, it is the growth rate that is used here to make direct comparisons with the result of numerical simulations. These were carried out under ideal MHD conditions using the numerical code HYDRA. The linear growth rate of the instability was then determined, and compared to that found in the linear analysis carried out by Miura & Pritchett (1982) for an incompressible plasma. Unfortunately, linearly derived growth rates for the KH instability in a compressible plasma are not available. However, as our system consists of an isothermal plasma that does not undergo any large changes in pressure during the linear regime, it behaves in a similar fashion to an incompressible plasma. Therefore examination of the two can still provide a useful comparison.

The initial set-up of our system was the same as that in the linear study (Miura & Pritchett, 1982). The computations were carried out on a 2.5 D slab grid in the xy-plane. This allows 3D dynamics to be captured on a 2 D grid. The grid consists of $400 \times 200 \times 1$ cells, in the x, y, and z directions respectively. Previous studies of the KH instability (Malagoli et al., 1996; Keppens et al., 1999; Palotti et al., 2008) have used a variety of resolutions and grid widths, but it can be seen that our choices are sufficient to capture the initial linear growth of the system (Keppens et al., 1999). The initial set-up used was that of two fluids flowing anti-parallel side-by-side on a grid of size $x = [0, 2L]$ and $y = [0, L]$. The plasma velocities are given by $+\frac{V_0}{2}$ and $-\frac{V_0}{2}$ in the y-direction, with a tangential shear layer of width $2a$ at the interface at $x = L$. This velocity profile is described by

$$\mathbf{v}_0 = \frac{V_0}{2} \tanh\left(\frac{x-L}{a}\right) \hat{\mathbf{y}}. \tag{3.1}$$

and a cross-section in the xz-plane has been plotted in figure 3.1. The width of the shear layer is chosen to be small but resolvable, and is set using $\frac{a}{L} = 0.05$. This means that there are 20 grid zones across the shear layer of width $2a$.

As in the parallel case in the linear analysis study, the initial magnetic field is set to be uniform and aligned with the direction of the plasma flow:

$$\mathbf{B}_0 = B_0 \hat{\mathbf{y}}. \tag{3.2}$$

The initial velocity field is then subjected to a small perturbation, given by

$$\delta \mathbf{v}_x = \delta V_0 \sin(-k_y y) \exp\left(-\frac{(x-L)^2}{\sigma^2}\right). \tag{3.3}$$

It is required that the amplitude of the perturbation $\delta V_0 \ll V_0$, and in the following study it has been set to $10^{-4}\, V_0$.

The wavelength of the perturbation is set equal to the characteristic length scale , $\lambda = \frac{2\pi}{k_y} = L$, so that a single wavelength fits exactly into the computational domain. This maximises the possibility of resolving structures that are small relative to the initial perturbed wavelength, (Frank et al., 1996). The pertur-

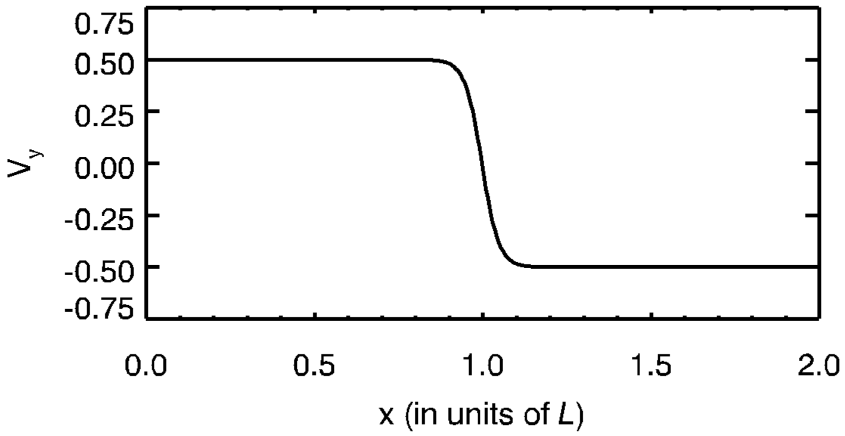

Figure 3.1: Initial y-velocity profile of the system, plotted against x.

bation attenuation scale is chosen so that it is larger than the shear layer, but small enough so that the instability can be assumed to interact only minimally with the x-boundaries (Palotti et al., 2008), and is set using $\frac{\sigma}{L} = 0.2$ (Keppens et al., 1999; Palotti et al., 2008).

The physical parameters are then chosen using normalised, dimensionless quantities. The wavenumber k_y is chosen to be 2π, in order to maximise the growth rate of the instability (Keppens et al., 1999). This normalises the length-scale of the simulation, so that $L = 1$. The timescale is then normalised by the sound speed, so that $c_\mathrm{s} = \frac{L}{T} = 1$. The mass scale is chosen such that the initial mass density is set to unity, $\rho_0 = 1$. In the isothermal case the adiabatic index $\gamma = 1$, and this gives us a sound speed $c_\mathrm{s} \equiv \sqrt{\frac{\gamma p_0}{\rho_0}} = 1$, and the initial pressure is therefore also equal to unity, $p_0 = 1$. A transonic flow is chosen with sonic Mach number $M_\mathrm{s} = \frac{V_0}{c_\mathrm{s}} = 1$, so that the plasma has velocity $\pm\frac{V_0}{2} = \pm 0.5$. In order for the KH instability to grow, it is required that the flow be super-Alfvénic (Chandrasekhar, 1961), and so for this study, an Alfvén Mach $M_\mathrm{A} = \frac{V_0}{v_\mathrm{A}} = 10$ is chosen. This sets the Alfvén velocity, $v_\mathrm{A} = \sqrt{\frac{B_0^2}{\rho_0}} = 0.1$, and the initial magnetic field strength to $B_0 = 0.1$. Finally, the boundary conditions are set. At the y-boundaries periodic conditions are used, while the x- and z-boundaries are set

In dimensionless parameters	
Physical parameters:	$\rho_0 = 1$, $c_s = 1 \Rightarrow p_0 = 1$ $M_{\mathrm{s}} = 1 \Rightarrow \frac{V_0}{2} = 0.5$ $M_{\mathrm{A}} = 10 \Rightarrow B_0 = 0.1$
Computational set-up:	$\sigma = 0.2$, $a = 0.05$ $k_y = 2\pi$, $\delta V_0 = 10^{-4}$
Grid parameters:	$x = [0, 2]$ and $y = [0, 1]$ $NX = 400$, $NY = 200$, $NZ = 1$

Table 3.1

to be zero-gradient.

In order to study the growth of the instability, the evolution of a number of parameters can be measured with time. In particular, we measure the transverse kinetic energy, $KE_x = \int\int dxdy \frac{1}{2}\rho \mathbf{v}_x^2$, in the system. As the entire plasma flow is initially in the y-direction, with only a very small perturbation in the x-direction, any growth of the kinetic energy is due to the growth of the instability. Linear analysis predicts an exponential growth in this transverse kinetic energy, and numerical studies concur.

It is possible to determine the growth rate of the instability directly from the growth of the transverse kinetic energy (Keppens et al., 1999). It is recalled from section 1.4.1 that each perturbed quantity in the system can expressed in the form of a sum of an initial constant value and a smaller time-dependent parameter,

$$Q_i \equiv Q_{0,i} + q_i$$

where $q_i \propto \exp[i(\mathbf{k} \cdot \mathbf{r} - \omega t)]$ and $q_i \ll Q_{0,i}$. The transverse kinetic can thus be expressed as

$$\begin{aligned} KE_x &= (\rho_0 + \delta\rho)(|v_x|_0 + \delta v_x)^2 && (3.4)\\ &= (\rho_0 + \delta\rho)(\delta v_x)^2 \text{ , as } |v_x|_0 = 0 && (3.5)\\ &\approx \rho_0 \delta v_x^2 \text{ , as } \rho_0 \gg \delta\rho && (3.6)\\ &\propto \exp[2i(\mathbf{k} \cdot \mathbf{r} - \omega t)] && (3.7) \end{aligned}$$

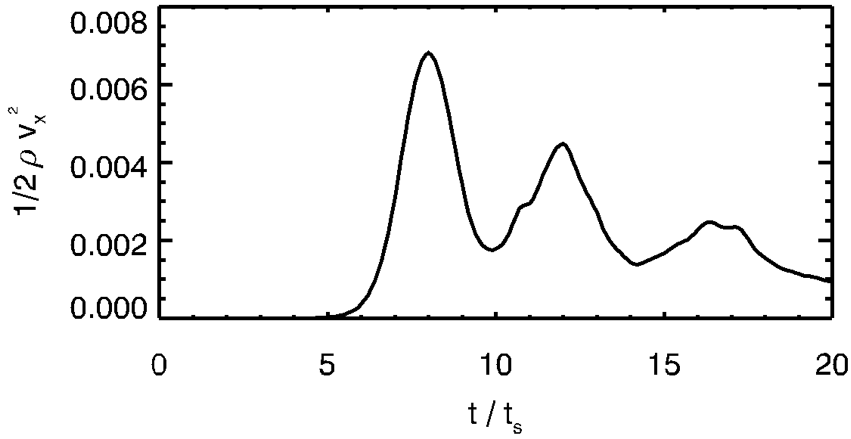

Figure 3.2: Plot of the growth the transverse kinetic energy in the system with time for ideal MHD.

which is an exponential function with a growth rate of 2ω, where ω is the growth rate of the instability.

Figure 3.2 is a plot of the growth of the transverse kinetic energy with time. Time is measured in units of the sound-crossing time, $t_{\mathrm{s}} = \frac{L}{c_{\mathrm{s}}}$.

It can be seen from the plot that this is indeed an exponential function. In order to calculate the growth rate from this, the natural log of the transverse kinetic energy is plotted against time. The straight-line plot corroborates the predictions from linear analysis. The linear function that has been overplotted on the graph serves to demonstrate the growth rate for this case.

The growth rate, 2ω, measured from this plot of the natural log of the transverse kinetic energy is 2.63. This is normalised using the width of the shear layer a and the initial relative velocity V_0 of the plasma flow to get a growth rate $\frac{\omega a}{(V_0/2)} = 0.1315$.

The growth rate can also be measured by examining the growth of the KH modes with time. A power spectrum is performed on the plasma density using the fast Fourier transform. The amplitude of this first mode is plotted against time in figure 3.4.

This can also seen to be an exponential function, as expected. A plot of the

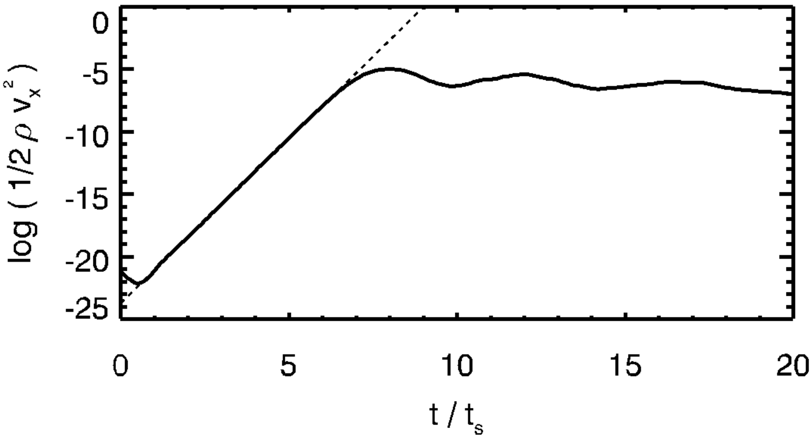

Figure 3.3: Plot of the natural log of the transverse kinetic energy with time for ideal MHD. A linear function (dashed line) has been overplotted in order to demonstrate the slope of the curve. The equation of the linear function is $y = 2.63\,x - 23.7$.

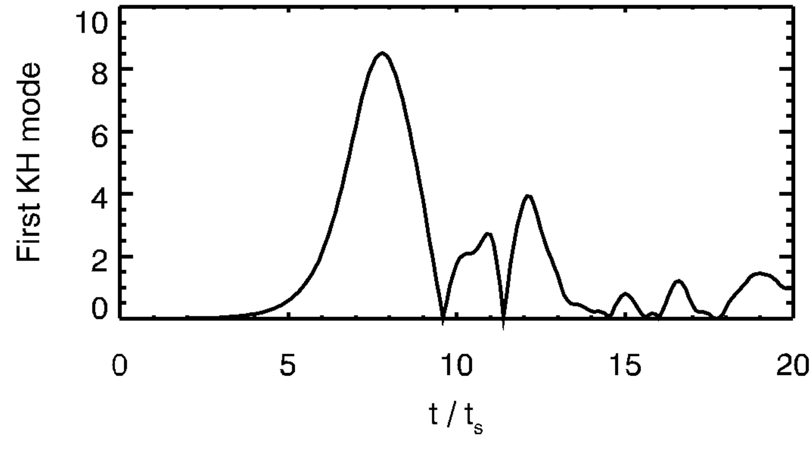

Figure 3.4: Plot of the amplitude of the first KH mode with time for ideal MHD.

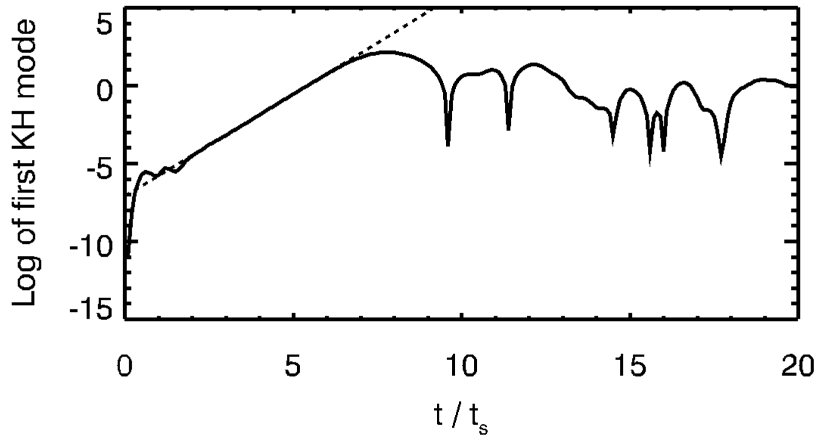

Figure 3.5: Plot of the natural log of the amplitude of the first KH mode with time for ideal MHD. A linear function (dashed line) has been overplotted to demonstrate the slope of the curve. The equation of the linear function is $y = 1.315x - 7.1$.

natural logarithm of this, as in figure 3.5, gives a straight-line function of slope also equal to the growth rate ω.

From figure 3.5 it can be seen that $\omega = 1.315$, and so the normalised growth rate is $\frac{\omega a}{(V_0/2)} = 0.1315$, which concurs with the value determined from the exponential growth of the transverse kinetic energy.

This growth rate can now be compared to that calculated analytically by Miura & Pritchett (1982). Their growth rates Γ are plotted as normalised by $\frac{2\Gamma a}{V_0}$ against the wavenumber, normalised by $2ka$. Using wavenumber $k_y = 2\pi$ and shear width $a = 0.05$, the normalised wavenumber in our simulation equates to $\frac{\pi}{5} \approx 0.628$. Reading from Figure 4 in Miura & Pritchett (1982), for an Alfvén Mach number of 10, their normalised growth rate at this wavenumber is $\frac{2\Gamma a}{V_0} = 0.13$. The difference between this value and the value calculated from our numerical simulation is $\approx 1\%$.

While comparisons between linear studies of incompressible flows, and numerical studies of compressible flows are bound to differ to some extent, these results are seen to agree exceptionally well.

3.2 Comparisons with previous numerical studies

We have demonstrated that the numerical code HYDRA is capable of simulating the KH instability under ideal MHD conditions and to demonstrate growth rates equivalent to those derived analytically. The code is next examined for its ability to reproduce results from the nonlinear numerical studies on the KH instability in Malagoli et al. (1996), Keppens et al. (1999) and Palotti et al. (2008). The same initial system of parameters were used in these three paper, and were carried out using resistive MHD. Using only different initial magnetic field configurations, each study examined the linear growth of the KH instability, and the subsequent nonlinear decay. However, all three studies were performed under the assumption of an adiabatic gas, while our system consists of an isothermal plasma. As will be seen below, however, the results are qualitatively very similar. The only explicitly quantitative comparison made here is between linear growth rates, and this is given only in the paper by Keppens et al. (1999).

The results of our simulations are first compared to those obtained by Malagoli et al. (1996). In figure 3.6, the evolution of the magnitude of the magnetic energy in the system has been plotted against time. This is calculated from $\int\int \frac{1}{2}\big(B_x^2 + B_y^2 + B_z^2\big)\, dx\, dy$. This can be compared directly with Fig. 5 (upper panel) from Malagoli et al. (1996), as both represent simulations parameterised by a sonic Mach number $M_{\mathrm{s}} = 1$ and an Alfvén Mach number $M_{\mathrm{A}} = 10$. The plot by Malagoli et al. (1996) shows two simulations of different resolutions. The greater of the two resolutions used is closer to that used in our simulations. The growth of the magnetic energy in this case, compared to our own, is quantitatively very similar. Both grow to an initial maximum, before saturating and slowly decaying. The initial maxima reached in the two cases are within approximately 10% of each other. It can be seen that the system in Malagoli et al. (1996) reaches saturation at an earlier time. This time taken to reach saturation depends on the amplitude of the initial perturbation (Frank et al., 1996) and also on the timescale being used, both of which may be different to our own.

Our simulations are next compared with those by Palotti et al. (2008). First to be examined are the results of non-magnetised hydrodynamic (HD) systems. Figure 3.7 given here, and the top panel of Fig. 3 in the paper by Palotti et al.

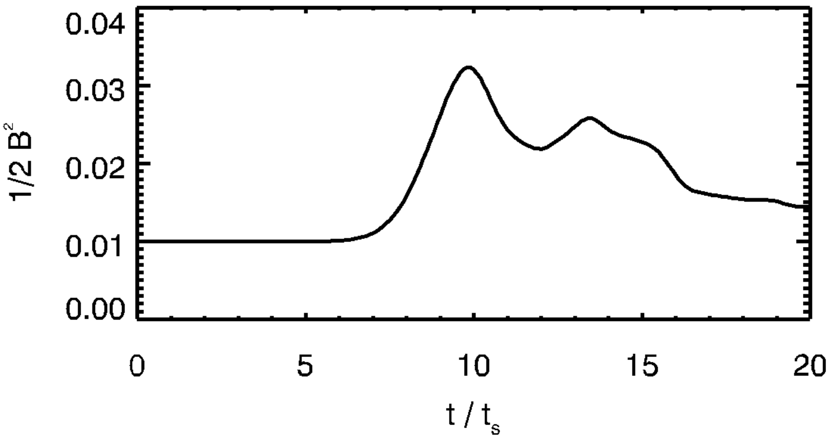

Figure 3.6: Plot of the evolution of the magnetic energy with time, using a resolution of $400 \times 200 \times 1$ grid zones.

(2008) plot the time evolution of the transverse kinetic energy for the HD simulations. While differing initial parameters again lead to quantitatively different results, extremely similar qualitative behaviour is observed.

Next the magnetised systems are compared. Comparisons can be made between plots of the transverse kinetic energy (figure 3.8 given here and the top panel of Fig. 11 in Palotti et al. 2008) and plots of perturbed magnetic energy (figure 3.9 given here and the bottom panel of Fig. 11 in Palotti et al. 2008). The perturbed magnetic energy is calculated as $\int\int dxdy\left(\frac{1}{2}\left(B_x^2+B_y^2+B_z^2\right)-\frac{1}{2}\left(B_0^2\right)\right)$. The plots from Palotti et al. (2008) show the results from systems with a range of magnetic Reynolds numbers. In both cases, our results agree closely with their simulations of $Re_{\rm m} \approx 5000$. This is roughly as expected, as while our simulations are currently using ideal MHD conditions, under which there is no resistivity, there is some numerical dissipation which will act in a similar fashion.

The most noticeable result from the plots of the transverse kinetic energy is that the initial maximum reached is lower than it was in the hydrodynamic case. This drop is relatively similar in both studies. Other than that, the general qualitative behaviour is very similar for each. From the plots of the perturbed magnetic energy, it can be seen that the magnetic field also behaves in a qualitatively similar

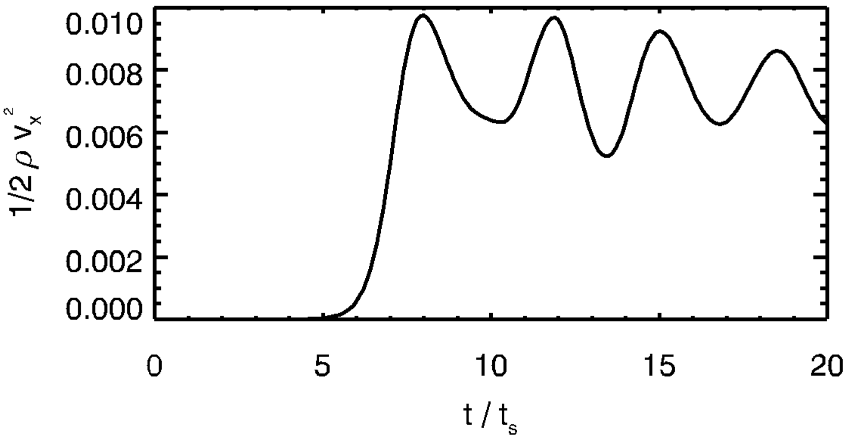

Figure 3.7: Plot of the growth the transverse kinetic energy in the system with time for the HD model.

fashion in both studies.

The third and final comparison is with the results obtained by Keppens et al. (1999). The study allows for a more quantitative comparison, as values are given for the linear growth rate of the instability. Using the same method as carried out in section 3.1, Keppens et al. (1999) calculate the growth rate of the instability in their system by plotting the log of the transverse kinetic energy and determining its slope (Figure 2 in Keppens et al. 1999). Taking this slope to be equivalent to twice the growth rate of the instability (Γ), and normalising it using the width of the shear layer and the magnitude of the initial velocity, the result is given as $\frac{\Gamma a}{V_0} = 0.131$ for the magnetised system with a parallel magnetic field (see Table 1 of Keppens et al. 1999). It can be recalled from section 3.1 that the normalised growth rate for our ideal MHD system was 0.1315. We conclude that not only are our ideal MHD results qualitatively similar to previous studies of the KH instability, but given an equivalent initial set-up, are extremely quantitatively similar too.

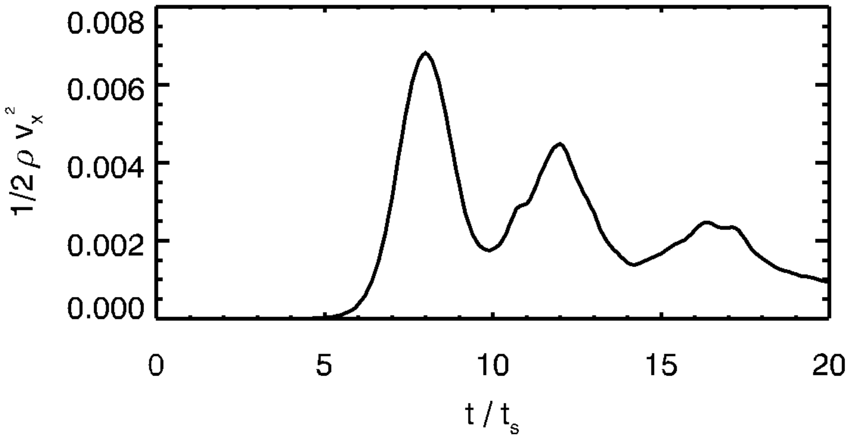

Figure 3.8: Plot of the growth the transverse kinetic energy in the system with time for ideal MHD.

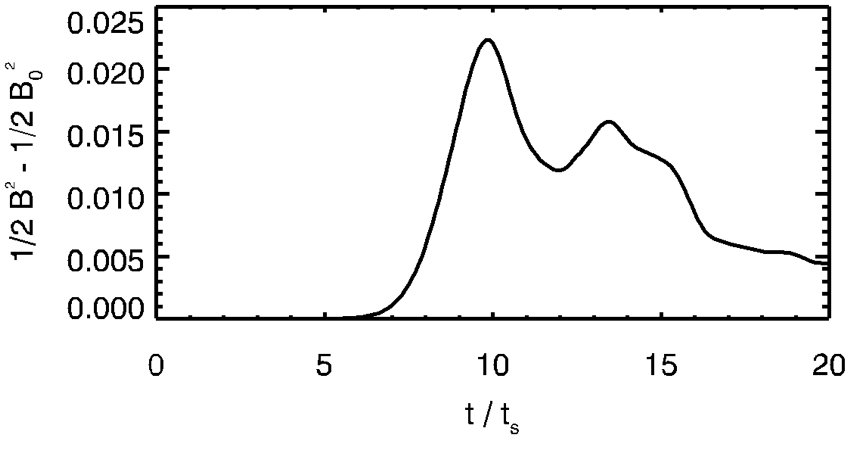

Figure 3.9: Plot of the perturbed magnetic energy in the system with time for ideal MHD.

Chapter 4

Ambipolar-dominated multifluid MHD study of the KH instability

In this chapter and the next, our simulations are expanded on so as to include the nonideal effects of ambipolar diffusion and the Hall effect. It is known that there are astrophysical systems in which each dominates, from the ambipolar-dominated molecular clouds (Wardle & Ng, 1999), to the Hall-dominated regions in protoplanetary disks (Wardle, 2007). Here each effect is studied in isolation, so that it can be understood precisely how it affects the KH instability, relative to an ideal MHD system. In some instances, the addition of nonideal effects can cause decoupling of the plasma in such a way that the bulk fluid evolves almost independently of the magnetic field. For this reason, non-magnetised HD systems are included in some of the comparisons.

4.1 Computational Set-Up

As in the previous chapter, these simulations are carried out using dimensionless parameters. Physical units will be included in chapter 6 when the KH instability is studied with respect to its applicability to molecular clouds. The computational parameters used in both this and the following two chapters are decided on by the requirements of the nonideal KH instability. The studies are carried out using 2.5 D simulations as some nonideal effects could be lost in two dimensions, such as regenerative dynamo action (Malagoli et al., 1996). Also, the Hall effect introduces another dimensional aspect to the simulations that does not occur in ideal MHD, and which requires a third dimension in order to capture these physical processes (Palotti et al., 2008).

4.1.1 Perturbation study

From linear analysis studies of the Kelvin-Helmholtz instability, it is expected that different perturbation modes in a system will grow at different rates. In order to find the fastest growing KH mode in our system, a large grid of length $8\,L$ was used. This set-up allows for the growth of any mode with a wavelength of which the length of the grid is an integer multiple. The system is given an initial perturbation with one such mode, of wavelength $\lambda = 8\,L$ and wavenumber $k_y = \frac{2\pi}{\lambda} = \frac{\pi}{4}$. Other modes that experience growth are those with wavelengths $\lambda = 2\,L$, $\lambda = 1\,L$, $\lambda = 0.8\,L$, $\lambda = \frac{2}{3}\,L$ and $\lambda = 0.5\,L$. These latter modes correspond to wavenumbers $k_y = \pi$, $k_y = 2\pi$, $k_y = 2.5\pi$, $k_y = 3\pi$, $k_y = 4\pi$.

As the ideal MHD system is allowed to evolve, the strongest growing mode is seen to dominate. It can be seen from figure 4.1 that the mode with $k_y = 2.5\pi$ mode grows strongest, with its wavelength $\lambda = 0.8\,L$ fitting into the grid an even ten times.

The growth rates of each mode in the system are calculated in the same manner as for the ideal MHD case earlier. The Fourier transform is taken of the fluid mass density. Each mode is examined in turn, and the logarithm of the corresponding transform is plotted with time. The slope of this function gives the growth rate for that particular mode. Figure 4.2 plots the calculated growth rates as a function of the wavenumber.

It can be seen that the fastest growing modes have wavenumbers $k_y = 2\pi$, $k_y = 2.5\pi$, and $k_y = 3\pi$. In order to assist in the choice of wavenumber for the perturbation in our studies, simulations are run using grids of length equal to the wavelength for each the three modes with high growth rates. Figure 4.3 demonstrates the growth of the instability through the evolution of the transverse kinetic energy for each case.

It can be seen that the mode of wavenumber $k_y = 2\pi$ has both a high growth rate and demonstrates the strongest growth of transverse kinetic energy. For this reason, this is chosen for the initial perturbation in our studies. It also has a convenient wavelength $\lambda = \frac{2\pi}{k_y} = 1$.

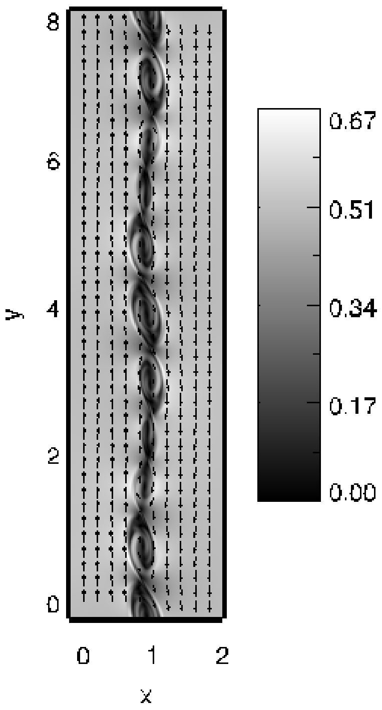

Figure 4.1: Plot of the magnitude and vector field of the velocity in the system at time $t = 17\,t_\mathrm{s}$. It can clearly be seen that ten individual vortices have developed in the grid, demonstrating that the $k_y = 2.5\pi$ mode has dominated the system.

4.1.2 Grid width study

The initial set-up for the Kelvin-Helmholtz simulations involves the active shear layer being placed in the centre of the grid, away from the zero-gradient x-boundaries. In order to ensure that the boundaries do not interfere with the dynamics of the system at any time, a study of the dependence on the width of the grid is carried out. The ideal MHD simulations were carried out on grids of width $2\,L$, where L is the characteristic lengthscale of the system. This width was chosen in Chapter 3 as it was found to be sufficiently wide so as to not affect the initial linear growth of the instability. However, after closer examination, it is found that this width of the grid does interfere with the subsequent nonlinear evolution of the instability.

As the KH instability grows in the centre of the grid, it is seen to develop

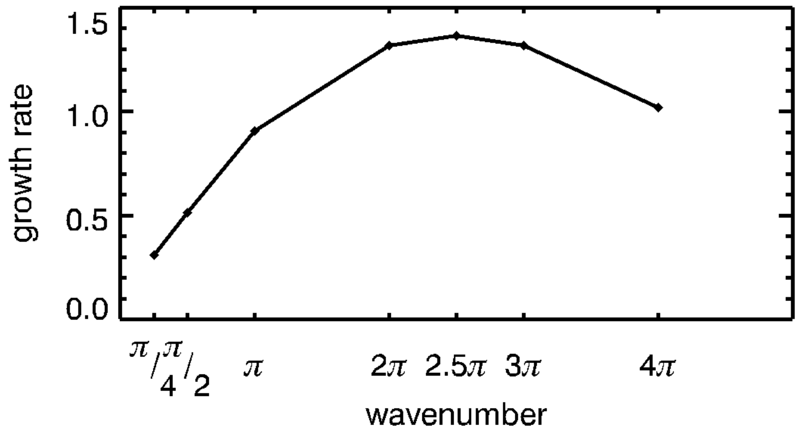

Figure 4.2: Plot of the growth rates of each of the seven modes in the system as a function of their wavenumber. There are three modes with stronger growth rates than the others.

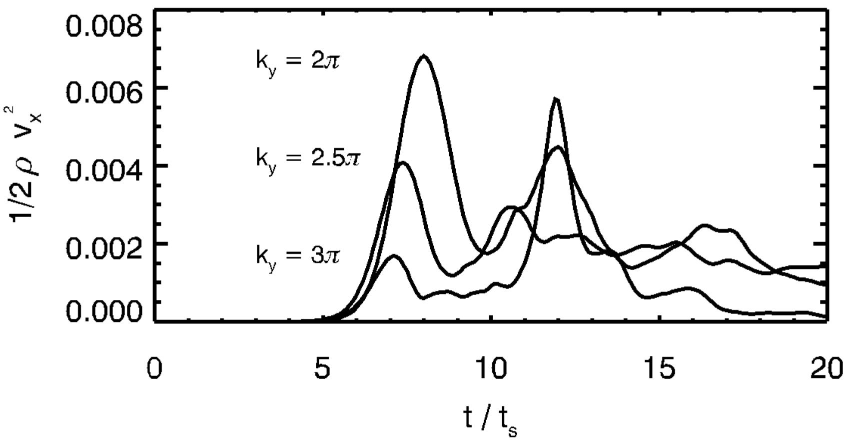

Figure 4.3: Plot of the transverse kinetic energy in the system with time for each of the three modes with high growth rates. It can be seen that the instability grows strongest in the case where the perturbation has wavenumber $k_y = 2\pi$.

what is known as the "Kelvin's Cat's eye" vortex. During this initial growth, several parameters undergo exponential growth. This growth reaches a saturation point around time $t = 8\,t_{\rm s}$. At this time, the vortex can be observed to change its orientation slightly, from being somewhat oblique and inclined towards the diagonal from the top right to the bottom left of the grid (such as in figure 4.4), to being inclined toward the opposite diagonal (such as in figure 4.5).

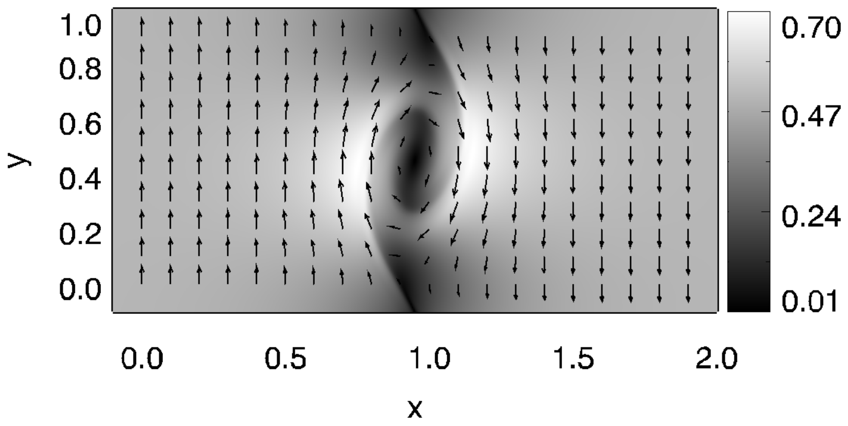

Figure 4.4: Plot of the magnitude and vector field of the velocity in the system at time $t = 7.5\,t_{\rm s}$. It can be seen that the vortex is slightly inclined towards the diagonal from the top right to the bottom left of the grid.

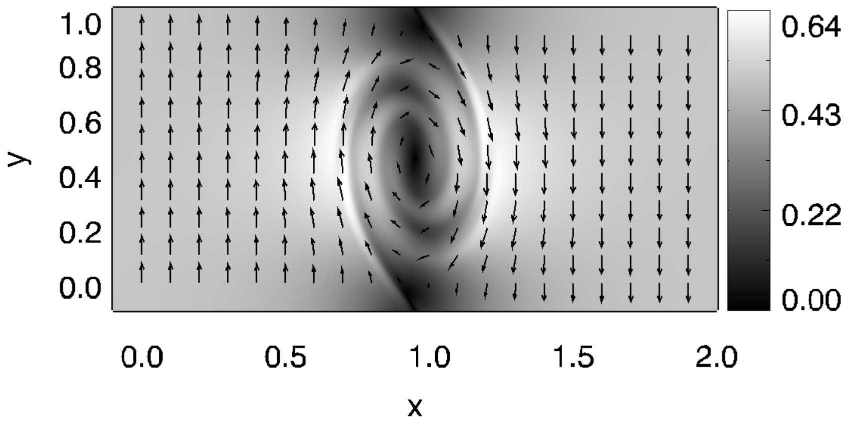

Figure 4.5: Plot of the magnitude and vector field of the velocity in the system at time $t = 8.5\,t_{\rm s}$. It can be seen that the vortex is now inclined towards the diagonal from the top left to the bottom right of the grid.

By studying the configuration of the vortex at the earlier time, it can be seen that in the centre of the KH vortex, there is an inward net fluid flow along the x-direction, and an outward net fluid flow along the y-direction. As the instability reaches this saturation point (which will be studied in more detail later), the vortex tilts towards the opposite diagonal and this net flow is suddenly reversed. Figure 4.6 plots the transverse velocities through the centre of vortex along x at times $t = 7.5\,t_{\rm s}$, $8\,t_{\rm s}$ and $9\,t_{\rm s}$. This clearly demonstrates the reversing of the transverse velocities in the centre of the vortex as described. Initially the velocities were positive to the left of the centre of the vortex, and negative on the right. This results in the net flow towards the centre of the vortex. At the later times, the x-velocities are now negative at the left of the centre, and positive on the right. This results in a net flow away from the centre of the vortex.

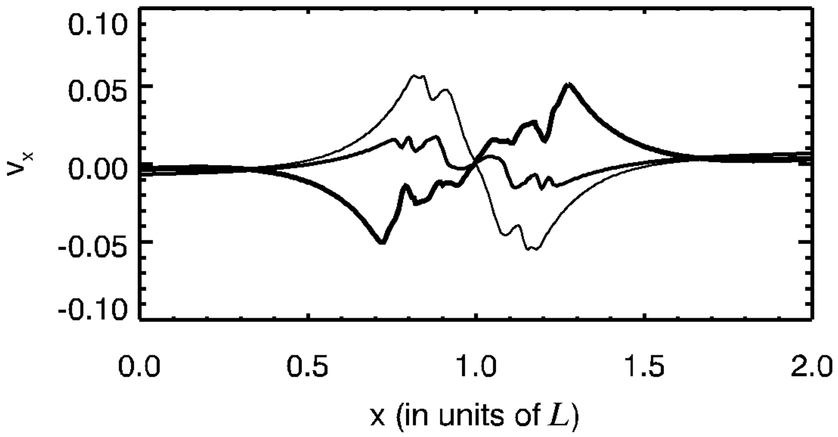

Figure 4.6: Plot of the bulk velocities in the x-direction, plotted against x, in the ideal MHD case. The different plots describe the situation at times $t = 7.5$, 8, and $9\,t_{\rm s}$. The later times are denoted by the thicker lines. The velocities are initially positive to the left of the centre of the vortex, and negative on the right. This results in the net flow towards the centre of the vortex. At the later times, the x-velocities are now negative at the left of the centre, and positive on the right. This results in a net flow away from the centre of the vortex.

There is a distinct consequence of this sudden velocity reversal. As the transverse velocities are given a sudden outward net flow, a wave is emitted from the centre of the vortex through the velocity field. This wave is observed in all KH simulations, HD and MHD, and on simulations carried out on wider grids, can be observed to propagate steadily away from the KH vortex along the x-directions.

Analysis of the nonideal effects on the development of the KH instability requires that the entire grid consists only of dynamics due to the instability, and does not suffer from reflections from the boundaries. It is therefore necessary that the grid be wide enough that this wave does not travel further than its boundaries. In order to calculate the necessary width, a hydrodynamic simulation of the KH instability was run, using the same initial set-up but with a width of $64\,L$.

Figure 4.7 shows the x-velocities from this simulation plotted against x at several times. In each case, the wave front can clearly be seen. By calculating the distance traveled by the wave, it can be found that the wave is traveling at approximately the speed of sound in the system. In order for the simulation to be allowed to run until a time chosen to be $t = 20\,t_{\rm s}$, the grid must be sufficiently wide that the wave has not reached the boundaries by this time. The wave is seen consistently to be created at a time of approximately $t = 8\,t_{\rm s}$, and at a distance within $1\,L$ from the vortex, and to propagate with a steady velocity from either side of the vortex. This results in a minimum width of $26\,L$ being required. In the following studies, a width of $32\,L$ has been chosen.

The wave emitted from the KH vortex occurs at a time when the transverse kinetic energy has reached its initial maximum. The transverse kinetic energy generally undergoes periods of growth and decay. In some simulations, when the transverse kinetic energy reaches a subsequent maximum, it is possible to see another wave produced in a similar manner to the first.

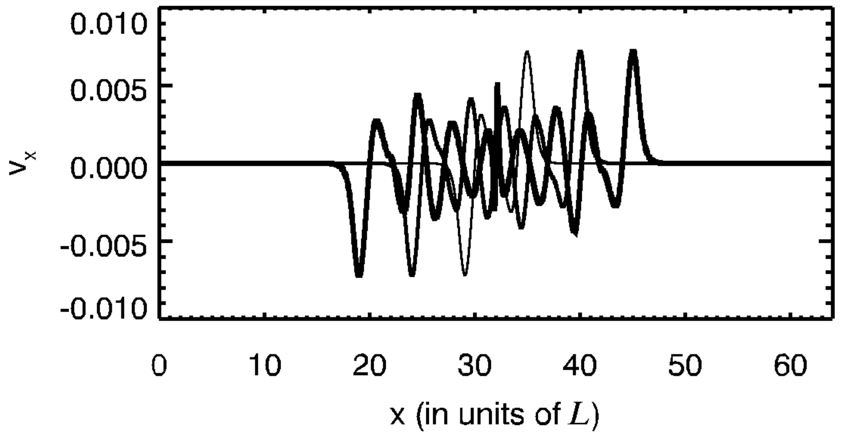

Figure 4.7: Plots of the x-velocities plotted against x at times $t = 10t_\mathrm{s}$, $15t_\mathrm{s}$ and $20t_\mathrm{s}$. Later times are denoted by thicker lines. This plot allows the velocity of the wave front to be calculated as approximately equal to the sound speed.

4.1.3 Choosing the multifluid parameters

The simulations in this study are of a three-fluid system, consisting of a neutral fluid, as well as a positively and a negatively charged fluid. Following the derivation of the weakly ionised equations in section 1.3.2, the mass density and velocity of the neutral fluid is approximated to be equal to that of the bulk flow. Following Chapter 3, the mass density of the bulk flow is set to $\rho_0 = 1$ and the initial velocities of all three fluids are $\mathbf{v} = \pm\frac{1}{2}\hat{y}$, using dimensionless quantities. The condition of charge neutrality requires that the charge densities of the two charged fluids have equal magnitude but opposite signs of charge. As the system is taken to be weakly ionised, the mass density of the positively charged fluid is set to $\rho_2 = 2 \times 10^{-7}$. The charge-to-mass ratios of the two charged fluids are initially set to $\alpha_1 = -1.0 \times 10^{17}$ and $\alpha_2 = 1.42 \times 10^{11}$. By charge neutrality, the mass density of the negatively charged fluid is $\rho_1 = 2.84 \times 10^{-13}$. Finally, the collision rates of the two charged fluids with the neutral fluid are set to $K_{1,\mathrm{n}} = 2.0 \times 10^4$ and $K_{2,\mathrm{n}} = 1.42 \times 10^{10}$. The resistivities can be calculated following section 1.3.2. These are found to be $r_\mathrm{O} = 7.04 \times 10^{-18}$, $r_\mathrm{H} = r_\mathrm{A} = 3.52 \times 10^{-6}$. In all of the following cases, the Ohmic resistivity r_{O} is very small and considered to be negligible. Ohmic resistivity has also been studied using resistive MHD, and unlike the other two, is not a purely multifluid effect.

In the system described above, the charge-to-mass ratios of both charged fluids are very high, which means that the charged fluids are strongly tied to the magnetic field. As well as this, the collision rates of the charged fluids with the neutral fluid are also very high, allowing for strong coupling between the fluids. This results in a weakly ionised plasma that is frozen-in to the magnetic field. The two charged fluids approximately simulate the behaviour of a fluid of electrons which are always strongly tied to the magnetic field, and a fluid of much larger ions, with which the neutral fluid experiences the majority of its collisional coupling. In this case, the Hall resistivity is minimised by the ions also remaining well coupled to the magnetic field, while the ambipolar resistivity is minimised by the ions having a high enough collision rate with the neutrals to sufficiently couple the magnetic field to the the neutral fluid.

The resistivities calculated above are very small, and as it stands, this system can accurately reproduce ideal MHD results. The magnetic Reynolds number for this low resistivity system is:

$$Re_{\mathrm{m}} \equiv \frac{u\mathcal{L}}{\eta} = \frac{(1)(1)}{3.52 \times 10^{-6}} \approx 2.84 \times 10^{5} \tag{4.1}$$

where $\mathcal{L}$ is a characteristic length, and u is a characteristic velocity. For these, the length of the grid $L = 1$ and the sound speed $c_{\mathrm{s}} = \frac{L}{T} = 1$ are chosen.

4.2 Including ambipolar resistivity in the system

In order to introduce ambipolar diffusion into the system, the collision rate of the positive ion fluid with the neutrals, $K_{2,\mathrm{n}}$, is reduced. Ideal MHD is based on the assumption that there is perfect coupling between the neutral and ion fluid through a sufficiently high collision rate. Reducing $K_{2,\mathrm{n}}$ means that there are fewer collisions between the ion fluid and the neutral fluid. The coupling between the fluids is weaker, and a drift is created between the two. This is the source of the ambipolar diffusion, as it allows for a diffusion of the field through the bulk fluid in the xy-plane.

In order to examine the evolution of the system with time, simulations with successively decreasing $K_{2,\mathrm{n}}$, and thus increasing ambipolar resistivity r_A, have been run. The initial conditions for the three simulations are:

$$K_{2,\mathrm{n}} = (K_{2,\mathrm{n}})_0 = 1.42 \times 10^{10} \quad \longrightarrow \quad r_\mathrm{A} = 3.5 \times 10^{-6} \tag{4.2}$$

$$K_{2,\mathrm{n}} = 10^{-3} \times (K_{2,\mathrm{n}})_0 \quad \longrightarrow \quad r_\mathrm{A} = 3.5 \times 10^{-3} \tag{4.3}$$

$$K_{2,\mathrm{n}} = 10^{-4} \times (K_{2,\mathrm{n}})_0 \quad \longrightarrow \quad r_\mathrm{A} = 3.5 \times 10^{-2} \tag{4.4}$$

In all cases, the Hall resistivity remains low, so that any change in the evolution of the system can be attributed to the introduction of ambipolar diffusion. The magnetic Reynolds for the three systems can be calculated respectively as: $Re_\mathrm{m} = 2.84 \times 10^5$, $Re_\mathrm{m} = 2.84 \times 10^2$, and $Re_\mathrm{m} = 2.84 \times 10^1$.

4.3 Resolution study for ambipolar-dominated system

One of the conditions of ideal MHD is that any magnetic diffusion that occurs does so on much shorter length scales and larger time scales than those of interest in a study. In order to include nonideal MHD effects into a model, the length scales over which this diffusion takes place must be taken into account. In order to ensure that the simulations capture these small-scale dissipative effects, a resolution study is carried out.

Simulations are run at three different resolutions. For a grid of width 32, these simulations consist of $6400 \times 200 \times 1$, $3200 \times 100 \times 1$, and $1600 \times 50 \times 1$ grid cells. These simulations are run with the highest level of ambipolar resistivity. Sufficient resolution has already been determined for the case of ideal MHD (see section 3.1) so this ensures that the most extreme nonideal dissipative effects are in place when examining whether they are sufficiently resolved.

As will be seen in the following sections, the introduction of nonideal effects does not tend to greatly influence the linear growth rate of the instability. For this reason, the growth rate cannot be used as a measure of convergence with increasing resolution. It will be seen however, that the nonlinear evolutions of both the transverse kinetic energy $\int\int dx\, dy\, \frac{1}{2}\rho \mathrm{v}_x^2$, and the perturbed magnetic energy $\int\int dx\, dy \big(\frac{1}{2}(B_x^2 + B_y^2 + B_z^2) - \frac{1}{2}(B_0^2)\big)$, are strongly influenced by the nonideal effects. The evolutions of these two parameters are plotted in figures 4.8 and 4.9. It can clearly be seen that, in both graphs, the early nonlinear behaviour in the systems have started to converge at higher resolutions. While is there is a notable difference between the two simulations of lower resolution, the gap closes significantly in the comparison between the two simulations of higher resolution.

As will be seen later, the initial maxima reached by the transverse kinetic energies and perturbed magnetic energies are strongly influenced by the inclusion of nonideal effects. For this reason, comparisons of these values can lead to quantitative measurements of the gap between the simulations of different resolutions. These maxima are plotted in figures 4.10 and 4.11 as a function of the number of grid cells in the x-direction. In the case of the transverse kinetic energy, the gap reduces from a difference of $\approx 19\,\%$ to $\approx 2\,\%$ as the resolution increases. In

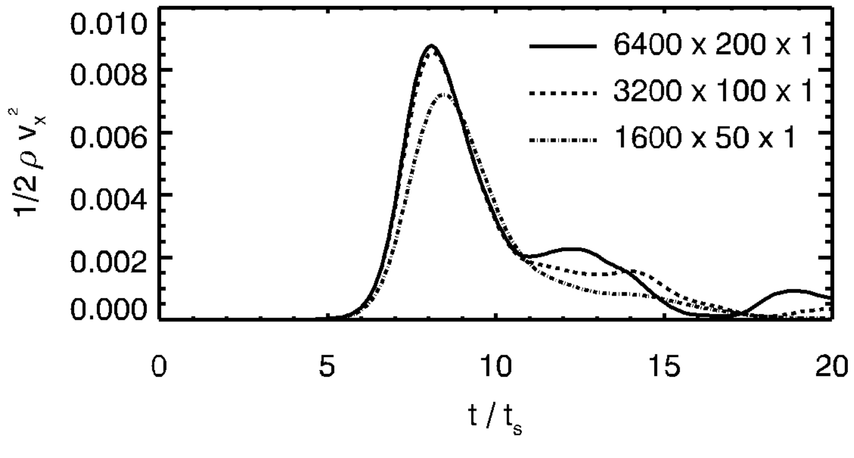

Figure 4.8: Plot of the transverse kinetic energy against time in the case of high ambipolar resistivity for three different resolutions.

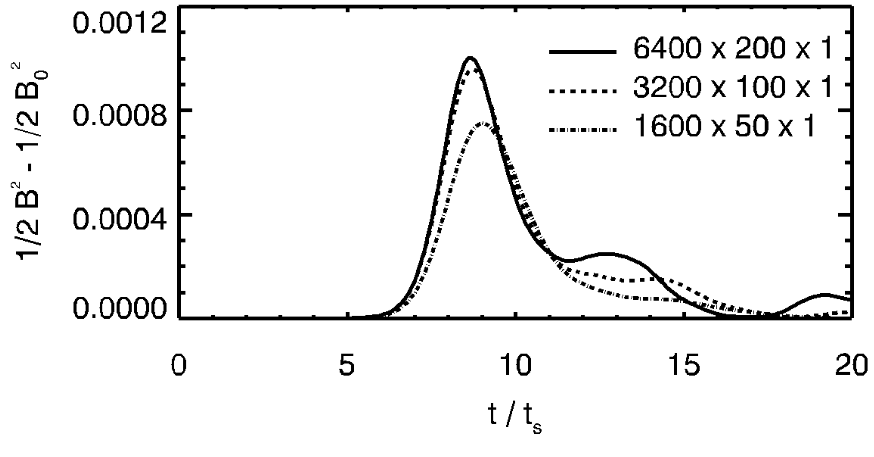

Figure 4.9: Plot of the perturbed magnetic energy against time in the case of high ambipolar resistivity for three different resolutions.

the case of the perturbed mangetic energy, the gap reduces from a difference of $\approx 28\,\%$ to $\approx 4\,\%$. It is expected that in both cases, if the resolution was to be doubled again, the difference would be negligible. It is therefore concluded that the highest resolution used here, $6400 \times 200 \times 1$ cells, is sufficiently high to capture the effects due to ambipolar resistivity.

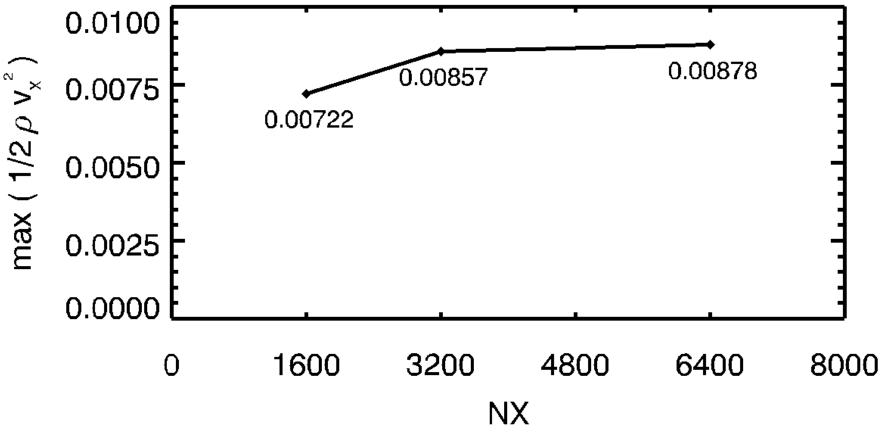

Figure 4.10: Plot of the initial maxima reached by the transverse kinetic energy for the three simulations of different resolutions, plotted against the number of grid cells in the x-direction for that simulation.

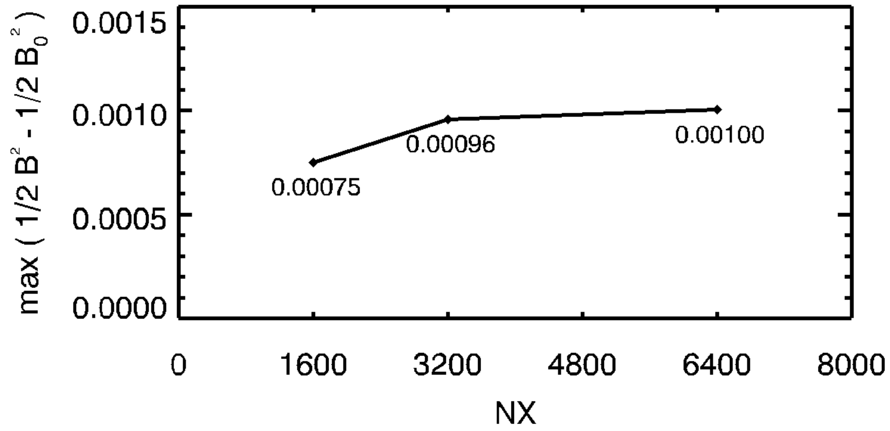

Figure 4.11: Plot of the initial maxima reached by the perturbed magnetic energy for the three simulations of different resolutions, plotted against the number of grid cells in the x-direction for that simulation.

4.4 Results for ambipolar-dominated system

In the low resistivity case, the Kelvin-Helmholtz instability causes a wind-up of the plasma at the interface between the two layers, resulting in the "Kelvin's cat's eye" vortex. This can be seen in figure 4.12. When nonideal effects are included in the systems, the effect of this instability on the dynamics of the system can be altered significantly.

As ambipolar resistivity is introduced to the systems, one of the primary effects to be observed is the influence on the magnetic field. As the collision rate between the ion and neutral fluid is decreased, the ion fluid is allowed to decouple from the bulk fluid, and thus the magnetic field becomes decoupled from the bulk flow: the frozen-in approximation of ideal MHD is broken. The topology of the field is therefore no longer preserved, and magnetic reconnection can occur. In figure 4.13, magnetic reconnection can be identified as the cause of the decrease of the amplification of the magnetic energy with time for increasing ambipolar resistivity.

It can be seen that the geometry of the wind-up of the magnetic field, as shown

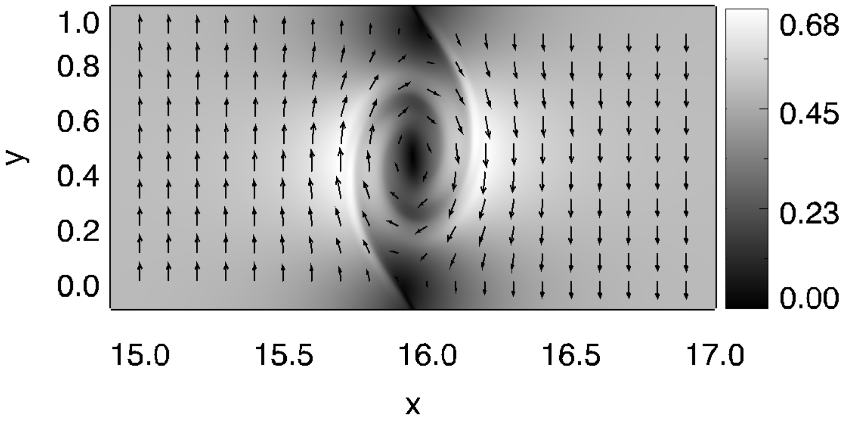

Figure 4.12: Plot of the magnitude and vector field of the bulk velocity field for the low resistivity case, at time $t = 8\,t_\mathrm{s}$.

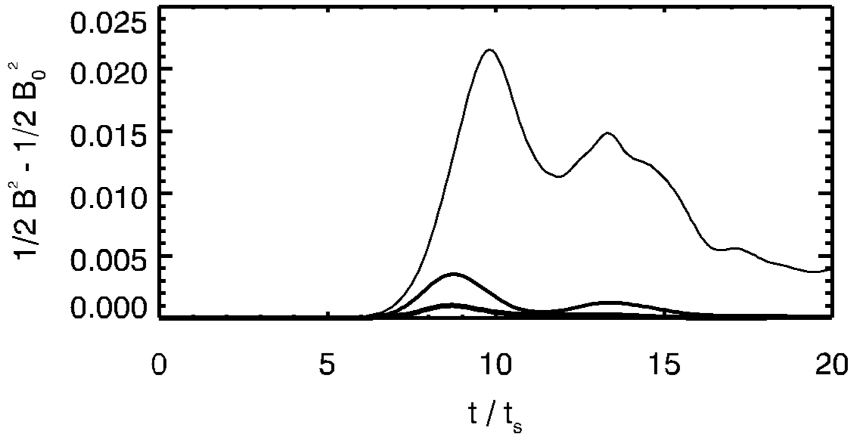

Figure 4.13: The perturbed magnetic energy in the system is plotted against time in the three cases of varying ambipolar resistivity. The thicker lines represent the models with higher ambipolar resistivity. Higher ambipolar resistivity causes the magnetic field to experience less amplification, through magnetic reconnection and decoupling of the bulk fluid from the magnetic field.

in the low resistivity case in figure 4.14, is particularly prone to magnetic reconnection. This occurs when magnetic field lines of opposite direction are brought together. As the magnetic field lines reconnect, the system experiences a sudden loss of energy, and the magnetic field becomes weaker and less wound up than before. The effect of reconnection on the magnetic field in the case of high ambipolar resistivity can be seen in figure 4.15.

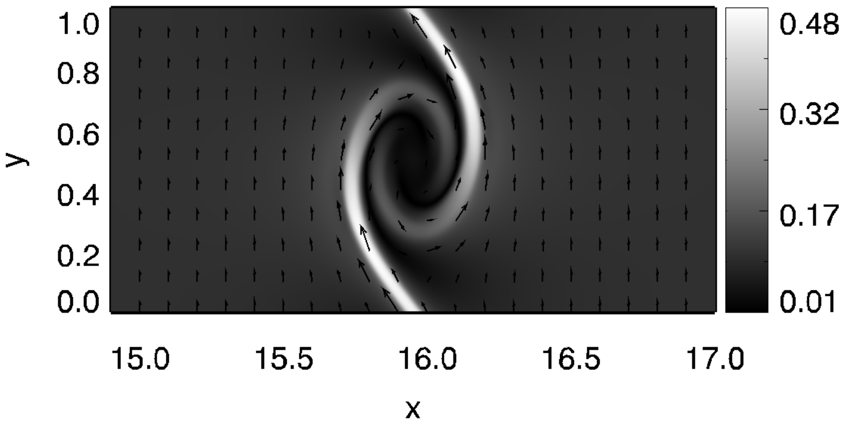

Figure 4.14: Plot of the magnitude and vector field of the magnetic field for the low resistivity case, at time $t = 8\,t_\mathrm{s}$. The magnetic field can be seen to have undergone a similar wind-up to that of the velocity field.

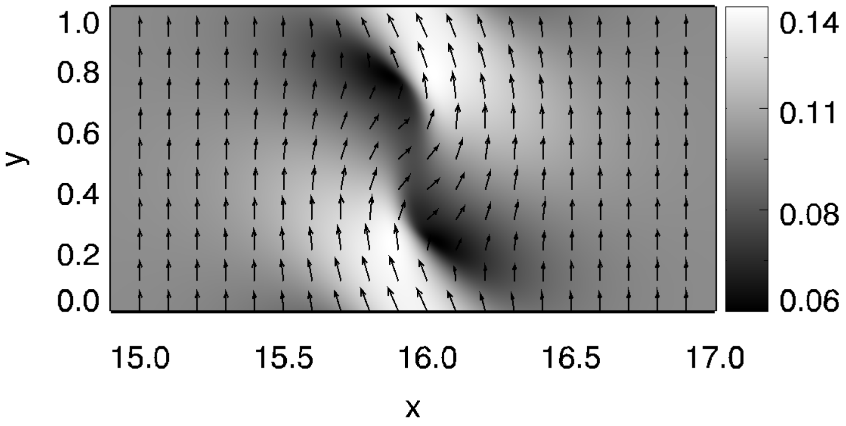

Figure 4.15: Plot of the magnitude and vector field of the magnetic field for the high ambipolar case, at time $t = 8\,t_\mathrm{s}$. As a result of magnetic reconnection, the magnetic field no longer reflects the wind-up of the velocity field. It can also be seen to be much weaker in magnitude than in the low resistivity case.

From figure 4.13, it is possible to see that significant magnetic reconnection occurs, even for only a moderate amount of ambipolar resistivity. As the magnetic field experiences this reconnection and therefore undergoes less growth, it is less able to suppress the wind-up of the bulk fluid. The efficiency of the wind-up of the bulk fluid is measured by the growth of the transverse kinetic energy. In figure 4.16 it can be seen that as the ambipolar resistivity is introduced into the system, the maximum reached by the transverse kinetic energy increases.

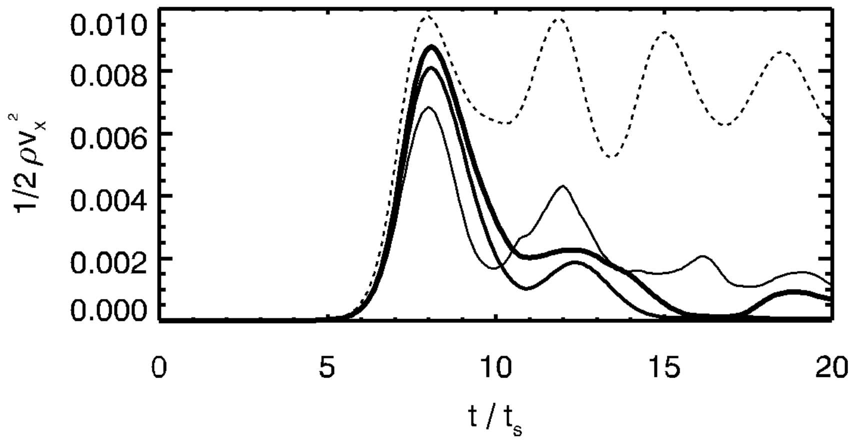

Figure 4.16: The transverse kinetic energy in the system is plotted against time in each case. The thicker lines represent the models with higher ambipolar resistivity. The dashed line represents the hydrodynamic case. Higher ambipolar resistivity allows the vector field to experience further wind-up due to a weaker magnetic field and greater decoupling of the bulk fluid from the magnetic field.

With larger values of ambipolar resistivity, the transverse kinetic energy increase even more, as the bulk fluid experiences even more wind-up. In this system, the cause of this further wind-up can be attributed to two sources. As seen above, the weaker magnetic field is less able to suppress the wind-up of the bulk flow. Secondly, as the coupling between the neutral fluid and the ion fluid decreases further, and thus the coupling between the neutral fluid and the magnetic field decreases, the magnetic field is progressively less capable of influencing the behaviour of the bulk flow.

It can be shown that for a moderate amount of ambipolar diffusion, the increase in the wind-up of the bulk fluid is due solely to the first source: the magnetic reconnection. The slight decoupling of the ion and neutral fluid is sufficiently high to allow magnetic reconnection, while still being sufficiently low to force the charged fluids to behave in a manner similar to the bulk fluid. This can be seen in a plot of the transverse kinetic energy of the ion fluid, as shown in figure 4.17. With moderate amount of ambipolar diffusion, the transverse kinetic energy of the ion fluid (and electron fluid) reaches a higher maximum, meaning that the fluid experiences more wind-up.

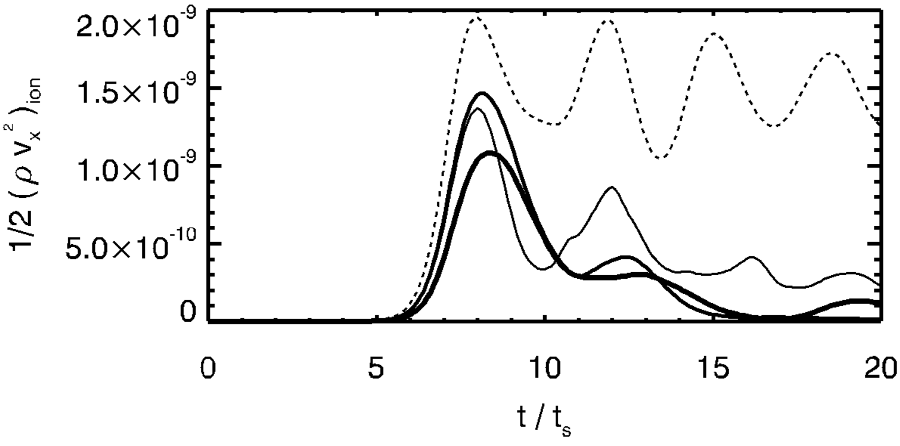

Figure 4.17: The transverse kinetic energy of the ion fluid is plotted against time in each case. The thicker lines represent the models with higher ambipolar resistivity. The dashed line represents the hydrodynamic case. Moderate ambipolar resistivity allows the bulk fluid to experience further wind-up. The fact that the ion fluid experiences further wind-up shows that this is due to a weaker magnetic field, and not decoupling. With higher ambipolar resistivity, the ion fluid experiences less wind-up. This is due to decoupling from the neutral fluid, as well as the weaker field.

However, as the ambipolar resistivity is increased further, the ion fluid becomes more decoupled from the neutral fluid, and is instead influenced primarily by the dynamics of the magnetic field. This significant decoupling occurs only for magnetic Reynolds number lower than $Re_{\rm m} \approx 100$. As the magnetic field therefore undergoes less wind-up than before, so does the ion (and electron) fluid. This decrease in the winding-up of the charged fluids is the cause of the decrease in the transverse kinetic energy of the fluids, as is seen for the case of high ambipolar resistivity in figure 4.17.

As the amplification of the magnetic energy decreases as a result of reconnection, the magnetic field is less able to suppress the wind-up of the bulk flow. However, the increase in the transverse kinetic energy of the bulk flow due to its stronger wind-up does not account for the energy lost through reconnection. Under the isothermal assumption, magnetic reconnection does not lead to a transfer of the energy, but rather to an instantaneous loss of total energy. This can be inferred from figure 4.18. In this figure, the growth of both the magnetic and transverse kinetic energies are plotted, as is the loss of parallel kinetic energy, for the cases of low resistivity and high ambipolar resistivity. While the transverse kinetic energy grows to a higher maximum for the ambipolar case, this does not make up for the loss of magnetic energy, and it can clearly be seen that the ambipolar case suffers a significantly greater loss of total energy during this period of the growth of the instability.

It has been seen that the decoupling of the neutral fluid from the magnetic field due to ambipolar resistivity results in the bulk flow experiencing a greater wind-up. This result of the decoupling can also be observed by examining the vortex created by the instability. Figure 4.19 plots the transverse velocities for the low and high resistivity cases, in the upper and lower panels respectively, as a cross-section through the centre of the KH vortex along x. Also plotted is the strength of the magnetic field in the y-direction for the same region in each case. In the case of low resistivity, the distinct neighbouring peaks and troughs in the magnetic field strength represent regions of strong positive magnetic field beside regions of strong negative magnetic field. This represents the area in the KH vortex in which the magnetic field lines have been wound up and compressed, so that magnetic field lines in the positive y-direction have been compressed side-by-side with magnetic field lines in the negative y-direction. It can clearly be seen that for each peak and trough in the magnetic field, i.e. in each region of strong positive or negative magnetic field, there exists an individual corresponding peak in the transverse velocity. This is caused by the bulk fluid being tied to the magnetic field lines, in either the positive or negative y-directions, and being unable to

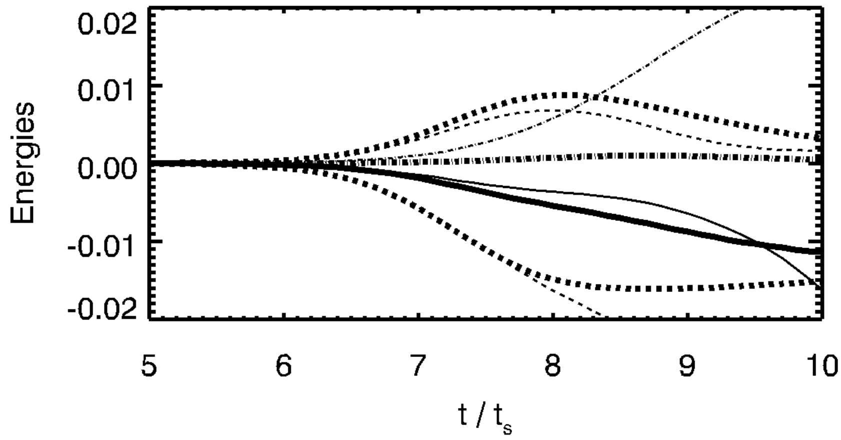

Figure 4.18: The respective positive and negative growths of the transverse and parallel kinetic energies (dashed lines) are plotted against time, as is the growth of the perturbed magnetic energy (dot-dashed lines). The sum of these gives the change in the total energy in the system, which is also plotted (solid lines). These are plotted for the both the cases of low resistivity (thin lines) and high ambipolar resistivity (thick lines). It can be seen that the increase in growth of the transverse kinetic energy in the high resistivity case does not make up for the loss in magnetic energy. This indicates that magnetic reconnection results in a further loss of total energy, as shown.

merge with the fluid tied to the magnetic field lines of the opposite direction. In the case of high ambipolar resistivity however, this phenomenon is not observed. In this case, the decoupling of the magnetic field from the bulk fluid leads to magnetic reconnection between the magnetic field lines of opposing directions. There are no strong peaks observed therefore in the magnetic field strength, and the regions of high transverse velocity are able to merge into single, wider peaks.

Another consequence of this is that when the magnetic field lines prevent the bulk fluid from crossing them, more structure is enforced on the velocity field. For the high ambipolar resistivity case on the other hand, the velocities experience a more gradual change across the vortex. This results in a more "blurry" velocity field in the ambipolar case, than in the "well-defined" velocity field of the low resistivity case. This can be observed by comparison of the velocity fields for the two cases (see figure 4.20). Close examination reveals that within the KH vortex,

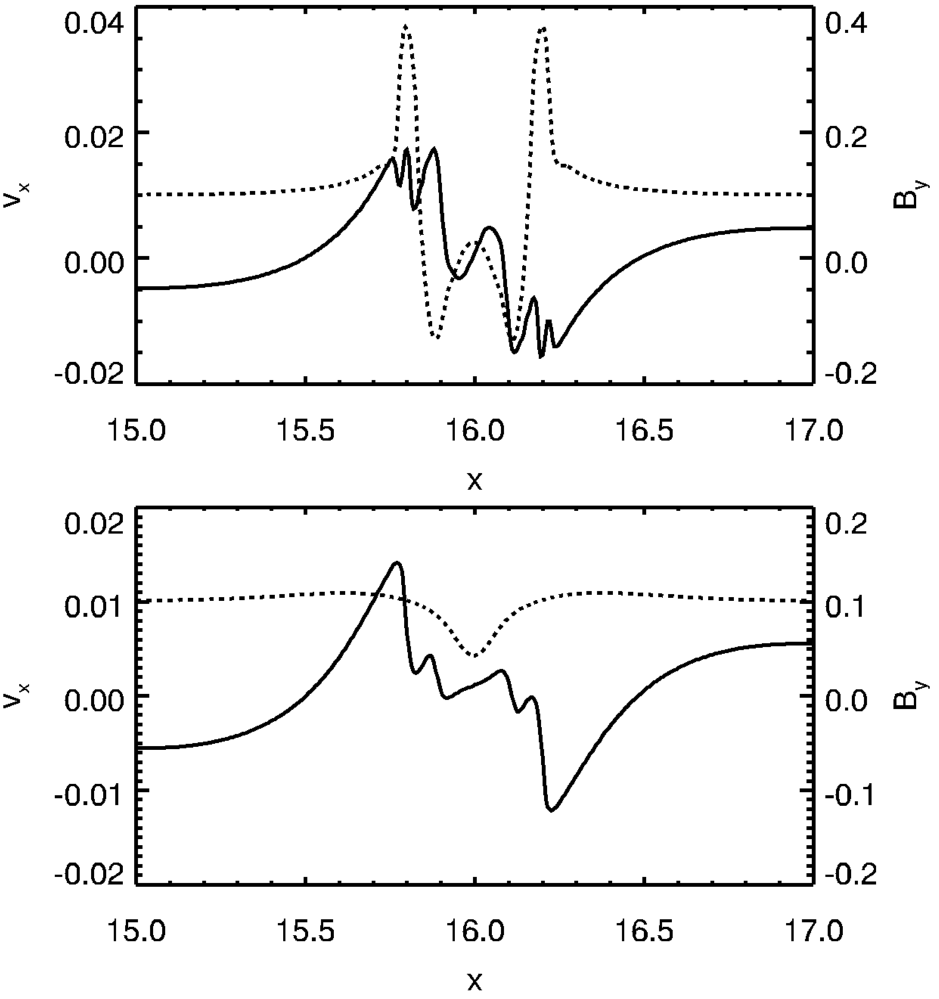

Figure 4.19: Plot of the bulk velocity in the x-direction (solid line) and the strength of the magnetic field in the y-direction (dashed line), for the cases of low resistivity (upper panel) and high ambipolar resistivity (lower panel) at time $t = 8\,t_{\mathrm{s}}$. The area plotted is a cross-section of the vortex through its centre along x.

there is in fact more well-defined structure in the low resistivity case.

Another interesting comparison between the simulations is that between the dynamics of the bulk fluids and the charged fluids. Figures 4.21 and 4.22 show the mass densities and velocity vector fields of the bulk fluid and charged fluids respectively, at the time of the peak of the instability for low resistivity. The KH

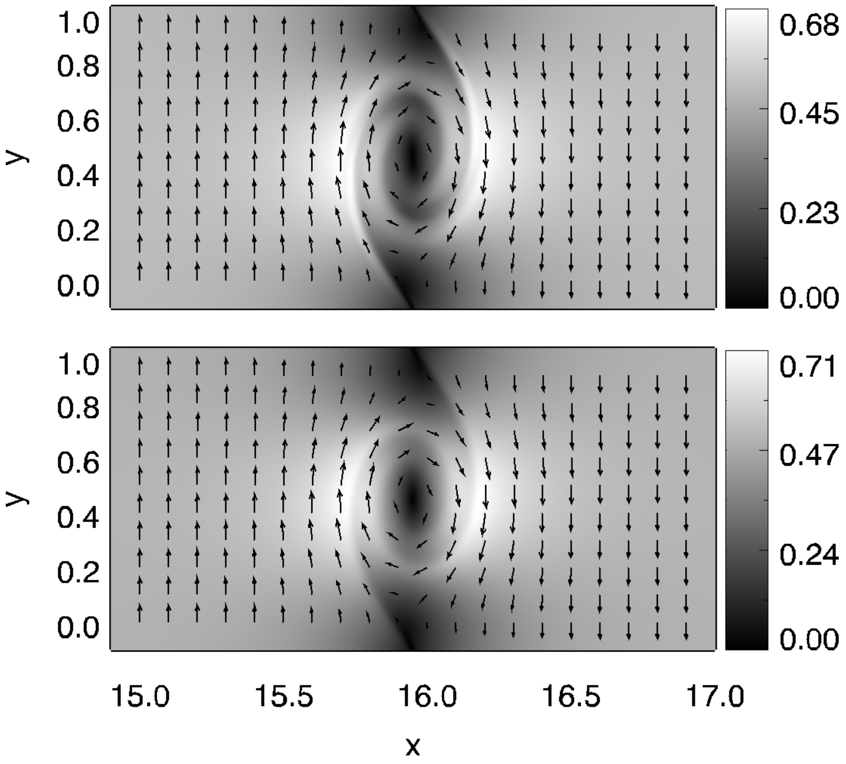

Figure 4.20: Plot of the magnitude and vector field of the bulk velocity field at time $t = 8\,t_{\mathrm{s}}$ for the low resistivity case (upper panel) and high ambipolar case (lower panel). Upon close examination, it can be seen that the velocity field contains more well-defined structure in the case of low resistivity than in the case of high ambipolar resistivity.

vortex is clearly seen in both images, and both closely reflect that of the magnetic field for the same case (see figure 4.14). This is to be expected, as the plasma remains strongly coupled to the magnetic field through coupling with the charged fluids.

In the case of high ambipolar resistivity, the bulk flow experiences considerable decoupling from the magnetic field through a lower collision frequency with the ion fluid. The mass density of the bulk fluid can be seen in figure 4.23 and the mass density of the ion fluid in figure 4.24. While the magnetic field has also developed a very different configuration (see figure 4.15), it is clear that the bulk fluid no longer reflects this form. The charged fluid does however, as is to be expected.

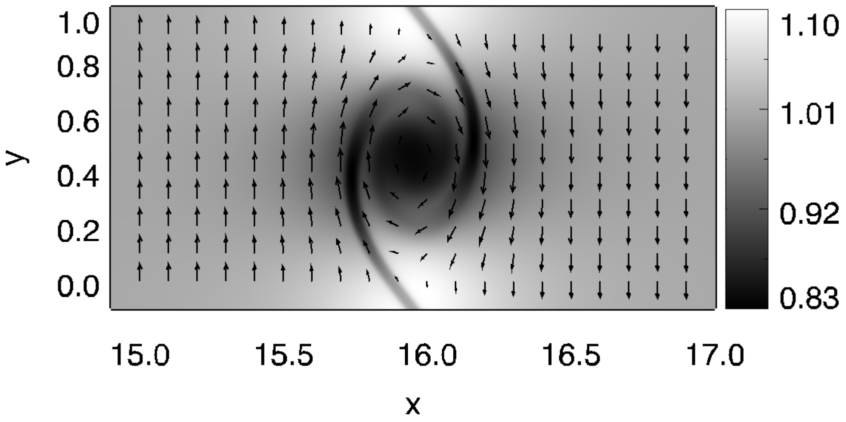

Figure 4.21: Plot of the mass density, as well as the velocity vector field, of the bulk fluid in the low resistivity case at time $= 8\,t_{\mathrm{s}}$.

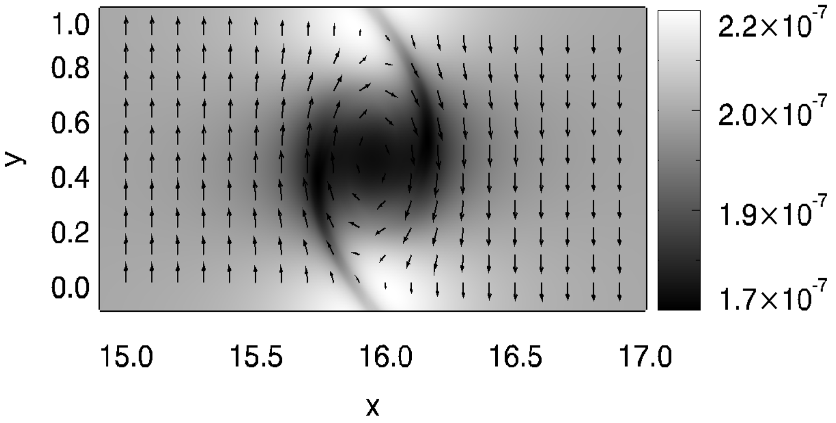

Figure 4.22: Plot of the mass density, as well as the velocity vector field, of the ion fluid in the low resistivity case at time $= 8\,t_{\mathrm{s}}$.

The area of low mass density in the bulk fluid at the centre of the vortex, in both the low and high resistivity cases, can be explained by the velocity field of the fluid. In each case, during the growth of the instability, there is an overall flow towards the centre of the vortex from the left and right of the vortex, and an overall flow away from the centre towards the top and bottom the vortex (as described earlier in section 4.1.2). This in fact results in a net flow away from the

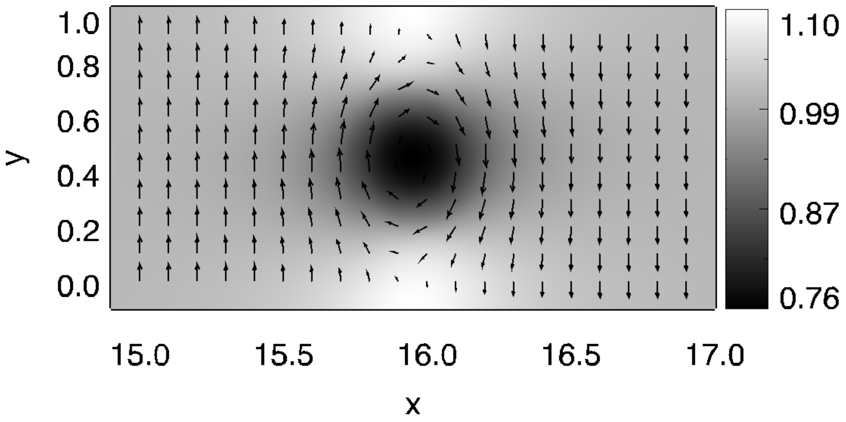

Figure 4.23: Plot of the mass density, as well as the velocity vector field, of the bulk fluid in the low resistivity case at time $= 8\,t_{\rm s}$.

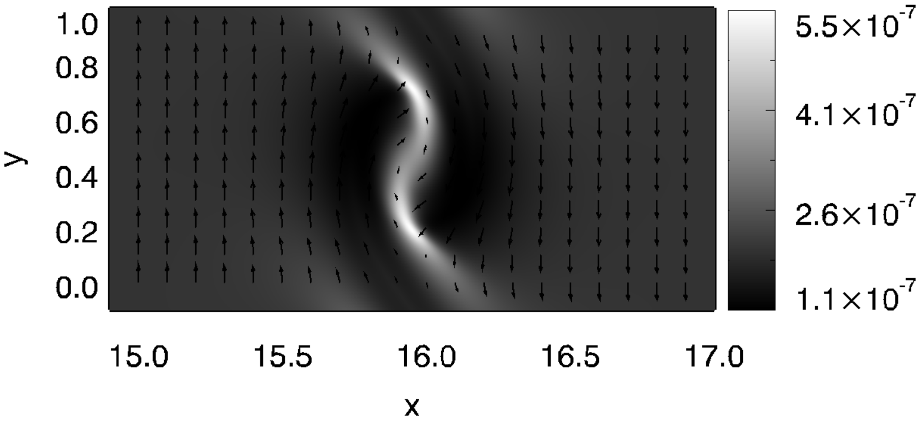

Figure 4.24: Plot of the mass density, as well as the velocity vector field, of the ion fluid in the high ambipolar resistivity case at time $= 8\,t_{\rm s}$.

centre of the vortex, resulting in this region of lower density. As the velocities in the vortex are of slightly greater magnitude in the case of high resistivity, this region of low density becomes even more pronounced.

There are further areas of high and low mass density visible in the charged fluid mass densities in the cases of both high and low resistivity, as well as the bulk fluid density in the low resistivity case. Comparisons with plots of the magnetic field at the same point in time show that these high and low density regions regions occur in areas of low and high magnetic pressure respectively. This can also be seen in other numerical KH studies (e.g. Keppens et al., 1999). The high magnetic pressure causes a region of evacuated charged plasma in the area, in order to maintain pressure equilibrium. Regions of low magnetic pressure act in the opposite manner. In the case of low resistivity, the regions of evacuated charged plasma in turn evacuate the bulk plasma through strong collisional coupling. Figure 4.25 is a plot of the total pressure in the system, magnetic pressure plus gas pressure. This confirms that the system is simply maintaining pressure equilibrium in these regions of interest. In the case of high resistivity however, decoupling of the neutral and charged fluids means that this does not affect the density of the neutral fluid, and no further regions of high or low mass density are observed in the bulk fluid. Comparisons can be made between the bulk fluid in this high resistivity case and in the hydrodynamic case, and they are seen to reflect each other. This is as expected, as magnetic pressure does not affect the density distribution of the bulk fluid in either case.

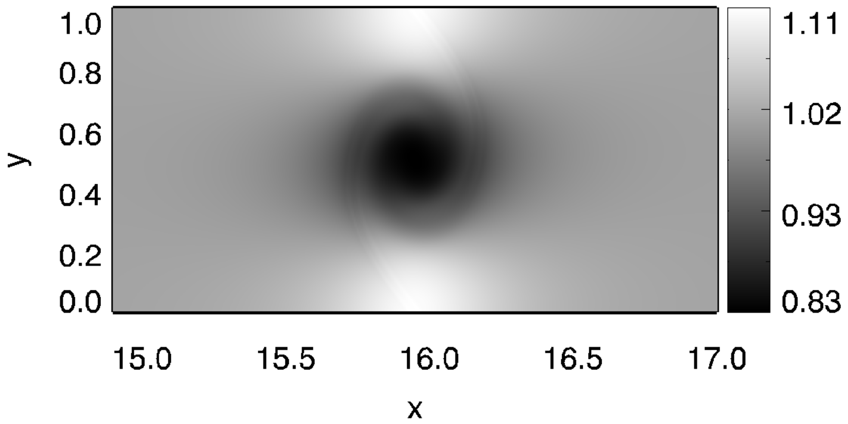

Figure 4.25: Plot of the total pressure (magnetic pressure plus gas pressure) in the system, for the case of low resistivity at time $= 8\,t_{\mathrm{s}}$.

Finally, the growth rates of the different systems are examined. In figure 4.26, the log of the transverse kinetic energy is plotted for each of the three cases, as well as for the hydrodynamic system.

It can be seen that the linear growth of the instability differs very little with

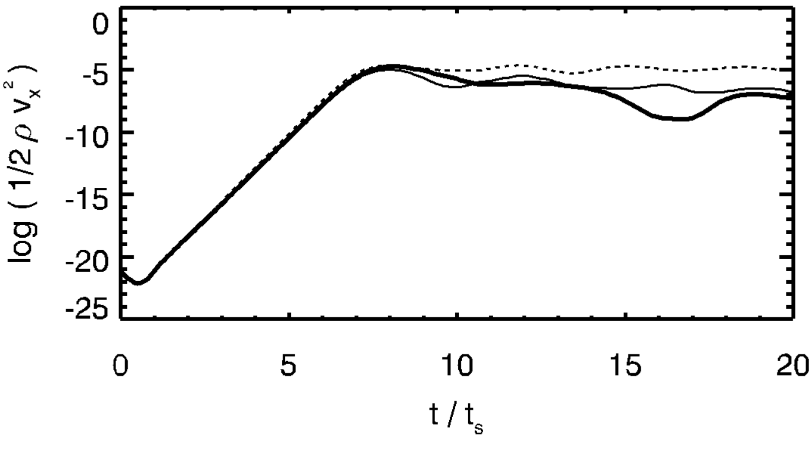

Figure 4.26: The log of the transverse kinetic energy in the system is plotted against time in each case. The thicker lines represent the models with higher ambipolar resistivity. The dashed line represents the hydrodynamic case. There is very little difference between the linear growths for the three magnetised cases.

varying ambipolar resistivity. The growth rate of the hydrodynamic system is slightly greater than that of the low resistivity system ($\approx$ 3%). However, the growth rate of even the system with the higher ambipolar resistivity is still within 1% of that of the low resistivity system. This implies that neither a strong amplification of the magnetic field nor very high coupling between the neutral and charged fluids are required for the magnetic field to enforce its small suppression on the initial growth of the Kelvin-Helmholtz instability. Of the parameters varied in these simulations, only the initial strength of the magnetic field affects the linear growth of the system.

It has been seen that the development of the KH instability differs for different values of resistivity. The subsequent behaviour of the fluid is next examined, and is also seen to develop differently with the introduction of ambipolar resistivity. In the case of low resistivity, the initial wind-up of the velocity field has been observed to cause the winding up the magnetic field, due to strong coupling between the two. After reaching its saturation point, the KH vortex is pulled and stretched by the newly amplified magnetic field, as shown in figure 4.27. Through its continuing rotation, the stretched vortex leads to further wind-up and distortion of the magnetic field lines (see figure 4.28). This leads to a small further amplification of the magnetic energy in the system.

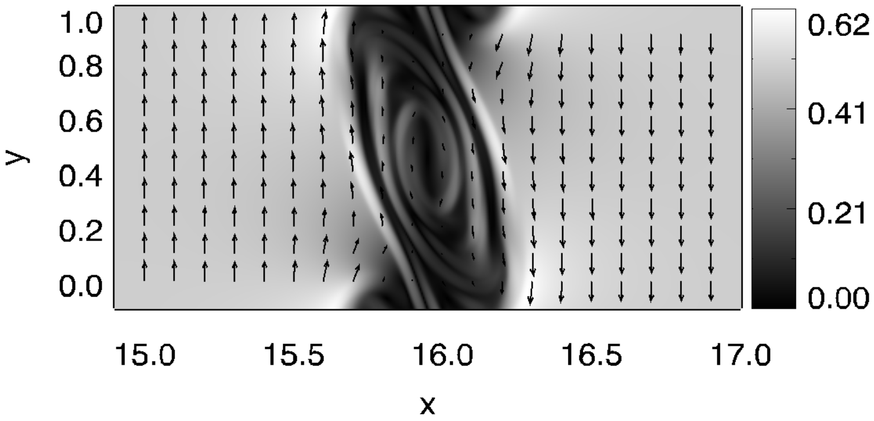

Figure 4.27: Plot of the magnitude and vector field of the bulk velocity field for the low resistivity case, at time $t = 10\,t_{\rm s}$. It can be seen that the KH vortex has been stretched and pulled by the magnetic field.

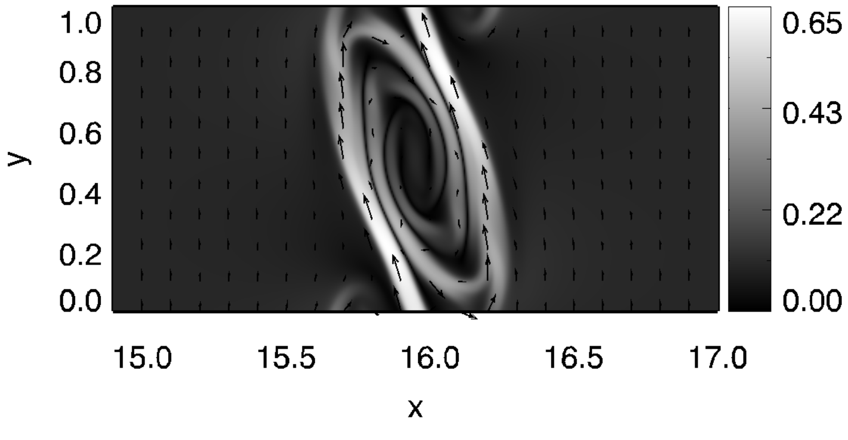

Figure 4.28: Plot of the magnitude and vector field of the magnetic field for the low resistivity case, at time $t = 10\,t_{\rm s}$. The magnetic field has undergone further wind-up and distortion.

As well as leading to a further growth in the magnetic energy, the stretching of the vortex has the result of lowering of the transverse velocities within it. This continues up until a certain point at around time $t = 10\,t_s$. This is the stage at which the KH vortex has expanded to such a degree that it reaches the periodic y-boundaries. This can be thought of as the vortex interacting with an identical neighbouring vortex. As the two begin to merge, the numerical viscosity within the code allows for magnetic reconnection to occur. This leads to the creation of magnetic islands and of smaller secondary vortices on either side of the original vortex. Through the reconnection and the decay of the primary vortex, the magnetic energy in the system is now seen to decrease. However, the creation of secondary vortices in regions of low magnetic field strength results in another growth of the transverse kinetic energy in the system. This has also been observed by Frank et al. (1996). As the system continues to evolve, this generation and decay of subsequent vortices leads to further periods of growth in the transverse kinetic energy in the system corresponding to periods of decreasing magnetic energy and vice-versa. This is clearly demonstrated in figure 4.29, where the peaks in each energy are seen to correspond to the troughs in the other. This behaviour continues until the system has reached a somewhat disordered state (see figure 4.30).

In the case of high ambipolar resistivity, the subsequent evolution of the KH instability is quite different. After the instability has reached its saturation point, the magnetic field strength again continues to grow slightly. However, this is seen to occur to a lesser degree and over a shorter period of time, for systems with more ambipolar resistivity. With greater decoupling from the bulk fluid, and with more reconnection occurring, the magnetic field experiences less and less further wind-up. Unlike the case of low resistivity, the magnetic field does not experience sufficient wind-up to stretch the KH vortex so that it interacts with the periodic y-boundaries, and there is no generation of further vortices. Instead, the magnetic field is drawn back towards its original configuration. The result of this is that neither the velocity field nor the magnetic field undergo a second period of growth (see figure 4.31). The magnetic field steadily stabilises the velocity field and the plasma returns almost to its original state, with simple laminar flow on either side of a shear layer (see figure 4.32). In this case, however, the shear layer is much wider, and no longer conducive to the growth of the Kelvin-Helmholtz instability. The high ambipolar resistivity case therefore reaches a stable state much quicker

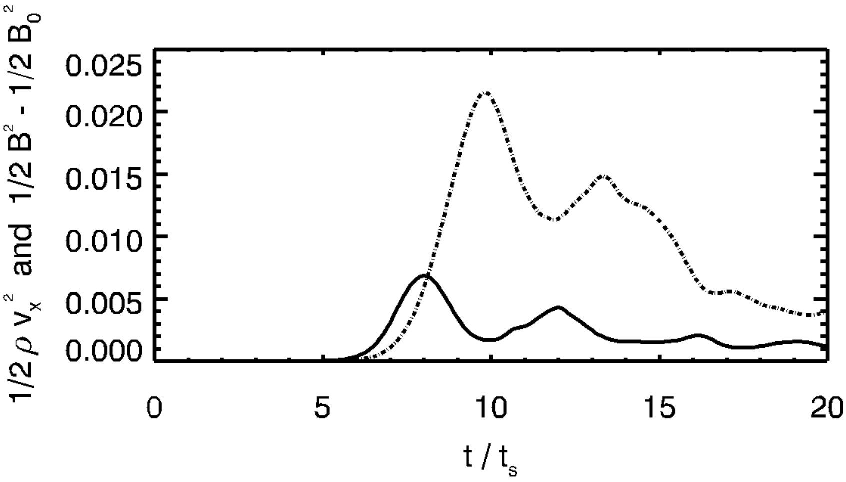

Figure 4.29: The growth of the perturbed magnetic energy (dot-dashed line) is plotted against time in the low resistivity case. Also plotted is the transverse kinetic energy (solid line) of the low resistivity case. It can be seen that, after the initial saturation point, the growth of magnetic energy is linked to the decay of kinetic energy, and vice-versa.

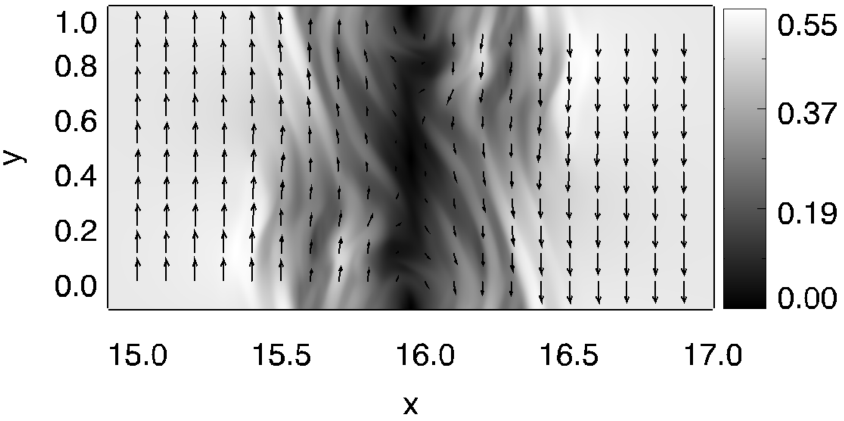

Figure 4.30: Plot of the magnitude and vector field of the velocity field for the low resistivity case, at time $t = 20\,t_\mathrm{s}$. The system has become somewhat disordered.

than the low resistivity case. This can be seen in figure 4.33, which plots the total energy of both systems with time. While the low resistivity case continues to lose energy throughout the simulation through disordered decay, it can clearly be seen that the high resistivity case reaches a stable state much earlier on, and its total energy levels off. In the hydrodynamic case, there is no magnetic field to destroy the KH vortex, and it remains indefinitely. This allows the hydrodynamic case also to reach a stable state.

The results of our simulations agree to some extent with previous multifluid studies of KH instability. It was found by both Wiechen (2006) and Watson et al. (2004) that introducing multifluid effects leads to decoupling of the charged fluids from the neutral fluid. However, the focus of the study by Wiechen (2006) is on the stability properties of the system and does not detail the dynamical evolution of the system. Watson et al. (2004) found that the charged fluids, having decoupled from the neutral fluid, would remain held in place by the magnetic field. This agrees to some extent with our findings, that the charged fluids do not undergo as much wind-up as in the low resistivity case. However, the study by Watson et al. (2004) is a linear study of the instability and does not extend to the nonlinear regime. At later stages, our simulations find that the magnetic field is eventually able to stabilise the neutral fluid and return the system to laminar flow more quickly than in the case of low resistivity.

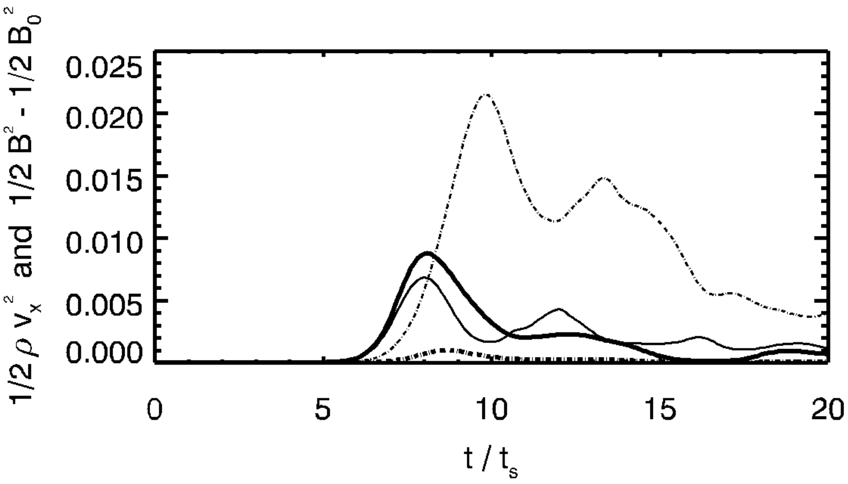

Figure 4.31: The growth of the perturbed magnetic energies (dot-dashed lines) and transverse kinetic energies (solid lines) are plotted against time, for the low resistivity (thin lines) and high ambipolar resistivity (thick lines) cases. It can be seen that, after the initial saturation point, the magnetic field has experienced little growth, and is unable to inject energy back into the system.

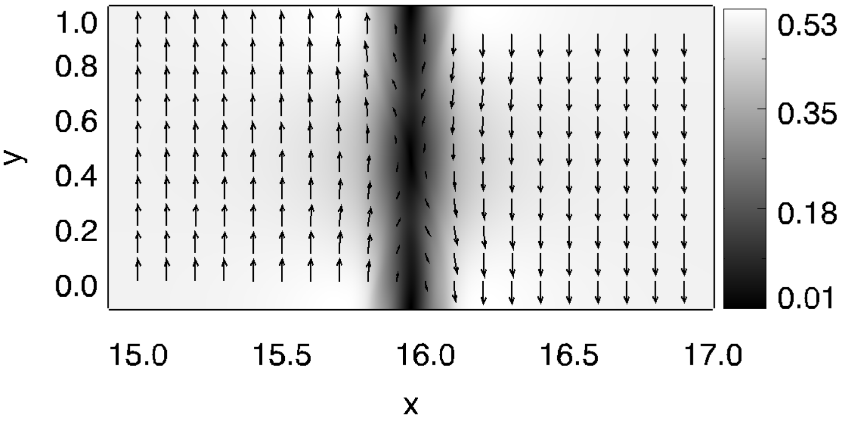

Figure 4.32: Plot of the magnitude and vector field of the velocity field for the high ambipolar case, at time $t = 20\,t_\mathrm{s}$. The system has almost returned to that of laminar flow.

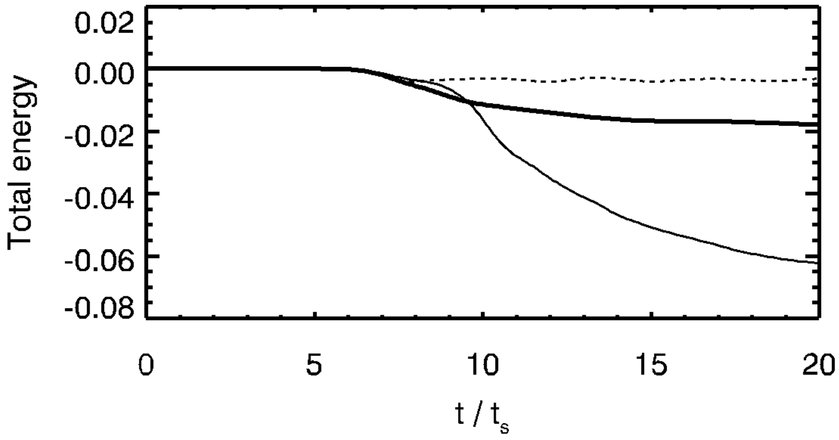

Figure 4.33: The total energy in the system of both the low resistivity (thin line) and high ambipolar resistivity (thick line) systems are plotted against time. Also plotted is the total energy in the hydrodynamic case (dashed line). While the low resistivity case continues to lose energy throughout the simulation through turbulent decay, the leveling off of the energy in the high resistivity case indicates that it has reaches a stable state.

Chapter 5

Hall-dominated multifluid MHD study of the KH instability

The motivation for the ambipolar-dominated study of the KH instability in the last chapter included ambipolar-dominated astrophysical systems such as molecular clouds. Similarly there exist systems in which the Hall effect is a dominant nonideal MHD effect, such as regions within protoplanetary disks (Wardle, 2007). For this reason, the Hall effect is studied here in isolation, so that it can be understood precisely how it affects the KH instability relative to an ideal MHD system. The computational set-up for this study follows directly from that of the ambipolar study, as described in section 4.1.

5.1 Including Hall resistivity in the system

In order to introduce the Hall effect into the system, the charge-to-mass ratio of the ion fluid, α_2, is reduced. The result of this change is that the Larmor radius of the fluid becomes larger, and its Hall parameter, $\beta_2 \equiv \frac{\alpha_2 B}{K_{2,\mathrm{n}}\rho_\mathrm{n}}$, becomes smaller. The ion fluid is thus less well-tied to the magnetic field lines. However, the coupling between the fluid and the neutral fluid remains unchanged, and so the dynamics of the ion fluid continue to reflect closely those of the bulk flow. As the electron fluid is still well-tied to the magnetic field, a relative drift arises between the two charged fluids. The direction of the flow of the ions is no longer along the magnetic field lines, so this relative velocity has a component which is not parallel to the magnetic field. As the Hall effect produces an electric field which is proportional to $\mathbf{J} \times \mathbf{B}$, this electric field is no longer equal to zero. The result is that the magnetic field lines are bent in the z-direction, re-orienting a portion of the magnetic field in that direction and causing a z-velocity flow in the electron fluid.

In order to examine the evolution of the system with time, simulations with varying Hall resistivity have been run. This is implemented by carrying out simulations with successively decreasing ion charge-to-mass ratios, α_2, and thus increasing the Hall resistivity r_{H} in the system. The initial set-up of the three simulations are:

$$\alpha_2 = (\alpha_2)_0 = 1.42 \times 10^{11} \quad \longrightarrow \quad r_{\mathrm{H}} = 3.5 \times 10^{-6} \tag{5.1}$$

$$\alpha_2 = 10^{-3} \times (\alpha_2)_0 \quad \longrightarrow \quad r_{\mathrm{H}} = 3.5 \times 10^{-3} \tag{5.2}$$

$$\alpha_2 = 10^{-4} \times (\alpha_2)_0 \quad \longrightarrow \quad r_{\mathrm{H}} = 3.5 \times 10^{-2} \tag{5.3}$$

In all cases, the ambipolar resistivity remains low, so that any change in the evolution of the system can be contributed to the introduction of the Hall effect. The magnetic Reynolds number for the three systems can be calculated as, respectively, $Re_{\mathrm{m}} = 2.84 \times 10^5$, $Re_{\mathrm{m}} = 2.84 \times 10^2$, and $Re_{\mathrm{m}} = 2.84 \times 10^1$. It will be seen that the two cases of increased Hall resistivity behave very differently. The intermediate case is examined within this chapter as a standard example of moderate Hall resistivity, while the latter case is an example of a more extreme situation and is focused on towards the end of the chapter. It should be noted that when very high Hall diffusion is introduced, the approximation of negligible charged particle inertia appears to breaks down. In this case, the numerical code HYDRA used in these simulations can experience numerical issues (O'Sullivan & Downes, 2006) The simulations with high Hall diffusion are only run up until time $t = 17t_s$ for this reason.

5.2 Resolution study for Hall-dominated system

As in the ambipolar resistivity study, a resolution study is carried out to ensure that the small-scale nonideal dynamics are captured. For this purpose, simulations are again run at three different resolutions. For a grid of width 32, these simulations consist of $6400 \times 200 \times 1$, $3200 \times 100 \times 1$, and $1600 \times 50 \times 1$ grid cells. These simulations are run with the highest level of Hall resistivity to ensure that the smallest-scale dispersive effects are in place when examining whether they are sufficiently resolved.

As has been seen, the introduction of nonideal effects does not tend to greatly influence the linear growth rate of the instability. As a result, the growth rate does not provide an ideal means of measuring convergence with increasing resolution. The nonlinear evolution of the transverse kinetic energy $\int\int dxdy\frac{1}{2}\rho\mathbf{v}_x^2$ is, however, strongly influenced by the nonideal effects. It is chosen not to examine the evolution of the perturbed magnetic energy as, in the case of high Hall resistivity, it no longer demonstrates a simple growth to an initial maximum. The evolution of the transverse kinetic energy for each simulation is plotted in figure 5.1. It can clearly be seen that the simulations have started to converge at higher resolutions. While there is a notable difference between the two simulations of lower resolution, the gap closes significantly in the comparison between the two simulations of higher resolution.

As has been seen, the initial maxima reached by the transverse kinetic energies are strongly influenced by the inclusion of nonideal effects. For this reason, comparison of these values can lead to quantitative measurements of the gap between the simulations of different resolutions. These maxima are plotted in figure 5.2 as a function of the number of grid cells in the x-direction. It can be seen from the plot that the gap reduces from a difference of $\approx\ 18\%$ to $\approx 2\,\%$ as the resolution increases. It is expected that if the resolution was to be doubled again, the difference between the maxima in this simulation and our current highest-resolution simulation would be negligible. It is therefore concluded that the highest resolution used here, $6400 \times 200 \times 1$ cells, is sufficiently high to capture the effects due to high Hall resistivity.

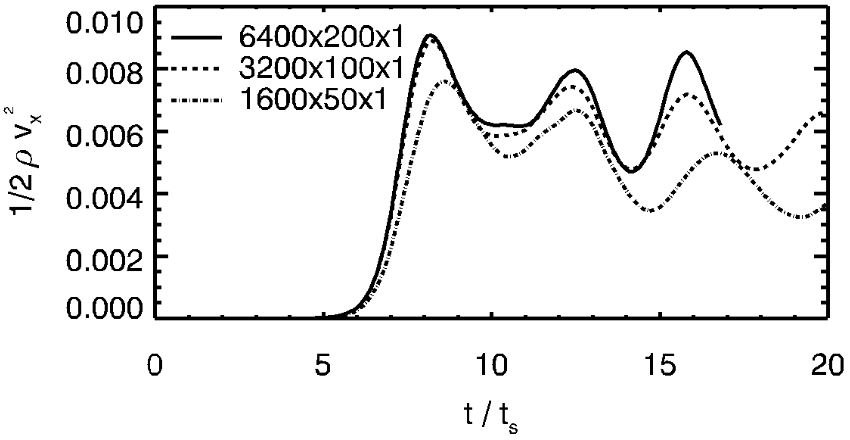

Figure 5.1: Plot of the transverse kinetic energy against time in the case of high Hall resistivity for three different resolutions.

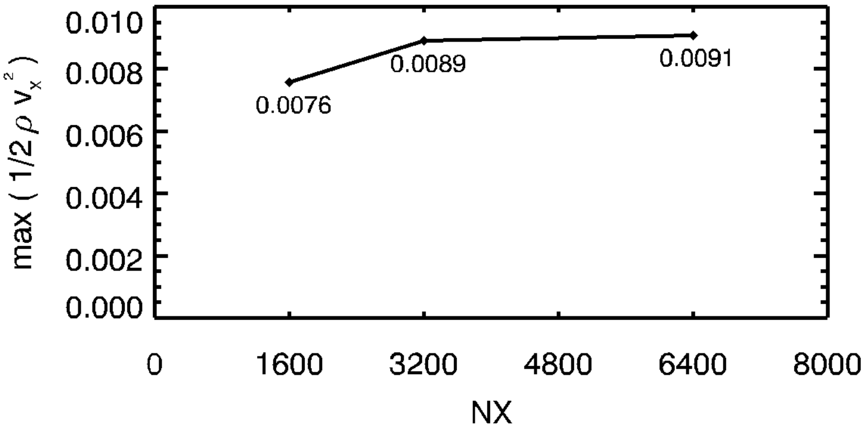

Figure 5.2: Plot of the initial maxima reached by the transverse kinetic energy for the three simulations of different resolutions, plotted against the number of grid cells in the x-direction for that simulation.

5.3 Results for Hall-dominated system with moderate Hall resistivity

As in the low resistivity case, as the Kelvin-Helmholtz instability develops, it causes a wind-up of the plasma at the interface between the two layers, resulting in the “Kelvin’s cat’s eye” vortex. For the case of moderate Hall resistivity, this is shown in figure 5.3.

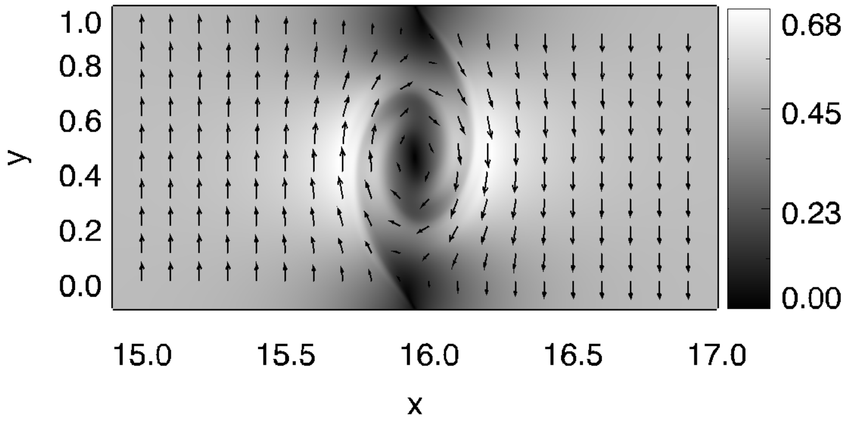

Figure 5.3: Plot of the magnitude and vector field of the bulk velocity field for the moderate Hall case, at time $t = 8\,t_\mathrm{s}$.

As in the case of ambipolar diffusion, when the Hall effect is introduced to the system, one of the primary effects observed is the influence on the magnetic field. It is known that by including a drift between the positively and negatively charged fluids, magnetic dispersion can occur. This does not have the effect of losing magnetic energy, as in the ambipolar case through reconnection, but rather to re-orient the magnetic field. As a result, the initial growth of the total magnetic energy in the system remains relatively unchanged from the case of low resistivity to that of moderate Hall resistivity, as can be seen in figure 5.4.

However, comparisons can be made between the growth of the magnetic field in the $xy-$plane of the initial system, and that in the z-direction, which has become significant with the introduction of the Hall effect. In figure 5.5, it can be seen that while the total magnetic field has undergone the same degree of ampli-

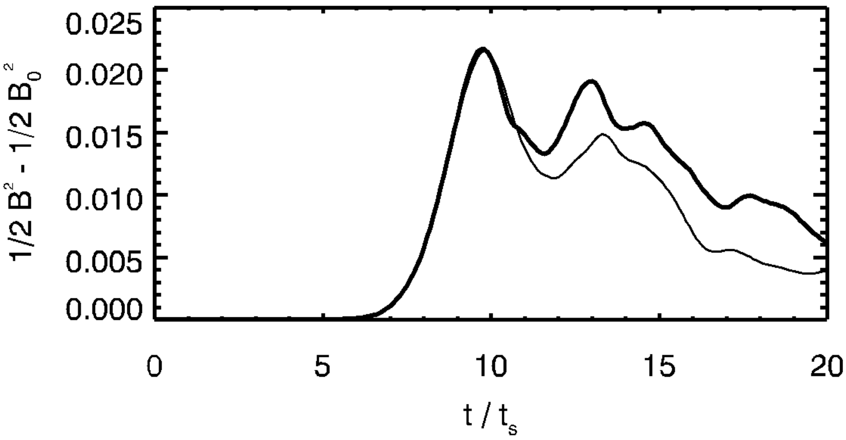

Figure 5.4: The perturbed magnetic energy in the system for both the low resistivity (thin line) and moderate Hall resistivity (thick line) cases are plotted against time. No significant difference can be seen between the maxima reached in each case.

fication, the introduction of Hall resistivity has had the effect of re-orienting the field and dispersing it through the three dimensions.

It is worth noting that the growth of the magnetic field in the z-direction occurs at a later stage than that in the x- and y-directions. The amount of Hall resistivity in the system depends on the magnetic field strength. As the magnetic field undergoes significant amplification, the magnitude of the Hall resistivity is also amplified. Thus the effect of the Hall resistivity only causes significant changes during the nonlinear saturation phase of the instability.

For this reason, closer examination of the magnetic field at the time of saturation of the kinetic energy of the system in the moderate Hall case shows very little difference from the case of low resistivity. The wind-up of the magnetic field in the low resistivity case was seen in figure 4.14. A plot of the magnetic field in the xy-plane in the Hall case is given in figure 5.6 for comparison. It can be seen that a wind-up has occurred, very similar to that of the low resistivity case. The only difference in this case is that there is now a slight additional magnetic field in the z-direction. This difference becomes more significant, however, at later times.

As the Hall effect has only a small impact on the initial linear growth of the

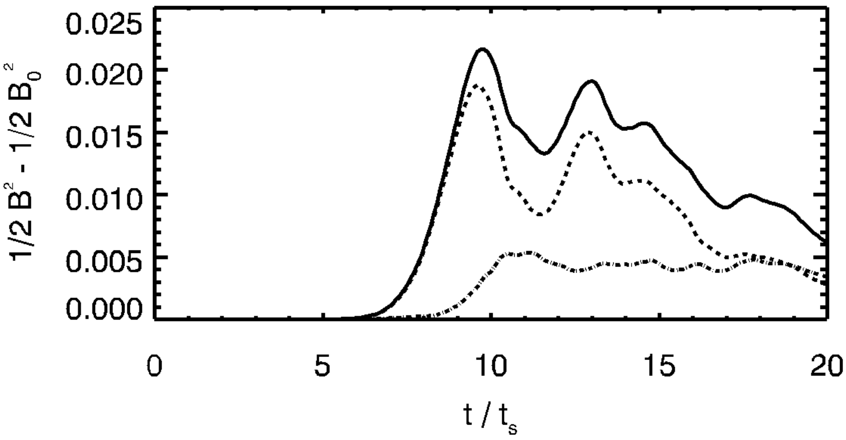

Figure 5.5: The total perturbed magnetic energy (solid line) in the system is plotted against time for the moderate Hall resistivity case. Also plotted for the Hall case are the evolutions of the perturbed magnetic energies in the xy-plane only (dashed line) and in the z-direction (dot-dashed line). While the maximum reached by the total magnetic energy is the same as in the low resistivity case, the magnetic field has experienced some re-orientation into the z-direction.

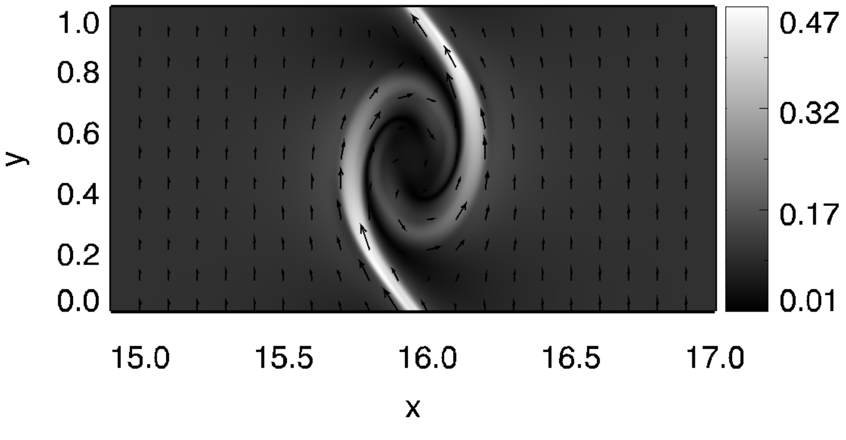

Figure 5.6: Plot of the magnitude and vector field of the magnetic field for the case of moderate Hall resistivity, at time $t = 8\,t_{\rm s}$. The magnetic field closely resembles that of the low resistivity case.

system, it is expected that little change will be seen in the dynamics of the bulk fluid during the initial growth of the instability. Comparisons with the low resistivity case confirm that a moderate amount of Hall resistivity has little impact on the linear growth rate of the instability (see figure 5.7) or the initial maxima reached by the transverse kinetic energy of either the bulk fluid (see figure 5.8) or the charged fluids (see figures 5.9 and 5.10).

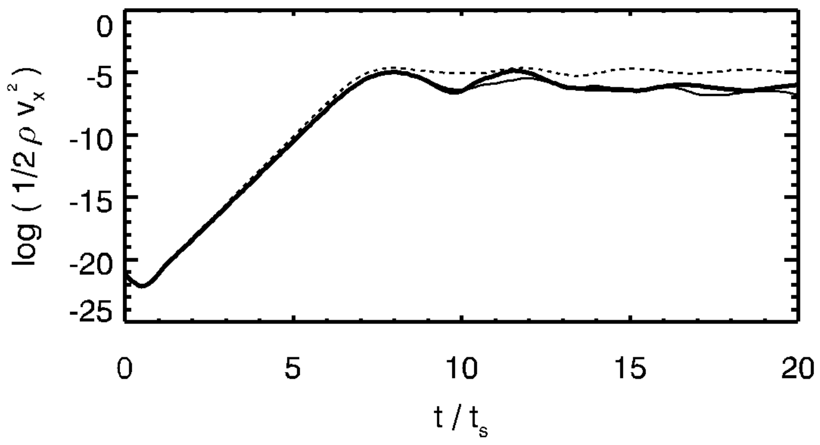

Figure 5.7: The log of the transverse kinetic energy in the system is plotted against time for the cases of low resistivity (thin line) and moderate Hall resistivity (thick line). The dashed line represents the hydrodynamic case. There is very little difference between the linear growths for the magnetised systems.

Following the initial linear growth of the instability, the system experiences a period of transferring energy back and forth between the magnetic field and velocity field, as in the case of low resistivity. In figure 5.11, this phenomenon can be observed for the case of moderate Hall resistivity. In comparison with the case of low resistivity, it can be seen that the subsequent peaks reached for both the magnetic and transverse kinetic energies are higher in the Hall case.

Another factor to include in this analysis is the growth of the kinetic energy in the z-direction. As was mentioned previously, the Hall effect is seen to have a greater impact following the initial linear growth stage of the instability. As the magnetic field is amplified, more growth in both the kinetic and magnetic

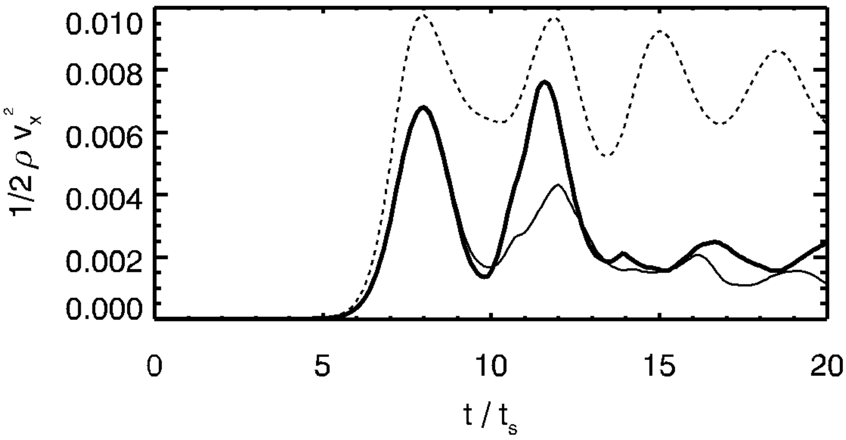

Figure 5.8: The transverse kinetic energy of the bulk fluid is plotted against time for the cases of low resistivity (thin line) and moderate Hall resistivity (thick line). The dashed line represents the hydrodynamic case. There is very little difference between the linear growths for the magnetised systems.

energies in the z-direction can be observed. The kinetic energy in the z-direction experiences a steady growth with time, eventually overtaking the kinetic energy in the x-direction, as seen in figure 5.12.

Figure 5.11 showed that, following their initial maxima, both the velocity and magnetic fields experienced stronger growth than in the low resistivity case. Despite this, figure 5.13 demonstrates that while both systems are continuously losing energy, the Hall case is in fact losing more. This energy loss can occur through reconnection, or through thermal energy that is immediately dissipated in our isothermal simulation. It should also be recalled that the zero-gradient boundary conditions on the x-boundaries of the grid allow for plasma, and thus energy, to flow freely out of the system. The important difference between the cases of low and moderate Hall resistivity, is that while the kinetic energy in the y-direction that is injected into the system gradually evens out with time in the low resistivity case, it continues to steadily decay in the Hall resistivity case. The conclusion is that in the low resistivity case, the instability has completed its growth and is returning to a quasi-steady state. In the Hall case however, the instability is

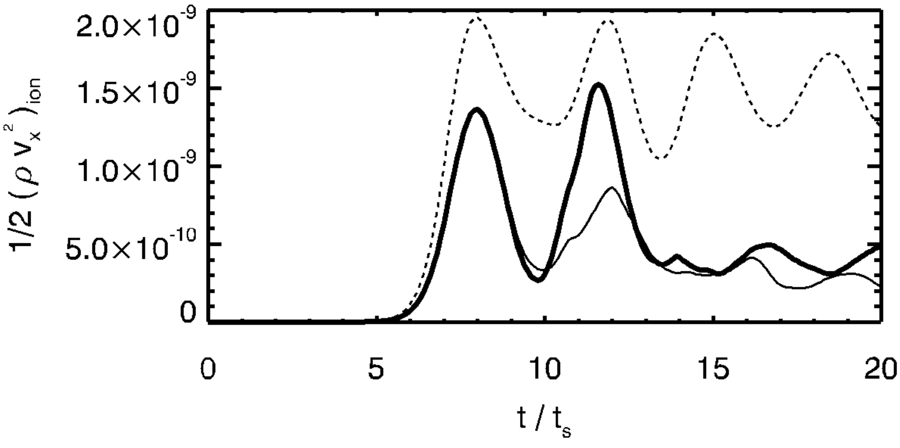

Figure 5.9: The transverse kinetic energy of the ion fluid is plotted against time for the cases of low resistivity (thin line) and moderate Hall resistivity (thick line). The dashed line represents the hydrodynamic case. There is very little difference between the linear growths for the magnetised systems.

continuing to consume the parallel kinetic energy available to it. In this way, the instability undergoes a further stage of development within the dynamics of the system.

In order to demonstrate the further consumption of parallel kinetic energy in the Hall case, figure 5.14 plots the parallel kinetic energy, integrated along the y-direction and plotted against x, for the cases of moderate Hall and low resistivities, at a time towards the end of the simulation. This demonstrates that in the Hall case, the instability has continued to cause re-orientation of the magnetic field lines and thus of the electron flow, through three dimensional space. During this process the electron fluid obtains a velocity outwards from the KH vortex, which results in a broader volume of plasma being disturbed.

Figures 5.15 and 5.16 plot the velocity field for the low and high resistivity cases respectively. Here it can clearly be seen that the instability has died down in the low resistivity case and the system appears to reaching a stable state. In the Hall case, it is clear that the system has remained unstable. The instability continues to feed on the energy available to it and the volume of fluid affected by

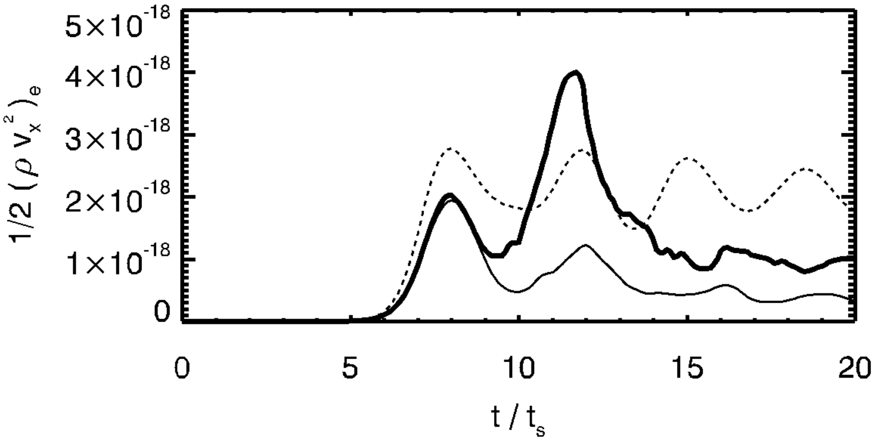

Figure 5.10: The transverse kinetic energy of the electron fluid is plotted against time for the cases of low resistivity (thin line) and moderate Hall resistivity (thick line). The dashed line represents the hydrodynamic case. There is very little difference between the linear growths for the magnetised systems.

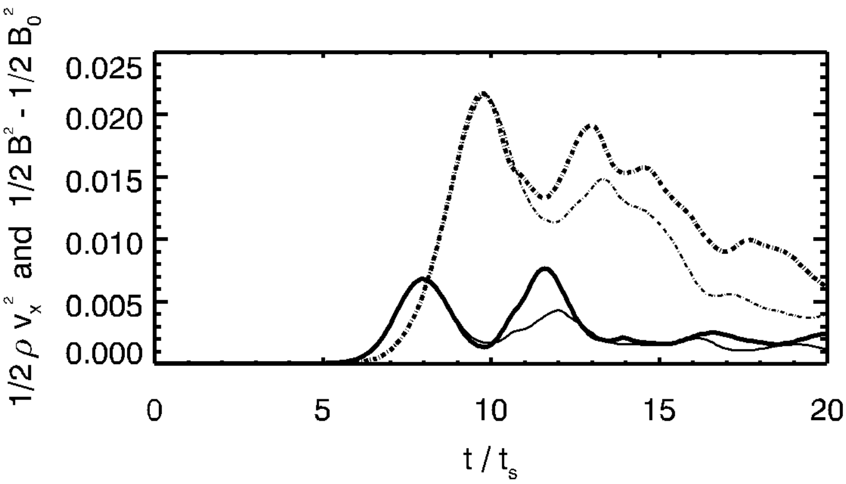

Figure 5.11: Plot of the total perturbed magnetic energy (dot-dashed lines) and transverse kinetic energy (solid lines) with time for the low resistivity (thin lines) and moderate Hall (thick lines) cases.

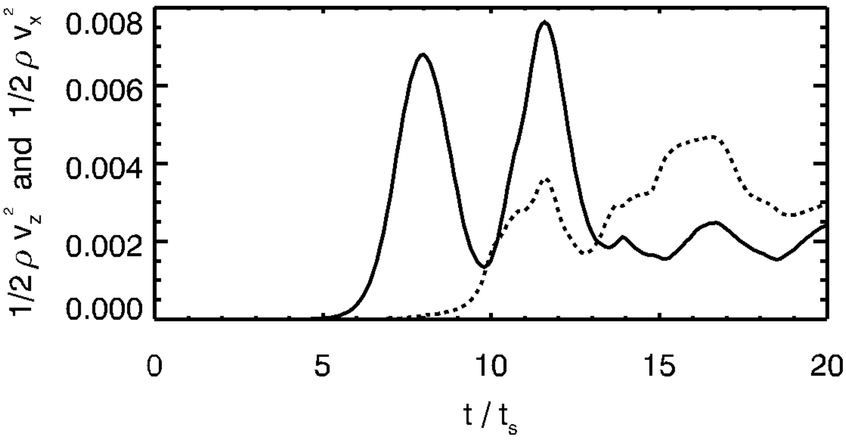

Figure 5.12: Plot of the transverse kinetic energy (solid line) and kinetic energy in the z-direction (dashed line) with time for the case of moderate Hall resistivity. It can be seen that at later times, the growth of energy in the z-direction has become significant.

the instability continues to grow.

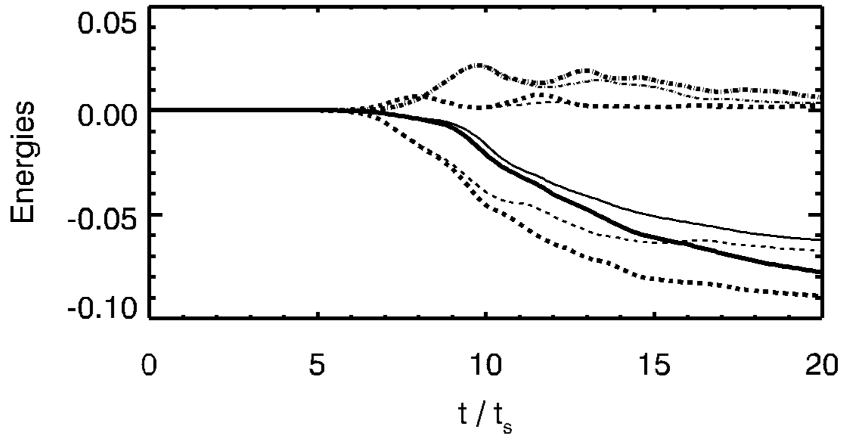

Figure 5.13: Plot of the parallel and non-parallel kinetic energies (dashed lines) and the perturbed magnetic energy (dot-dashed line) with time, for the low resistivity (thin line) and moderate Hall (thick line) cases. The sum of these energies give the change in total energy, which is also plotted (solid lines). It can be seen that the Hall case consumes more energy than the low resistivity case.

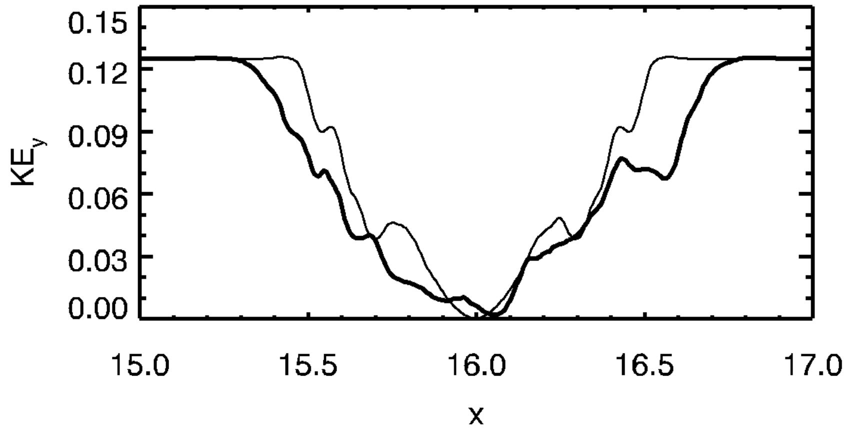

Figure 5.14: Plot of the parallel kinetic energy, integrated along the y-direction and plotted against x. Both the low resistivity case (thin line) and moderate Hall case (thick line) are given at time $20\,t_\mathrm{s}$.

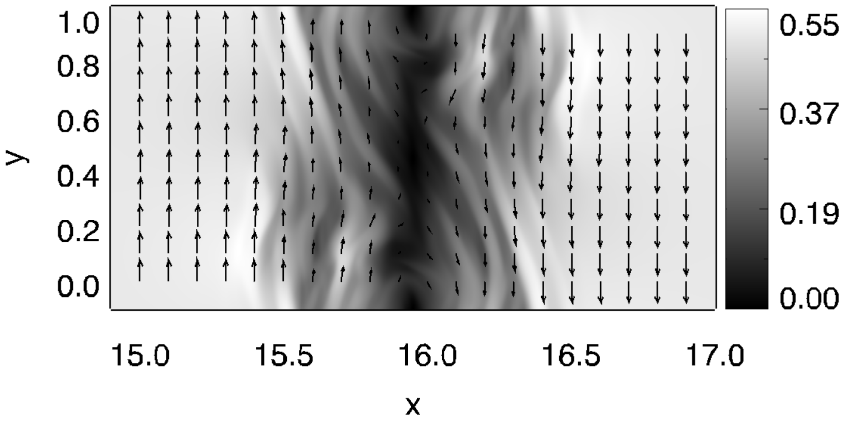

Figure 5.15: Plot of the magnitude and vector field of the velocity field for the case of low resistivity at time $20\,t_{\mathrm{s}}$.

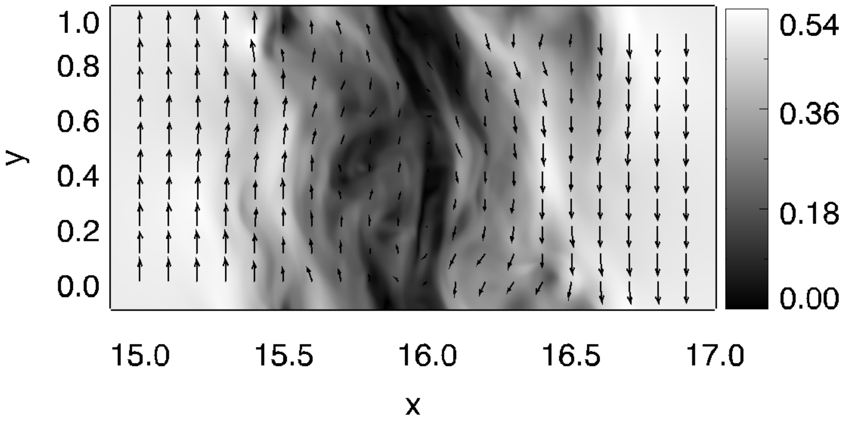

Figure 5.16: Plot of the magnitude and vector field of the velocity field for the case of moderate Hall resistivity at time $20\,t_{\mathrm{s}}$.

5.4 Results for Hall-dominated system with high Hall resistivity

In the very high Hall case, higher Hall resistivity is introduced into the system by requiring that the ion charged fluid is even less well-tied to the magnetic field as before, by further reducing its charge-to-mass ratio. This has the effect of allowing the ion fluid to completely decouple from the magnetic field, while remaining well-coupled to the neutral fluid through their unchanged collision rate. Therefore, as the bulk fluid undergoes a wind-up due to the velocity shear, as seen in figure 5.17, the ion fluid behaves in a similar manner to the neutral fluid, while the electron fluid remains tied to the magnetic field.

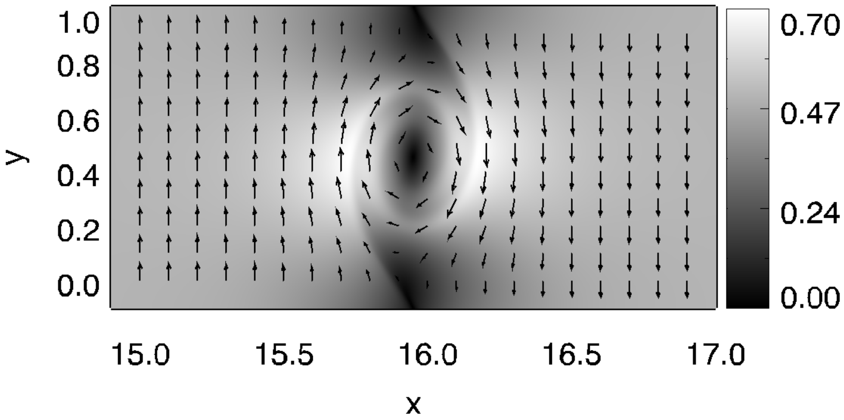

Figure 5.17: Plot of the magnitude and vector field of the bulk velocity field for the high Hall case, at time $t = 8\,t_{\mathrm{s}}$.

The bulk flow now interacts with the magnetic field only through collisions between the neutral fluid and the electron fluid, as well as the explicit requirement that charge neutrality holds at all points, which intrinsically ties the positively and negatively charged fluids together. The fact that the bulk flow and magnetic field are now so poorly coupled has a significant effect on both of them. The winding-up of the bulk flow has much less effect on the magnetic field than before and the magnetic field undergoes only a small wind-up in the xy-plane. This can be seen in figure 5.18.

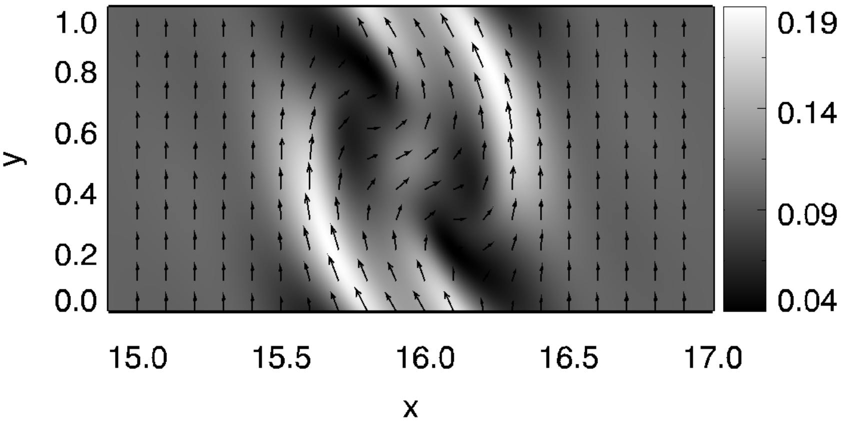

Figure 5.18: Plot of the magnitude and vector field of the magnetic field in the xy-plane in the high Hall resistivity case at time $8\,t_{\mathrm{s}}$. It can be seen that the magnetic field does not undergo as much wind-up as is seen in the velocity field (figure 5.17).

A primary role of the magnetic field in the development of the KH instability has been seen to be the suppression of the winding-up of the bulk fluid. In the initial stages of the growth of the instability, this occurs as normal and the linear growth rate of the instability can be seen to remain unchanged in figure 5.19.

However, as the magnetic field undergoes less wind-up and less growth in the xy-plane, and is increasingly decoupled from the bulk flow, it is less able to suppress the winding-up of the bulk fluid at later times. As a result, the velocity field reaches a greater wind-up, as can be seen by the higher maximum reached by the transverse kinetic energy of the system in figure 5.20. Also plotted on this graph is the evolution of the transverse kinetic energy for the hydrodynamic case. In this system, there is no magnetic field to suppress the growth of the instability, and the transverse kinetic energy reaches an even higher maximum. This demonstrates that while the magnetic field still does cause some suppression of growth of the instability in the high Hall case, it is dramatically less, and the bulk fluid is able to behave almost independently of the magnetic field.

It is worth noting that, as the ion fluid is well-coupled to the neutrals, and not to the magnetic field, its transverse kinetic energy is also seen to experience the same increase in growth, demonstrating the extent to which the fluid is truly decoupled from the magnetic field. This can be observed in figure 5.21.

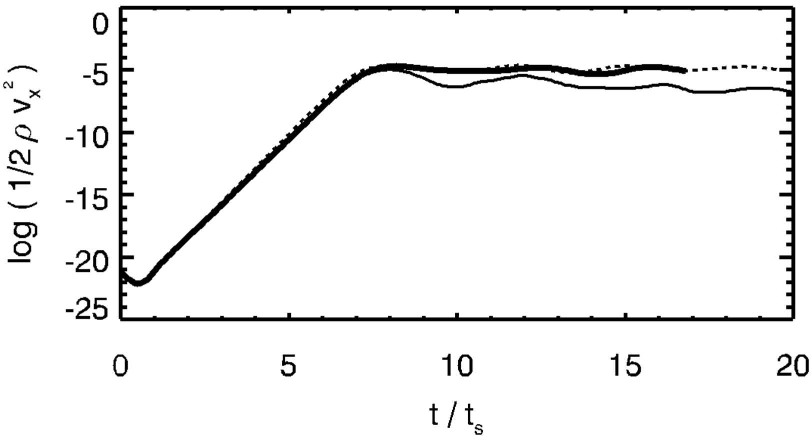

Figure 5.19: The log of the transverse kinetic energy in the system is plotted against time for the low resistivity (thin line) and high Hall resistivity (thick line) cases. The dashed line represents the hydrodynamic case. There is very little difference between the linear growths for the low and high resistivity cases.

The decoupling of the ion fluid from the magnetic field can also be seen in vector plots of the ion fluid's velocity. Figures 5.22 and 5.23 show plots of the velocities of the neutral and ion fluids respectively. It can clearly be seen that the two fluids are demonstrating the same dynamics. On the other hand, the electron fluid is still well-tied to the magnetic field, and its behaviour, as seen in figure 5.24, clearly reflects the dynamics of the magnetic field, as was seen in figure 5.18.

As the ion fluid is no longer tied to the magnetic field, while the electron fluid is, it can be seen from these plots that the two charged fluids have an obvious difference in their dynamics. Plots of their densities (see figures 5.25 and 5.26) show that while their velocity fields are significantly different, their density distributions are such that charge neutrality is conserved at all points.

The velocity of the ion fluid has developed to reflect the winding-up of the bulk fluid, while the electron fluid reflects the lack of wind-up in the magnetic field. The result of this difference is that there is now a distinct velocity difference between the ions and the electrons. This is occurring in the xy-plane, but as only

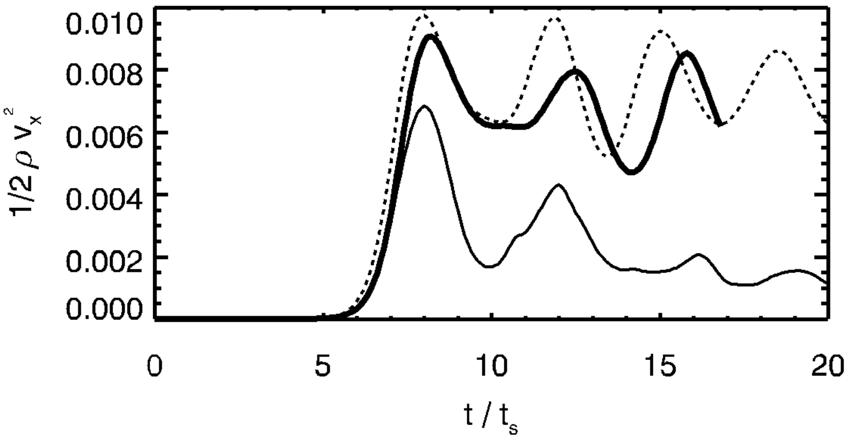

Figure 5.20: The transverse kinetic energy in the system is plotted against time for the cases of low resistivity (thin line) and high Hall resistivity (thick line). The hydrodynamic case has also been plotted for the sake of comparison (dashed line). It can be seen that the behaviour of the high Hall case is similar to that of the hydrodynamic case.

the electron fluid is flowing along the magnetic field lines, this velocity difference is not parallel to the magnetic field. This has the consequence of causing a current to flow in the plane that is not parallel to the magnetic field. This is the basis for the Hall effect, which requires a non-parallel current and magnetic field to occur. As the charged fluids are acted on by the magnetic field, they experience a force in the $\mathbf{J} \times \mathbf{B}$ direction, which in this case is the z-direction. As the particles of the electron fluid are more well-tied to the magnetic field, they experience a more significant velocity in the z-direction. The ion fluid is less influenced by the magnetic field. The resulting flow of electrons in the z-direction creates a bending of the magnetic field line in this direction, as these two are tightly coupled. The neutral fluid, as expected, experiences only the same small velocity in the z-direction that the ion fluid does. Through this, it can be seen how the relative velocity between the two charged fluids in the xy-plane is quickly transformed into a re-orientation of the electron fluid flow and magnetic field into the z-direction. Figure 5.27 shows the growth of the total magnetic energy in the system for the cases of low and and high Hall resistivity, and figure 5.28 compares the growth of the magnetic

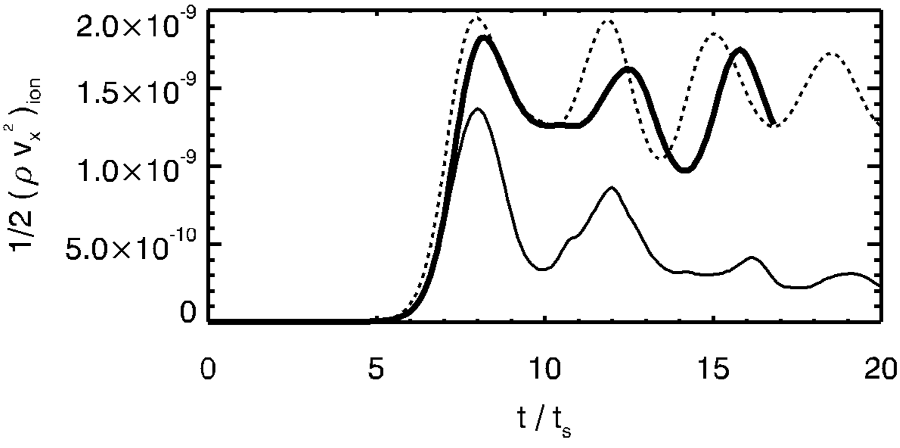

Figure 5.21: The transverse kinetic energy of the ion fluid is plotted against time for the cases of low resistivity (thin line) and high Hall resistivity (thick line). The hydrodynamic case has also been plotted for the sake of comparison (dashed line). The behaviour of the ion fluid closely reflects that of the neutral fluid.

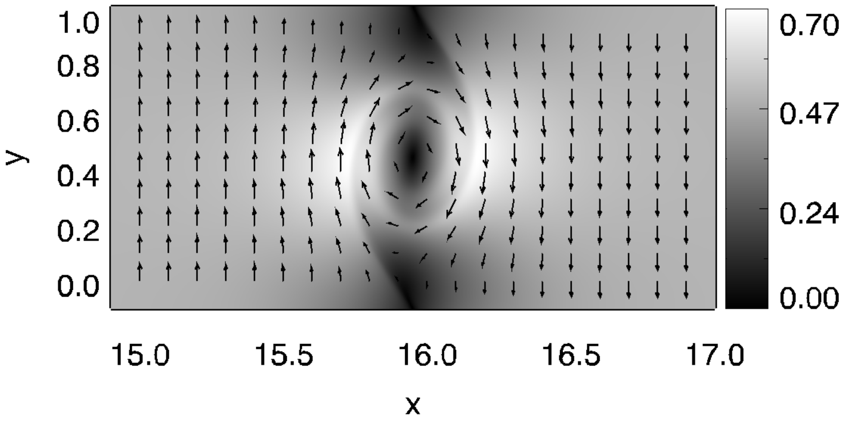

Figure 5.22: Plot of the magnitude and vector field of the bulk velocity field for the high Hall resistivity case, at time $t = 8\,t_{\mathrm{s}}$.

energy in the xy-plane with that in the z-direction.

Comparisons of figure 5.28 with figure 5.5 also demonstrates that the magnetic field in the xy-plane does not grow as quickly as in the case of lower Hall resistiv-

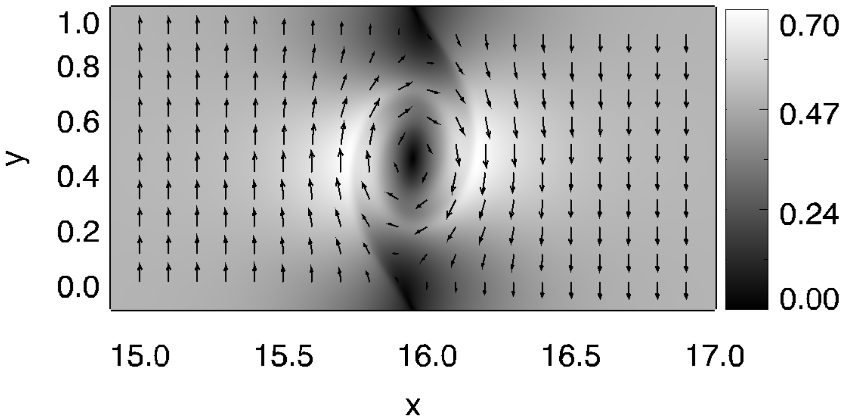

Figure 5.23: Plot of the magnitude and vector field of the ion velocity field for the high Hall resistivity case, at time $t = 8\,t_{\mathrm{s}}$. Again the behaviour of the ion fluid closely reflects that of the neutral fluid.

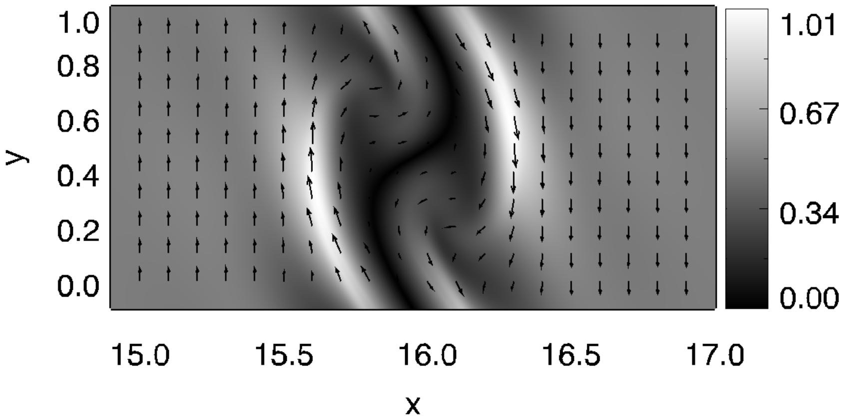

Figure 5.24: Plot of the magnitude and vector field of the electron velocity field for the high Hall resistivity case, at time $t = 8\,t_{\mathrm{s}}$. The behaviour of the electron fluid can be seen to closely reflect that of the magnetic field.

ity. This is understood by the lack of winding up of the magnetic field due to the decoupling of the field from the ion fluid, and thus from the bulk fluid. However, it should be noted that the increase in Hall resistivity, and a greater difference between the dynamics of the ion and electron fluids, means that the magnetic field in the z-direction undergoes stronger and faster growth.

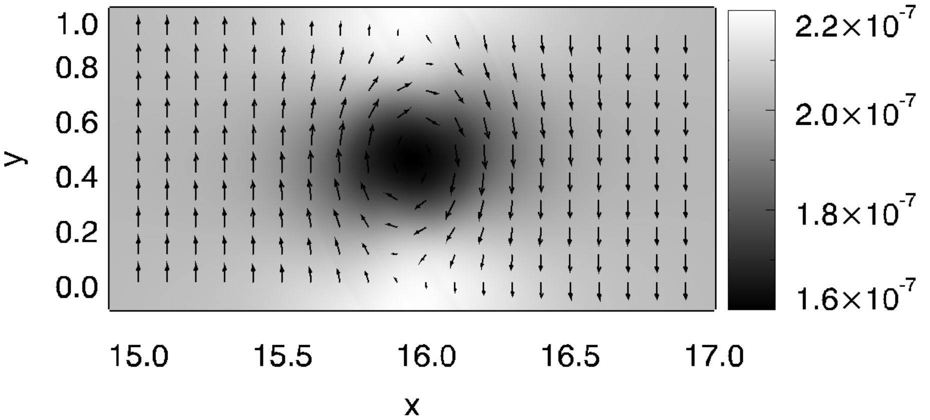

Figure 5.25: Plot of the mass density, as well as the velocity vector field, of the ion fluid in the high Hall case at time $= 8\,t_{\mathrm{s}}$.

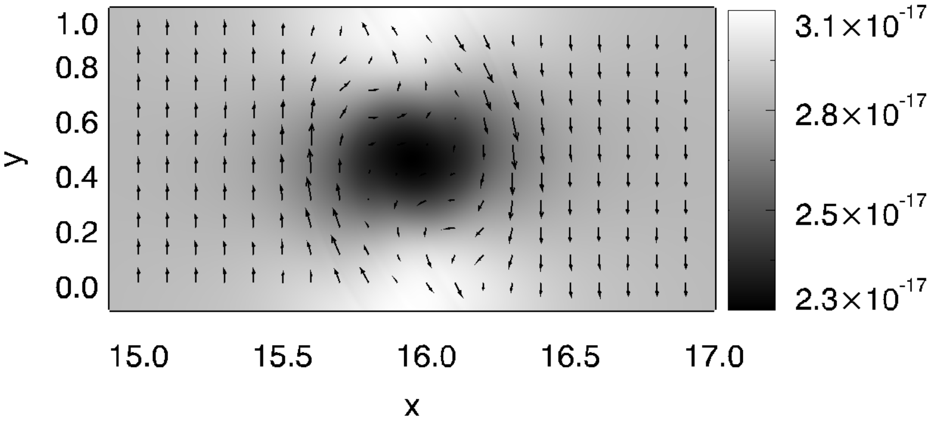

Figure 5.26: Plot of the mass density, as well as the velocity vector field, of the electron fluid in the high Hall case at time $= 8\,t_{\mathrm{s}}$.

In the case of low resistivity, the magnetic energy eventually grows to a point at which it is strong enough to oppose the wind-up of the instability. At this point, the magnetic field lines start to un-wind and attempt to return to their original states. In the case of high Hall resistivity, this does not occur. Such extensive decoupling has occurred between the ion fluid and magnetic field, that the magnetic field is no longer able to oppose the vortex that has developed in the bulk fluid. This

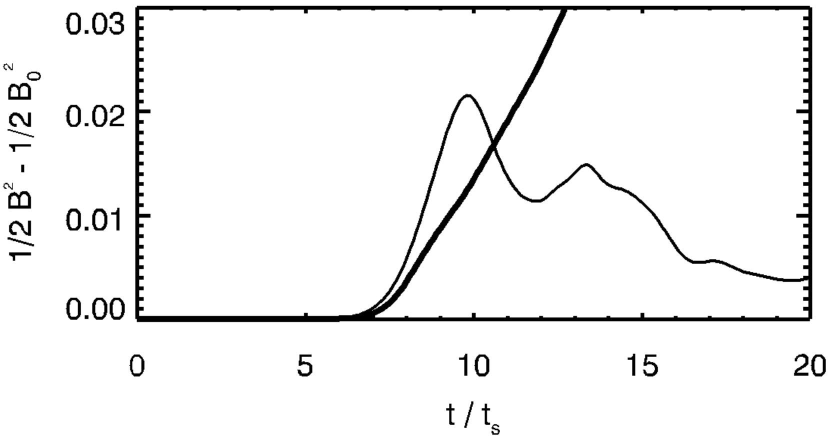

Figure 5.27: The total perturbed magnetic energy in the system is plotted against time for the low resistivity (thin line) and high Hall case (thick line). The magnetic energy is seen to experience very different growth in the high Hall case.

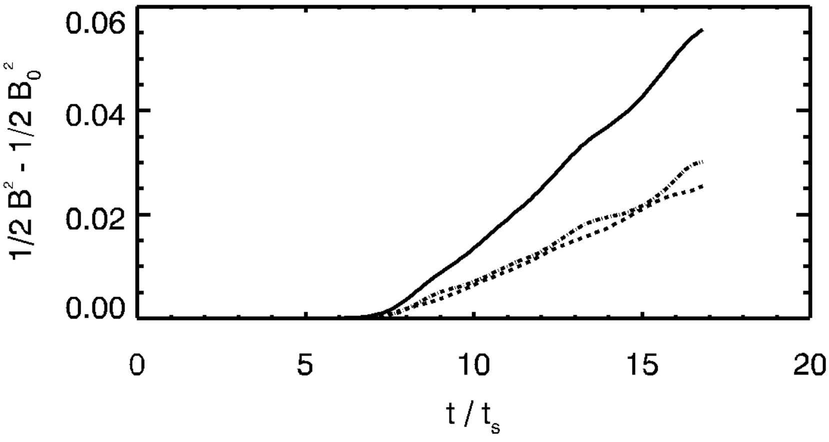

Figure 5.28: The total perturbed magnetic energy in the system is plotted against time for the high Hall case (solid line). Also plotted for comparison are the growth of the magnetic energies in the xy-plane (dashed line) and in the z-direction (dot-dashed line). It can be seen that there is significant growth in the z-direction.

is the primary difference between the moderate and high Hall cases. As a result of the decoupling in the high Hall case, the vortex is not destroyed, and instead remains untouched for the remainder of the simulation. This reflects the dynamics observed in the hydrodynamic case, where there is no magnetic field to break down the KH vortex, as was demonstrated in figure 5.20.

At these later times, with the magnetic field unable to break down the vortex, the ion fluid remains spinning in the KH vortex. This maintains a velocity difference with the electron fluids, which in turn continues to re-orient a component of the magnetic field into the z-direction through the Hall effect. This z-directional magnetic field, and thus the z-component of the electron's kinetic energy, are continually fed by the ion fluid in the ever-spinning KH vortex. This causes the system to begin to demonstrate dynamo action. This is observed by the magnetic field experiencing monotonical growth, as was seen in figure 5.27. As another consequence of this, the kinetic energy of the electron fluid in the z-direction also grows monotonically, as can be seen in figure 5.29.

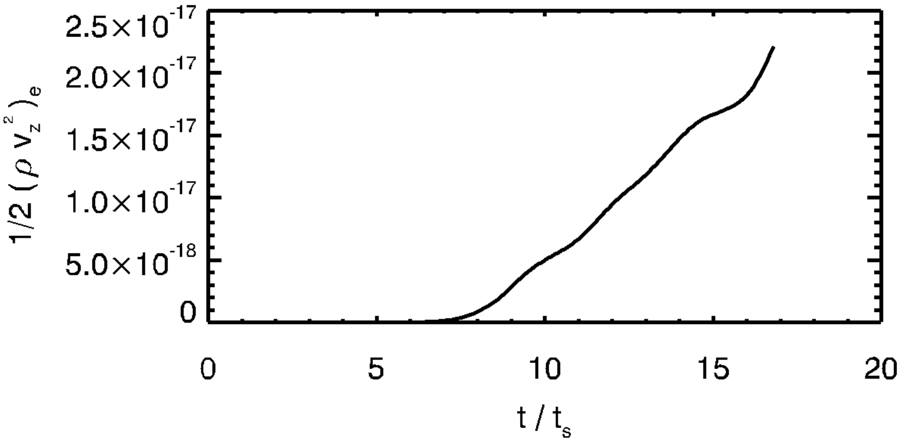

Figure 5.29: The kinetic energy of the electron fluid in the z-direction is plotted against time for the high Hall case. This can be seen to undergo monotonical growth, solely as a result of the Hall effect.

As the z-components of the current and magnetic field continue to grow, the Hall effect now acts on the non-parallel currents and magnetic fields that have arisen between the z-directions and the xy-plane. This has the result of re-orienting some of the magnetic field, and electron fluid flow, back onto the xy-plane. During this process the electron fluid obtains a velocity outwards from the KH vortex, which results in a broader volume of plasma being disturbed. This feeds the continuous growth of the magnetic energy in the xy-plane, and thus causing continuous growth of the electron transverse kinetic energy, as can be seen in figure 5.30.

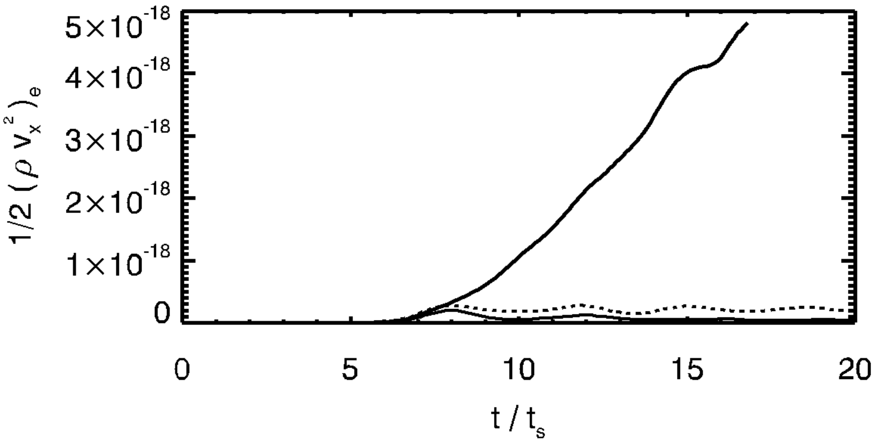

Figure 5.30: The transverse kinetic energy of the electron fluid is plotted against time for the low resistivity (thin line) and high Hall resistivity (thick line) cases. Also plotted in the electron transverse kinetic energy in the hydrodynamic case (dashed line).

As the magnetic field undergoes continuous growth, and continuous re-orientation due to the Hall effect, it quickly develops more complex structure. The distribution of the magnetic field at time $t = 16\,t_\mathrm{s}$ is given in figure 5.31.

As the magnetic field evolves dynamically, so too does the electron fluid, due to the strong coupling it has with the magnetic field. The mass density and vector field of the electron fluid at time $t = 16\,t_\mathrm{s}$ are plotted in figure 5.32.

In order to maintain charge neutrality, the ion fluid must be displaced in a similar fashion to the electron fluid. The mass density and velocity field of the ion fluid time $t = 16\,t_\mathrm{s}$ is thus plotted in figure 5.33. It can clearly be seen that the condition of charge neutrality has caused further structure to develop in the

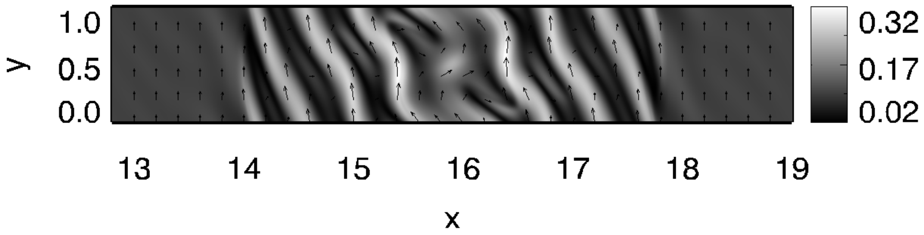

Figure 5.31: Plot of the magnitude and vector field of the magnetic field in the xy-plane in the high Hall resistivity case at time $16\,t_\text{s}$. A wider part of the grid is plotted in order to show the further developments in the magnetic field structure.

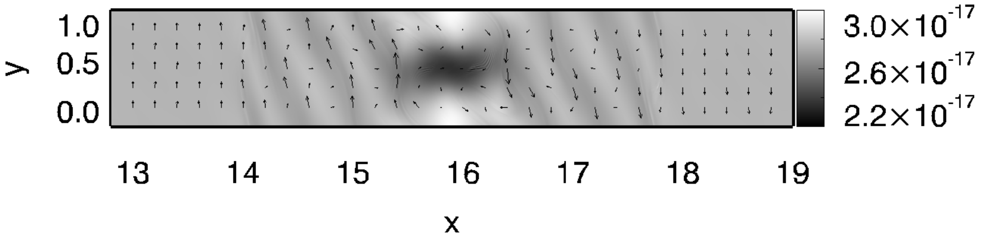

Figure 5.32: A wide plot of the mass density, as well as the velocity vector field, of the electron fluid in the high Hall case at time $= 16\,t_\text{s}$. The dynamics of the electron fluid reflects those of the magnetic field.

distribution of the ion fluid than would be observed in the low resistivity case.

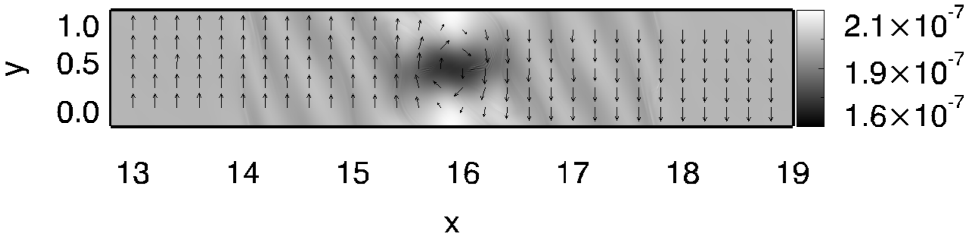

Figure 5.33: A wide plot of the mass density, as well as the velocity vector field, of the ion fluid in the high Hall case at time $= 16\,t_\text{s}$. Further structure has developed in the ion mass distribution as a result of the electron distribution through charge neutrality.

As the neutrals remain well coupled to the ion fluid through collisions, this has the consequence of also affecting the flow of the bulk fluid. This occurs as a result of the $\mathbf{J} \times \mathbf{B}$ term in the momentum equation (1.15). The resulting mass density distribution of the bulk flow at the same time can be seen in figure 5.34. It can clearly be seen that a wider volume of fluid has been disturbed by the instability than in the case of low resistivity.

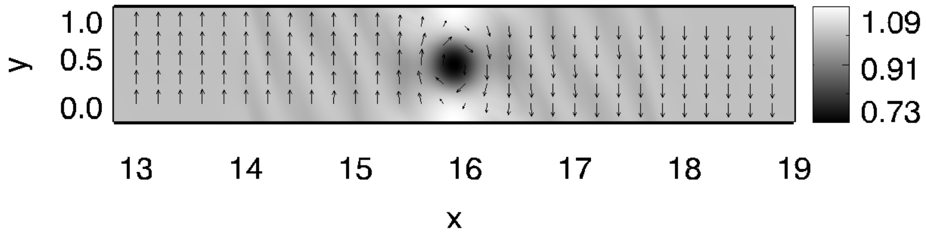

Figure 5.34: A wide plot of the mass density, as well as the velocity vector field, of the bulk fluid in the high Hall case at time $= 16\,t_\mathrm{s}$. Further structure has developed in the bulk mass distribution through collisional coupling with the ion fluid.

Through their strong decoupling from the magnetic field, the dynamics of the bulk fluid and ion fluid demonstrate behaviour very similar to that of the hydrodynamic case, in which the Kelvin-Helmholtz vortex remains undestroyed. The high Hall case can in fact be thought of as two separate systems occurring simultaneously; the bulk fluid demonstrating hydrodynamic behaviour and the continuously widening volume of perturbed fluid perpetually feeding the growth of the magnetic field through the Hall effect. These two systems are intrinsically intertwined through the requirement of charge neutrality, by which the electron fluid causes a widened area of perturbed ion fluid, and thus the bulk fluid. Both systems are relatively energy efficient, and following the initial growth of the KH instability, the overall system experiences little further loss of energy. This is shown in figure 5.35, which also demonstrates the continuous loss of parallel kinetic energy in favour of growth in the magnetic energy. The supply of energy to feed the magnetic field is limited only to the size of the grid on which the simulation is run.

It has thus been seen that even a moderate amount of Hall resistivity results in a wider volume of fluid being disturbed by the instability. This agrees with previous studies of the Hall effect on the KH instability (e.g. Huba, 1994). This study found that Hall MHD could lead to significantly more broadening of the boundary layer than in the ideal MHD case. The re-orientation of the magnetic field lines within the KH instability has also been observed before in studies of MRI in accretion disks (e.g. Wardle, 1999). A simpler model without rotation was used by Kunz (2008) and demonstrated how the combined actions of the shear instability and the Hall effect leads to further stretching of the magnetic field lines. This was shown to result in continued growth of the instability, which corresponds well to the dynamo action observed in our simulations with high Hall resistivity. However studies by both Kunz (2008) and Wardle (1999) are linear studies and, as such, do not extend to the nonlinear regime of the instability. A more recent numerical study by Nykyri & Otto (2004) demonstrates the twisting of magnetic field lines, but due to the inclusion of magnetic reconnection, doesn't produce the magnetic dynamo observed here.

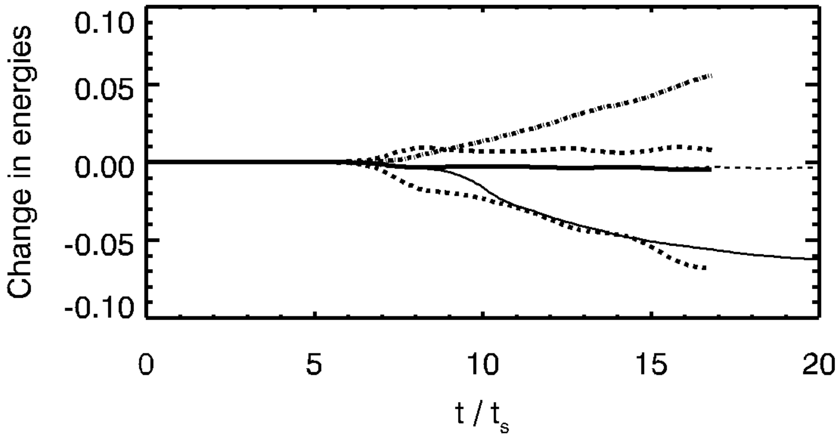

Figure 5.35: The change in total energy of the system is plotted against time in the cases of low resistivity (thin solid line) and high Hall resistivity (thick solid line). For comparison, the change in total energy of the hydrodynamic case is plotted (thin dashed line). Also plotted is the growth of the magnetic energy (thick dot-dashed line) as well as the growth and decay of the non-parallel and parallel kinetic energies respectively (thick dashed lines) in the case of high Hall resistivity. The Hall effect provides a means of continuous and efficient transfer of energy from the velocity field to the magnetic field, as can be seen by the constant total energy in the system.

Chapter 6

Multifluid MHD study of the KH Instability in Molecular Clouds

In this chapter we examine the changes to the evolution of the KH instability caused by the presence of the nonideal MHD effects that occur in molecular clouds. As the KH instability can occur at any velocity shear, there are numerous possible systems in a molecular cloud in which the instability could occur. One such application is the velocity shear between a jet-driven bowshock and its surrounding molecular cloud as discussed in section 1.4.2.

6.1 Motivation for studying KH instability in molecular clouds

The Kelvin-Helmholtz (KH) instability can occur anywhere that has a velocity shear. For this reason, it is a very common phenomenon. In astrophysical plasmas, the KH instability can provide the means of producing turbulence in a medium, or the mixing of material between two boundary layers.

The Kelvin-Helmholtz instability has been studied in a variety of astrophysical systems, from solar winds (Amerstorfer et al., 2007; Bettarini et al., 2006; Hasegawa et al., 2004) and pulsar winds (Bucciantini & Del Zanna, 2006) to thermal flares (Venter & Meintjes, 2006). Due to its ability to drive mixing and turbulence, the KH instability has been considered relevant in protoplanetary disks

(Johansen et al., 2006; Gómez & Ostriker, 2005), accretion disks and magnetospheres (Li & Narayan, 2004), and other jets and outflows (Baty & Keppens, 2006).

In each of these numerical studies, the approximation of ideal MHD has been made. However, this is not always a valid assumption. Weakly ionised plasmas, for example, contain a large fraction of neutral particles as well as a number of charged particle fluids, and so interactions between the various species can introduce non-ideal effects. Ambipolar dissipation and the Hall effect are two non-ideal effects that, as will be seen in this chapter, can greatly influence the development of the KH instability in a system by altering the dynamics of the plasma and the evolution of the magnetic field.

Two examples of weakly ionised systems include dense molecular clouds (e.g. Ciolek & Roberge, 2002) and accretion disks around young stellar objects (e.g. Wardle, 1999). In these systems, the relevant lengthscales are such that non-ideal effects can play a very important role (Wardle, 2004a; Downes & O'Sullivan, 2009).

The Kelvin-Helmholtz instability is of particular interest in molecular clouds. These clouds in which stars are born experience a significant self-gravitational force. The fact that the lifetimes of these clouds are longer than expected suggests that there exists enough turbulent energy within these clouds to support it from gravitational collapse. The exact source of this energy remains unknown (see Section 1.1.2). One possible source of this turbulent energy is the interaction of protostellar jets with the surrounding cloud, as first proposed by Norman & Silk (1980). The transfer of momentum from a jet to the cloud can be achieved in a number of ways (Dyson, 1984). As the supersonic protostellar jet propagates into the surrounding cloud, it forms a bow shock. The jet then interacts with the ambient medium through either "prompt" entrainment at the head of the bow shock (Padman et al., 1997), or through "steady-state" entrainment along the side of the jet (De Young, 1986).

As the the protostellar jet and enveloping bow shock propagate into the molecular cloud, there exists also a velocity shear between the entrained material within the edge of the bow shock, and the ambient medium outside. This swept-up material travels at a much slower velocity than the shocked material at the head of the bow shock, and thus the process of lateral entrainment may be applicable. During this process, the Kelvin-Helmholtz instability may occur along this edge of the bowshock, providing an additional means for supplying turbulent energy to the surrounding cloud.

The protostellar jet itself is hypersonic (Ray, 1988), but this study is restricted to the interaction between the transonic flow of the swept-up material along the edge of the bowshock and the ambient medium. It has been found that the Kelvin-Helmholtz instability plays a greater role in the transonic, rather than the supersonic, regime. Artola & Majda (1987) found that, in certain high Mach number regimes, the nonlinear instabilities that develop have a very different evolution from the nonlinear counterpart of the KH instability. Studies by Miura (1990, 1992) and Kobayashi et al. (2008) concluded that the supersonic regime is simply not conducive to vigorous growth of the KH instability. This was confirmed by Frank et al. (1996), who also found that while supersonic plasmas do experience the KH instability, its growth is generally much slower than the classical result.

The following study examines the KH instability under conditions in which nonideal effects are relevant. The changes in the evolution of the instability are examined as a result of introducing either Hall or ambipolar resistivity.

6.2 Computational Set-Up

This numerical study is carried out using the same computational parameters as the studies in the preceding two chapters, as described in section 4.1. This study aims to simulate the nonideal effects on the KH instability in the environment of a molecular cloud. In a jet-driven bowshock for example, both the swept-up material in the bowshock, as well the surrounding region, are understood to be made up of molecular cloud material. For this reason, the physical parameters observed in molecular clouds are applicable to this system.

6.2.1 Choosing the physical parameters

The molecular cloud material is modeled after the single-size grain model in Wardle & Ng (1999). The plasma is weakly ionised, and therefore consists primarily of a neutral particle fluid. The remainder of the plasma is made up of an electron fluid, a positively charged metal ion fluid, and a fluid of large, negatively charged dust grains. The average mass of the neutral particles is taken to be $m_{\rm n} = 2.33\, m_{\rm p}$, where $m_{\rm p}$ is the mass of a proton. This corresponds to a fluid of 90% molecular hydrogen and 10% atomic helium by number, which is representative of molecular clouds. The ion fluid represents an average of ions produced from a number of metal atoms, including Na, Mg, Al, Ca, Fe and Ni. These metals have sufficiently similar ionisation and recombination rates, and so can be modelled collectively as ions of a single positive charge $+e$ (Umebayashi & Nakano, 1990). The molecular ions, of which HCO^+ is the most numerous, are significantly less abundant than the metal ions, allowing us to neglect them. An average mass of $m_{\rm ion} = 24\, m_{\rm p}$ is assigned to the particles of the ion fluid, approximately equal to that of a magnesium ion. In the single-size grain model, the dust grains are characterised by a grain radius $a = 0.1\,\mu$m and a total grain mass that is 1% of the total neutral mass.

The simulations are parameterised by several properties that describe the overall system. The sound speed in the plasma is calculated from

$$c_{\rm s} \equiv \sqrt{\frac{\gamma k_{\rm B} T}{m_{\rm n}}},$$

where $k_{\rm B} = 1.38 \times 10^{-16}\,{\rm erg\,K^{-1}}$ is the Boltzmann constant, the adiabatic index γ is equal to unity for an isothermal system, and the constant temperature is taken to be $T = 30\,{\rm K}$, which is consistent with molecular clouds (Wardle & Ng, 1999). This results in a sound speed of $3.26 \times 10^4\,{\rm cm\,s^{-1}}$, or $c_{\rm s} = 0.326\,{\rm km\,s^{-1}}$.

The speed of the plasma in the simulations is determined by the requirement to have a transonic flow, as outlined in section 6.1. The sonic Mach number is set as:

$$M_{\rm s} = \frac{V_0}{c_{\rm s}} = 1,$$

so that the relative velocity between the bowshock and ambient medium is equal to the sound speed. In the reference frame of the instability, the velocity of the bulk fluid in the plasma can be given as $\pm\frac{V_0}{2} = \pm 0.188\,{\rm km\,s^{-1}}$.

The strength of magnetic fields in molecular clouds can vary greatly, but is generally observed as a few tens of microGauss (see section 1.1.2). The magnitude of the magnetic field in this study is chosen as $|B_0| = 22.8\,\mu$G so that the Alfvén velocity is:

$$v_{\mathrm{A}} = \sqrt{\frac{B_0^2}{4\pi\rho}} = 0.0326\,\mathrm{km\,s^{-1}}.$$

This gives an Alfvén Mach number of

$$M_{\mathrm{A}} = \frac{V_0}{v_{\mathrm{A}}} = 10,$$

so that the plasma is super-Alfvénic. It should be noted that there exists a wide range of fluid velocities and magnetic field strengths in molecular clouds, in which the average thermal and magnetic energies are approximately in equipartition. However, for this study, we have confined ourselves to regions of subsonic and super-Alfvénic flows as the KH instability in a sub-Alfvénic flow would be stabilised by the magnetic field (Chandrasekhar, 1961). This study is also applicable to regions of stronger magnetic fields that are not parallel to the plane of plasma flow. In this case it is only required that the strength of the magnetic field as projected onto the plane be equal to that specified above.

As noted in section 1.1.2, a typical number density of particles in a molecular cloud is $n \approx n_{\mathrm{n}} = 10^6\,\mathrm{cm^{-3}}$. The number density of the remaining fluids can then be derived from figure 2 in Umebayashi & Nakano (1990). The number density of the grain fluid is calculated to be $n_{\mathrm{dust}} \approx 1.85 \times 10^{-14}\,n_{\mathrm{n}}$. The number density of the ion and electron fluids, according to Umebayashi & Nakano (1990), are seen to be approximately $10^{-8} n_{\mathrm{n}}$. However, these parameters are for a molecular cloud with a magnetic field of magnitude 1 mG. In order to obtain similar conductivities as Wardle & Ng (1999) within the cloud but for a weaker magnetic field, the number density of the ion fluid is taken to be $n_{\mathrm{ion}} \approx 1.02 \times 10^{-11}\,n_{\mathrm{n}}$. The number density of the electron fluid is not set explicitly at this point, it is instead defined by the requirement that charge neutrality holds at all times. It will be seen that the number and mass density of the electron fluid is small, as expected.

The mass densities of the three dominant fluids can then be calculated. It is found, for the neutral fluid, that

$$\rho_{\mathrm{n}} \equiv m_{\mathrm{n}} n_{\mathrm{n}} = 3.89 \times 10^{-18}\,\mathrm{g\,cm^{-3}}.$$

For the ion fluid,

$$\rho_{\mathrm{ion}} \equiv m_{\mathrm{ion}} n_{\mathrm{ion}} = 4.08 \times 10^{-28}\,\mathrm{g\,cm^{-3}}.$$

The total mass of the dust grains in molecular clouds is taken to be equivalent to 1% of the total neutral mass (Wardle & Ng, 1999). This equates to $\rho_{\mathrm{dust}} = 0.01\,\rho_{\mathrm{n}} = 3.89 \times 10^{-20}\,\mathrm{g\,cm^{-3}}$. Equivalently, it can written that

$$m_{\mathrm{dust}} = 0.01 \frac{2.33 m_{\mathrm{p}}}{1.85 \times 10^{-14}} = 1.26 \times 10^{12}\, m_{\mathrm{p}}.$$

The charge-to-mass ratios for the three charged fluids can be calculated from their charges and masses, as given above, and converted into cgs units using $1\,\mathrm{C} \approx 3 \times 10^{9}$ statC. The charge-to-mass ratios are thus found to be

$$\alpha_{\mathrm{ion}} \equiv \frac{+1\,e}{m_{\mathrm{ion}}} = \frac{1.6 \times 10^{-19}\,\mathrm{C}}{24 m_{\mathrm{p}}} = 4.0 \times 10^{3}\,\mathrm{C\,g^{-1}} = 1.2 \times 10^{13}\,\mathrm{statC\,g^{-1}},$$

$$\alpha_{\mathrm{dust}} \equiv \frac{-1\,e}{m_{\mathrm{dust}}} = -7.6 \times 10^{-8}\,\mathrm{C\,g^{-1}} = -2.28 \times 10^{2}\,\mathrm{statC\,g^{-1}},$$

and

$$\alpha_{\mathrm{e}} \equiv \frac{-1\,e}{m_{\mathrm{e}}} = -1.76 \times 10^{8}\,\mathrm{C\,g^{-1}} = -5.27 \times 10^{17}\,\mathrm{statC\,g^{-1}}.$$

From these values, the necessary mass density for the electron fluid can be calculated from

$$\alpha_{\mathrm{ion}} \rho_{\mathrm{ion}} + \alpha_{\mathrm{dust}} \rho_{\mathrm{dust}} + \alpha_{\mathrm{e}} \rho_{\mathrm{e}} = 0$$

to give $\rho_{\mathrm{e}} = 9.25 \times 10^{-33}\,\mathrm{g\,cm^{-3}}$. This is much smaller than the mass density of the other three fluids, as expected.

The multifluid effects are implemented in the system through collisions between the various fluids. As detailed in section 1.3.2, only collisions between the neutral fluid and each charged fluid are included. Rate coefficients for momentum transfer for each fluid interaction are given in Wardle & Ng (1999). For collisions between the neutral and dust grain fluids, the collision rate is

$$K_{\mathrm{dust,n}} \equiv \frac{< \sigma v >_{\mathrm{dust}}}{m_{\mathrm{dust}} + m_{\mathrm{n}}},$$

where

$$< \sigma v >_{\rm dust} = \pi a^2 \left(\frac{128kT}{9\pi m_{\rm n}} \right)^{1/2} = 2.18 \times 10^{-5}\,{\rm cm^3 s^{-1}}.$$

The collision rate can then be calculated as

$$K_{\rm dust,n} \equiv \frac{< \sigma v >_{\rm dust}}{m_{\rm dust} + m_{\rm n}} = \frac{2.18 \times 10^{-5}\,{\rm cm^3 s^{-1}}}{1.26 \times 10^{12} m_{\rm p} + 2.33 m_{\rm p}} = 1.0 \times 10^7\,{\rm cm^3 g^{-1} s^{-1}}.$$

Similarly, for the ion and electron fluids, it can be found that

$$K_{\rm ion,n} \equiv \frac{< \sigma v >_{\rm ion}}{m_{\rm ion} + m_{\rm n}} = \frac{1.6 \times 10^{-19}\,{\rm cm^3 s^{-1}}}{24 m_{\rm p} + 2.33 m_{\rm p}} = 3.64 \times 10^{13}\,{\rm cm^3 g^{-1} s^{-1}}$$

and finally, following Wardle & Ng (1999),

$$K_{\rm e,n} \equiv \frac{< \sigma v >_{\rm e}}{m_{\rm e} + m_{\rm n}} = \frac{1 \times 10^{-15} cm^2 \left(\frac{128kT}{9\pi m_{\rm e}} \right)^{1/2}}{m_{\rm e} + 2.33 m_{\rm p}} = 1.16 \times 10^{15}\,{\rm cm^3 g^{-1} s^{-1}}.$$

Having determined the primary parameters of the fluids, the secondary parameters can be calculated. The Hall parameter, $\beta_i = \frac{\alpha_i (\frac{B}{c})}{K_{i,{\rm n}} \rho_{\rm n}}$, is derived in section 1.3.2 and is a measure of how well-tied a particle is to the magnetic field. Using the quantities above, the Hall parameters for each fluid can be calculated.

$$\beta_{\rm ion} = \frac{(1.2 \times 10^{13})(\frac{2.28 \times 10^{-5}}{3 \times 10^8})}{(3.64 \times 10^{13})(3.89 \times 10^{-18})} = 6.43 \times 10^1$$

$$\beta_{\rm dust} = \frac{(-2.28 \times 10^2)(\frac{2.28 \times 10^{-5}}{3 \times 10^8})}{(1.0 \times 10^7)(3.89 \times 10^{-18})} = -4.3 \times 10^{-3}$$

$$\beta_{\rm e} = \frac{(-5.27 \times 10^{17})(\frac{2.28 \times 10^{-5}}{3 \times 10^8})}{(1.16 \times 10^{15})(3.89 \times 10^{-18})} = -8.92 \times 10^4$$

The final calculations are to solve for the conductivities. From the expressions derived in section 1.3.2, the Ohmic, Hall and ambipolar resistivities can be calculated as:

$$\sigma_O \equiv \frac{1}{B} \sum_{i={\rm ion,dust,e}} \alpha_i \rho_i \beta_i = 413.6\,{\rm s^{-1}}$$

$$\sigma_H \equiv \frac{1}{B} \sum_{i=\mathrm{ion,dust,e}} \frac{\alpha_i \rho_i}{1+\beta_i^2} = 0.01\,\mathrm{s}^{-1}$$

$$\sigma_A \equiv \frac{1}{B} \sum_{i=\mathrm{ion,dust,e}} \frac{\alpha_i \rho_i \beta_i}{1+\beta_i^2} = 0.1\,\mathrm{s}^{-1}.$$

It can be seen that these values are equal to those calculated by Wardle & Ng (1999) for a weakly ionised molecular cloud.

It should be noted that this system consists of three charged fluids, while the earlier study on nonideal effects in the evolution of the KH instability had only two. In the previous study, the ion fluid was responsible for both the ambipolar and the Hall conductivity. As a result of having three charged fluids in this study, the ion fluid is now responsible only for the ambipolar conductivity, while the dust grain fluid provides the largest contribution to the Hall conductivity. This is the only difference, and the sole result is that the Hall conductivity is now of negative value, as the dust grains are negatively charged. This has the consequence that the bending experienced by the magnetic field as a result of the Hall effect is now in the opposite z-direction to before.

6.2.2 Transformation into dimensionless units

The physical parameters determined above are transformed into dimensionless units before being inputted into the numerical code. For this purpose, practical characteristic length, time and mass scales must be determined.

The lengthscale of the system is first chosen. The protostellar jet is understood to be approximately a parsec or two in length (Ray, 1987). It is chosen to focus on a fraction of this length, opting to simulate a region along the edge of the bowshock of length 0.2 pc. It has also been found that nonideal effects play an important role at this lengthscale (Downes & O'Sullivan, 2009). The lengthscale is thus set to

$$[L] = 0.2\,\mathrm{pc} = 6.17 \times 10^{17}\,\mathrm{cm}.$$

The timescale is chosen such that the sound speed is of order unity,

$$c_\mathrm{s} = 1.$$

The sound speed has been calculated as $c_\mathrm{s} = 3.26 \times 10^4\,\mathrm{cm\,s^{-1}}$. This implies a time scale

$$[T] = 1.9 \times 10^{13}\,\mathrm{s}.$$

Using these units, the velocity of the plasma flow is now

$$\mathbf{v} = \pm\frac{V_0}{2}\hat{y} = \pm\frac{1}{2}\hat{y}.$$

Finally, a mass scale is chosen. This is set so that the mass density of the plasma is of order unity,

$$\rho_0 = 1.$$

The mass density has been calculated as $\rho_\mathrm{n} = 3.89 \times 10^{-18}\,\mathrm{g\,cm^{-3}}$. Using the length scale chosen above, this gives a characteristic mass scale

$$[M] = 9.15 \times 10^{35}\,\mathrm{g}.$$

The magnitude of the magnetic field, $B_0 = 22.8\,\mu\mathrm{G}$, can also be transformed into a dimensionless quantity, by

$$|\mathbf{B}| = \frac{B_0}{\sqrt{4\pi}} \times \frac{[T][L]^{1/2}}{[M]^{1/2}} = 0.1$$

From this calculation onwards, the units of $\mathbf{B}$, $\mathbf{E}$ and $\mathbf{J}$ are written such that the factors of 4π and the speed of light no longer appear.

It is possible now to transform the conductivities, and the resulting resistivities, into dimensionless units. The following values are found:

$$\begin{aligned} r_O &= \frac{1}{\sigma_O} = 6.2 \times 10^{-9} \\ r_H &= \frac{\sigma_H}{\sigma_H^2 + \sigma_A^2} = -0.00352 \\ r_A &= \frac{\sigma_A}{\sigma_H^2 + \sigma_A^2} = 0.0352 \end{aligned}$$

These can be seen to lie within the range studied in the earlier multifluid study. The amount of ambipolar resistivity is equivalent to the earlier simulation with highest ambipolar resistivity and a magnetic Reynolds number $Re_{\mathrm{m}} = 28.4$, while the amount of Hall resistivity is equivalent to the simulation with moderate Hall resistivity and a magnetic Reynolds number $Re_{\mathrm{m}} = 284$.

6.3 Results for multifluid MHD system

In order to observe the differences in the evolution of the KH instability with the inclusion of nonideal effects, various parameters are measured and compared to those from simulations carried out in ideal MHD.

In the case of ideal MHD, the Kelvin-Helmholtz instability causes a wind-up of the plasma at the interface between the two layers, resulting in the "Kelvin's cat's eye" vortex. This can be seen in figure 6.1. Comparison of this plot with figure 4.12 from the low resistivity case in chapter 4 reveals that there are no discernible differences between these two systems, as expected. When nonideal effects are included in the system however, the effect of this instability on the dynamics of the system can be altered significantly.

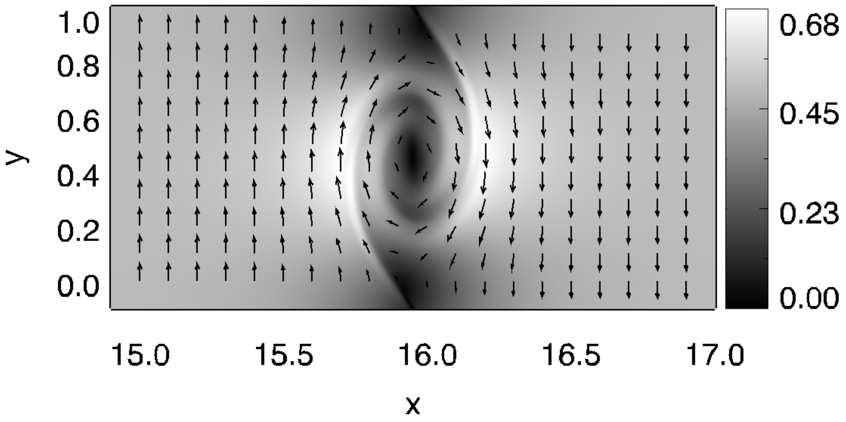

Figure 6.1: Plot of the magnitude and vector field of the bulk velocity field for the ideal MHD case, at time = $8\,t_s$.

As ambipolar and Hall resistivities are introduced to the system, one effect expected to be noticeable, as learned from the earlier multifluid study, is the influence that nonideal effects have on the magnetic field. On one hand, magnetic reconnection between opposing field lines is expected to occur, while the Hall effect is expected to have a noticeable impact by re-orienting the field. Figure 6.2 shows the evolution of the perturbed magnetic energy with time, for cases of ideal MHD and nonideal MHD, as found in a molecular cloud.

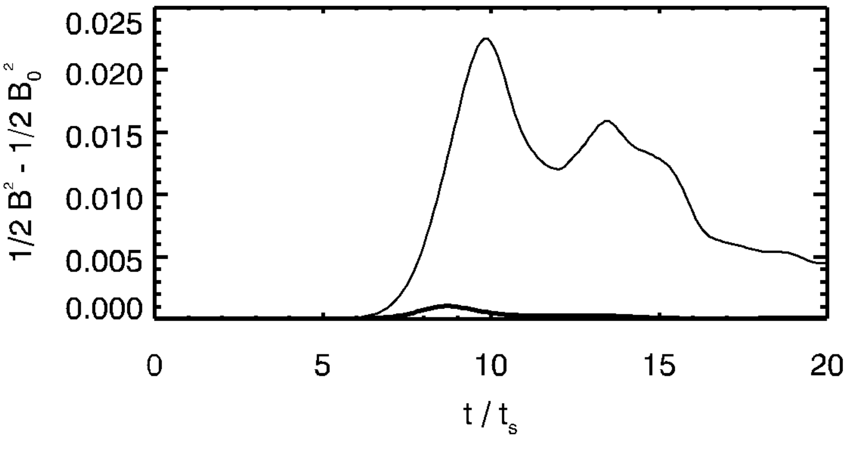

Figure 6.2: The perturbed magnetic energy in the system is plotted against time in the ideal MHD case (thin line) and nonideal MHD case (thick line). The introduction of nonideal effects significantly dampens the amplification of the magnetic energy.

As expected, the magnetic energy does not undergo as strong an amplification as in the ideal case. This is due to magnetic reconnection, introduced into the system by the ambipolar resistivity which in turn breaks down the frozen-in approximation.

The effect reconnection has on the geometry of the magnetic field can be seen in figure 6.4. This can be compared to the ideal MHD case, as shown in figure 6.3.

Thus the effect of magnetic reconnection, as caused by the ambipolar resistivity, can clearly be seen. The influence on the magnetic field by the Hall effect is next examined. With moderate Hall resistivity, a small but significant re-orientation of the magnetic field is expected, from the xy-plane into the z-direction. Plotting the evolution of the magnetic energies in each of three directions however, shows that there is, in fact, no significant growth in the z-direction (see figure 6.5).

This can be compared to figure 5.5 from the earlier study of moderate Hall resistivity, in which significant growth of the magnetic energy in the z-direction was observed. The inclusion of ambipolar resistivity has clearly minimised the

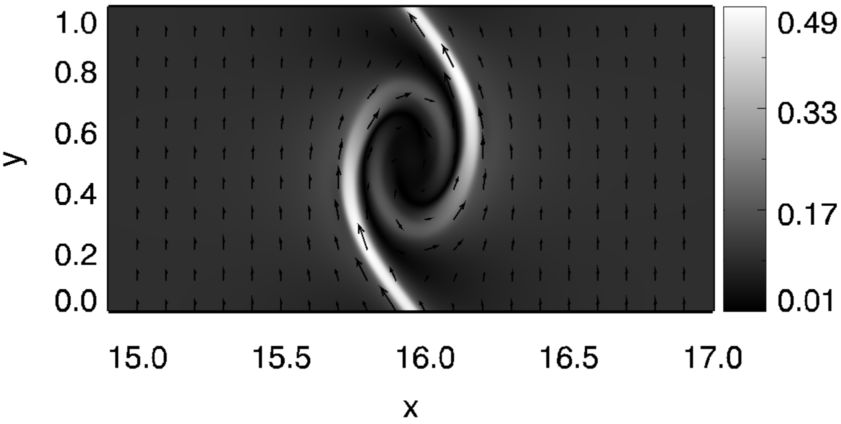

Figure 6.3: Plot of the magnitude and vector field of the magnetic field for the ideal MHD case, at time = $8\,t_\mathrm{s}$. The magnetic field can be seen to have undergone a similar wind-up to that of the velocity field.

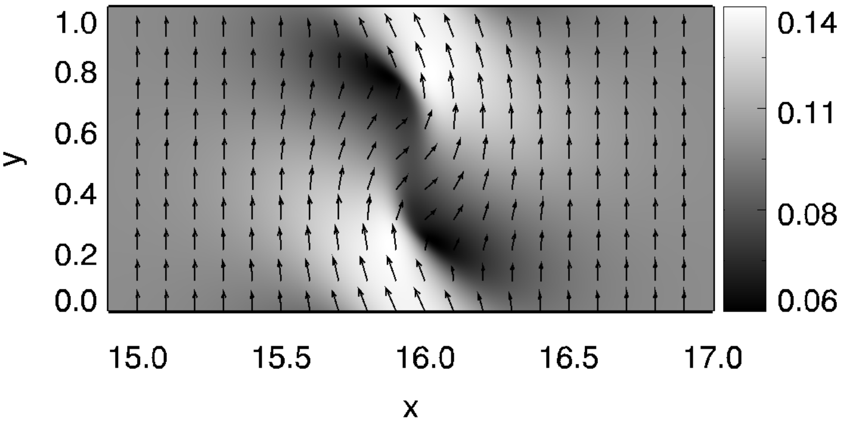

Figure 6.4: Plot of the magnitude and vector field of the magnetic field for the nonideal MHD case, at time = $8\,t_\mathrm{s}$. The magnetic field does no longer demonstrates a similar wind-up to that seen in the ideal MHD case, as a result of magnetic reconnection and decoupling.

impact of the Hall effect. In order to understand how, the behaviour of each of the four fluids in the system must be examined.

Figures 6.6 to 6.9 show the mass densities and velocity vector fields of each fluid at the time of the peak on the instability. It can be seen that the mass density of dust grain fluid closely reflects that of the bulk fluid, signifying a strong

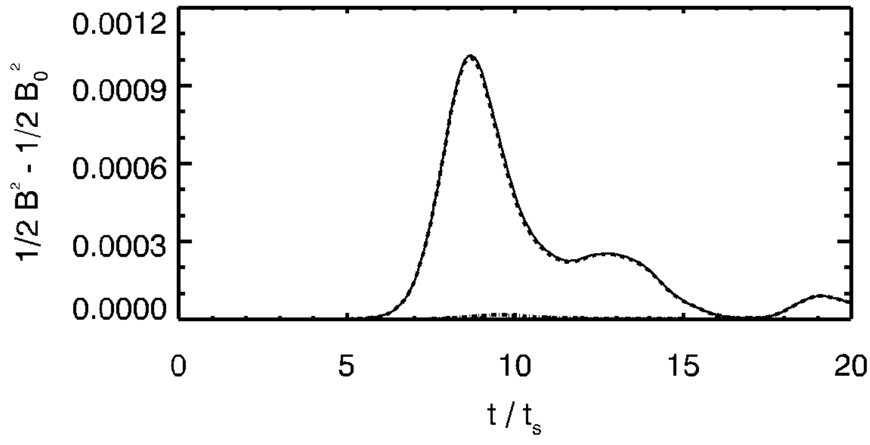

Figure 6.5: The total perturbed magnetic energy (solid line) in the system is plotted against time in the nonideal MHD case. This is almost identical to the magnetic energy in the xy-plane (dashed line), while there is very little growth in the magnetic energy in the z-direction (dot-dashed line).

coupling between the two. On the other hand, the ion and electron fluids closely reflect the configuration of the magnetic field, implying that they are still strongly coupled to the magnetic field lines, as expected by their high Hall parameter. Conversely, the fact that the dust grains are not well-tied to the magnetic field is to be expected by their very low Hall parameter. This decoupling of the dust grain fluid from the magnetic field is the source of the Hall resistivity in the system, in the same way that the decoupling of the ion fluid caused Hall resistivity in the multifluid study carried out earlier. The decoupling of the ion fluid from the neutral fluid, on the other hand, is the source of the ambipolar diffusion in the system, as was also seen earlier.

It is important to recall that the strength of the Hall effect depends on the current in the system. The current, in turn, depends on the charge densities of the three charged fluids. The charge density of the dust grain fluid, $\alpha_{\rm dust}\rho_{\rm dust} \approx -8 \times 10^{-18}\,{\rm statC\,cm^{-3}}$. However, for ion and electron fluids, the charge densities are much higher, approximately $\pm 5 \times 10^{-15}\,{\rm statC\,cm^{-3}}$. Therefore the current in the system, $\mathbf{J} = \sum_i \alpha_i \rho_i \mathbf{v}_i$, is primarily due to the velocity difference between

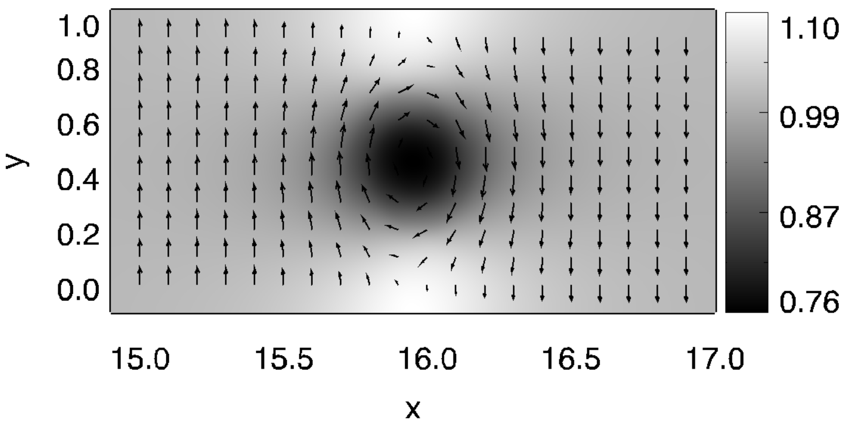

Figure 6.6: Plot of the magnitude of the mass density, as well as the velocity vector field, of the bulk fluid in the nonideal case at time $= 8\,t_\mathrm{s}$.

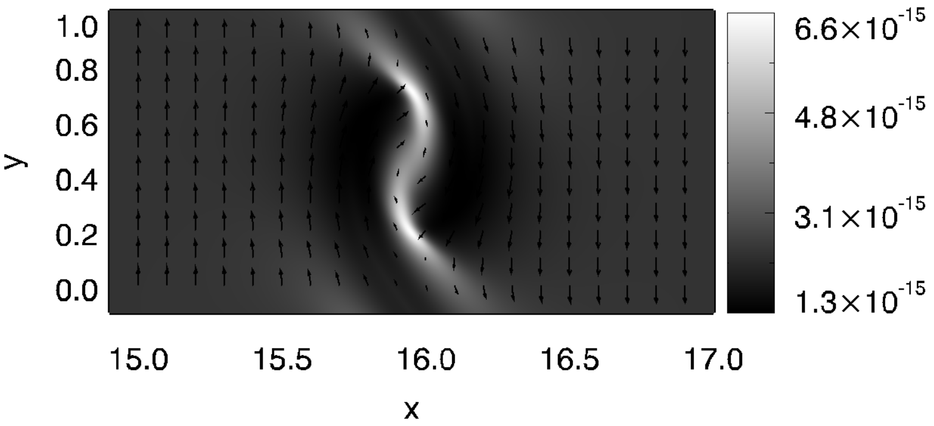

Figure 6.7: Plot of the magnitude of the mass density, as well as the velocity vector field, of the electron fluid in the nonideal case at time $= 8\,t_\mathrm{s}$.

the ion and electron fluids.

Therefore, while the decoupling of dust grain fluid from the magnetic field provides a high Hall conductivity, the strength of the Hall effect is in fact dependent more on the dynamics of the ion fluid relative to the electron fluid. As the ion fluid is decoupled from the neutral fluid in order to introduce ambipolar resistivity into the system, and instead strongly tied to the magnetic field, the relative

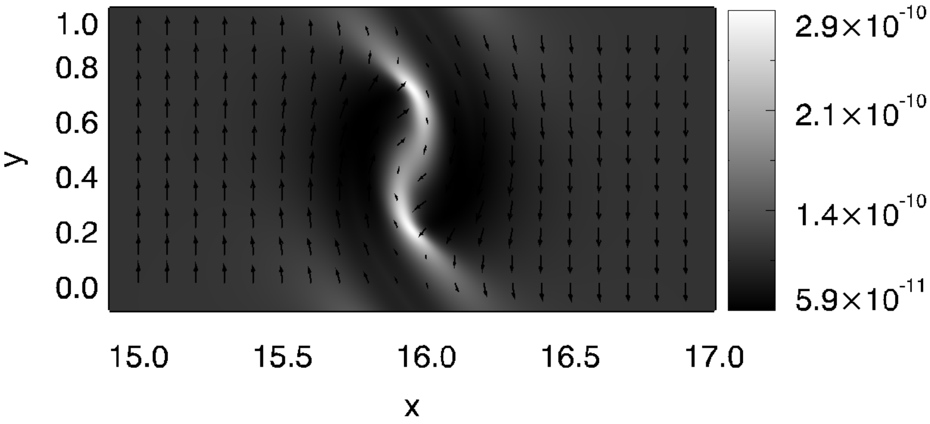

Figure 6.8: Plot of the magnitude of the mass density, as well as the velocity vector field, of the ion fluid in the nonideal case at time $= 8\,t_{\rm s}$.

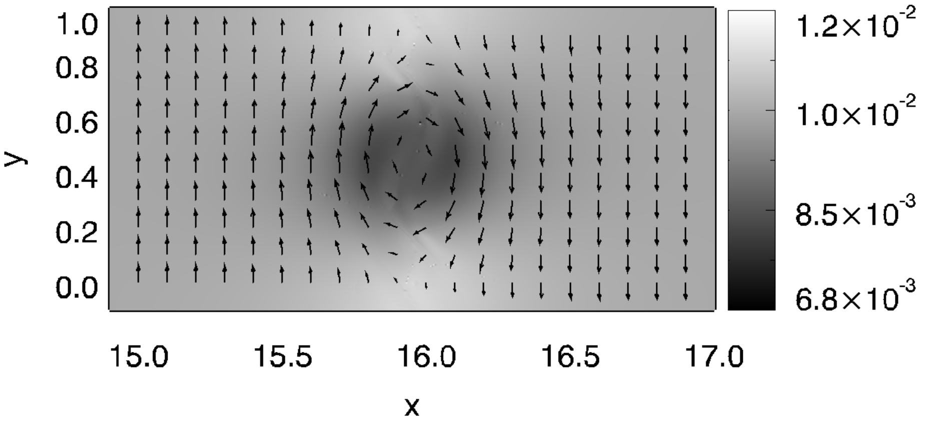

Figure 6.9: Plot of the magnitude of the mass density, as well as the velocity vector field, of the dust grain fluid in the nonideal case at time $= 8\,t_{\rm s}$.

velocity between the ion and electron fluid is minimised. As a result, the majority of current in the system remains parallel to the magnetic field, and the strength of the Hall effect, which is proportional to $\mathbf{J} \times \mathbf{B}$, is very small. This accounts for the growth of the magnetic field in the z-direction being much smaller than expected. Put simply, the introduction of ambipolar resistivity changes which fluids are coupled to which, and in doing so, effectively eliminates the Hall effect.

It can be seen that this occurs in a system with only two charged fluids as well. In this case, it is the ion fluid that is the larger contributor to both the Hall and ambipolar conductivity. By being decoupled from the magnetic field, the ion fluid causes Hall resistivity, as a potential velocity difference between the ion and electron fluid would give rise to a current with a component not parallel to the magnetic field. However, the ambipolar resistivity arises due to a low collision rate between the ion fluid and the neutral fluid. As a result, the ions do not in fact behave in the same way as the neutrals, and the weak coupling with the magnetic field is sufficient to ensure only a minimal relative velocity between the ions and electrons. In this way, the impact of the Hall effect is similarly minimised.

The effect of being coupled to either the neutral fluid or the magnetic field can finally also be seen in the growth of the transverse kinetic energy for each charged fluid. It has been seen that, in the nonideal case, the magnetic field undergoes significantly less wind-up than in the ideal MHD case. This results in a much smaller growth of the perturbed magnetic energy in the system. On the other hand, through decoupling from the magnetic field, it is expected that the bulk fluid will experience even more wind-up during the growth of the KH instability. This indeed occurs, and figure 6.10 demonstrates this through a stronger growth of the transverse kinetic energy in the system. Similar to the earlier multifluid study, it can be seen that the weaker magnetic field and stronger decoupling allows the bulk flow to experience a wind-up almost as strong as the non-magnetised hydrodynamic case.

For each of the charged fluids, examination of plots of their transverse kinetic energy (figures 6.11 to 6.13) can confirm whether they are more coupled to the magnetic field or the bulk flow. Also plotted for comparison on these graphs are the growths observed in the ideal MHD case and in the hydrodynamic case.

It has been seen that, as the magnetic field experiences reconnection and the magnetic energy undergoes only a small amplification, the growth of the transverse kinetic energy is increased. However, as in the earlier multifluid study, it is not simply a matter of the energy being transferred elsewhere. Instead, under the isothermal assumption, reconnection results in an instantaneous loss of total energy. This can again be seen in figure 6.14. Here the growth of the magnetic energy and non-parallel kinetic energies, as well as the decay of the parallel kinetic

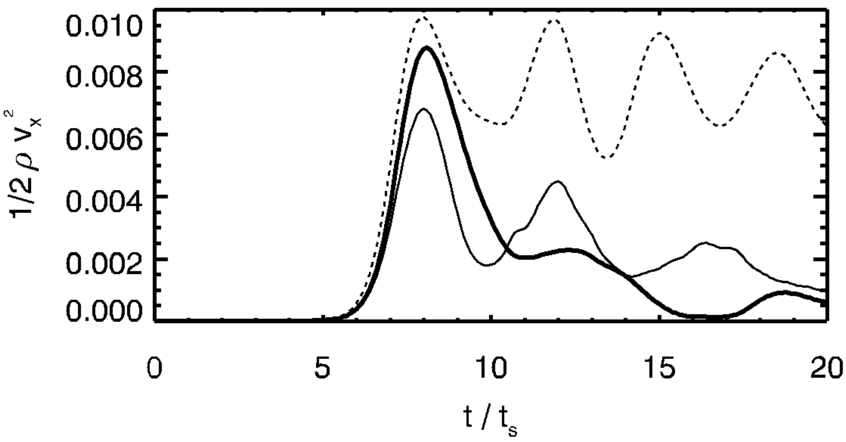

Figure 6.10: The transverse kinetic energy in the system is plotted against time for the ideal MHD (thin line) and nonideal MHD (thick line) cases. Also plotted is the evolution of the transverse kinetic energy in the hydrodynamic case (dashed line). It can be seen that the nonideal system experiences a stronger initial wind-up than in the ideal MHD case.

energy, can be seen for the ideal and nonideal MHD cases. While the non-parallel kinetic energies grow to a higher maximum for the nonideal case, this does not make up for the loss of magnetic energy. By comparing the time evolution of the total energies in the two systems, it can clearly be seen that the nonideal case suffers a greater loss of total energy during this initial growth of the instability.

When examining the non-parallel kinetic energies, both the transverse kinetic energy and the kinetic energy in the z-direction are included. As the Hall effect introduces dynamics in this third dimension, it is expected to see some growth of the kinetic energy in this direction. However, as has been seen in the case of the magnetic field, the inclusion of ambipolar resistivity greatly limits the impact that the Hall effect has on the system. With strong ambipolar resistivity, the ion and electron fluids are closely linked, and there is very little current produced that is not parallel to the magnetic field. This causes the Hall effect, which is proportional to $\mathbf{J} \times \mathbf{B}$ to have little impact. Thus the magnetic field experiences only a small re-orientation into the z-direction, and only the fluids that are tightly coupled to

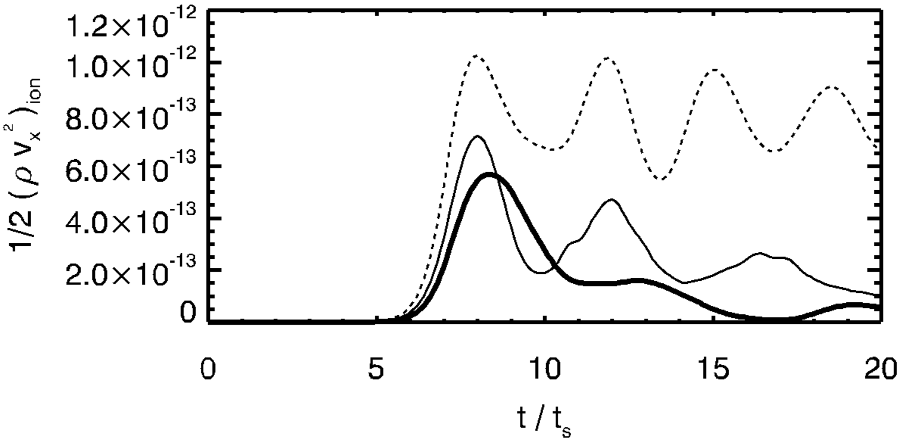

Figure 6.11: The transverse kinetic energy of the ion fluid is plotted against time for the ideal MHD (thin line) and nonideal MHD (thick line) cases. Also plotted is the evolution of the ion fluid's transverse kinetic energy in the hydrodynamic case (dashed line).

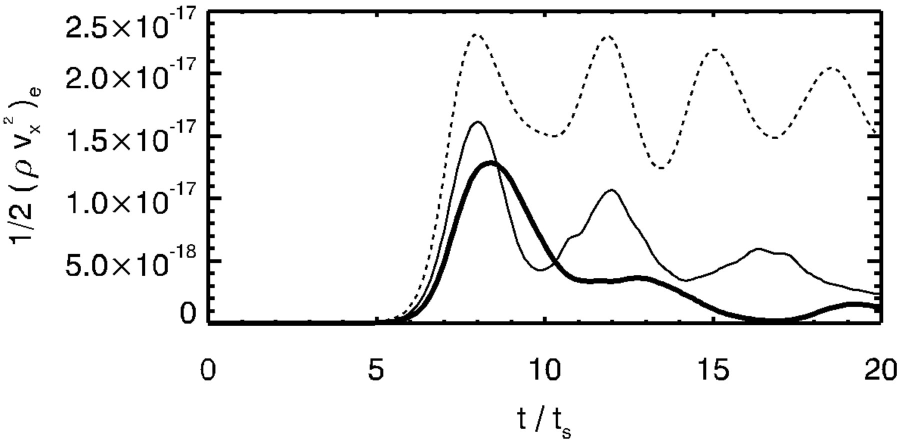

Figure 6.12: The transverse kinetic energy of the electron fluid is plotted against time for the ideal MHD (thin line) and nonideal MHD (thick line) cases. Also plotted is the evolution of the electron fluid's transverse kinetic energy in the hydrodynamic case (dashed line).

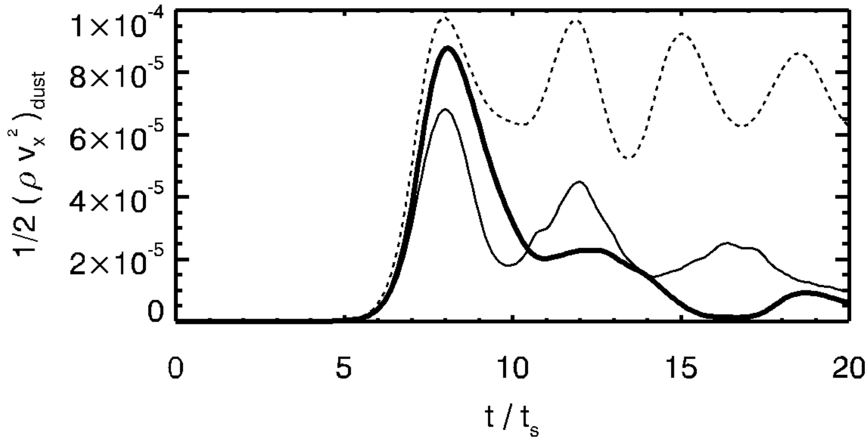

Figure 6.13: The transverse kinetic energy of the dust grain fluid is plotted against time for the ideal MHD (thin line) and nonideal MHD (thick line) cases. Also plotted is the evolution of the dust grain fluid's transverse kinetic energy in the hydrodynamic case (dashed line).

the magnetic field will experience any noticeable dynamics in this direction.

Figure 6.15 plots the growth of the non-parallel kinetic energies in the system, that is, those in the x- and z-direction. It can be seen that the growth of kinetic energy in the z-direction is negligible, and thus that no significant bulk flow has been produced in this direction. However, the charged fluids that are tightly coupled to the magnetic field do experience a non-negligible, if small, velocity in the z-direction. This is demonstrated in figure 6.16, a plot of the comparative growth of the kinetic energy of the ion fluid in the x- and z-directions.

Other than this small growth of magnetic energy and charged fluid flow in the z-direction, there is little other difference between this set-up and the pure ambipolar system that was studied earlier. As a result, many of the results given here have been detailed in the earlier multifluid study of chapter 4.

One such result is the ability of the neutral fluid to decouple from the magnetic field, allowing the bulk flow to experience a greater wind-up. This result of the decoupling can be observed by examining the vortex created by the instability. Figure 6.17 plots the transverse velocities for the ideal and nonideal MHD

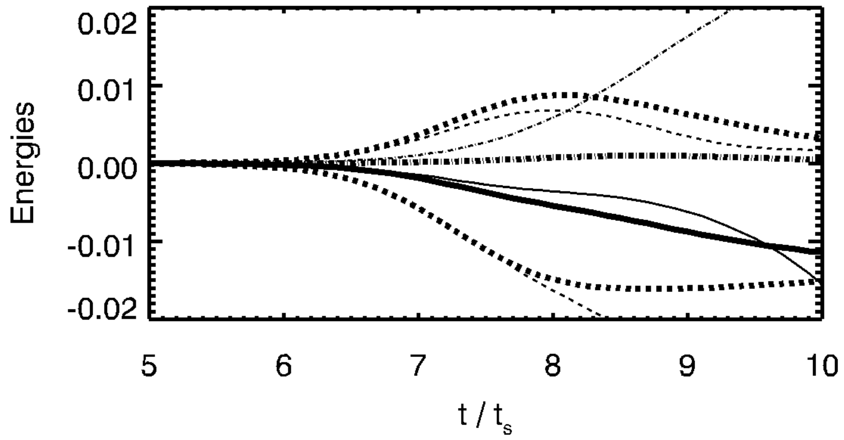

Figure 6.14: The respective positive and negative growths of the transverse and parallel kinetic energies (dashed lines) are plotted against time, as is the growth of the perturbed magnetic energy (dot-dashed lines). The sum of these gives the change in the total energy in the system, which is also plotted (solid lines). These are plotted for the both the ideal case (thin lines) and nonideal MHD case (thick lines). It can be seen that the increase in growth of the transverse kinetic energy in the nonideal case does not make up for the loss in magnetic energy. This indicates that magnetic reconnection results in a further loss of total energy, as shown.

cases, in the upper and lower panels respectively, as a cross-section through the centre of the KH vortex along x. Also plotted is the strength of the magnetic field in the y-direction for the same region in each case. In the ideal case, the distinct neighbouring peaks and troughs in the magnetic field strength represent regions of strong positive magnetic field beside regions of strong negative magnetic field. This represents the area in the KH vortex in which the magnetic field lines have been wound up and compressed, so that magnetic field lines in the positive y-direction have been compressed side-by-side with magnetic field lines in the negative y-direction. It can clearly be seen that for each peak and trough in the magnetic field, i.e. in each region of strong positive or negative magnetic field, there exists an individual corresponding peak in the transverse velocity. This is caused by the bulk fluid being tied to the magnetic field lines, in either the positive or negative y-directions, and being unable to merge with the fluid tied to the

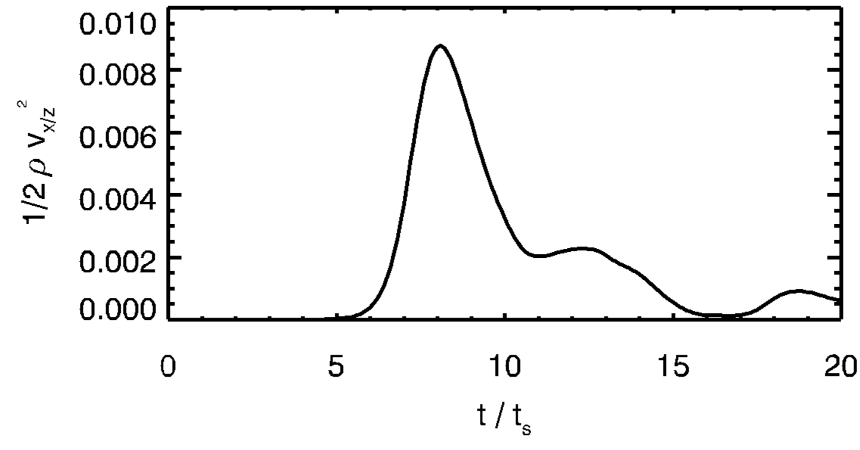

Figure 6.15: The growth of the kinetic energy in the system is plotted against time in both the x-direction (solid line) and z-direction (dashed line, indistinguishable from the x-axis). The growth in the z-direction is clearly negligible.

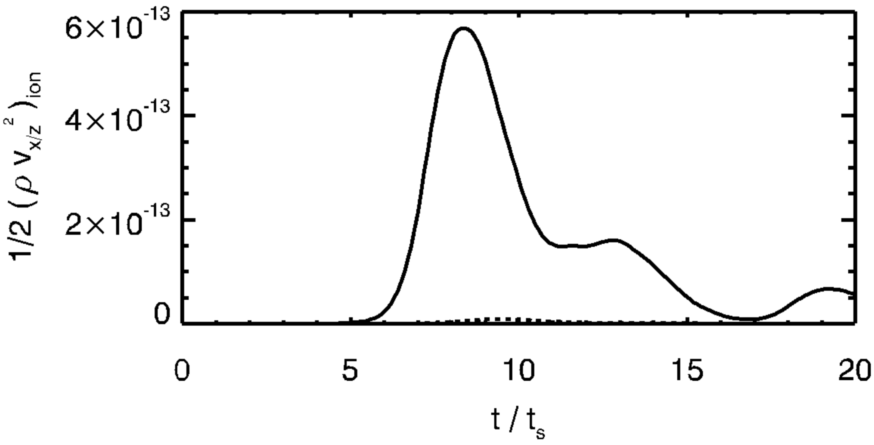

Figure 6.16: The growth of the kinetic energy of the ion fluid is plotted against time in both the x-direction (solid line) and z-direction (dashed line). The growth in the z-direction is very small, but non-negligible.

magnetic field lines of the opposite direction. In the nonideal case however, this phenomenon is not observed. In this case, the decoupling of the magnetic field from the bulk fluid leads to magnetic reconnection between the magnetic field lines of opposing directions. There are no strong peaks observed therefore in the magnetic field strength, and the regions of high transverse velocity are able to merge into single, wider peaks.

Another consequence of this is that when the magnetic field lines prevent the bulk fluid from crossing them, more structure is enforced on the velocity field. For the nonideal case on the other hand, the velocities experience a more gradual change across the vortex. This results in a more "blurry" velocity field in the nonideal case, than in the "well-defined" velocity field of the ideal case. This can be observed by comparison of the velocity fields for the two cases (see figure 6.18). Close examination reveals that within the KH vortex, there is in fact more well-defined structure in the ideal MHD case.

Finally, the growth rates of the different systems are examined. In figure 6.19, the log of the transverse kinetic energy is plotted for the ideal and nonideal MHD cases.

It can be seen that the linear growth of the instability differs very little with the inclusion of nonideal effects. Despite the addition of decoupling from the magnetic field, and a greatly reduced amplification in the magnetic energy, the growth rates are found to be within 1% of each other. This confirms that the only parameter varied in these simulations that affect the linear growth rate is the initial value of the magnetic field strength.

It has been seen that the growth of the KH instability differs as nonideal effects are included in the system. The subsequent behaviour of the fluid is next examined, and is also seen to develop differently in the nonideal case. In the ideal case, the initial wind-up of the velocity field has the effect of also winding up the magnetic field, due to strong coupling between the two. As the KH vortex is caused to stretch and expand by the amplified magnetic field, it reaches the periodic y-boundaries. As the neighbouring vortices merge, numerical viscosity allows for magnetic reconnection, which results in the creation of magnetic islands and secondary vortices. The generation and decay of these vortices results in further periods of growth in the transverse kinetic energy in the system

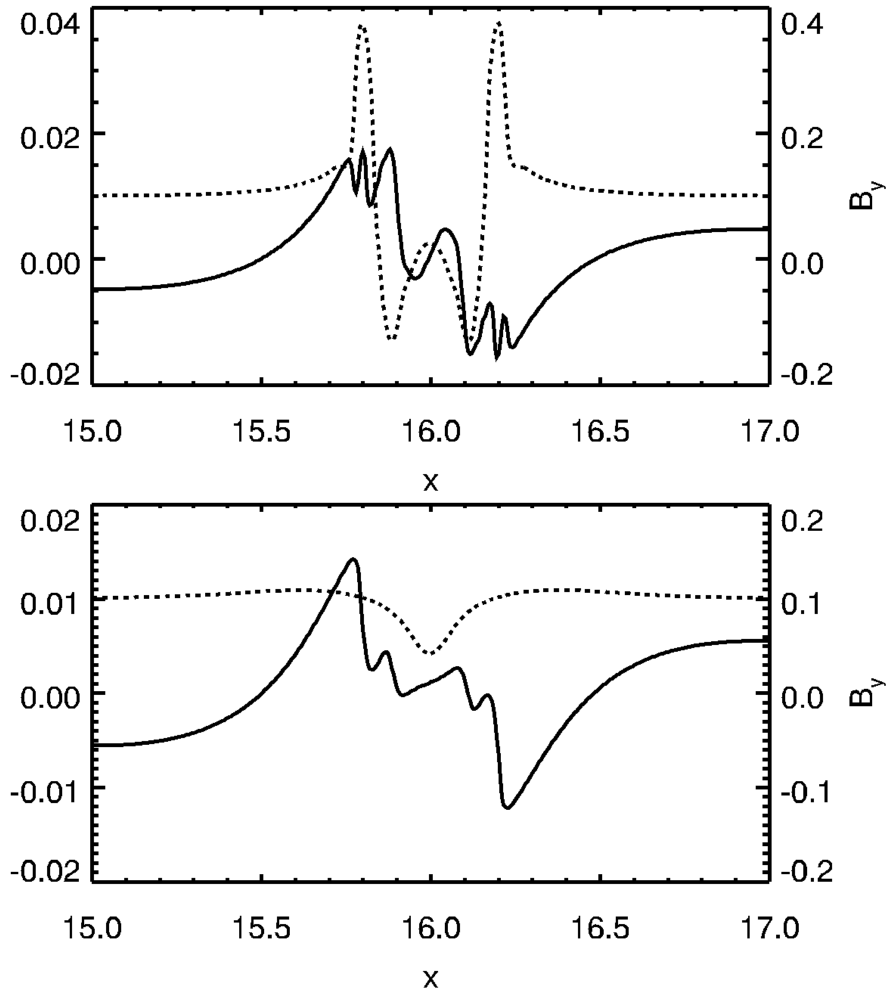

Figure 6.17: Plot of the bulk velocity in the x-direction (solid line) and the strength of the magnetic field in the y-direction (dashed line), for the cases of ideal MHD (upper panel) and high nonideal MHD (lower panel) at time $t = 8\,t_s$. The area plotted is a cross-section of the vortex through its centre along x.

corresponding to periods of decreasing magnetic energy and vice-versa. This is clearly demonstrated in figure 6.20, where the peaks in each energy are seen to correspond to the troughs in the other. This behaviour continues in the ideal MHD system until the system has reached a somewhat disordered state (see figure 6.21).

In the nonideal case, on the other hand, the subsequent evolution of the KH

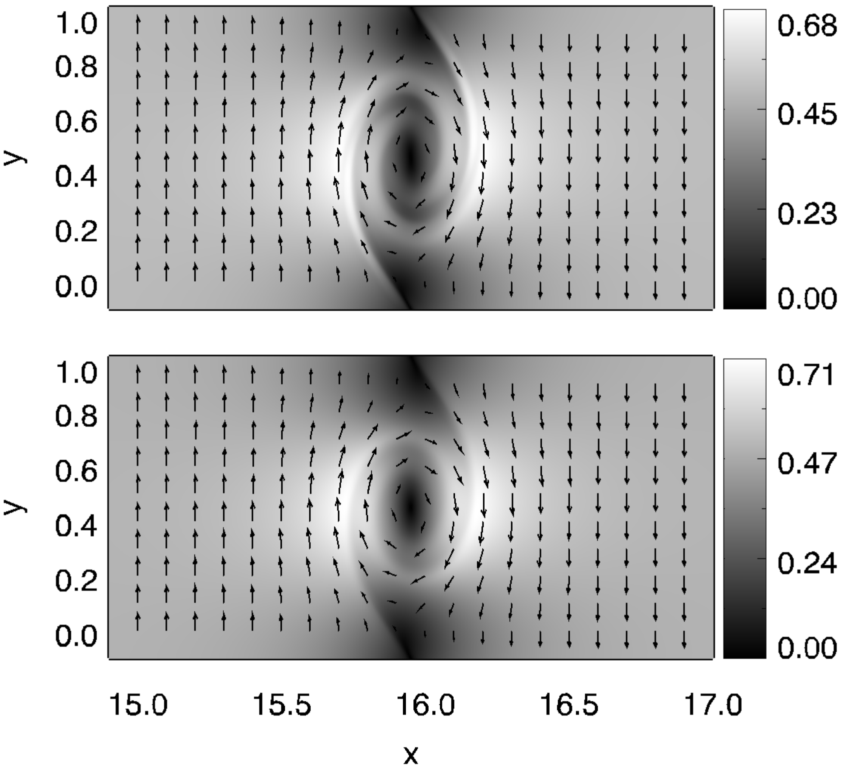

Figure 6.18: Plot of the magnitude and vector field of the bulk velocity field at time $t = 8\,t_{\mathrm{s}}$ for the ideal case (upper panel) and nonideal case (lower panel). Upon close examination, it can be seen that the velocity field contains more well-defined structure in the case of ideal MHD than in the case of nonideal MHD.

instability is quite different. The high ambipolar resistivity causes the magnetic field to experience very little wind-up, through decoupling and reconnection. As a result, the KH vortex undergoes no stretching or expansion as a result of the magnetic field. Following the saturation of the instability, the magnetic field is seen simply to steadily return to its original configuration, and neither the velocity field nor the magnetic field undergo a second period of growth (see figure 6.22). Instead, the magnetic field eventually stabilises the velocity field, and the plasma returns almost to its original state, with simple laminar flow on either side of a shear layer (see figure 6.23). In this case, however, the shear layer is much wider, and no longer conducive to the growth of the Kelvin-Helmholtz instability.

As the vortex is broken down and the system returns to a stable state, the

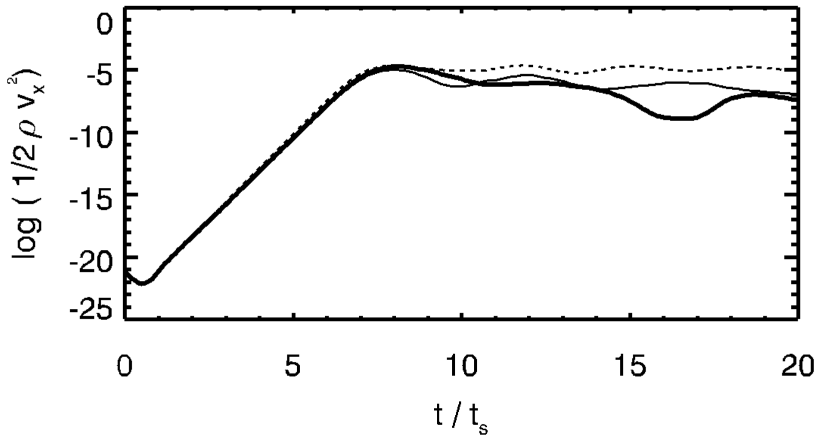

Figure 6.19: The log of the transverse kinetic energy in the system is plotted against time for the ideal MHD (thin line) and nonideal MHD (thick line) cases. The dashed line represents the hydrodynamic case. There is very little difference between the linear growths for the ideal and nonideal cases.

energy consumed by the instability flattens out. The system has lost some energy during the initial growth of the instability, but this levels off at later times. This is a deviation from the ideal MHD case, in which the system continues to lose energy as the KH vortex is broken down into disordered decay. Figure 6.24 plots the total energies of the ideal and MHD cases, as well as the hydrodynamic case. In the hydrodynamic case, the KH vortex remains indefinitely, as there is no magnetic field to lead to its decay. For this reason, the total energies in the nonideal MHD and HD cases are seen to level off, while the ideal MHD system continues to lose energy through decay.

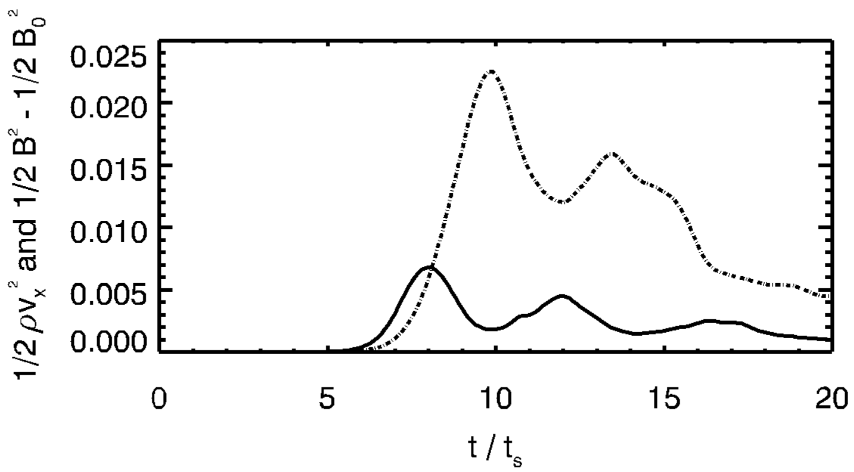

Figure 6.20: The growth of the perturbed magnetic energy (dot-dashed line) is plotted against time in the ideal case. Also plotted is the transverse kinetic energy (solid line) of the ideal case. It can be seen that, after the initial saturation point, the growth of magnetic energy is linked to the decay of kinetic energy, and vice-versa.

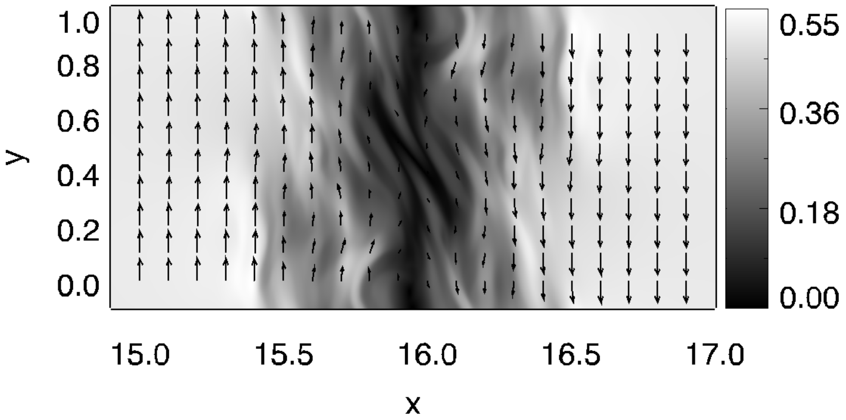

Figure 6.21: Plot of the magnitude and vector field of the velocity field for the ideal MHD case, at time = $20\,t_\mathrm{s}$. The system has become somewhat disordered.

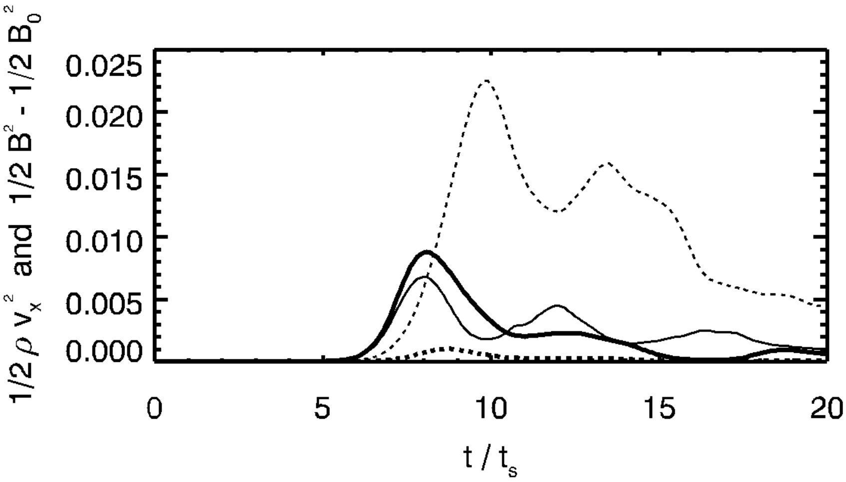

Figure 6.22: The evolution of the transverse kinetic energy and magnetic energy for the nonideal case. It can be seen that, after the initial saturation point,the magnetic field has experienced little growth, and is unable to inject energy back into the system.

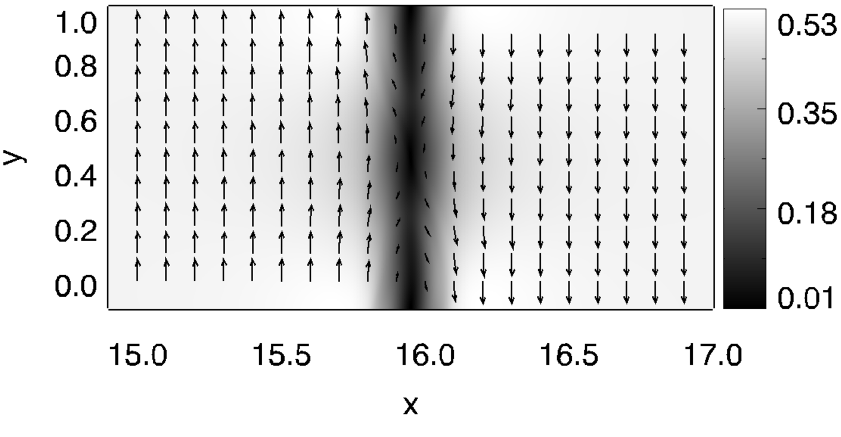

Figure 6.23: Plot of the magnitude and vector field of the velocity field for the high ambipolar case, at time = $20\,t_s$. The system has returned to that of laminar flow.

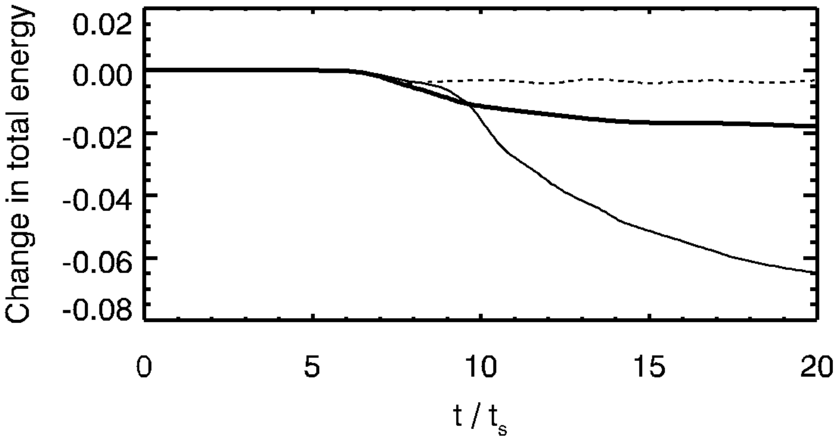

Figure 6.24: The total energy in the system of both the ideal MHD (thin line) and nonideal MHD (thick line) systems are plotted against time. While the ideal case continues to lose energy throughout the simulation through disordered decay, the leveling off of the energy in the nonideal case indicates that it has reaches a stable state.

Chapter 7

Protostellar jet-driven molecular outflows

Jets from young stars and jet-driven molecular outflows are of particular interest as a source of turbulent energy in molecular clouds in which the stars are being born (see section 1.1.2). Protostellar jets have been at the centre of many in-depth studies as they play a crucial role in the star formation process. However, only a few studies have examined them as sources of turbulence.

7.1 Observed characteristics of protostellar jets

Protostellar jets are produced during the major accretion phase in the star formation process. It is now believed that every star experiences an outflow phase during its early evolution (Bachiller, 2009). Since there are thousands of stars within 500 pc of the Sun, observational searches have resulted in many jets being discovered. To this day, several hundred protostellar jets have been identified (Bachiller, 2009). These jets exhibit a wide variety of structure, but in general can be shown to consist of four primary dynamical structures (Frank, 1998): a beam of unshocked jet material, a jet shock which decelerates material in the beam, a bow shock which accelerates ambient material, and a cocoon of decelerated jet gas that surrounds the beam.

The lengths of protostellar jets have been measured from approximately 0.01

to a few parsecs (De Gouveia dal Pino, 2005). A number of jets have also been measured as greater than $10\,\mathrm{pc}$ (Bally, 2009). Larger jets can reach a size at which they blow out of their molecular clouds (Bally & Devine, 1994).

Early studies of protostellar jets found their velocities to be within 200 to $400\,\mathrm{km\,s^{-1}}$ (Mundt, 1986). More recent surveys show that the jet velocities can range from under 20 to over $500\,\mathrm{km\,s^{-1}}$ (Bally, 2009). However, typical sonic Mach numbers for the jet remain between 20 and 40 (Raga, 1993), corresponding to a sound speed $c_\mathrm{s} \approx 10\,\mathrm{km\,s^{-1}}$ for a jet of temperature not much larger than 1-2 $\times 10^4$ K (De Gouveia dal Pino, 2005).

In the cases of all jets, from YSOs to AGNs, the velocities are usually of the order of the escape velocity from the central object (Livio, 2009). The velocities given here for protostellar jets are, in general, several times the escape velocity from the protostellar disk (Bally, 2007). When faster jet material impacts with slower moving gas, internal shocks are formed. These bright radiative shocks are the Herbig-Haro (HH) objects by which protostellar jets were first identified. Once thought to be entities within themselves, the bowshock-like structure of these knots confirms that they are simply internal working surfaces within the jet, caused by variations in the supersonic flow (Ray et al., 1996).

As a supersonic jet plows into the molecular cloud, a double shock pattern is produced at the head of the flow. The impacted ambient medium is accelerated in a forward bowshock, while the jet beam itself is decelerated in a jet shock or Mach disk. For a protostellar jet, the velocity of this bowshock is close to that of the jet, and therefore little material is accumulated within the cocoon surrounding the jet (De Gouveia dal Pino, 2005).

The electron densities at the jet surface can be estimated from the observed [SII] line emission, and ranges from approximately $10\,\mathrm{cm^{-3}}$ to greater than $10^5\,\mathrm{cm^{-3}}$, for the faintest to brightest objects respectively (Reipurth & Bally, 2001). This measurement allows for calculations of the jet densities and mass-loss rates (Bally et al., 2006). While early studies suggested typical hydrogen atom jet densities of between 20 and $100\,\mathrm{cm^{-3}}$ and a typical density ratio to the ambient medium to be between 1 and 2 (Mundt, 1986), more recent studies obtained an average of $10^4\,\mathrm{cm^{-3}}$ (Bacciotti & Eislöffel, 1999), with a density ratio to the ambient medium between 1 and 20 (Reipurth & Bally, 2001). The larger jets can provide constraints on the mass-loss histories of their source stars. These timescales range from 10^4 to 10^5 years, which is comparable to the timescale over which the young stars are formed.

In protostellar jets, low mass stars produce highly collimated jets, while stars of masses above $10\,M_\odot$ tend to generate wider-angled outflows (Bally, 2007). However, it is likely that the same collimation process applies to all jets, as the following two contributing factors occur in all cases (De Gouveia dal Pino, 2005). Firstly, almost all systems that produce jets have been observed to also contain an accretion disk. The disk provides both the energy and axial symmetry required for collimation. Secondly, the velocity of the jet is always of the order of the escape velocity from the disk, as mentioned above. This indicates that the jet originates from the centre of the accretion disk.

Another important contributor to the launching and collimation of the protostellar jet is the presence of a magnetic field (De Gouveia dal Pino, 2005). If the magnetic field plays a role in the collimation of the jet, then it is expected that the field will remain embedded in the jet as it propagates (Frank, 1998). The precise magnitude and orientation of the magnetic field can prove very difficult to observe within jets (Ray et al., 1997). Measurements by Morse et al. (1993) imply estimated values of between 10^{-6} and $10^{-5}\,G$ for the field, suggesting that the magnetic field does not play a major role in the core dynamics of the jet. However, more recent polarisation observations by Ray et al. (1997) measured a strong, ordered magnetic field in the jet of T Tau S at a distance of a few tens of AU from the source. This suggests that there could exist areas in which compression effects cause the magnetic field to become amplified to a degree at which it may play a greater role in the dynamics of the gas.

Since early studies of protostellar jets (e.g. Mundt et al., 1987), it has been observed that there are not only are these fast, highly collimated jets associated with protostars, but also less-collimated molecular outflows with velocities less than $20\,\mathrm{km\,s^{-1}}$ (De Gouveia dal Pino, 2005). The strong correlation between the two suggests that the jets are the driving force behind the molecular outflows, through prompt entrainment of molecular ambient gas at the bowshock. Alternative theories suggest that wide-angled stellar winds power the observed molecular outflows (Shu et al., 1991), claiming that jets may not have enough momentum to drive them. Observations of several jets, however, indicate that their momentum rates (Bacciotti et al., 1995) and lifetimes (Eislöffel & Mundt, 1997) are sufficient to drive a molecular outflow. Molecular outflows can have masses ranging from a few $10^{-4}\,M_\odot$ to several hundred $M_\odot$, and with timescales from 10^3 yr to 10^5 yr (Bachiller, 2009). Currently neither outflow model can yet sufficiently explain both the collimation and morphology observed in most jets (Downes, 2009).

Protostellar jets and molecular outflows can have a significant impact on the molecular cloud in which they occur. By generating turbulent motions, energy and momentum is injected back into the cloud. Outflows must also carry away some of the angular momentum from matter accreting onto the protostar. In cloud cores or regions in which only low-mass stars are being formed, the turbulent feedback may be sufficient to self-regulate star formation (Bally, 2007). On larger scales however, other sources of energy may be required.

7.2 Review of Numerical Studies

Amongst the first numerical MHD studies of protostellar jets were Uchida & Shibata (1985) and Shibata & Uchida (1986). Their simulations of jets from accretion disks demonstrated the necessity of magnetic fields in the launching and acceleration of jets. The role of protostellar jets as the driving mechanism behind molecular outflows has since been studied by a number of authors (e.g. Padman et al., 1997). Alternative models for explaining these observed bipolar molecular outflows include the wide-angled wind-driven model (Shu et al., 1995) and the steady-state filled flow (Stahler, 1994). The various hydrodynamics models are reviewed by Cabrit et al. (1997), which concludes that the jet-driven model best explains many of the observational features of molecular outflows.

7.2.1 Ideal MHD simulations

As mentioned above, magnetic fields cannot be ignored in jet processes, especially the role played by the field in the collimation of a jet. The magnetic field will then remain embedded in the jet as it propagates. The first multi-dimensional simulations of radiative MHD jets were carried out by Cerqueira et al. (1997) and Frank (1998). Both studies found that the dynamics of the jet propagation differed significantly with the inclusion of a strong toroidal field. The magneto-centrifugal forces required for the collimation of these magnetised jets were taken as support for disk-wind or x-wind models for jet launching.

In numerical simulations of jets, there exist a number of possible choices for an initial magnetic field configuration, as magnetic field strengths and field geometries are not well-constrained by observations. Some of these different set-ups and their results are outlined by Stone & Hardee (2000). Strong toroidal fields for example can cause result in the accumulation of dense shocked gas in a nose cone at the head of the jet. The formation of a nose cone is also observed by Todo et al. (1992), in which a jet is propagated into a uniform ambient medium that contains a helical magnetic field. Cerqueira et al. (1997) found that the fragmentation of the dense shell formed by cooling at the head of the jet is strongly affected by magnetic forces, and they thus conclude that the clumpy structure observed in jets provides evidence that the field must be primarily axial rather than helical near the head of the jet. The choice by Stone & Hardee (2000) to focus their simulations on toroidal fields is motivated by jet production theory. In most of their models, the jet propagates into an unmagnetised medium, although in some cases a poloidal field is added that initially threads both the jet and the ambient gas.

For the most part, strong magnetic fields are used in the above studies. It can be seen that weak fields are negligible in the case of adiabatic simulations. However, in simulations in which cooling is taken into account, the compression of gas can result in the amplification of the magnetic field up to a point at which magnetic pressure is comparable to the shocked gas pressure. In these cases, initially weak magnetic fields are no longer negligible (Stone & Hardee, 2000).

The consequences of using different initial magnetic field configurations was examined by De Gouveia dal Pino (2005). She found that an initial helical or toroidal field had a greater effect on the propagation of a jet than a longitudinal field, when compared to hydrodynamic simulations. However, these differences were found to be less obvious in 3 D simulations than in 2 D. It was also found that in some 3 D simulations, the magnetic field tended to affect only the detailed structure behind the shocks at the head of the jet and at the internal knots within the jet. Again, these differences were observed to be stronger in simulations with initial helical or toroidal magnetic fields.

As well as defining the initial jet parameters in numerical studies, the ambient medium must also be initialised. De Gouveia dal Pino (2005) explains that while the majority of jet models assume an initially homogeneous ambient medium, the molecular clouds that surround protostellar jets are generally non-homogeneous and formed of many dense clouds. More precise modeling of the ambient medium can help further progress understanding of molecular outflows. The jet-driven model, for example, has been shown to reproduce the poor collimation observed in some outflows only when taking into account the variations in the density of the ambient medium (Corkery, 2008). Molecular outflows are so massive that they cannot contain only mass from the the accretion disk, but must consist also of entrained material from this ambient medium (Downes, 2009). 3 D simulations by Raga et al. (2002) have shown this to be numerically possible, through the ablation of of the dense cloud molecular material by an ionic jet.

Our numerical study in the next section focuses on simulations of a jet-driven bowshock. In this case, the jet will be simulated only as an injection of momentum. The density of the jet gas and the configuration of the embedded magnetic field will be assumed to be equal to that of the surrounding molecular cloud. The effect of including nonideal MHD effects will then be observed on the propagation of the jet and the development of the magnetic field structure.

7.2.2 Multifluid MHD simulations

A small number of numerical studies on protostellar jets have approached the subject of nonideal MHD effects. Frank et al. (1999) examine the assumption that the magnetic field remains embedded in a jet following its role in the initial launching of the jet. This would not hold true if the magnetic diffusion in the gas was sufficiently high. Following observations by Bacciotti & Eislöffel (1999) of the low ionisation fraction in protostellar jets, such nonideal MHD effects are expected to occur. Ambipolar resistivity is thus examined as a possible cause of allowing the magnetic field to diffuse within the jet. Reconnection is not expected to occur due to the helical topology of the initialised magnetic field. Frank et al. (1999) find that the timescales and lengthscales involved are sufficient for ambipolar diffusion to become important, but their analysis did not extend to examining the effect of this would have on the evolution of the jet.

In Meliani et al. (2006) and Casse et al. (2007), the first ever simulations of nonideal MHD stellar winds and disk-driven jets are presented, with a self-consistently described resistive and viscous accretion disk. The nonideal effects, however, are focused on the accretion disk in this work, and the outflow that is ejected by the system is described using ideal MHD.

Recently, nonideal effects on jets have been studied by Carver et al. (2010) using laboratory astrophysics. The flows generated by these high powered lasers are analogous to jets driven from young stars. It is found that the morphology of laboratory jets is reproduced to a much higher degree by numerical simulations when nonideal MHD equations of state are implemented into the code. While computational restrictions limit the study by resolution and to two dimensions, the conclusion can be reached that the inclusion of nonideal effects may substantially improve current jet simulation studies.

7.3 A Multifluid MHD study of protostellar jet-driven bowshocks

In sections 1.1.2 and 7.1 we have seen that protostellar jets and jet-driven molecular outflows are a possible source of turbulent energy injected back into the molecular cloud in which the protostar is born. It is proposed that the Kelvin-Helmholtz instability may add to the transfer of momentum through the interaction of the bowshock of the outflow with the ambient molecular cloud (see section 1.4.2). In the previous three chapters we observed that the introduction of multifluid effects could greatly influence the evolution of the KH instability in that system. Similarly, it is expected that nonideal MHD effects would affect the evolution of the KH instability, if it was to occur along the bowshock of a molecular outflow.

The aim of this chapter is to carry out a preliminary study of the bowshocks of molecular outflows in a nonideal MHD system. Numerical simulations are run on a 3 D grid into which a jet is injected. The purpose of this study is not to produce growth of the KH instability along the edge of the resulting bowshock; the simulations have lifetimes much less than the growth time of the instability. Nor is the aim to investigate in depth the propagation of the outflow and bowshock. The simulation is isothermal, and contains no radiation or cooling, nor the resolution required to carry out such a study. However, by introducing multifluid effects to the system, we will examine the impact of nonideal MHD phenomena on the evolution of the bowshock and investigate the manner in which the morphology is changed or unchanged under nonideal MHD conditions.

7.3.1 Initial computational parameters

The following simulations are carried out on a 3 D grid, of size $1.5\,L \times 1.5\,L \times 2.5\,L$, where $x, y \in (-0.75\,L, 0.75\,L)$ and $z \in (0, 2.5\,L)$, and the characteristic length scale L will be defined in the next section. This is performed on a grid of $600 \times 600 \times 1000$ cells. The jet is injected with a velocity in the z-direction from the centre point of the xy-plane at $z = 0$ and with a radius of $0.2\,L$. The jet injection is kept at a constant velocity for the duration of the simulations. All other boundaries on the grid are set to zero-gradient. By simulating the entire cylinder of the jet, boundary conditions are not problematic and non-symmetric forces such as the Hall effect are simulated effectively.

7.3.2 Initial physical parameters

The choices for the initial fluid physical parameters in our simulations follow from the study in Section 6 on the Kelvin-Helmholtz instability in molecular clouds. In the following study, the grid into which the jet is injected simulates a similar ambient molecular cloud. As this is a study of the dynamics in the bowshock rather than the jet, the injected jet material is simply described using the same parameters as the ambient molecuar cloud.

The plasma is weakly ionised, and therefore consists primarily of a neutral particle fluid, such that $\rho_0 \approx \rho_\mathrm{n}$. The average mass of the neutral particles is taken $m_\mathrm{n} = 2.33\, m_\mathrm{p}$, where m_p is the mass of a proton, as in Section 6. The number density of neutral particles in the ambient medium is taken to be $n_\mathrm{n} = 100\,\mathrm{cm}^{-3}$. While this is in the lower range expected for neutral densities in molecular clouds, a much larger value would result in a smaller Alfvén velocity, reducing the significance of the magnetic field. So then, for the neutral fluid:

$$\rho_\mathrm{n} \equiv m_\mathrm{n} n_\mathrm{n} = 3.89 \times 10^{-18}\,\mathrm{g\,cm}^{-3}.$$

In the following simulations, the density of the jet is taken to be equal to that of the ambient medium. This is at the lower end, but within the range, of the observed ratios of jet to ambient medium densities (see section 7.1).

The sound speed in the plasma is calculated from

$$c_\mathrm{s} \equiv \sqrt{\frac{\gamma k_\mathrm{B} T}{m_\mathrm{n}}},$$

where $k_\mathrm{B} = 1.38 \times 10^{-16}\,\mathrm{erg\,K}^{-1}$ is the Boltzmann constant, the adiabatic index γ is equal to unity for the isothermal system, and the constant temperature is taken to be $T = 1.2 \times 10^4\,\mathrm{K}$, which is consistent with protostellar jets (see section 7.1). This results in a sound speed of $c_\mathrm{s} = 6.5\,\mathrm{km\,s}^{-1}$.

The velocity of the jet is chosen to have a sonic Mach number of 15, in agreement with both section 7.1 and some previous simulations (e.g. De Colle et al., 2008).

$$M_{\mathrm{s}} = \frac{V_0}{c_{\mathrm{s}}} = 15,$$

so that the velocity of the jet is $V_0 \approx 100$km s^{-1}.

The strengths of magnetic fields in protostellar jets have not been well established observationally. Following sections 1.1.2 and 6, the magnitude of the magnetic field in this study is chosen as $|B_0| = 22.8\,\mu$G. Thus the initial Alfvén velocity can be calculated as:

$$v_{\mathrm{A}} = \sqrt{\frac{B_0^2}{4\pi\rho_0}} = 3.26\,\mathrm{km\,s^{-1}}.$$

This gives an Alfvén Mach number of

$$M_{\mathrm{A}} = \frac{V_0}{v_{\mathrm{A}}} \approx 30,$$

which agrees with values used in some previous studies (e.g. De Colle et al., 2008).

In order to depart from ideal MHD, resistivity must be introduced into the system. From Wardle & Ng (1999), we require the Hall and ambipolar conductivities in a molecular cloud to be $\sigma_{\mathrm{H}} = 1 \times 10^{-2}\,\mathrm{s}^{-1}$ and $\sigma_{\mathrm{A}} = 1 \times 10^{-1}\,\mathrm{s}^{-1}$. These are also the same values used in section 6.

Transforming into dimensionless units

The physical parameters determined above are transformed into dimensionless units before being inputted into the numerical code. For this purpose, practical characteristic length, time and mass scales must be determined.

The lengthscale of the system is first chosen. It has been seen that protostellar jet vary greatly in length, from 0.01 pc to several parsecs. Here we simulate only a small jet, of length 0.025 pc. As the grid is of length $2.5\,L$, the characteristic lengthscale is thus

$$[L] = 0.01\,\mathrm{pc} = 3.2 \times 10^{16}\,\mathrm{cm}.$$

The timescale is chosen such that the sound speed is of order unity, $c_{\rm s} = 1$. The sound speed has been calculated as $c_{\rm s} = 6.5\,{\rm km\,s^{-1}}$. This implies a time scale

$$[T] = 4.7 \times 10^{10}\,{\rm s} = 1500\,{\rm yr}.$$

Using these units, the velocity of the jet is now

$$V_0 = 15.$$

Finally, a mass scale is chosen. This is set so that the mass density of the plasma is of order unity, $\rho_0 = 1$. The mass density has been calculated as $\rho_{\rm n} = 3.89 \times 10^{-22}\,{\rm g\,cm^{-3}}$. Using the length scale chosen above, this gives a characteristic mass scale

$$[M] = 1.14 \times 10^{28}\,{\rm g}.$$

The magnitude of the magnetic field, $B_0 = 22.8\,\mu{\rm G}$, can also be transformed into a dimensionless quantity, by

$$|\mathbf{B}| = \frac{B_0}{\sqrt{4\pi}} \times \frac{[T][L]^{1/2}}{[M]^{1/2}} = 0.5$$

From this calculation onwards, the units of $\mathbf{B}$, $\mathbf{E}$ and $\mathbf{J}$ are written such that the factors of 4π and the speed of light no longer appear.

The values for the conductivities are also transformed into dimensionless units. We find

$$\sigma_{\rm H} = 1 \times 10^{-2}\,{\rm s^{-1}} = 0.01 \times \frac{4\pi}{\left(c_{\rm s}({\rm in\ cm\,s^{-1}})\frac{[L]}{[T]}\right)^2} \times [T] = 2.81$$

and

$$\sigma_{\rm A} = 1 \times 10^{-1}\,{\rm s^{-1}} = 0.1 \times \frac{4\pi}{\left(c_{\rm s}({\rm in\ cm\,s^{-1}})\frac{[L]}{[T]}\right)^2} \times [T] = 28.1.$$

The final values to be specified describe the charged fluids, and include their mass densities ρ_i, charge-to-mass ratios α_i and rates at which each fluid collides with the neutral fluid, K_{i1}. The mass density of the ion fluid is required to be significantly less than that of the neutral fluid, and is set to $\rho_{\rm ion} = 2 \times 10^{-7}\, \rho_n$. This value is taken from Umebayashi & Nakano (1990) for molecular clouds of the density used here. The charge-to-mass ratios are chosen to be, in dimensionless units, $\alpha_{\rm ion} = 7.1 \times 10^8$, and $\alpha_{\rm e} = -1 \times 10^{17}$. The requirement charge neutrality requirement, $\sum_i \alpha_i \rho_i = 0$ determines the mass density of the electron fluid, $\rho_{\rm e} = 1.42 \times 10^{-15}\, \rho_{\rm n}$. The collision rates are set, in dimensionless units, to be $K_{ion,1} = 3.55 \times 10^7$ and $K_{e,1} = 5.0 \times 10^5$. These give, following the definitions in section 1.3.2, Hall parameters for the two fluids of $\beta_{\rm ion} = 1 \times 10^1$ and $\beta_{\rm e} = -1 \times 10^{11}$. It can be seen by calculation that the conductivities are then $\sigma_{\rm H} = 2.81$ and $\sigma_{\rm A} = 28.1$. These are the values expected in a molecular cloud, as derived above. Calculations also give a value of $\sigma_{\rm O} = 2.8 \times 10^{13}$, which is very large, as required.

Isolating nonideal MHD effects

This set-up includes the necessary parameters to describe the nonideal MHD system of a molecular cloud. The resistivities of the system can be calculated as $r_{\rm H} = 3.52 \times 10^{-3}$ and $r_{\rm A} = 3.52 \times 10^{-2}$. The simulations are also carried out under HD and ideal MHD conditions for comparative purposes. In order to identify the changes observed in the multifluid MHD system as due to either the inclusion of ambipolar diffusion or the Hall effect, simulations are run in which the Hall effect or ambipolar diffusion are isolated by altering the initial parameters of the charged fluids. By increasing the charge-to-mass ratio of the ion fluid from $\alpha_{\rm ion} = 7.1 \times 10^8$ to $\alpha_{\rm ion} = 7.1 \times 10^{11}$, the Hall resistivity is reduced to a negligible 3.52×10^{-6}, thus effectively isolating the ambipolar diffusion as the only nonideal MHD effect at work. Conversely, the collision ratio of the ion fluid with the neutrals can be increased from $K_{ion,1} = 3.55 \times 10^7$ to $K_{ion,1} = 3.55 \times 10^{11}$, thus reducing the ambipolar resistivity to a negligible 3.52×10^{-6}. As a result, the Hall effect remains as the only nonideal MHD effect at work. In this manner, results observed in the multifluid case can be attributed to either the inclusion of ambipolar diffusion or the Hall effect.

7.3.3 Results for multifluid bowshock study

Pressure at the head of the bowshock Comparisons are made of the evolution of the jet-driven bowshock in the hydrodynamic, ideal MHD and nonideal MHD systems. Figure 7.1 shows a plot of the density structure of the bowshocks in these three cases. It can be seen that the ideal MHD system experiences the greatest build-up of density at the head of the jet. This is due to the presence of the magnetic field which constrains the flow of plasma in this region. As nonideal MHD effects are included in the system, the magnetic field lines are no longer as tightly coupled to the plasma and this constraint does not occur.

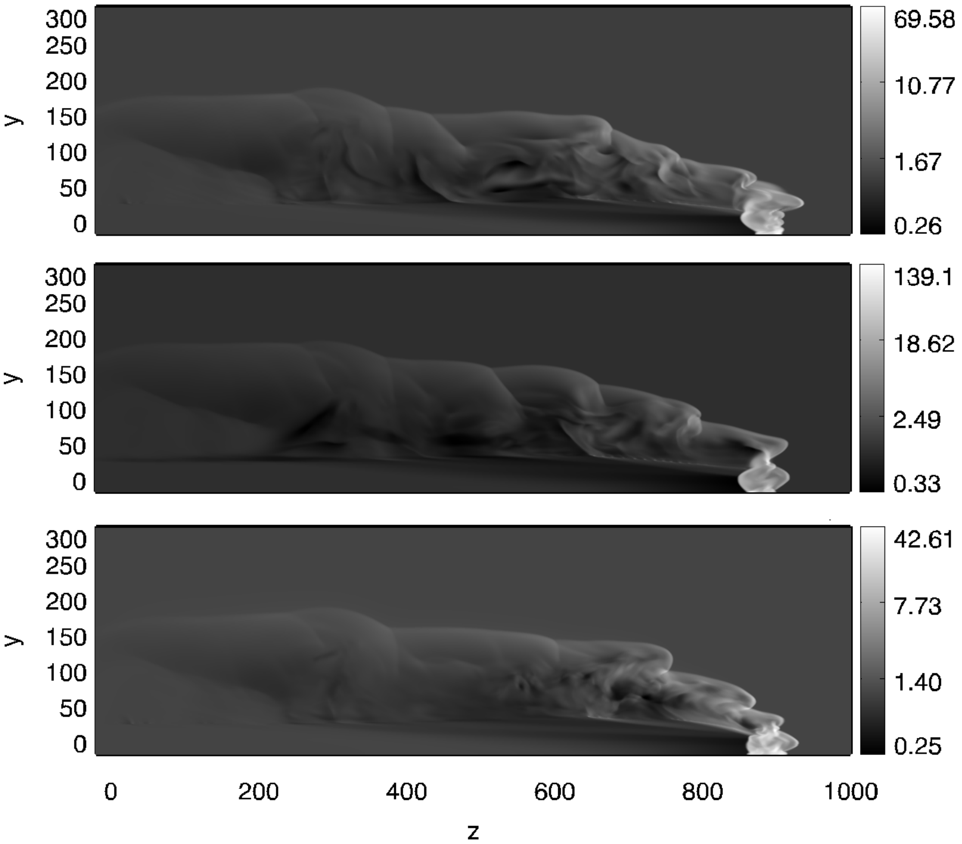

Figure 7.1: Plot of the mass density of the bulk fluid for the HD case (upper panel), ideal MHD case (middle panel) and nonideal MHD case (lower panel). Note that the maximum values for the density differ significantly in the three cases.

Lateral velocities at the head of the bowshock As the jet propagates into the ambient medium and pressure builds at the head of the jet, the plasma is forced laterally away from this region. The lateral velocity of this plasma is related to the pressure at the head of the jet and can be examined in figure 7.2. This figure shows the radial velocity of the plasma by plotting the velocity in the x-direction for a slice in the xz-plane for each of the three cases.

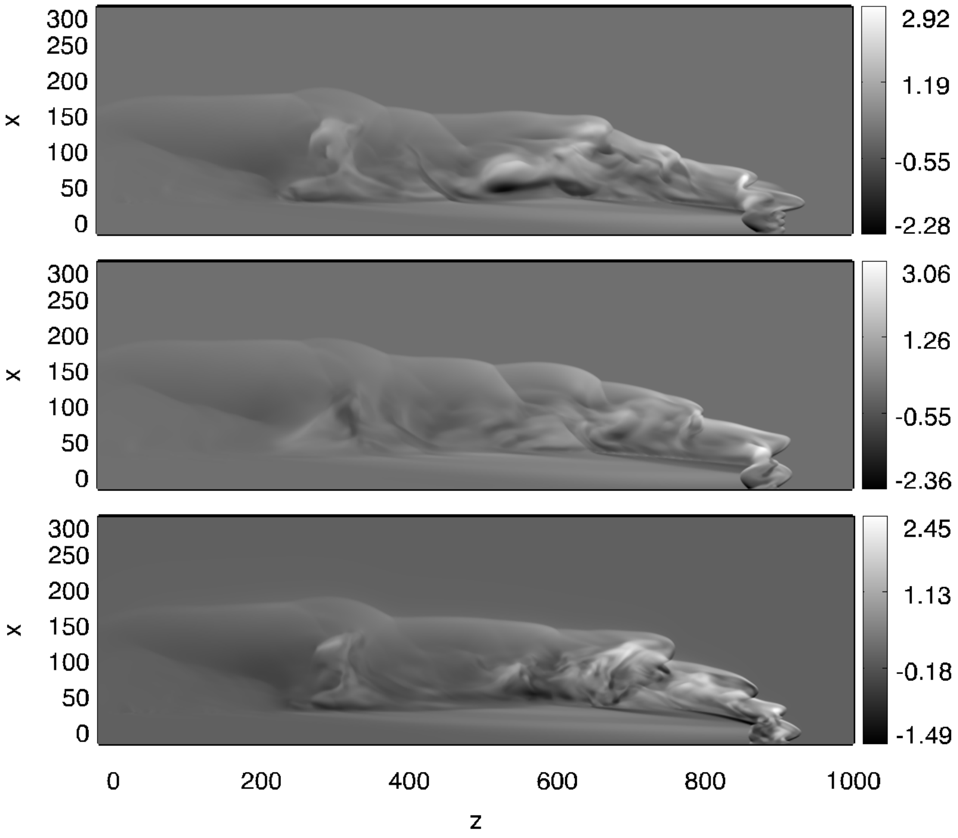

Figure 7.2: Plot of the lateral velocity of the fluid for the HD case (upper panel), ideal MHD case (middle panel) and nonideal MHD case (lower panel). Note that the maximum values for the lateral velocity differ significantly in the different cases.

It can be seen from figures 7.1 and 7.2 that the hydrodynamic case experiences less pressure at head of the jet than in the ideal MHD case and that the maximum lateral velocity experienced by the plasma is approximately 4% smaller in magnitude. The nonideal MHD case experiences even less pressure (thermal and magnetic pressures combined - the magnetic field will be examined later) and the plasma ejected from the area has a maximum lateral velocity of approximately 8% less than in the ideal MHD case. These results agree with the expectation that higher thermal pressure at the head of the jet leads to greater lateral velocity of the plasma away from the head of the jet.

General shape of the bowshock One consequence of the initial lateral velocities is the shape of the bowshock near the head of the jet. Larger lateral velocities will create a wider, blunter head to the bowshock, while smaller lateral velocities create a narrow, sharper head. The general shape of the bowshocks can be seen in figure 7.1. A more quantitative examination of the width of the head of the bowshock is carried out in figure 7.3, a plot of the density as a function of distance from the centre of the jet beam at a distance of $z = 900$ grid cells. For the purpose of this analysis, we define the edge of the bowshock as the distance at which the density decreases to within 1% of that of the ambient medium. From this data, we find that the bowshock extends to a distance of 67, 75 and 54 grid cells from the centre of the jet for the HD, ideal MHD and nonideal MHD cases respectively. This shows that the ideal MHD case leads to the most blunt bowshock, followed in order by the HD and nonideal MHD cases. This result agrees with the bluntness of the bowshock expected from the values of lateral velocity measured for each of the three cases.

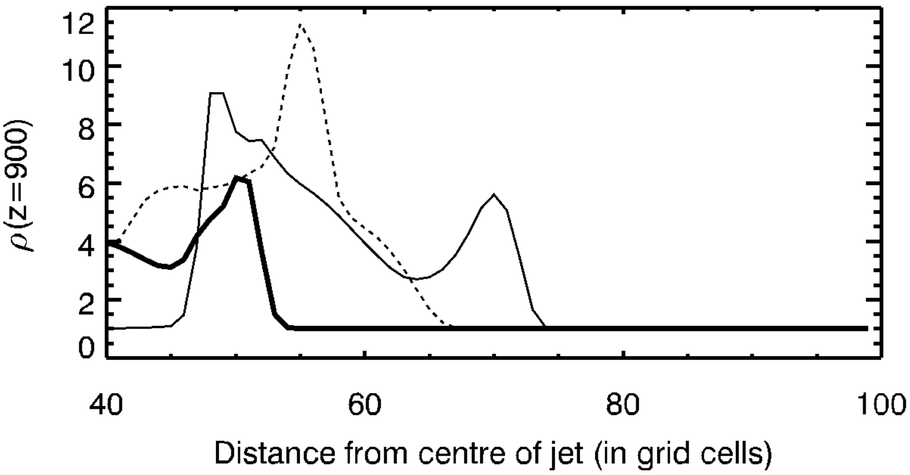

Figure 7.3: Plot of density as a function of distance from the centre of the jet beam, at a distance of $z = 900$ grid cells. The thin and thick solid lines represent the ideal MHD and nonideal MHD cases respectively, and the thin dashed line represents the hydrodynamic case.

Momentum in the wings of the bowshock In sections 1.1.2 and 1.4.2 we outlined a number studies investigating the transfer of momentum from a protostellar jet into a molecular cloud through entrainment of the ambient medium by the bowshock. Downes & Ray (1999) find that the amount of momentum transferred to the ambient medium by a jet-driven bowshock is very low. This motivates the following study on whether the amount of momentum in the bowshocks is significantly altered under nonideal MHD conditions. We calculate the total momentum in a 2 D plane of the system by:

$$\text{momentum}(x) = \int_{k=0}^{k=NZ} \rho_{i,j=\frac{NY}{2},k} \cdot \left(\sqrt{v_x^2 + v_y^2 + v_z^2}\right)_{i,j=\frac{NY}{2},k} (x = i)\, dz\ . \tag{7.1}$$

This is plotted against x in figure 7.4 using a log-scale in order to focus on the dynamics in the wings of the bowshock rather than in the beam of the jet.

As expected, the majority of the momentum in the system is located within the jet beam itself and at the head of the bowshock. The wings of the bowshock

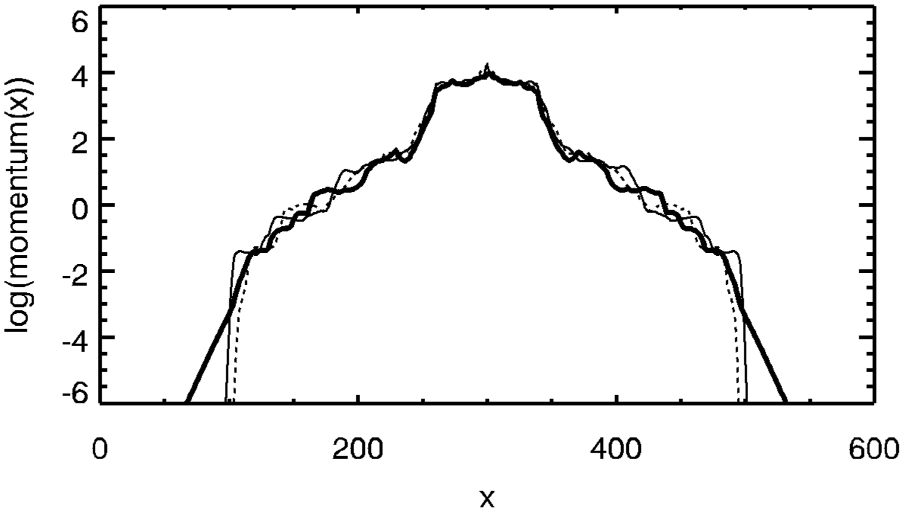

Figure 7.4: Plot of the log of the momentum using an xz-slice through the centre of the jet for each system, integrated along z and plotted against x. The thin and thick solid lines represent the ideal MHD and nonideal MHD cases respectively, and the thin dashed line represents the hydrodynamic case.

contain the remainder. The initial jet beam has a radius of 40 grid cells and so for the purpose of this analysis we define the wings of the bowshock as starting from 100 grid cells from the centre of the jet beam to the outer boundary of the bowshock, and from the base of the jet to 60% of the distance across the grid in the z-direction. Thus the total momentum in the wings of bowshocks is calculated by:

$$\begin{aligned}\text{momentum}_{\text{wings}} &= \int_{k=0}^{k=600}\int_{i=0}^{i=200} \rho_{i,j=\frac{NY}{2},k} \cdot \left(\sqrt{v_x^2+v_y^2+v_z^2}\right)_{i,j=\frac{NY}{2},k} dx\,dz \\ &\quad + \int_{k=0}^{k=600}\int_{i=400}^{i=600} \rho_{i,j=\frac{NY}{2},k} \cdot \left(\sqrt{v_x^2+v_y^2+v_z^2}\right)_{i,j=\frac{NY}{2},k} dx\,dz\,. \end{aligned} \tag{7.2}$$

By carrying out this calculation for each system, we find that there is a small increase in the momentum in the wings of the bowshock of 1% from the HD case to the ideal MHD case, and a decrease of 8% from the ideal MHD case to the nonideal MHD case. The momentum found in the wings of the bowshocks is predominantly determined by the momentum of the plasma at the time of ejection from the head of the jet into the wings of the bowshock. Thus measurements of initial lateral velocity of the plasma are expected to show a relation to these calculations of momentum. A simplified calculation finds that the maximum lateral velocities of the ejected plasma were 4% and 8% smaller in the HD and nonideal MHD cases respectively than in the ideal MHD case. This is a good indication that these two variables are closely linked.

Magnetic field in the ideal MHD bowshock For a large fraction of the system the magnetic energy is dominated by the kinetic energy and, as Cerqueira & de Gouveia dal Pino (1999) and references within observe, a weak magnetic field within the jet does not significantly alter the core dynamics of the jet. In some regions however, such as the head of the bowshock, the magnetic field causes a constraint on the flow of plasma, as observed in figure 7.1. This results in a higher density of plasma in this region for the ideal MHD case. There also exist regions in which the flow of the plasma is slower moving, and the magnetic energy is no longer dominated by the kinetic energy. In these areas the field may then play a more important role. One such region is in the wings of the bowshock, where the velocities of the fluid is considerably smaller. Figure 7.2 demonstrates that the velocity of the plasma in the radial direction decreases to a level comparable to the sound speed ($c_\mathrm{s} = 1$) in the wings of the bowshock.

The presence of a magnetic field introduces an Alfvén wave into the system with a particular velocity ($\mathbf{v}_\mathrm{A} = 0.5$ for these simulations), as well as slow and fast magnetosonic waves. In the ideal MHD case, this fast magnetosonic wave becomes important in the wings of the bowshock where the velocity of the plasma has slowed to a velocity comparable to the fast magnetosonic speed, $v_f = \sqrt{c_\mathrm{s}^2 + v_\mathrm{A}^2} \approx 1.12$. This allows for the faster wave to travel further outwards through the plasma, resulting in a widening of the bowshock. The widths of the three systems will be calculated quantitatively later on, but this effect can be preliminarily observed by direct comparisons of the velocity profiles of the HD and ideal MHD cases, taken as a cross-section near the base of the jet, as seen in figure 7.5 (upper and middle panels). It should be noted that there exists a deviation from cylindrical symmetry observed within these simulations, as a result of dependency on grid geometry. However, this is most prevalent at the boundary of the jet beam itself and has only negligible effects on the calculations being carried out in the wings of the bowshocks.

The lower panel of figure 7.5 shows the magnetic field profile of the ideal MHD system, also taken as a cross-section near the base of the jet. By comparison with the velocity field profile of the ideal MHD system in the middle panel, it can be seen that both fields have the same diameter. This is expected as the magnetic field is “frozen-in” to the plasma in the ideal MHD case.

Magnetic field in the nonideal MHD bowshock Figure 7.6 plots the magnetic field configuration for the ideal and nonideal MHD cases (upper and lower panels respectively). The nonideal system includes ambipolar diffusion and the Hall effect. The consequences of ambipolar diffusion can clearly be seen in the configuration of the magnetic field. In the region of strongest magnetic field in the ideal MHD case, at the head of the jet, ambipolar diffusion results in the amplification of the magnetic field being reduced by almost half. This magnetic diffusion is a direct result of the magnetic field no longer being “frozen-in” to the plasma. Furthermore, the structure observed in the magnetic field in the wings of the bowshock in the ideal MHD case is smoothed out following the inclusion of magnetic diffusion.

The inclusion of ambipolar diffusion in the system is implemented by decreasing the coupling of the charged fluids with the neutral fluid. This not only allows the magnetic field to diffuse through the plasma, but the charged fluids can behave almost independently of the neutrals. It was observed above that the Alfvén speed in the magnetised plasma allowed for a faster wave to propagate through the plasma. In the case of partial decoupling of the charged and neutral fluids, the Alfvén velocity in the ion fluid is recalculated for the density of the ion fluid, $(\mathbf{v}_{\mathrm{A}})_{\mathrm{ion}} = \sqrt{\frac{B^2}{\rho_{\mathrm{ion}}}}$. For a weakly ionised plasma, we get $(\mathbf{v}_{\mathrm{A}})_{\mathrm{ion}} \gg c_{\mathrm{s}}$. This allows a much faster wave to travel through the charged fluids and magnetic field than in the ideal MHD case. This results in a further outwards broadening of the magnetic field at the wings of the bowshock. Through collisions with the neutral fluid, the charged fluids also accelerate the neutrals, resulting in the creation of a C shock

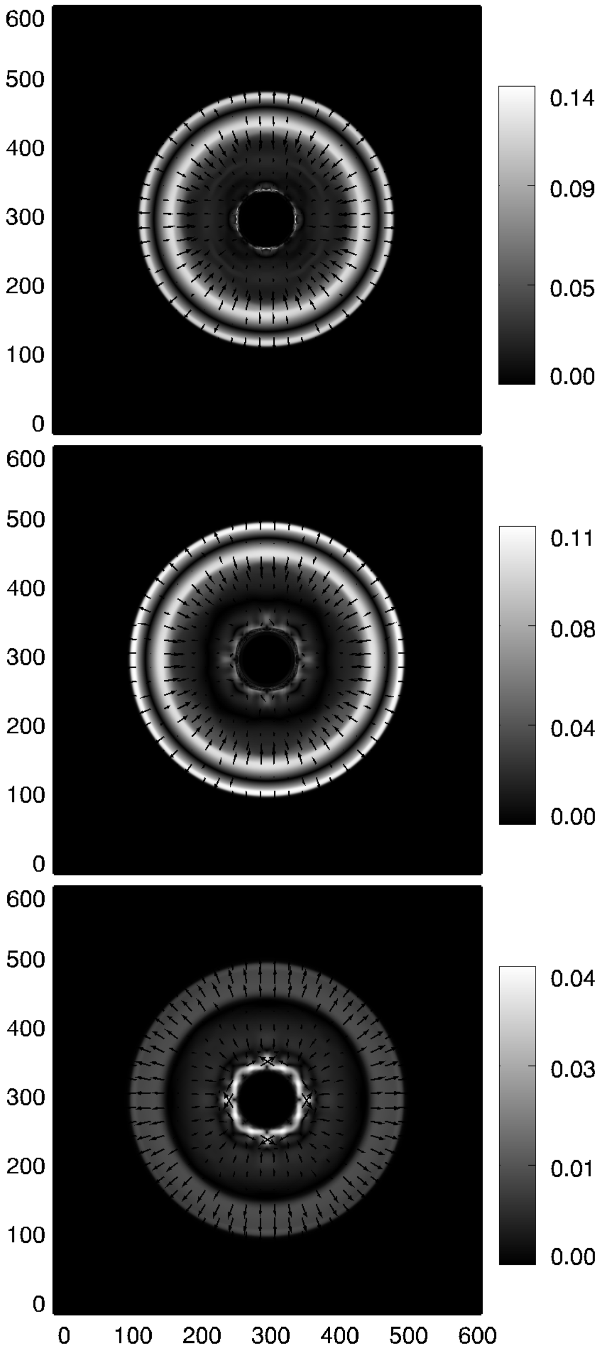

Figure 7.5: Plot of the velocity profile of the bulk fluid through an xy-slice near the base of the jet for the HD case (upper panel) and the ideal MHD case (middle panel) and of the magnetic field profile for the ideal MHD case (lower panel).

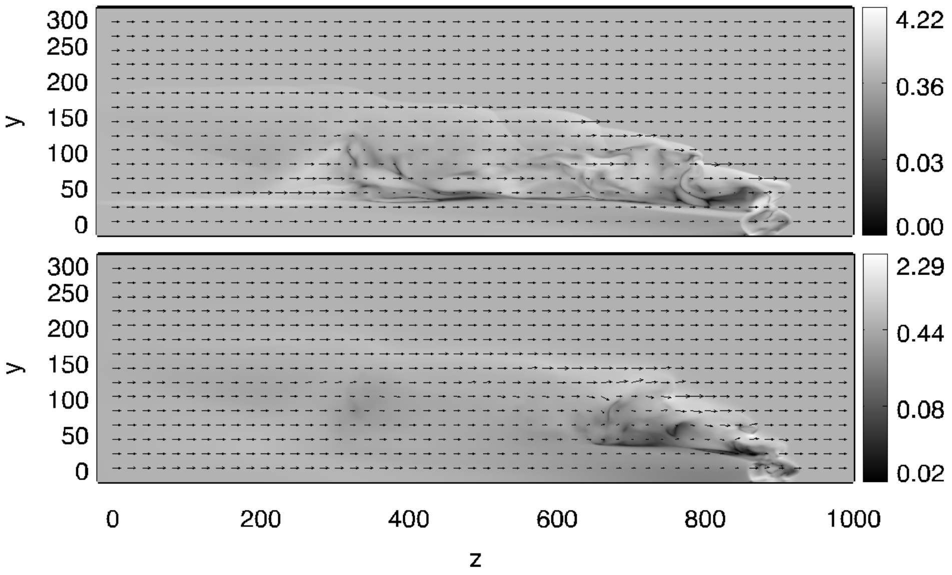

Figure 7.6: Plot of the magnitude and vector field of the magnetic field for the ideal MHD case (upper panel) and nonideal MHD case (lower panel). Note that the maximum magnetic field strength is less extreme in the nonideal MHD case.

at the boundary of the bowshock. These effects can be observed in the following figures. Figure 7.7 shows a plot of the velocity and magnetic field profiles for the nonideal MHD case. Comparison with figure 7.5 demonstrates that the bulk fluid has been accelerated to the greater width at the boundary of the bowshock. The magnetic field can also be seen to have broadened, and to a greater extent than the bulk fluid. This is made possible by the decoupling of the charged and neutral fluids and thus the breaking of the "frozen-in" approximation. Figure 7.8 plots the lateral velocities at a certain point in the wings of the bowshock for the three systems. Taken as a slice in the xz-plane and plotted against x, these lateral velocities are those measured in the x-direction. This is similar to the data plotted in figure 7.2, only here we examine the velocities for a single point at $z = 500$ grid cells. This plot also allows the structure of the shock at the bowshock to be observed. While the HD and ideal MHD demonstrate classical shock behaviour, the nonideal MHD case clearly shows a C shock.

We have seen that the magnetic field in the three systems results in three different signal speeds, which thus affect the width of the bowshock. These widths are

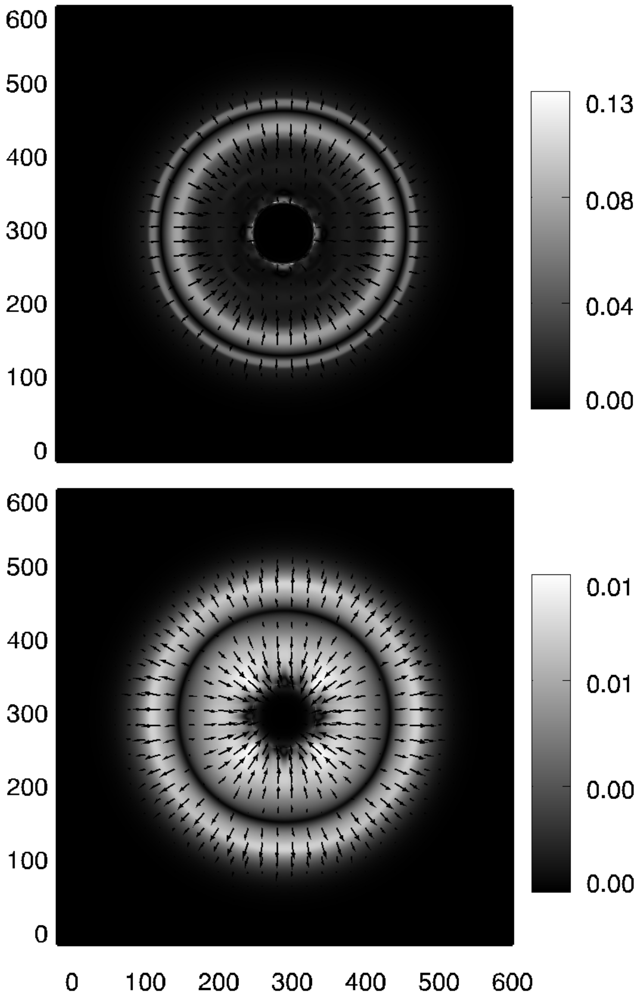

Figure 7.7: Plot of the velocity profile of the bulk fluid (upper panel) and of the magnetic field profile (lower panel) through an xy-slice near the base of the jet for nonideal MHD case.

now quantitatively measured, by calculating the maximum density of the bowshock wing along z, and plotting this as a function of the distance from the jet beam. The result is given in figure 7.9. By again defining the width of the bowshock as the distance out to which the density is more than 1% greater than the ambient medium, this data allows us to calculate the diameters of the bowshocks as 392, 404 and 434 grid cells, for the HD, ideal MHD and nonideal MHD systems respectively. These results agree with the expectation that the faster signal

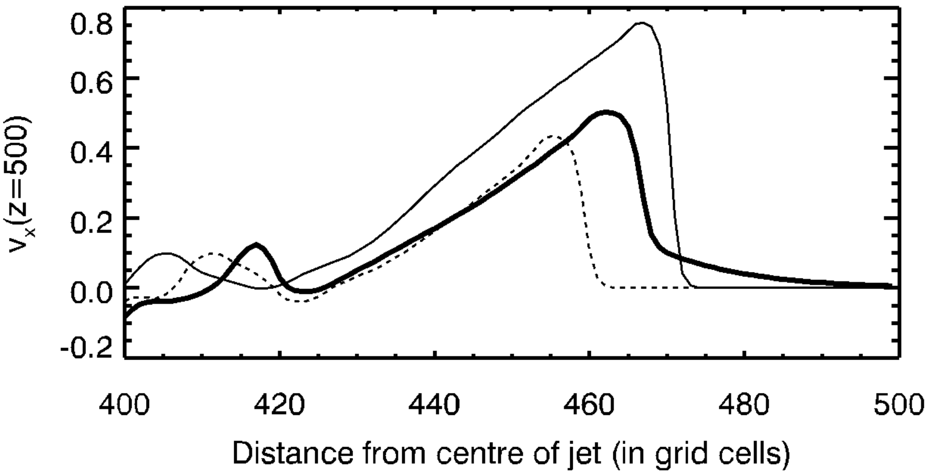

Figure 7.8: Plot of the lateral (v_x) velocities of the bulk fluid as a function of distance from the centre of the jet beam, at a distance of $z = 500$ grid cells. The thin and thick solid lines represent the ideal MHD and nonideal MHD cases respectively, and the thin dashed line represents the hydrodynamic case.

speeds in the plasmas allow for a wider bowshock.

Determining the multifluid effect at work Having examined the changes to the bowshock morphology following the inclusion of nonideal MHD effects, these changes can be identified as being due to either ambipolar diffusion or the Hall effect by carrying out simulations in which the ambipolar or Hall diffusion are made negligibly small, leaving only the other nonideal effect remaining. This process is detailed in section 7.3.2. The quantitative measurements carried out above are then calculated for these two simulations, and compared to that of the nonideal MHD system. As expected for ambipolar-dominated molecular clouds, the ambipolar-only results show good agreement with the nonideal MHD system, while the results of the Hall-only simulation are more similar to that of the ideal MHD system. From calculations of the momentum in the wings of the bowshock, in the ambipolar-only system is found to have 8% less than in the ideal MHD system. This is the same decrease observed in the nonideal MHD case. On the other hand there is no significant loss of momentum in the bowshock wings compared

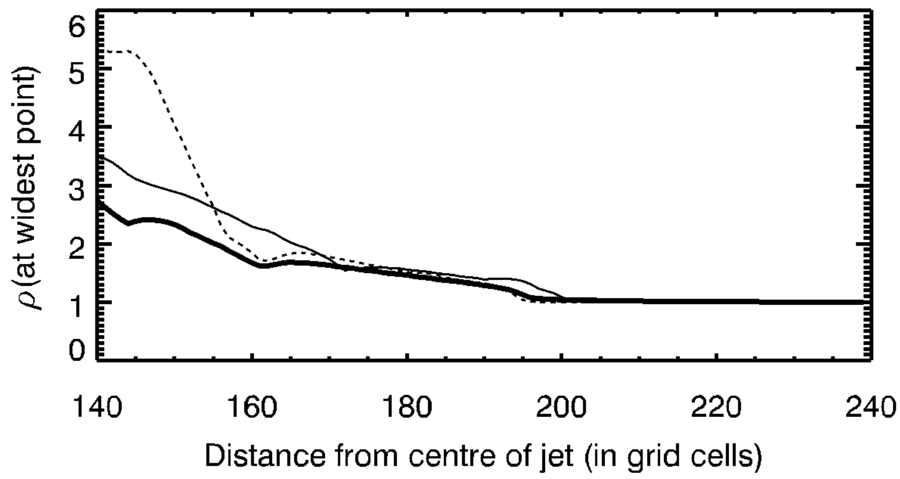

Figure 7.9: The maximum density, as calculated along z, is plotted as a function of distance from the centre of the jet beam. The thin and thick solid lines represent the ideal MHD and nonideal MHD cases respectively, and the thin dashed line represents the hydrodynamic case.

to that found in the ideal MHD case.

In the regions of slow moving plasma in the wings of the bowshock the magnetic field plays a greater role, as its energy becomes comparable to the kinetic energy of the plasma. For this reason we expect multifluid MHD effects to be important in these regions. The presence of a magnetic field was earlier found to result in an increase in the signal speed in the plasma. If the charged fluids become decoupled from the neutral fluid through ambipolar diffusion, this signal speed increases further. The effect of this process is measured by the widths to which the bowshock expands. Following the same calculation as in the nonideal MHD case, we find the diameters of the bowshocks to be 434 and 402 grid cells across, for the ambipolar-only and Hall-only cases respectively. Recalling the values calculated earlier, it can be seen that the width of the ambipolar-only bowshock matches exactly that of the nonideal MHD case, while the width of the Hall-only bowshock is within 2 grid cells of that of the ideal MHD case.

Helicity The magnetic helicities of the various nonideal MHD systems are calculated from

$$H = \int_x \int_y \int_z \mathbf{B} \cdot (\nabla \times \mathbf{B}) \, dx \, dy \, dz \, . \tag{7.3}$$

The helicity of the nonideal MHD system is found to be of the order 10^{-7}, while the helicities of the ambipolar-only and Hall-only cases are found to be of the order 10^{-7} and 10^{-6} respectively. This shows that the Hall effect causes a noticeably larger increase in the helicity of the system when it is the only nonideal MHD effect at work. The increased helicity in this case is caused by a winding up of the magnetic field due to the re-orientation of the field lines by the Hall effect. This leaves the system with a strong positive helicity. Figure 7.10 compares the configuration of the magnetic field near the base of the jet for the ideal MHD and Hall-only systems, and clearly demonstrates the anti-clockwise wind-up of the magnetic field lines as a result of the Hall effect.

Comparison of the magnetic field in these ideal MHD and Hall-only cases (figure 7.10, upper and lower panels) with that in the nonideal MHD case (figure 7.7, lower panel) demonstrates that the field lines in the nonideal system do not undergo the same wind-up as in the Hall-only case, despite including the same initial value of Hall resistivity. This is reflected in the calculation of the helicities above as the nonideal MHD case does not exhibit the same amount of helicity as the Hall-only case, but instead is much closer to that of the ambipolar-only system. This agrees with the phenomenon observed in chapter 6; the inclusion of ambipolar diffusion in the system suppresses the impact of the Hall effect.

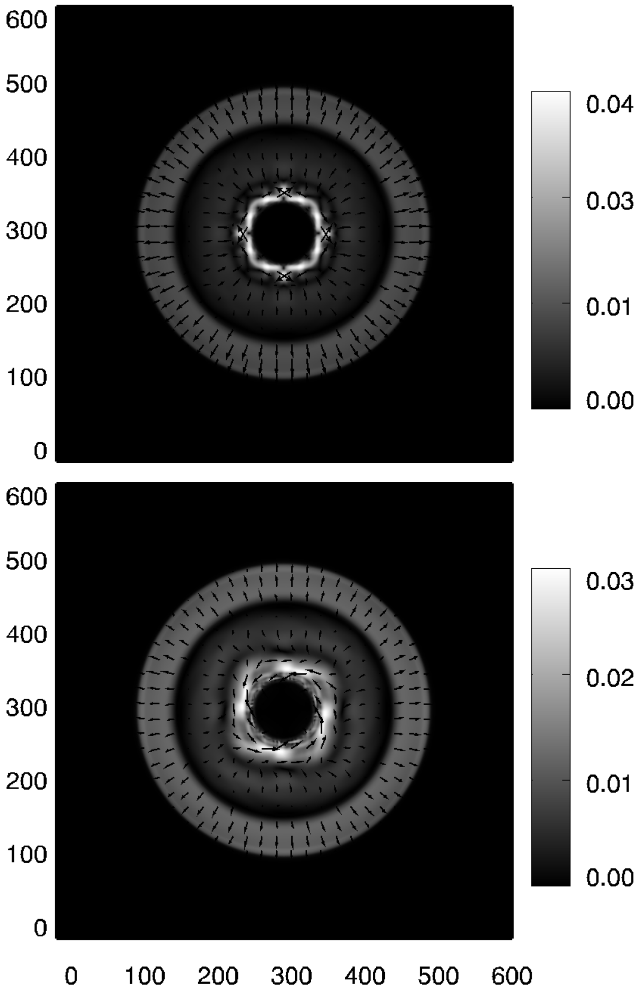

Figure 7.10: Plot of the magnetic field profile in the xy-plane through a slice near the base of the jet for the ideal MHD case (upper panel) and the Hall-only case (lower panel). There is an obvious anti-clockwise wind-up observed in the magnetic field for the Hall-only system.

Chapter 8

Conclusions

This thesis describes a number of multifluid MHD studies of weakly ionised astrophysical plasmas. In particular, we simulate and study the impact on the development of the Kelvin-Helmholtz instability and jet-driven bowshocks due to the inclusion of the multifluid effects expected to occur in molecular clouds, namely ambipolar diffusion and the Hall effect. These simulations are carried out using the numerical code HYDRA. As HYDRA uses an explicit scheme to integrate the MHD equations, parallelisation of the code allows us to carry out multifluid high resolution 2 D simulations of the Kelvin-Helmholtz instability, as well as 3 D simulations of jet-driven bowshocks in lower resolution.

By isolating each of the nonideal MHD effects in different simulations, the impact of the individual effects on the nonlinear growth of the KH instability is studied in more detail than ever before in the literature. This enables us to provide a detailed explanation of the dynamics resulting from the inclusion of either ambipolar diffusion or the Hall effect. This is applicable to any system in which either effect occurs individually. The third and final KH simulation combines the two nonideal effects. This allows us to describe not only their combined impact on the development of the instability, but also the manner in which the two effects influence one another.

The effect that ambipolar diffusion has on the development of the KH instability is studied initially in chapter 4. In the linear regime of the instability, we calculate the growth rates for systems with varying initial values of ambipolar resistivity, as well as a hydrodynamical system. We conclude that while the magnitude of the initial magnetic field does affect the results as expected, for a system with constant initial magnetic field strength and fluid parameters, varying the amount of ambipolar resistivity does not affect the linear growth rate of the instability.

Ambipolar diffusion is introduced into the system by decreasing the collision rate between the neutral and ion fluids. The decoupling of the magnetic field lines from the bulk fluid is observed in two independent processes, which can be distinguished by two separate set-ups. A moderate amount of ambipolar resistivity leads to the reconnection of magnetic field lines, resulting in less amplification of the magnetic energy in the system and greater wind-up of all of the fluids in the plasma. A higher value of ambipolar resistivity results in the dynamics of the charged fluids no longer reflecting those of the neutral fluid, but instead reflecting that of the magnetic field. This occurs for a magnetic Reynolds number $Re_{\mathrm{m}} \leq 100$, and is demonstrated by the wind-up of the ion fluid. This reaches a greater maximum in the case of moderate ambipolar resistivity, but a smaller wind-up in the case of high ambipolar resistivity.

Our simulations continue to follow the evolution of the KH instability in order to examine the effects of ambipolar diffusion at later stages in its development. The KH vortex is subjected to very different dynamics during these later stages for the different systems. In the hydrodynamical case, the system is observed to reach a stable state with a perpetual KH vortex. In the case of negligible resistivity, the system experiences further growth and decay of the kinetic energy and magnetic energy in the system respectively, as the amplified magnetic field stretches and distorts the vortex until it merges with its neighbouring vortex, creating secondary vortices. In the case of high ambipolar resistivity, the magnetic field is not strong enough to stretch the vortex in this manner and instead the field gradually unwinds and returns to its original configuration. This results in a gradual stabilisation of the plasma, which eventually returns to simple laminar flow on either side of a widened KH-resistive shear layer.

We conclude that the inclusion of ambipolar diffusion greatly influences the evolution of the KH instability. While not affecting the linear growth rate, the nonlinear stage sees the magnetic field undergoing a very different dynamical process and the decay of the KH vortex is brought about much sooner than it would have otherwise.

A study of the Hall effect on the development of the KH instability is carried out in chapter 5. In the initial linear stage of the instability, we calculate that neither moderate nor high Hall resistivity causes the system to experience a deviation from the KH growth rate calculated for the system with negligible resistivity. With a moderate value of Hall resistivity, the initial wind-up of the plasma is unaffected. Consequently, the degree to which the winding-up of the plasma affects the magnetic field is unchanged and the magnetic energy in the system reaches the same initial maximum. However, this does not result in the same winding-up of the magnetic field. As the ion fluid is less strongly coupled to the magnetic field than the electron fluid is, a relative velocity is observed between these two fluids. This results in the Hall term, $\mathbf{J} \times \mathbf{B}$, with a current that is not parallel to the magnetic field. As a result, some of the magnetic energy is transferred from the xy-plane into the z-direction through twisting of the magnetic field lines.

The simulation with high Hall resistivity shows a much greater deviation from the system of negligible resistivity. Further decoupling results in the ion and neutral fluid behaving almost independently of the magnetic field and the electron fluid. As a result, the magnetic field provides little resistance to the evolution of the KH vortex, and the plasma undergoes a wind-up almost equal to that in the hydrodynamic system. Conversely, the magnetic field undergoes little wind-up, due to its decoupling from the bulk plasma. This quickly results in a large velocity difference between the ion and electron fluids, leading to a strong $\mathbf{J} \times \mathbf{B}$ term.

The behaviour of the high Hall simulation continues in an interesting manner. The system can be thought of as two almost independent systems. The neutral and ion fluid continue almost unaffected by the magnetic field, and as in the hydrodynamic case, the KH vortex remains undisturbed. The twisting of the magnetic field lines into the z-direction causes flow of the electron fluid in the same direction. This results in a current in the z-direction, which in turns causes the magnetic field lines and flow of electrons to be twisted in three dimensional space. During this re-orientation the electron fluid obtains a velocity outwards from the KH vortex, which results in a broader volume of plasma being disturbed. This plasma effectively injects further kinetic energy into the system. The twisting of further field lines that follows causes the magnetic energy to continue to grow. This is an energy-efficient system and demonstrates continuous dynamo behaviour. The total energy of the system therefore experiences a loss during the initial growth of the KH instability, but then levels off as the system evolves. The continued growth of the magnetic energy is limited only by the volume of plasma in the system and its available kinetic energy.

We conclude that the Hall effect can greatly influence the evolution of the KH instability, depending on the value of the initial Hall resistivity in the system. The simulation in this study with moderate Hall resistivity contains the same value of Hall resistivity determined to be in molecular clouds and clearly demonstrates a re-orientation of the magnetic field into the z-direction, along with a flow of plasma in that same direction. We would therefore naively expect to observe the same results from a simulation with initial conditions representing a molecular cloud. For larger values of Hall resistivity, the twisting of magnetic field lines has been seen to lead to magnetic dynamo action, as has been only previously predicted by linear studies. In this case the growth of magnetic energy in the system is limited only by the size of the grid on which the simulation is run.

A study of the KH instability under molecular cloud conditions is carried out in chapter 6. This allows for the combined effects of ambipolar diffusion and the Hall effect to be examined in comparison to an ideal MHD system. As molecular clouds are dominated by ambipolar diffusion, it is expected that the results will closely reflect those of the ambipolar-only simulation, and this is indeed observed. However, our naive expectation suggests that the Hall effect should also be observed through twisting of the magnetic field lines. In the initial linear regime, the growth rates of the instability remain unchanged. As the instability continues to develop, magnetic reconnection leads to less amplification of the magnetic energy in the system and therefore a stronger wind-up of the plasma. This is very similar to the results observed in the ambipolar-only system. Later behaviour of the instability, including the breakdown of the KH vortex and its return to a stable state and laminar flow, also closely reflects that observed in the ambipolar-only system.

The most noteworthy result from this chapter is the lack of impact on the system due to the inclusion of the Hall effect. This particular set-up includes three charged fluids (ions, electrons and dust grains) as well as the neutral fluid, however the same result can be observed in a system with two charged fluids (ions and electrons) as well as the neutral fluid. In the case of two charged fluids, Hall resistivity is introduced into the system by initialising the ion fluid to be weakly coupled to the magnetic field. Ambipolar resistivity is then introduced by reducing the collision rate of this same fluid with the neutral fluid. As the ion fluid is no longer subject to collisions with the neutrals, it is the magnetic field that plays the dominant role on its dynamics, despite the weak coupling. This minimises the impact of the Hall effect in the system. In the case of three charged fluids, Hall resistivity is introduced into the system by initialising the dust grain fluid to be weakly coupled to the magnetic field. The collision rate of the ion fluid is then decreased in order to introduce ambipolar diffusion. However, the dust grain fluid has a much smaller charge density in comparison to that of the ion and electron fluids. As a result, the effective current is due to the relative velocities of the ion and electron fluids and not the dust grain fluid. As both the electron and ion fluids remain tightly coupled to the magnetic field, their relative velocity will continue to be in the direction of the magnetic field lines, resulting again in a suppression of the Hall effect in the system.

We conclude that for the parameters observed in ambipolar-dominated molecular clouds, the evolution of the KH instability is indeed dominated by the presence of ambipolar diffusion. However, the system does not demonstrate the twisting of the magnetic field lines due the inclusion of the Hall effect as naively expected. This suppression of the Hall effect by ambipolar diffusion is given an original and detailed explanation based on basic physics principles and for set-ups using a variety of charged fluids.

We have found that multifluid MHD effects can greatly influence the development of the Kelvin-Helmholtz instability in weakly ionised molecular clouds. As the KH instability can occur anywhere with a velocity shear, it has numerous applications in molecular clouds. One such possible application is at the boundary of a jet-driven bowshock with the ambient molecular cloud. Limited by resolution and timescales, we do not attempt to produce the growth of the KH instability at the bowshock boundary. Instead, chapter 7 gives a broad overview of the changes to the general morphology of a jet-driven bowshock as a result of introducing nonideal MHD effects. The simulations provide the first preliminary 3 D numerical study of bowshocks under multifluid MHD conditions.

One result of introducing nonideal MHD effects to the system is a lowering of the density of plasma at the head of the jet. This in turns results in a slower lateral ejection of the fluid out along the wings of the bowshock. As the plasma has a lower lateral velocity, the bowshock develops a narrower, less blunt shape around the head of the jet. Another consequence of the smaller lateral velocities is that the momentum measured in the wings of the bowshock is considerably lower. This is an important result for studies of the ability of jet-driven bowshock to account for the momentum measured in molecular clouds.

The kinetic energy of the jet is found to dominate most of the dynamics in the system, except where the plasma flow is slow enough that the magnetic energy becomes relevant. In such regions as the wings of the bowshock, the velocity of the plasma decreases to a point where the fast magnetosonic wave is found to be capable of accelerating the plasma. In the nonideal MHD case, the Alfvén speed in the ion fluid is calculated to be very high, and so the charged fluids and the magnetic field are accelerated outwards even further. We propose that the fast magnetosonic wave in the ideal MHD case causes a slight widening of the bowshock. In the nonideal MHD case the decoupling of the charged fluids from the neutrals should result in a further widening of the bowshock. These processes are confirmed through quantitative calculations of the width of the bowshock. In the nonideal MHD case, it can be seen that it is the magnetic field and charged fluids that are measured to have been widened the furthest. Through collisions with the neutrals, the bulk fluid is also found to have traveled further out than in the ideal MHD case. This acceleration of the neutrals by the charged fluids results in a C shock that can be seen in plots of the lateral velocities in the region.

As the nonideal MHD simulation contains both ambipolar diffusion and the Hall effect, further simulations are run in order to attribute the various results to one effect or the other. Calculations of the momentum in the wings of the bowshock for these two simulations indicate that the decrease in the momentum found in the nonideal MHD case can be attributed solely to the inclusion of ambipolar diffusion. As the increased signal speed in the nonideal MHD case relies on decoupling of the charged fluids from the neutral fluid, it is no surprise to find that this result is echoed in the ambipolar-only simulation and not in the Hall-only case. Finally the helicity is calculated for each of the three systems with nonideal MHD effects. It is found that while the Hall-only system demonstrates strong positive helicity, this result is not reflected in the nonideal MHD case. This is another example of the phenomenon explained earlier; the inclusion of ambipolar diffusion suppresses the impact of the Hall effect.

We conclude that the inclusion of multifluid effects may be important in further studies of the evolution of a bowshock. The embedded magnetic field is weak and the differences between the HD and ideal MHD systems are restricted to regions in the bowshock in which the magnetic energy can compare with the high kinetic energy of the jet. Similarly, the effect of multifluid MHD conditions are observed only in certain regions. While our simulations do not show drastic changes to the overall morphology of the bowshock, some results may be important in certain studies of jet-driven bowshocks.

This concludes the work carried out in this thesis. The Kelvin-Helmholtz instability in weakly ionised plasmas has been studied to the extent currently allowed by the numerical code HYDRA. However, further adaptations of this code could be made in the future, allowing for further study of the instability. The process of adapting the code for a fully ionised plasma, for example, has already been initiated by deriving the Generalised Ohm's Law in section 2.4.1 for a fully ionised plasma using the same format as was used in the weakly ionised case. Implementation of the fully ionised MHD equations into the code is centred on attaining the Generalised Ohm's Law in this format. However, while solving the remaining variables for a fully ionised plasma should be straightforward to implement, a certain amount of work remains to be done. Although 2-fluid MHD has been used before in order to study the Hall effect, our derivation shows that there exist certain conditions under which ambipolar diffusion could also exist, and this should prove interesting to study.

Further work can also be carried out on the subject of multifluid MHD simulations of jet-driven bowshocks. Currently our simulations are limited by resolution and the assumption of an isothermal system. However, HYDRA has recently been adapted for adiabatic systems, and with access to greater computing power, simulations of improved resolution will be achievable. A high resolution study using an adiabatic system will enhance the study carried out here on jet-driven bowshocks under nonideal MHD conditions.

Bibliography

Alexiades V., Amiez G., Gremaud P.A., 1996, Com. Num. Meth. Eng., 12, 31

Amerstorfer U.V., Erkaev N.V., Langmayr D., Biernat H.K., 2007, P&SS, 55, 1811

Artola M., Majda A., 1987, PhyD, 28, 253

Bacciotti F., Chiuderi C., Oliva E., 1995, A&A, 296, 185

Bacciotti F., Eislöffel J., 1999, A&A, 342, 717

Bacciotti F., Ray T.P., Eislöffel J., Woitas J., Solf J., Mundt R., Davis C.J., 2003, Ap&SS, 287, 3

Bachiller R., 2009, Protostellar Jets in Context pp. 381, Springer

Bally J., Devine D., 1994, ApJ, 428, 65

Bally J., Licht D., Smith N., Walawender J., 2006, AJ, 131, 473

Bally J., 2007, Ap&SS, 311, 15

Bally J., 2009, Protostellar Jets in Context pp. 11, Springer

Baty H., Keppens R., 2006, A&A, 447, 9

Bertoldi F., McKee C.F., 1992, ApJ, 395, 140

Bettarini L., Landi S., Rappazzo F.A., Velli M., Opher M., 2006, A&A, 452, 321

Birk G.T., Wiechen H., 2002, PhPl, 9, 964

Birkinshaw M., 1991, Beams and Jets in Astrophysics (Chapt. 6). Cambridge University Press

Blitz L., Fukui Y., Kawamura A., Leroy A., Mizuno N., Rosolowsky E., 2007, Protostars and Planets V, 81

Blumen W., 1970, JFM, 40, 769

Bodo G., Massaglia S., Ferrari A., Trussoni E., 1994, A&A, 283, 655

Bontemps S., Andre P., Terebey S., Cabrit S., 1996, A&A, 311, 858

Bucciantini N., Del Zanna L., 2006, A&A, 454, 393

Bührke T., Mundt R., Ray T.P., 1988, A&A, 200, 99

Cabrit S., Raga A., Gueth F., 1997, IAUS, 182, 163

Carver R.L., Cunningham A.J., Frank A., Hartigan P., Coker R., Wilde B.H., Foster J., Rosen P., 2010, HEDP, in press

Casse F., Meliani Z., Sauty C., 2007, Ap&SS, 311, 57

Cerqueira A.H., de Gouveia dal Pino E.M., Herant M., 1997, ApJ, 489, 185

Cerqueira A.H., de Gouveia dal Pino E.M., 1999, ApJ, 510, 828

Chandrasekhar, S., 1961, Hydrodynamic and hydromagnetic stability. Clarendon, Oxford

Ciolek G.E., Roberge W.G., 2002, ApJ, 567, 947

Corkery S., 2008, “Propagation of molecular clouds into inhomogenous media”, MSc thesis, Dublin City University

Cowling T.G., 1957, Magnetohydrodynamics. Interscience Publishers, Inc., New York

Crutcher R.M., 1999, ApJ, 520, 706

De Colle F., Raga A.C., Esquivel A., 2008, ApJ, 689, 302

De Gouveia dal Pino E.M., 2005, AdSpR, 35, 908

De Young D.E., 1986, ApJ, 307, 62

Dedner A., Kemm F., Kröner D., Munz C.-D., Schnitzer T., Wesenberg M., 2002, JCoPh, 175, 645

Downes T.P., Ray T.P., 1998, A&A, 331, 1130

Downes T.P., Ray T.P., 1999, A&A, 345, 977

Downes T.P., 2009, Protostellar Jets in Context pp. 395, Springer

Downes T.P., O'Sullivan S., 2009, ApJ, 701, 1258

Draine B.T., Roberge W.G., Dalgarno A., 1983. ApJ, 264, 485

Dyson J.E., 1984, Ap & SS, 106, 181

Eislöffel J., Mundt R., 1997, AJ, 114, 280

Elmegreen B.G., 1979, ApJ, 232, 729

Engargiola G., Plambeck R.L., Rosolowsky E., Blitz L., 2003, ApJS, 149, 343

Falle S.A.E.G., 2003, MNRAS, 344, 1210

Fiege J.D., Pudritz R.E., 2000, MNRAS, 311, 85

Fix, J.D., 1995, Astronomy: Journey to the Cosmic Frontier. Times Mirror Higher Education Group, Inc.

Franco J., 1983, ApJ, 264, 508

Frank A., Jones T.W., Ryu D., Gaalaas J.B., 1996, ApJ, 460, 777

Frank A., 1998, AIPC, 431, 513

Frank A., Gardiner T.A., Delemarter G., Lery T., Betti R., 1999, ApJ, 524, 947

Goldreich P., Reisenegger A., 1992, ApJ, 395, 250

Goldsmith P.F., Li D., 2005, ApJ, 622, 938

Gómez G.C., Ostriker E.C., 2005, ApJ, 630, 1093

Guelin M., Langer W.D., Snell R.L., Wootten H.A., 1977, ApJ, 217, 165

Hardee P.E., Norman M.L., 1988, ApJ, 334, 70

Hardee P.E., Norman M.L., 1989, ApJ, 342, 680

Hardee P.E., Stone J.M., 1997, ApJ, 483, 121

Hardee P., Stone J., Rosen A., 1997, IAUS, 182, 132

Hasegawa H., Fujimoto M., Phan T.-D., Rème H., Balogh A., Dunlop M.W., Hashimoto C., TanDokoro R., 2004, Nat, 430, 755

Heiles C., Troland T.H., 2005, ApJ, 624, 773

Helfer T.T., Thornley M.D., Regan M.W., Wong T., Sheth K., Vogel S.N., Blitz L., Bock D.C.-J, 2003, ApJS, 145, 259

Huba J.D., 1994, PhRvL, 72, 2033

Jeong H., Ryu D., Jones T.W., Frank A., 2000, ApJ, 529, 536

Johansen A., Henning T., Klahr H., 2006, ApJ, 643, 1219

Jones T.W., Gaalaas J.B., Ryu D., Frank A., 1997, ApJ, 482, 230

Kant I., 1755, Allgemeine Natur Geschichte and Theorie des Himmels

Keppens R., Tóth G., Westermann R.H.J., Goedbloed J.P., 1999, JPlPh, 61, 1

Kobayashi Y., Kato M., Nakamura K.T.A., Nakamura T.K.M., Fujimoto M., 2008, AdSpR, 41, 1325

Krall N.A., Trivelpiece A.W., 1973, Principles of Plasma Physics. McGraw-Hill, Kogakusha

Kunz M.W., 2008, MNRAS, 385, 1494

Laplace P.S. de, 1796, Exposition du Système du Monde

Li L.-X., Narayan R., 2004, ApJ, 601, 414

Liszt H.S., 1993, ApJ, 411, 720

Livio M., 2009, Protostellar Jets in Context pp. 3, Springer

Lopéz R., Raga A., Riera A., Anglada G., Estalella R., 1995, MNRAS, 274, 19

Luo Q.Z., D'Angelo N., Merlino R.L., 2001, PhPl, 8, 31

Malagoli A., Bodo G., Rosner R., 1996, ApJ, 456, 708

Massaglia S., Trussoni E., Bodo G., Rossi P., Ferrari A., 1992, A&A, 260, 243

Matzner C.D., 2002, ApJ, 566, 302

Meliani Z., Casse F., Sauty C., 2006, A&A, 460, 1

Mestel L., Spitzer L. Jr., 1956, MNRAS, 116, 503

Mitchner M., Kruger C.H., 1973, Partially Ionized Gases. John Wiley & Sons Inc.

Miura A., Pritchett P.L., 1982, JGR, 87, 7431

Miura A., 1990, GeoRL, 17, 749

Miura A., 1992, JGR, 97, 10655

Morse J.A., Heathcote S., Cecil G., Hartigan P.; Raymond J.C., 1993, ApJ, 410, 764

Mundt R., Fried J.W., 1983, ApJ, 274, 83

Mundt R., 1986, CaJPh, 64, 407

Mundt R., Brugel E.W., Bührke T., 1987, ApJ, 319, 275

Muxlow T.W.B., Garrington S.T., 1991, Beams and Jets in Astrophysics (Chap. 2). Cambridge University Press

Norman C., Silk J., 1980, ApJ, 238, 158

Nykyri K., Otto A., 2004, AnGeo, 22, 935

O'Sullivan S., Downes T. P., 2006, MNRAS, 366, 1329

O'Sullivan S., Downes T. P., 2007, MNRAS, 376, 1648

Padman R., Lasenby A.N., Green D.A., 1991, Beams and Jets in Astrophysics (Chapt. 10). Cambridge University Press

Padman R., Bence S., Richer J., 1997, IAUS, 182, 123

Padmanabhan, T., 2002, Theoretical Astrophysics. Cambridge University Press

Palotti M.L., Heitsch F., Zweibel E.G., Huang Y.-M., 2008, ApJ, 678, 234

Pandey B.P., Wardle M., 2006, astro.ph, 8008

Parker E.N., 1966, ApJ, 145, 811

Pelletier, G., 2007, Lect. Notes Phys. 723, 77

Phillips A.C., 1994, The Physics of Stars. John Wiley and Sons, Inc., New York

Piddington J.H., 1954, MNRAS, 114, 638

Raga A.C., 1993, Ap&SS, 208, 163

Raga A., Cabrit S., 1993, A&A, 278, 267

Raga A.C., de Gouveia Dal Pino E.M., Noriega-Crespo A., Mininni P.D., Velázquez P.F., 2002, A&A, 392, 267

Ray T.P., 1987, A&A, 171, 145

Ray T.P., 1988, IrAJ, 18, 219

Ray T.P., Mundt R., Dyson J.E., Falle S.A.E.G., Raga A.C., 1996, ApJ, 468, 103

Ray T.P., Muxlow T.W.B., Axon D.J., Brown A., Corcoran D., Dyson J., Mundt R., 1997, Nat, 385, 415

Reipurth B., 1989, Nat, 340, 42

Reipurth B., Bally J., 2001, ARA&A, 39, 403

Rees M.J., 1971, Nat, 229, 312

Richardson L.F., 1911, Phil. Trans. R. Soc. London, Ser. A, 210, 307

Shadmehri M., Downes T.P., 2008, MNRAS, 387, 1318

Shibata K., Uchida Y., 1986, PASJ, 38, 631

Shu F.H., Adams F.C., Lizano S., 1987, ARA&A, 25, 23

Shu F.H., Ruden S.P., Lada C.J., Lizano S., 1991, ApJ, 370, 31

Shu F.H., Najita J., Ostriker E.C., Shang H., 1995, ApJ, 455, 155

Solomon P.M., Sanders D.B., Rivolo A.R., 1985, ApJ, 292, 19

Solomon P.M., Rivolo A.R., Barrett J., Yahil A., 1987, ApJ, 319, 730

Song P., Gombosi T.I., Ridley A.J., 2001, JGR, 106, 8149

Spitzer Jr. L., 1956, Physics of Fully Ionized Gases. Interscience Publishers, Inc., New York

Stahler S.W., 1994, ApJ, 422, 616

Stone J.M., Norman M.L., 1993, ApJ, 413, 210

Stone J.M., Xu J., Hardee P., 1997, ApJ, 483, 136

Stone J.M., Hardee P.E., 2000, ApJ, 540, 192

Strang G., 1968, SJNA, 5, 506

Todo Y., Uchida Y., Sato T., Rosner R., 1992, PASJ, 44, 245

Uchida Y., Shibata K., 1985, PASJ, 37, 515

Umebayashi T., Nakano T., 1990, MNRAS, 243, 103

Vázquez-Semadeni E., Gómez G.C., Jappsen A.K., Ballesteros-Paredes J., González R.F., Klessen R.S., 2007, ApJ, 657, 870

Venter L.A., Meintjes P.J., 2006, MNRAS, 366, 557

Walawender J., Bally J., Reipurth B., 2005, AJ, 129, 2308

Ward-Thompson D., André P., Crutcher R., Johnstone D., Onishi T., Wilson C., 2007, Protostars and Planets V, 33

Wardle M., 1999, MNRAS, 307, 849

Wardle M., Ng C., 1999, MNRAS, 303, 239

Wardle M., 2004a, Ap&SS, 292, 317

Wardle M., 2004b, IAUS, 221, 395

Wardle M., 2007, Ap&SS, 311, 35

Watson C., Zweibel E.G., Heitsch F., Churchwell E., 2004, ApJ, 608, 274

Wiechen H.M., 2006, PhPl, 13, 2104

Zuckerman B., Palmer P., 1974, ARA&A, 12, 279

Zweibel E.G., McKee C.F., 1995, ApJ, 439, 779